Ahmad, Jakaria (2015) ***Synthesis and characterization of plasma polymer thin films from γ-terpinene for encapsulation of electronic devices.*** **PhD thesis, James Cook University.**

Synthesis and Characterization of Plasma Polymer Thin Films from γ–terpinene for Encapsulation of Electronic Devices

Thesis submitted by

Jakaria Ahmad

in January 2015

for the degree of Doctor of Philosophy
in the College of Science, Technology and Engineering
James Cook University

Supervisors: Assoc Prof. Mohan Jacob, Prof. Ron White, Dr. Kateryna Bazaka

DECLARATION

I hereby declare that the work presented in this thesis entitled ***"Synthesis and Characterization of Plasma Polymer Thin Films from γ–terpinene for Encapsulation of Electronic Devices"*** is based on the original research work done by me in the College of Science, Technology and Engineering, James Cook University (JCU), Townsville, QLD Australia, and has never been submitted in any form for another degree or diploma at any university or other institute of tertiary education. Information derived from the published and unpublished work of others has been acknowledged in the text, and a list of references is given.

Jakaria Ahmad

January 2015

STATEMENT OF ACCESS TO THIS THESIS

I, the under-signed, the author of this work, understand that James Cook University (JCU) will make this work available for use within the University Library, and via the Australian Digital Thesis Network, for use elsewhere.

I understand that as an unpublished work, a thesis has significant protection under the Copyright Act. I do not wish to place any restriction on access to this thesis. However, any use of its content must be acknowledged and could potentially be restricted by future patents.

Jakaria Ahmad

January 2015

STATEMENT ON THE CONTRIBUTIONS FROM OTHERS

This thesis included the following contributions of others:

Funding: Support was provided from International Research Alliances Program (NIRAP) and James Cook University Postgraduate Research Award (JCUPRS) throughout the duration of this thesis. Additional support was provided from the College of Science, Technology and Engineering and Graduate Research Scheme funding.

Editorial assistance: Assoc Prof. Mohan Jacob, Prof. Ronald White, Dr. Kateryna Bazaka and Assoc Prof Michael Oelgemöller of James Cook University provided editorial assistance. Dr. Jason Whittle of University of South Australia also provided assistance with chapter III.

Experimental assistance and data analysis: Assoc Prof. Mohan Jacob and Dr. Kateryna Bazaka provided me with experimental assistance and guidelines for data analysis throughout the duration of this research work. Solar stability study was performed with assistance from Assoc Prof Michael Oelgemöller of James Cook University and Assoc Prof. Ashraf Uddin of University of New South Wales. Mass spectroscopy and XPS measurements and extraction of data from these were obtained by the assistance of Dr. Jason Whittle of University of South Australia.

Contributions to co-authored publications: Assoc Prof. Mohan Jacob and Dr. Kateryna Bazaka assisted me with their valuable comments to edit the papers I published. Although I have co-authored papers, I have received partial assistance in terms of access to facilities not available at James Cook University; this is substantiated by my first authorship on all papers relevant to this thesis. In the publication *Wetting, solubility and chemical characteristics of plasma polymerized 1-isopropyl-4-methyl-1,4-cyclohexadiene thin films,* editorial assistance was provided by Assoc Prof Michael Oelgemöller of James Cook University. Chapter relevant to *mass spectroscopy of γ–terpinene* include experimental and editorial contributions from collaborator at the University of South Australia. Chapter relevant to stability study include experimental and editorial contributions from Assoc Prof Michael Oelgemöller of James Cook University and Assoc Prof. Ashraf Uddin of University of New South Wales.

Except for the cases noted above, I performed all experimental, analytical and editorial work.

ACKNOWLEDGEMENTS

First, I would like to thank my research advisor, Assoc Prof. Mohan Jacob for providing valuable guidance, financial support, and encouraging creative ideas and critical thinking throughout my PhD at College of Science, Technology and Engineering, James Cook University (JCU), Townsville, QLD Australia. I also wish to thank my supervisory committee members Prof. Ron White and Dr. Kateryna Bazaka for their supervision, suggestions, feedback, and critique of my work throughout this project. Without their assistance, encouragement and patience this wouldn't have been possible.

Thanks to the academic and support staff of College of Science, Technology and Engineering, James Cook University (JCU), for all of their assistance with things small and large over the years, and the academic opportunities given to me.

Thanks to everyone I have collaborated with; Assoc Prof Michael Oelgemöller from School of Pharmacy and Molecular Sciences, Dr. Jason Whittle from University of South Australia and Assoc Prof. Ashraf Uddin of University of New South Wales.

I am grateful for the financial support provided to me throughout this PhD through the NIRAP, JCUPRS scholarships and GRS funding.

Thanks to all my friends. There are too many of you to name, but I appreciate everything.

Finally, thanks to my wife and son who inspired and supported me through my PhD. It would not have been possible to write this doctoral thesis without the help and support from them. Thanks to my parents, brother and sister for their love, encouragement, and precious support over the years.

ABSTRACT

The rapid development of polymers and polymer based materials is leading to a number of promising organic devices e.g., solar cells and solid-state lighting, advancing display technology, sensors, and thin-film transistors. One obstacle to this development is the susceptibility of these devices to water vapor and oxygen that causes rapid degradation in many organic electronic devices. In order to maintain the efficiency and guarantee the minimum lifetime needed for various applications, high barrier performance encapsulation materials and structures must be developed. In this work, radio frequency (RF) plasma deposited γ–terpinene thin films were considered as a potential candidate for OPVs, specifically as encapsulation coatings, and as insulating layers in flexible electronics.

γ-terpinene is a non-synthetic isomeric hydrocarbon derived from *Melaleuca alternifolia* essential oil. Thin films from this monomer were fabricated using plasma enhanced chemical vapor deposition in this research work under varied process conditions. The resultant polymer, plasma polymerized γ-terpinene (pp–GT) thin films were found to be optically transparent, with refractive indices in a range of 1.57–1.58 (500 nm). The optical band gap (E_g) of pp–GT thin films were ~3 eV that fell into the insulating E_g region. Independent of deposition conditions, the surfaces were smooth and defect-free, with uniformly distributed morphological features. Films fabricated at higher deposition power displayed enhanced resistance to delamination and wear, and improved hardness, from 0.40 GPa (10 W) to 0.58 GPa (75 W).

Investigations on the wetting, solubility and chemical composition of pp–GT thin films revealed that the polymers were structurally dissimilar to the original monomer and highly cross-linked. The polymer surfaces were hydrocarbon-rich, with oxygen present in the form of O–H and C=O functional groups. The oxygen content decreased with deposition power, with films becoming more hydrophobic and, thus, less wettable. The polymers were determined to resist solubilisation in solvents commonly used in the deposition of organic semiconducting layers, including chloroform and chlorobenzene, with higher stability observed in films fabricated at higher RF power.

Electrically, pp–GT thin films were highly insulating, possessing decreasing conductivity from 1.39×10^{-12} S/cm (10W) to 1.02×10^{-13} S/cm (75W), attributed to the change in the chemical composition and structure of the polymer. At a frequency of 100 kHz, the dielectric constant varied from 3.69 (10 W) to 3.24 (75 W). The current density–voltage ($J-V$) characteristics revealed that at higher applied voltage region, Richardson Schottky conduction was the dominant DC conduction mechanism.

pp–GT thin films were demonstrated to be optically, physically and chemically stable under the ambient conditions. The bulk of aging occurred after fabrication was attributed to oxidation and volumetric relaxation. Photostability experiments showed that photooxidation takes place under UV irradiation in oxygen–rich conditions. With UV–C light, photodegradation occurred by additional cleavage pathways. Photostability could be improved (UV-C) or completely achieved (UV-A) in an oxygen-poor environment.

Finally, fully characterized pp–GT encapsulation layers were integrated with organic PCPDTBT:PC$_{70}$BM solar cell to validate the effectiveness of the barrier layers. The encapsulated solar cell exhibited very slow decrease in efficiency compared to the non-encapsulated device.

CONTENTS

A.1 Materials and methods for encapsulation of OPV: A review

A.2 Optical and Surface Characterization of Radio Frequency Plasma Polymerized 1-Isopropyl-4-Methyl-1,4-Cyclohexadiene Thin Films

A.3 Wetting, Solubility and Chemical Characteristics of Plasma-Polymerized 1-Isopropyl-4-Methyl-1,4-Cyclohexadiene Thin Films

LIST OF FIGURES

LIST OF TABLES

LIST OF PUBLICATIONS

1. Ahmad, J., Bazaka, K., Anderson, Liam J., White, R. D., and Jacob, M. V. (2013) *Materials and methods for encapsulation of OPV: a review*. Renewable and Sustainable Energy Reviews, 27. pp. 104-117.
2. Ahmad, J., Bazaka, K., and Jacob, M. V. (2014) *Optical and surface characterization of radio frequency plasma polymerized 1-isopropyl-4-methyl-1,4-cyclohexadiene thin films*. Electronics, 3 (2). pp. 266-281.
3. Ahmad, J., Bazaka, K., Oelgemöller, M., and Jacob, M. V. (2014) *Wetting, solubility and chemical characteristics of plasma-polymerized 1-isopropyl-4-methyl-1,4-cyclohexadiene thin films*. Coatings, 4 (3). pp. 527-552.
4. Ahmad, J., Bazaka, K., Whittle, J., Michelmore, A. and Jacob, M. V. (2014) *Structural Characterization of γ-Terpinene Thin Films Using Mass Spectroscopy and X-ray Photoelectron Spectroscopy*. *Plasma Processes and Polymers*. doi: 10.1002/ppap.201400220.
5. Ahmad, J., Bazaka, K., and Jacob, M. V. (2014) *Electrical conduction in plasma polymerized thin films of γ-terpinene* (accepted for publication in the *Journal of Applied Polymer Science).*
6. Ahmad, J., Bazaka, K., Oelgemöller, M., Uddin, A. and Jacob, M. V. (2014) *Aging, thermal degradation, and solar stability of plasma polymerized γ-terpinene thin films* (submitted to *Polymer Degradation and Stability* for publication).

CHAPTER I

INTRODUCTION

I.1 RATIONALE

In spite of slowing growth of electricity consumption in developed countries due to efficiency gains from new appliance standards and advances in power-efficient technologies, increasing urbanization and economic growth in countries such as China and India continues to drive worldwide demand for energy. This need for energy is likely to expand even more in the coming years [1]. To meet the energy demand, fossil fuel (oil, gas and coal) is currently the most widely used energy source, accounting for up to 70% of electricity produced globally. In China, electricity generation continues to be dominated by coal, at 80% of total power produced. Such high dependence on burning of natural resources raises significant concerns, in terms of both limited availability of fossil fuels and energy-associated emissions [2, 3].

Growing environmental concerns, depleting natural resources, and associated price volatility of crude and refined oil have stimulated the demand for alternative energy sources. Amongst alternative energy sources, photovoltaics (PV) hold a considerable promise for it is a plentiful, easily accessible and renewable source of power, whereby solar radiation is directly converted to electricity. Photovoltaics are regarded as an environmentally friendly and a non-pollutant low maintenance energy source [4]. However, in spite of significant recent advancements in the area of solar energy generation and declining prices for PV units, the overall cost of generating electricity using this method remains high compared to both traditional (fossil fuel based) and other renewable power generation (e.g. hydro) [5]. At present, crystalline silicon (*Si*) cells remain the dominant PV technology, accounting for close to 90% of all commercially available PV products. However, the fabrication of the simplest *Si* cell is a complex and expensive process that has to take place under controlled conditions, such as high vacuum and temperatures of up to 1,400ºC. Concerns have also been raised regarding other materials used in PV devices, e.g. cadmium telluride (*CdTe*) and copper indium gallium selenide (*CIGS*). Among the most notable issues are those related to environment (e.g. toxicity of cadmium), price volatility (in particular with indium), and shortage of rare earth elements (e.g. tellurium) [6]. Finding an alternative PV technology is therefore essential and organic PV (OPV) have gained much attention in this regard during the past decade [6, 7].

Organic thin film PVs are an emerging economically competitive photovoltaic technology that combines manufacturing adaptability, low-cost processing and a lightweight, flexible device end product. The key property that makes OPV attractive is the potential to lower manufacturing costs by using reel-to-reel processing on low cost substrates, with numerous printing techniques, namely screen, inkjet, offset or flexo printing, already available [8]. In addition to printing, high throughput deposition processes such as physical vapor deposition (PVD), plasma enhanced chemical vapor deposition (PECVD) and other low temperature processes are widely used for fabrication of devices based on organic materials [6]. Considering the aforementioned attractive features of OPV, there has been a growing interest in the technology from industry and research groups alike, as reflected through a number of high quality reviews and special issues with different degrees of specialization [4, 8-40].

Undoubtedly promising, currently available OPV technology is yet to reach a desirable level of performance, which would render it suitable for wide commercial use. Present power conversion efficiency (PCE) and operational stability of OPV are considerably lower than those offered by *Si* technology. Significant research efforts have been devoted to development of materials, designs and structures to improve PCE of OPV, with a recent report of 11.9% for an organic cell [41]. Although this value falls short of 25–30% PCE level offered by *Si* PV cells, it may well be sufficient for a feasible commercial proposition when substantially less expensive production budget for OPV is considered. Long-term operation stability of OPV, however, is far below what would be considered acceptable for a commercial product, with the replacement costs negating the cost savings from inexpensive manufacturing. Currently, the acceptable lifetime of an inorganic solar cell is 20–25 years [42], well beyond the lifetime achievable by the most advanced organic solar cells currently available. Such profound discrepancy in device life expectancy between inorganic and organic PV cells stems from relatively high susceptibility of organic materials to water vapor and oxygen, which lead to reduced reliability and lifetime of organic devices under normal environmental conditions. As such, untimely degradation of individual materials and loss of device integrity are key limitations that hinder advancement and commercialization of OPV technology [42].

The past decade has seen the development of main mechanisms responsible for degradation of properties within the individual layers within polymeric OPV cell, from photoactive layer to electrode to interconnection to encapsulation. *Grossiord et. al.* reviewed the present understanding of the degradation mechanisms within OPV [5], highlighting the multi-trigger, multi-site and interrelated nature of these mechanisms and their synergistic effect on temporal decay in I–V curves. From their work and reports of others [5, 43], it is evident that the overall stability of OPV cell is dependent on stability of the actual photoactive component, the barrier and substrate layers and the interfacial stability. As such, significant research efforts have been directed towards increasing these stabilities, with most efforts concentrated on improving the intrinsic stability of photoactive materials within the cell structure [8, 14, 44-46]. Some of the approaches included use of photoactive layers with more stable monomer units and minimal number of reactive side groups [47], stabilization through introduction of additives [48], optimization of polymer synthesis routes to minimize incidence and concentration of impurities [49], and post-synthesis purification treatments [47], to name but a few [5]. Another highly effective strategy to extend the device lifetime involves changes in the device architecture to inverted geometry [50].

Much work has been devoted to the development of superior quality encapsulation technologies to limit oxygen and moisture permeation from the environment into device layers. Suitably high barrier performance encapsulation materials and structures can further extend device stability and life expectancy providing sufficient durability to render OPV commercially attractive [51-54]. However, these materials have to meet the requirements of good processability, high optical transmission, high dielectric constant, low water absorptivity and permeability, high resistance to ultra-violet (UV) degradation and thermal oxidation, good adhesion, mechanical strength, and chemical inertness [55]. Due to the good combination of these properties and established history of acceptable durability, inorganic materials are most commonly used as encapsulants [56]. However, organic encapsulation materials offer significant advantages over inorganic counterparts, including flexibility in the synthesis of the organic molecules, which allows parameters such as the molecular weight, energy levels, bandgap and solubility to be altered [8]. They are also disposable and have lower negative impact on the environment [27]. Therefore, organic encapsulating materials may be more suited for the development of inexpensive all–organic PV cells [57-59].

Organic thin film materials fabricated from renewable precursors using low-cost deposition methods, such as plasma-assisted nanoassembly, have lower environmental and economic costs [27]. Low-temperature plasma deposition is a highly engineering-friendly, economical method of polymer synthesis, that delivers practically pollutant free surface chemistry, and can be easily integrated into manufacturing processes [60, 61]. The method offers a level of confidence and deposition quality comparable to and in many cases superior to other widely-used techniques, such as thermal chemical vapor deposition, wet chemistry processing, laser assisted microfabrication, etc. [62, 63]. Films fabricated using plasma-assisted synthesis are typically smooth, ultrathin and pinhole free, with good spatial uniformity, conformal coverage, and high adhesion to the substrate [64].

The compound 1-isopropyl-4-methyl-1,4-cyclohexadiene, also known as γ-terpinene, is a non-synthetic isomeric hydrocarbon derived from *Melaleuca alternifolia* essential oil. Earlier, Jacob and co-workers have successfully used plasma-assisted deposition to fabricate thin films from other renewable precursors for application in electronics and biomedical fields, reporting property variability linked to both deposition conditions and the chemistry of the monomer [22–26]. Based on the aforementioned considerations, this project reports on the plasma-assisted fabrication of new polymer thin films from γ-terpinene, with intention to use these films in OPVs, specifically as encapsulation coatings.

I.2 RESEARCH OBJECTIVES

This project aimed to fabricate low cost, transparent thin films from environmentally friendly low-cost resource with precisely defined properties, suitable for use in electronic devices, particularly for encapsulation of OPV devices. This was achieved by addressing the following goals, each of which contributed to the project aim:

- To improve fundamental understanding of plasma polymerization process.
- To fabricate organic polymer thin films from low-cost, renewable resource derived from γ-terpinene monomer using the radio frequency (RF) PECVD technique.
- To determine the material's properties (optical, chemical, morphological, electrical etc.) using appropriate methodology and to compare those against materials currently in use within the chosen application.
- To investigate the relationship between the investigated properties and fabrication conditions to further optimise most promising polymer thin films for the chosen application.
- To test performance of the developed thin film structures incorporating them over OPV device for the desired application to assess the viability and efficiency of such implementation.

Achieving the above objectives led to several contributions in the field of materials development and characterization. RF Plasma deposited γ-terpinene (pp–GT) thin films constituted a new material that has the potential to assist in design and realization of environmentally friendly fully flexible low-cost electronic devices. The knowledge obtained in the course of this project also contributed towards achieving a better understanding of the relation between materials and device performance. This project provided a solid framework for development of polymer materials based on essential oils i.e. γ-terpinene for advanced electronic applications, particularly OPV devices. Potential utilization of such Australian environmentally friendly renewable resources in high-tech electronic applications seems to be viable through achieving the objectives of this project.

I.3 CONCEPT OF THE THESIS

This thesis contains nine chapters, the body of which addresses directly the objectives of this research work. Each chapter represents a manuscript or parts of manuscripts at various stages of publication joined by a common argument.

Chapter II presents an overview of the basic principles of water vapor and oxygen permeation through organic thin films used in PV applications. First, the various permeation mechanisms of water vapor and oxygen through encapsulation films are reviewed. The next section in chapter II introduces and compares the most commonly used techniques for surface modification of polymers, with a particular focus on the RF PEVCD process. This chapter also serves as a general introduction to plasma polymerization, and covers the fundamental aspects of plasma physics that are necessary for a good understanding of this work. In this chapter, current progress in the fields of organic electronics, particularly OPV is reviewed. Recent developments in the area of flexible electronics are also discussed, with particular focus on the role plasma polymer thin films play in the advancement of encapsulation technologies of OPV devices. Some sections of this chapter are reported in the journal article *J. Ahmad, K. Bazaka, L. J. Anderson, R. D. White, and M. V. Jacob, "Materials and methods for encapsulation of OPV: A review," Renewable and Sustainable Energy Reviews, vol. 27, pp. 104-117, 2013.*

Chapter III presents the plasma polymer thin film fabrication procedure, and details experimental procedures employed throughout this research.

Chapter IV explores the fragmentation mechanisms of γ-terpinene during plasma polymerization under various RF power conditions. The plasma chemistry is correlated to the film chemical composition and the degree of cross-linking. The plasma chemistry was studied by residual gas analysis (RGA) mass spectrometry. The findings were reported in the journal article *Ahmad, J., Bazaka, K., Whittle, J., Michelmore, A. and Jacob, M. V. (2014) Structural Characterization of γ-Terpinene Thin Films Using Mass Spectroscopy and X-ray Photoelectron Spectroscopy. Plasma Processes and Polymers. doi: 10.1002/ppap. 201400220.*

Chapter V presents the optical properties of pp–GT thin films through spectroscopic studies. The next section in chapter V presents the surface morphological and tribological properties, investigated through Atomic Force Microscopy (AFM) and nano-indentation measurements. Film-substrate adhesion properties of pp–GT thin films are also discussed in this chapter. The findings were reported in the journal article *Ahmad, J., Bazaka, K. and M. and Jacob, M. V., "Optical and Surface Characterization of Radio Frequency Plasma Polymerized 1-Isopropyl-4-Methyl-1,4-Cyclohexadiene Thin Films," Electronics, vol. 3, pp. 266-281, 2014.*

Chapter VI presents the chemical properties of pp–GT thin films investigated by Fourier Transform Infrared (FTIR) spectroscopy and X-ray Photoelectron Spectroscopy (XPS). The wetting and solubility characteristics of these films were also examined and the compatibility of the material with solvents utilized in the manufacturing of organic electronic devices has been assessed. Work in this chapter is published as the journal article *Ahmad, J., Bazaka, K., Oelgemöller, M. and Jacob, M. V., "Wetting, solubility and chemical characteristics of plasma polymerized 1-isopropyl-4-methyl-1,4-cyclohexadiene thin films," Coatings, vol. 4, pp. 527-552, 2014.*

Chapter VII details the electrical properties of the pp–GT thin films under varied input power conditions, beginning with characterizations at direct current (dc) frequencies that determined the conductivity of the films, their charge transport mechanism and dielectric strength using current-voltage (IV) measurements. The frequency dependent dielectric properties at multiple temperatures are presented, obtained through dielectric impedance spectroscopy, and a detailed overview of the analytical techniques is given. The findings were reported in the journal article *Ahmad, J., Bazaka, K., and Jacob, M. V. (2015) Electrical conduction in plasma polymerized thin films of γ-terpinene* that is accepted for publication in the *Journal of Applied Polymer Science*.

Chapter VIII deals with stability aspects of pp–GT thin films. The stability of the films under ambient conditions and when subjected to environmental factors are investigated here. Thermal stability of the plasma polymers is also discussed in the next section in chapter VIII. Final section demonstrates the effectiveness of pp–GT barrier layers by encapsulating organic devices. The compatibility of the thin-film encapsulation process with organic solar cells is verified by comparing the basic performance parameters of the devices before and after the encapsulation process. A manuscript outlining the findings of this study are communicated as *Ahmad, J., Bazaka, K., Oelgemöller, M., Uddin, A. and Jacob, M. V. (2015) Aging, thermal degradation, and photo–stability of plasma polymerized γ-terpinene thin films* (submitted to *Polymer Degradation and Stability* for publication)**.**

Chapter IX provides the concluding remarks of this research work. Recommendations for directions of possible future work in the area are also provided in this chapter.

REFERENCES

[1] U. S. E. I. A. (EIA), "The Annual Energy Outlook 2013 (AEO2013) " Office of Integrated and International Energy Analysis, U.S. Department of Energy, Washington, DC 205852013.

[2] M. E. Borges and L. Díaz, "Recent developments on heterogeneous catalysts for biodiesel production by oil esterification and transesterification reactions: A review," *Renewable and Sustainable Energy Reviews,* vol. 16, pp. 2839-2849, 2012.

[3] J. Ahmad, K. Bazaka, L. J. Anderson, R. D. White, and M. V. Jacob, "Materials and methods for encapsulation of OPV: A review," *Renewable and Sustainable Energy Reviews,* vol. 27, pp. 104-117, 2013.

[4] B. Christoph J, "Organic photovoltaics: technology and market," *Solar Energy Materials and Solar Cells,* vol. 83, pp. 273-292, 2004.

[5] N. Grossiord, J. M. Kroon, R. Andriessen, and P. W. M. Blom, "Degradation mechanisms in organic photovoltaic devices," *Organic Electronics,* vol. 13, pp. 432-456, 2012.

[6] L. El Chaar, L. A. lamont, and N. El Zein, "Review of photovoltaic technologies," *Renewable and Sustainable Energy Reviews,* vol. 15, pp. 2165-2175, 2011.

[7] R. García-Valverde, J. A. Cherni, and A. Urbina, "Life cycle analysis of organic photovoltaic technologies," *Progress in Photovoltaics: Research and Applications,* vol. 18, pp. 535-558, 2010.

[8] H. Spanggaard and F. C. Krebs, "A brief history of the development of organic and polymeric photovoltaics," *Solar Energy Materials and Solar Cells,* vol. 83, pp. 125-146, 2004.

[9] C. J. Brabec, N. S. Sariciftci, and J. C. Hummelen, "Plastic Solar Cells," *Advanced Functional Materials,* vol. 11, pp. 15-26, 2001.

[10] K. M. Coakley and M. D. McGehee, "Conjugated Polymer Photovoltaic Cells," *Chemistry of Materials,* vol. 16, pp. 4533-4542, 2004/11/01 2004.

[11] H. Hoppe and N. S. Sariciftci, "Organic solar cells: An overview," *Journal of Materials Research,* vol. 19, pp. 1924-1945, 2004.

[12] S. Günes, H. Neugebauer, and N. S. Sariciftci, "Conjugated Polymer-Based Organic Solar Cells," *Chemical Reviews,* vol. 107, pp. 1324-1338, 2007/04/01 2007.

[13] C. Winder and N. S. Sariciftci, "Low bandgap polymers for photon harvesting in bulk heterojunction solar cells," *Journal of Materials Chemistry,* vol. 14, pp. 1077-1086, 2004.

[14] E. Bundgaard and F. C. Krebs, "Low band gap polymers for organic photovoltaics," *Solar Energy Materials and Solar Cells,* vol. 91, pp. 954-985, 2007.

[15] B. P. Rand, J. Genoe, P. Heremans, and J. Poortmans, "Solar cells utilizing small molecular weight organic semiconductors," *Progress in Photovoltaics: Research and Applications,* vol. 15, pp. 659-676, 2007.

[16] X. Crispin, "Interface dipole at organic/metal interfaces and organic solar cells," *Solar Energy Materials and Solar Cells,* vol. 83, pp. 147-168, 2004.

[17] N.-K. Persson, M. Schubert, and O. Inganäs, "Optical modelling of a layered photovoltaic device with a polyfluorene derivative/fullerene as the active layer," *Solar Energy Materials and Solar Cells,* vol. 83, pp. 169-186, 2004.

[18] J.-F. Nierengarten, "Fullerene-(π-conjugated oligomer) dyads as active photovoltaic materials," *Solar Energy Materials and Solar Cells,* vol. 83, pp. 187-199, 2004.

[19] H. Neugebauer, M. A. Loi, C. Winder, N. S. Sariciftci, G. Cerullo, A. Gouloumis, P. Vázquez, and T. Torres, "Photophysics and photovoltaic device properties of phthalocyanine–fullerene dyad:conjugated polymer mixtures," *Solar Energy Materials and Solar Cells,* vol. 83, pp. 201-209, 2004.

[20] F. C. Krebs, O. Hagemann, and M. Jørgensen, "Synthesis of dye linked conducting block copolymers, dye linked conducting homopolymers and preliminary application to photovoltaics," *Solar Energy Materials and Solar Cells,* vol. 83, pp. 211-228, 2004.

[21] S. Heutz, P. Sullivan, B. M. Sanderson, S. M. Schultes, and T. S. Jones, "Influence of molecular architecture and intermixing on the photovoltaic, morphological and spectroscopic properties of CuPc–C_{60} heterojunctions," *Solar Energy Materials and Solar Cells,* vol. 83, pp. 229-245, 2004.

[22] T. Jeranko, H. Tributsch, N. S. Sariciftci, and J. C. Hummelen, "Patterns of efficiency and degradation of composite polymer solar cells," *Solar Energy Materials and Solar Cells,* vol. 83, pp. 247-262, 2004.

[23] A. J. Breeze, Z. Schlesinger, S. A. Carter, H. Tillmann, and H. H. Hörhold, "Improving power efficiencies in polymer – polymer blend photovoltaics," *Solar Energy Materials and Solar Cells,* vol. 83, pp. 263-271, 2004.

[24] F. C. Krebs, J. Alstrup, H. Spanggaard, K. Larsen, and E. Kold, "Production of large-area polymer solar cells by industrial silk screen printing, lifetime considerations and lamination with polyethyleneterephthalate," *Solar Energy Materials and Solar Cells,* vol. 83, pp. 293-300, 2004.

[25] M. Adi, T. Yohannes, and T. Solomon, "Solid-state photoelectrochemical device based on poly(3-hexylthiophene) and an ion conducting polymer electrolyte, amorphous poly(ethylene oxide) complexed with $I3^{-}/I^{-}$ redox couple," *Solar Energy Materials and Solar Cells,* vol. 83, pp. 301-310, 2004.

[26] J.-D. Kwon, P.-H. Kim, J.-H. Keum, and J. S. Kim, "Polypyrrole/titania hybrids: synthetic variation and test for the photovoltaic materials," *Solar Energy Materials and Solar Cells,* vol. 83, pp. 311-321, 2004.

[27] S. E. Shaheen, D. S. Ginley, and G. E. Jabbour, "Organic-Based Photovoltaics: Toward Low-Cost Power Generation," *MRS Bulletin,* vol. 30, pp. 10-19, 2005.

[28] D. J. Milliron, I. Gur, and A. P. Alivisatos, "Hybrid Organic–Nanocrystal Solar Cells," *MRS Bulletin,* vol. 30, pp. 41-44, 2005.

[29] R. A. J. Janssen, J. C. Hummelen, and N. S. Sariciftci, "Polymer–Fullerene Bulk Heterojunction Solar Cells," *MRS Bulletin,* vol. 30, pp. 33-36, 2005.

[30] S. R. Forrest, "The Limits to Organic Photovoltaic Cell Efficiency," *MRS Bulletin,* vol. 30, pp. 28-32, 2005.

[31] F. C. Krebs, "Low band gap polymer materials for organic solar cells," *Solar Energy Materials and Solar Cells,* vol. 91, p. 953, 2007.

[32] R. Koeppe, O. Bossart, G. Calzaferri, and N. S. Sariciftci, "Advanced photon-harvesting concepts for low-energy gap organic solar cells," *Solar Energy Materials and Solar Cells,* vol. 91, pp. 986-995, 2007.

[33] M. H. Petersen, O. Hagemann, K. T. Nielsen, M. Jørgensen, and F. C. Krebs, "Low band gap poly-thienopyrazines for solar cells – Introducing the 11-thia-9,13-diaza-cyclopenta[b]triphenylenes," *Solar Energy Materials and Solar Cells,* vol. 91, pp. 996-1009, 2007.

[34] W. Mammo, S. Admassie, A. Gadisa, F. Zhang, O. Inganäs, and M. R. Andersson, "New low band gap alternating polyfluorene copolymer-based photovoltaic cells," *Solar Energy Materials and Solar Cells,* vol. 91, pp. 1010-1018, 2007.

[35] E. Bundgaard and F. C. Krebs, "Large-area photovoltaics based on low band gap copolymers of thiophene and benzothiadiazole or benzo-bis(thiadiazole)," *Solar Energy Materials and Solar Cells,* vol. 91, pp. 1019-1025, 2007.

[36] F. Banishoeib, P. Adriaensens, S. Berson, S. Guillerez, O. Douheret, J. Manca, S. Fourier, T. J. Cleij, L. Lutsen, and D. Vanderzande, "The synthesis of regio-regular poly(3-alkyl-2,5-thienylene vinylene) derivatives using lithium bis(trimethylsilyl)amide (LHMDS) in the dithiocarbamate precursor route," *Solar Energy Materials and Solar Cells,* vol. 91, pp. 1026-1034, 2007.

[37] R. W. Miles, G. Zoppi, and I. Forbes, "Inorganic photovoltaic cells," *Materials Today,* vol. 10, pp. 20-27, 2007.

[38] A. C. Mayer, S. R. Scully, B. E. Hardin, M. W. Rowell, and M. D. McGehee, "Polymer-based solar cells," *Materials Today,* vol. 10, pp. 28-33, 2007.

[39] M. T. Lloyd, J. E. Anthony, and G. G. Malliaras, "Photovoltaics from soluble small molecules," *Materials Today,* vol. 10, pp. 34-41, 2007.

[40] G. Conibeer, "Third-generation photovoltaics," *Materials Today,* vol. 10, pp. 42-50, 2007.

[41] H. GmbH. (Dec 22). *Heliatek consolidates its technology leadership by establishing a new world record for organic solar technology with a cell efficiency of 12%.*

[42] F. C. Krebs, "Alternative PV: Large scale organic photovoltaics," *Refocus,* vol. 6, pp. 38-39, 2005.

[43] J. E. Carlé and F. C. Krebs, "Technological status of organic photovoltaics (OPV)," *Solar Energy Materials and Solar Cells,* vol. 119, pp. 309-310, 2013.

[44] J. Hierso, P. Boy, K. Vallé, J. Vulliet, F. Blein, C. Laberty-Robert, and C. Sanchez, "Nanostructured ceria based thin films (≤1 μm) as cathode/electrolyte interfaces," *Journal of Solid State Chemistry,* vol. 197, pp. 113-119, 2013.

[45] R. S. Koti, S. R. Sanjaykumar, S.-J. Hong, C. E. Song, I.-N. Kang, S. K. Lee, W. S. Shin, S.-J. Moon, and J.-C. Lee, "3,8-Dialkoxynaphthodithiophene based copolymers for efficient polymer solar cells," *Solar Energy Materials and Solar Cells,* vol. 108, pp. 213-222, 2013.

[46] J. Yin, H. Zhu, Y. Wang, Z. Wang, J. Gao, Y. Mai, Y. Ma, M. Wan, and Y. Huang, "A study of ZnO:B films for thin film silicon solar cells," *Applied Surface Science,* vol. 259, pp. 758-763, 2012.

[47] A. Yassar, L. Miozzo, R. Gironda, and G. Horowitz, "Rod–coil and all-conjugated block copolymers for photovoltaic applications," *Progress in Polymer Science,* vol. 38, pp. 791-844, 2013.

[48] Y. Kann and N. C. Billingham, "Chemiluminescence is shedding light on degradation and stabilisation of plasticised poly(vinyl chloride)," *Polymer Degradation and Stability,* vol. 85, pp. 957-966, 2004.

[49] N. Asim, K. Sopian, S. Ahmadi, K. Saeedfar, M. A. Alghoul, O. Saadatian, and S. H. Zaidi, "A review on the role of materials science in solar cells," *Renewable and Sustainable Energy Reviews,* vol. 16, pp. 5834-5847, 2012.

[50] Y. Jouane, S. Colis, G. Schmerber, A. Dinia, P. Bazylewski, G. S. Chang, and Y.-A. Chapuis, "Impact of sputtered ZnO interfacial layer on the S-curve in conjugated polymer/fullerene based-inverted organic solar cells," *Thin Solid Films,* vol. 576, pp. 23-30, 2015.

[51] D.-w. Choi, S.-J. Kim, J. H. Lee, K.-B. Chung, and J.-S. Park, "A study of thin film encapsulation on polymer substrate using low temperature hybrid ZnO/Al_2O_3 layers atomic layer deposition," *Current Applied Physics,* vol. 12, Supplement 2, pp. S19-S23, 2012.

[52] S.-W. Seo, E. Jung, H. Chae, and S. M. Cho, "Optimization of Al_2O_3/ZrO_2 nanolaminate structure for thin-film encapsulation of OLEDs," *Organic Electronics,* vol. 13, pp. 2436-2441, 2012.

[53] B. Ketola, C. Shirk, P. Griffith, and G. Bunea, "Demonstration of the Benefits of Silicone Encapsulation of PV Modules in a Large Scale Outdoor Array," presented at the 5th World Conference on Photovoltaic Energy Conversion, Valencia, Spain, 2010.

[54] N. Kim, W. J. Potscavage Jr, A. Sundaramoothi, C. Henderson, B. Kippelen, and S. Graham, "A correlation study between barrier film performance and shelf lifetime of encapsulated organic solar cells," *Solar Energy Materials and Solar Cells,* vol. 101, pp. 140-146, 2012.

[55] E. Cuddihy, C. Coulbert, A. Gupta, and R. Liang, "Electricity from photovoltaic solar cells: Flat-Plate Solar Array Project final report. Volume VII: Module encapsulation," Jet Propulsion Laboratory1986.

[56] N. Kim, "Fabrication and characterization of thin-film encapsulation for organic electronics," PhD Dissertation, Mechanical Engineering, Georgia Institute of Technology, Georgia, 2009.

[57] J. Kalowekamo and E. Baker, "Estimating the manufacturing cost of purely organic solar cells," *Solar Energy,* vol. 83, pp. 1224-1231, 2009.

[58] G. Dennler and C. J. Brabec, "Socio-Economic Impact of Low-Cost PV Technologies," in *Organic Photovoltaics*, ed: Wiley-VCH Verlag GmbH & Co. KGaA, 2009, pp. 531-566.

[59] J. Schmidtke, "Commercial status of thin-film photovoltaic devices and materials," *Opt. Express,* vol. 18, pp. A477-A486, 2010.

[60] S. R. Forrest, "The path to ubiquitous and low-cost organic electronic appliances on plastic," *Nature,* vol. 428, pp. 911-918, 2004.

[61] K. Vasilev, S. S. Griesser, and H. J. Griesser, "Antibacterial Surfaces and Coatings Produced by Plasma Techniques," *Plasma Processes and Polymers,* vol. 8, pp. 1010-1023, 2011.

[62] K. Ostrikov, E. C. Neyts, and M. Meyyappan, "Plasma nanoscience: from nano-solids in plasmas to nano-plasmas in solids," *Advances in Physics,* vol. 62, pp. 113-224, 2013/04/01 2013.

[63] A. Michelmore, C. Charles, R. W. Boswell, R. D. Short, and J. D. Whittle, "Defining Plasma Polymerization: New Insight Into What We Should Be Measuring," *ACS Applied Materials & Interfaces,* vol. 5, pp. 5387-5391, 2013/06/26 2013.

[64] M. J. Rahman and A. H. Bhuiyan, "Structural and optical properties of plasma polymerized o-methoxyaniline thin films," *Thin Solid Films,* vol. 534, pp. 132-136, 2013.

CHAPTER II

LITERATURE REVIEW

The main goal of this chapter is to provide an overview of thin-film encapsulation technologies for protecting organic electronic devices, particularly OPV devices from water vapor and oxygen in order to improve the efficiency and extend the shelf-lifetime of devices.

Section II.1 gives an overview of the basic principles of water vapor and oxygen permeation through various thin films, beginning with the current understanding of OPV. Recent achievements in various thin-film barrier technologies comprised of high quality single and multilayer coatings are also introduced and compared. Along with barrier performance, the extended shelf-lifetime of encapsulated organic devices is discussed. One review article has been published detailing these aspects – *J. Ahmad, K. Bazaka, L. J. Anderson, R. D. White, and M. V. Jacob, "Materials and methods for encapsulation of OPV: A review," Renewable and Sustainable Energy Reviews, vol. 27, pp. 104-117, 2013.*

Section II.2 covers the surface modification techniques and plasma deposition of organic materials as the scope of this thesis was limited to the investigation of a new material derived from γ-terpinene and fabricated using PECVD for use in organic electronic applications. Plasma deposition of thin films is reviewed in this section, beginning with the current understanding of the growth mechanisms involved. The relationship between the deposition parameters and properties of the resulting thin films is also discussed.

II.1 ORGANIC PHOTOVOLTAICS (OPV) – CONCEPT

OPV, a novel technology, is based on thin films of organic semiconducting polymers [1]. The ability to tailor the molecular properties to fit the application is an important advantage of these materials. The modules built are lighter and more flexible compared to their heavy and rigid inorganic counterparts, and thus less prone to damage and failure [2]. Moreover, semiconducting polymers combine the opto-electronic properties of conventional semiconductors with the excellent mechanical and processing properties of polymeric materials [2]. These can be processed from solution at room temperature onto flexible substrates using simple and therefore cheaper deposition methods [3]. As a result, considerably less effort and production energy is needed. In addition, OPV shows other advantages including low material requirements and the utilization of eco-friendly materials [2].

Energy conversion efficiencies achieved to date using organic polymers are low compared to inorganic materials. However, OPVs have improved quickly in the last decade and recent progress achieved using organic mono-crystalline, multilayered thin films and interpenetrated network technologies show the potential of a very fast increase in the conversion yield of OPVs [4-9]. External quantum efficiencies (EQE) have been increased by 50% using the bulk heterojunction structure [10] and 80% EQE is reported for blends of conjugated polymers with fullerenes [11]. The conversion efficiency of OPV solar cells has significantly increased over the last decade as depicted in Figure II.1 [5].

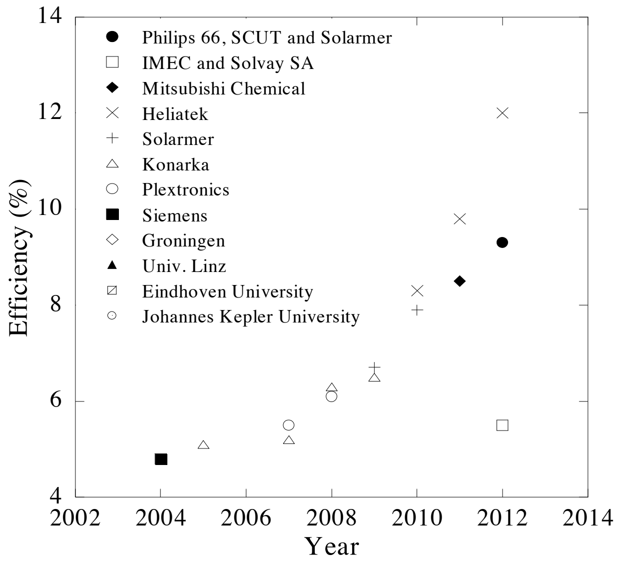

Figure II.1. OPV cell efficiency (Source: Solarmer Energy Inc.)

II.1.1 RELIABILITY ISSUES OF OPV

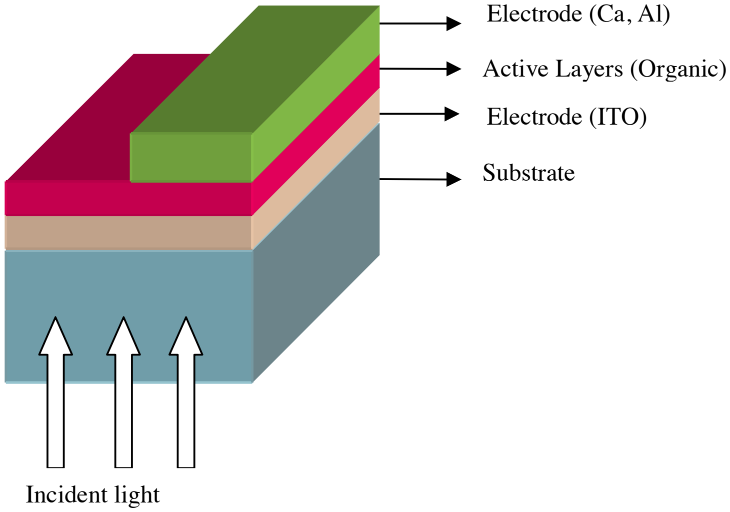

Figure II.2. Schematic diagram of the basic structure of OPVs

Organic materials are by nature more susceptible to degradation from oxygen and water than inorganic materials. A number of studies have been carried out and they show that the stability/ degradation issue is quite complicated and not yet fully understood, though progress has been made [1, 12-15].

Chemical degradation of OPV devices (Figure II.2) is mainly attributed to interactions between the active polymer layer and oxygen, water and electrode materials [1]. Oxygen is readily activated by UV illumination in the presence of sensitizers such as titanium oxide or other organic molecules [12]. The superoxide or hydrogen peroxide formed may then forcefully attack any organic substance present including the active polymers. Some materials are more vulnerable to degradation than others, e.g. oxygen and water can diffuse into the device through a simple layer of poly[[[(2-ethylhexyl)oxy]methoxy-1,4-phenylene]-1,2-ethenediyl] i.e. MEH-PPV sandwiched between indium tin oxide (ITO) and aluminium (*Al*) electrodes [16]. This diffusion through thin films is addressed elsewhere [17-24]. Furthermore, diffusion through outer electrode proceeds via microscopic pinholes present [12]. Metal grains that evaporated electrodes typically consist of are other possible diffusion channels. Swelling is observed on the outer electrode surface centered on the microscopic pinholes in the electrode surface due to the oxidization and expansion of the organic material in all directions [23]. This degradation of the electrodes generally leads to the degradation of the photoactive layer (PAL)–electrode interface due to a decrease of the interfacial area because of formation of insulating patches and/or voids [1]. All of these changes deteriorate the charge transfer between the PAL and electrodes, which can be coupled to mechanical breakdown and ultimately to delamination when longer exposure times and/or mechanical stresses are considered [13, 25-29]. Alternatively, insulating patches can also be created by other chemical reactions between the PAL and the metal electrode. As an example, radical species formed in the PAL may react with the aluminum (Al) electrode, leading to a gradual degradation of the PAL/electrode interface quality [30].

The mechanical properties of various polymers with high device PCE have been studied [1, 12, 14, 23, 26, 27, 31-33]. An important parameter for the quality of these polymer films is their resistance to mechanical damage. However, scratch resistant polymer films very often cause embrittlement of the system [34]. The decrease of molar mass resulting from chain scission process is responsible for this [35]. Chain scission also induces chemicrystallization. These two processes can lead to embrittlement through two possible causal chains: (1) chain scission → molar mass decrease → chemicrystallization → decrease of the interlamellar spacing → embrittlement; and (2) chain scission → molar mass decrease → chemicrystallization → decrease of the tie-macromolecule concentration → embrittlement [35]. This may also result in modification of the optical properties of the polymer (i.e. decrease of transparency), as well as an increase of light scattering due to physical reorganization of the polymer chains [1]. Samples fabricated from poly(methylmethacrylate) (brittle layer) and polycarbonate (substrate) as well as from styrene–acrylonitrile and acrylonitrile–butadiene–styrene copolymers show this phenomenon [36]. Furthermore, if the system is stressed, cracks can be initiated in the film, and trigger fracture in the polymeric substrate due to the stress intensity at the crack tip [23].

In addition to the degradation mechanisms listed above, electrical output of PV module can be significantly affected by various factors such as moisture, UV light, temperature etc. [37]. Exposure to oxygen has been found to lower the conductivity of thin films. Upon oxygen uptake, the electron mobility is reduced by several orders of magnitude because the introduced oxygen acts as an electron trap [38]. The permeability of polymers is influenced by both the mobility of the polymer chains and the strength of the interaction between the polymer and penetrant. Moreover, chain scission increases the free volume of the polymer system, which can lead to an increase in permeability and decrease in mobility [12]. This reaction also affects the ordering of the polymer chains that contributes to cell degradation as they affect charge transport. As a result, short circuit current density, J_{sc} decreases, which induces a drop of the OPV cell efficiency [1].

Optical properties of polymers typically are not influenced by changes in temperature or the application of stress [12]. However, simultaneous application of stress and temperature can induce crystallization and the growth of spherulitic structures that scatter light and decrease clarity. Chain scission reactions can lead to the formation of chromophores that may drastically increase absorption in either the UV or visible spectral range or both [1].

Soil accumulation is another issue that reduces light transmission of the solar cells and therefore, reduces power output [31]. Presence of dust particles in the stacking or the organic PAL layer–electrode interface can induce higher local electrical fields, paving the way to the formation of microscopic conduction paths through the organic layer during operation [39].

The reliability issues discussed above should be solved to maintain stability and lifetime of OPV. Encapsulation can be a solution to these issues [40]. The desired encapsulation method may block oxygen and water effectively which in turn provides a solution to the diffusion through microscopic pinholes [41]. This also prevents insulating patches and/or voids and therefore, photoactive layer (PAL)–electrode interface remains stable. As a result, charge transfer between the PAL and electrodes does not deteriorate. Encapsulation also provides resistance to mechanical damage and structural support. By absorbing stress, it prevents initiation of cracks and triggering of fractures. Encapsulation offers optical coupling, electrical isolation, physical isolation and thermal conduction for the solar cell assembly that keeps the electrical output and the optical properties stable for the desired lifetime [42]. It should be thin and lightweight to take full advantage of the potentials of OPV cells in practical applications [42]. However, currently available materials do not satisfy all of these requirements [43].

II.1.2 BASIC PRINCIPLES OF PERMEATION

The basic function of encapsulation barrier films is to limit the exposure of OPV devices to water vapor and oxygen. This is done by controlling the permeation through barrier films [44]. Permeation is usually a two-step process beginning with the absorption of a substance into the solid followed by diffusion of the substance [45]. Therefore, in the case of a homogenous film at steady state, the permeability *P* is equal to the product of solubility coefficient *S* and diffusion coefficient *D:* [20]

$$\mathrm{P} = \mathrm{S.D} \tag{II.1}$$

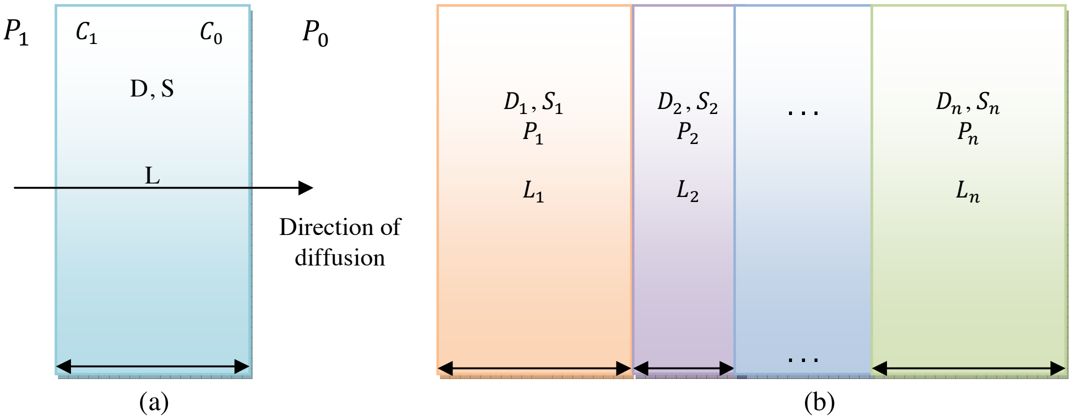

Figure II.3. Permeation of gas or vapor through (a) single layer and (b) multiple composite

P, C, L, D, and *S* in Figure II.3 (a) indicate vapor or gas pressure, concentration, thickness, and diffusion and solubility coefficients respectively. *Fick's first law of diffusion* and *Henry's law* can describe this process and permeation model with boundary conditions are also shown in Figure II.3 (a). Permeant flux *J* is therefore proportional to the concentration as

$$\mathrm{J} = -\mathrm{D}.\nabla(\mathrm{c}) \quad , \tag{II.2}$$

where, *c* is the concentration. With the assumption of Henry's law which relates the concentration (*c*) to the partial pressure (*ΔP*) through the linear relationship, $c = S\Delta P$, the concentration in Eq. (II.2) can then be re-written as

$$\mathrm{J} = \frac{\mathrm{DS}(\mathrm{P_0} - \mathrm{P_1})}{\mathrm{L}} \tag{II.3}$$

However, transient study of permeation has drawn much attention due to the introduction of barrier layers having long lag times. In the case of time dependent gas permeation, *Fick's second law* can be used:

$$\frac{\partial \mathrm{c}}{\partial \mathrm{t}} = \nabla(\mathrm{D}.\nabla(\mathrm{c})) = \mathrm{D}.\left(\frac{\partial^2 \mathrm{c}}{\partial \mathrm{x}^2} + \frac{\partial^2 \mathrm{c}}{\partial \mathrm{y}^2} + \frac{\partial^2 \mathrm{c}}{\partial \mathrm{z}^2}\right) \tag{II.4}$$

where the diffusion coefficient has been assumed spatially constant. In the case of multilayer encapsulation architectures, the equation for the total permeability coefficient P_T of a multilayer structure with *n* layers each with a uniform thickness L_n and permeability coefficient P_T (as illustrated in Figure II.3 (b)) is

$$\frac{1}{P_T} = \frac{L_{total}}{\frac{L_1}{P_1}+\frac{L_2}{P_2}+\frac{L_3}{P_3}+ \ldots + \frac{L_n}{P_n}} \tag{II.5}$$

In Eq. (II.5), L_{total} is the total thickness of the multilayer structure. Assuming a constant permeant flux through all layers under steady state conditions, this total permeability coefficient of the multilayer film is derived.

II.1.3 THE PERMEATION MECHANISM OF WATER VAPOR AND GAS

The entrapment of polymer chains creates interstitial spaces that can change with time due to the dynamic internal lattice structure of polymers. The permeation through the deposited thin film is expected to occur through macro defects and nano-scale defects including these interstitial spaces [20]. Imperfect structure of the deposited thin films such as voids, columnar structures and grain formation etc. can create these defects that have been widely investigated in other reports [17, 20, 21, 46]. The AFM image in the Figure II.4 (a) shows the grain-like structure of PECVD deposited SiO_x film on PET substrate [47]. TEM image in Figure II.4 (b) reveals the presence of nanoscale defects between adjacent SiO_x grains and these defects can be further reduced by optimizing process conditions [48].

(a) (b)

Figure II.4. (a) AFM image for surface morphology of SiO_x deposited on the PET substrate by PECVD [48]. (b) TEM image of a relatively poor SiO_x barrier coatings deposited by PECVD on the PET substrate [49].

Imperfect structures of deposited films are understood better if SiO_x is deposited on glass instead of PET. Figure II.5 (a)-(c) show surface morphologies of SiO_x deposited by PECVD on glass substrates that clearly contains voids and grain formation resulting in relatively rough surface (RMS surface roughness: 3.8 nm). This imperfect structure provides a permeation path for water vapor and oxygen as illustrated in Figure II.5 (d).

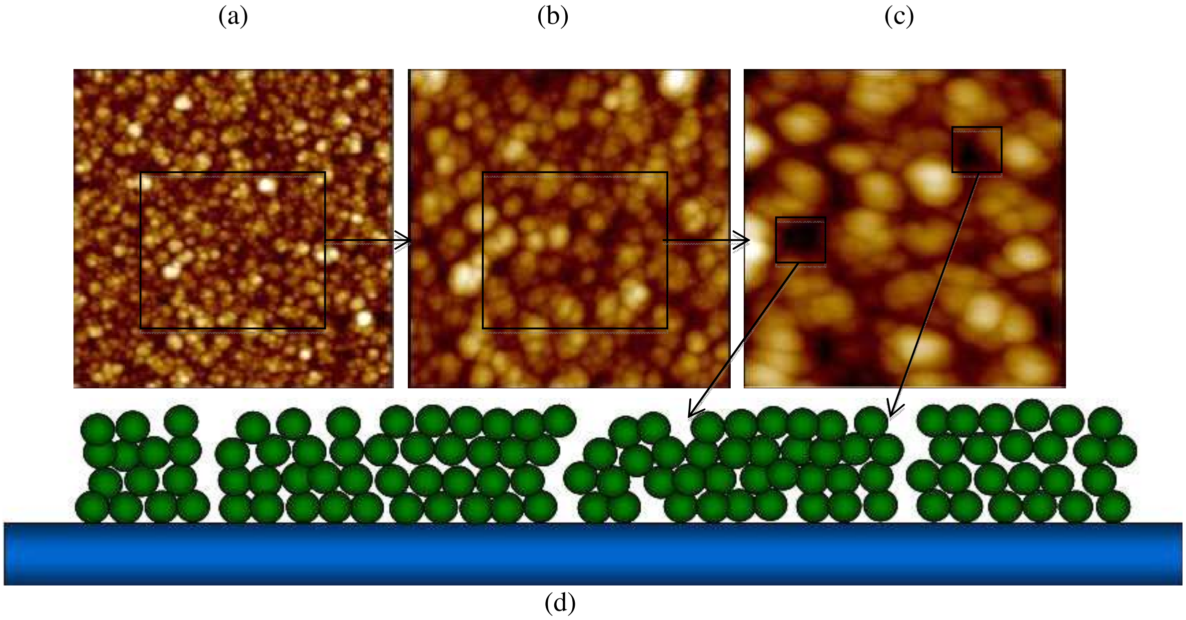

Figure II.5. ((a)-(c)): The surface morphology (200nm, 100nm and 40 nm respectively) of SiO_x deposited by PECVD on glass substrates (d) The expected cross-section of SiO_x based upon AFM images and defects

Micro-size defects in films originate from particles on the substrate and geometrics shadowing by structural topography. These defects attribute to defect controlled permeation as do the intrinsic defects from the growth mechanism [50]. These micro-size defects largely determine the barrier performance and a defect driven permeation model was proposed to render visible defects by using atomic oxygen etching [51, 52]. Briefly, the SEM image in the Figure II.6 (a) shows a micro-sized defect caused by a particle and the optical microscope image in Figure II.6 (b) shows the evolution of defect size with initially a 1μm diameter and after 120 min of exposure [51].

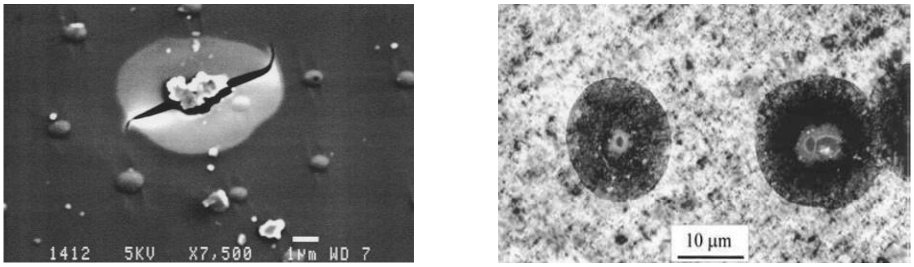

(a) (b)

Figure II.6. (a) SEM image of defects caused by a dust particle. (b) After 120 min AO exposure, defects identified by optical microscope [53]

Activation rate theory has been widely used in many references [18, 51, 52] for the investigation of diffusion mechanism for water vapor and oxygen. Activation energy for water permeation is a measure of the energy needed to promote the permeant to the activated state and to deform the barrier matrix so that the permeant may move into the next vacancy. The transport of ideal gas below glass transition temperature (T_g) can be described by *Arrhenius* equation [54];

$$P = P_0 e^{-\Delta E_p/RT} \qquad \text{(II.6)}$$

where P, P_o and ΔE_p are the permeability, pre-exponential factor, and activation energy for permeation in kJ/mol, respectively. This theory can also be used to predict the temperature dependency of barrier layers [55, 56]. Activation rate theory was employed by *Sobrinho et al.* for the diffusion of oxygen and water vapor through SiO_x and SiN_x coated PET and bare PET substrate [51]. Diffusion of water vapor deviates from the diffusion of an ideal gas and cannot be explained solely by defect dominant permeation mechanisms. Also, other phenomena such as water-induced swelling of polymers and adsorption of water vapor molecules in nanopores of different barriers are possible reasons for non-Fickian behavior of water vapor through barrier layers [57]. It is therefore necessary to consider the interaction of water vapor with barrier layers to characterize the barrier performance and design adequate thin film encapsulation for OPV.

II.1.4 ENCAPSULATION REQUIREMENTS

Due to the young age and rapidly evolving nature of the OPV technology, as well as complex mechanism of OPV device degradation, the encapsulation requirements for OPVs are not fully defined even though the ongoing research efforts are devoted to determine these. However, some important aspects of encapsulants are high dielectric breakdown, high volume resistivity and matching refractive index (n) with other layers. Water vapor transmission rate (WVTR) and oxygen transmission rate (OTR) are the steady state rates at which water vapor and oxygen (respectively) gas can penetrate through a film that affects the encapsulation layer. Another important material property often discussed in encapsulation is the glass transition temperature (T_g), which is a function of chain flexibility. The glass transition occurs when there is enough vibrational (thermal) energy in the system to create sufficient free-volume to permit sequences of 6-10 main-chain carbons to move together as a unit. At this point, the mechanical behavior of the polymer changes from rigid and brittle to tough and leathery (plastic behavior). In case of temperature extremes, it is important to know what the potential exposure temperatures are and how they will affect the mechanical behavior of the material. Moreover, measurement of light transmission is important for encapsulation due to the need for transparent materials. Hydrolysis, UV absorption degradation and some other aspects are also important to define the encapsulation requirements. A list of these requirements and specifications is given in Table II.6.1 [31].

Table II.1. Specifications and requirements for encapsulant materials

Characteristics	Specification or requirement
WVTR	$10^{-4} – 10^{-6}$ g m^{-2} day^{-1}
OTR	$10^{-3} – 10^{-5}$ cm^3 m^{-2} day^{-1} atm^{-1}
Glass transition temperature (T_g)	< – 40°C (during winter in deserts)
Total hemispherical light transmission over the wavelength range from 400 nm to 1100 nm	> 90% of incident light
Hydrolysis	None (80°C, 100% RH)
Water absorption	< 0.5 wt% (20°C/100% RH)
Resistance to thermal oxidation	Stable (up to 85°C)
Mechanical creep	None (90°C)
Tensile modulus	< 20.7 MPa (< 3000 psi) at 25°C
Chemical inertness	No reaction (with embedded Cu coupons at 90°C)
UV absorption degradation	None (> 350 nm)
Hazing or clouding	None (80°C, 100% RH)

II.1.5 THIN FILM ENCAPSULATION

The relatively strong sensitivity of OPV devices to water vapor and oxygen, which induces degradation, places stringent demands on the barrier performance of encapsulation materials and structures. To meet these encapsulation requirements, different approaches have been adopted such as single layer and multi-layer encapsulation.

II.1.5.1 SINGLE LAYER THIN FILM ENCAPSULATION

Single layer thin films are attractive because of the simplicity of the manufacturing process compared to multilayer thin film encapsulation methods that require multiple processing steps. Inorganic single layer encapsulating films are limited in their performance mainly due to the existence of defects in the films, which provide pathways for water vapor and oxygen to permeate through the barrier layers [50]. In fact, research into developing single layer encapsulation films has mainly focused on the reduction of these defects to improve barrier performance and organic films can address this issue effectively [58].

II.1.5.1.1 INORGANIC MATERIALS

SILICON (Si): Thin films of *Si* are noted to be suitable for encapsulating solar cells [59, 60]. This is primarily due to its high transparency in the UV–visible wavelengths, excellent tolerance to high optical flux and excellent thermal and environmental stability [59]. Depending upon the chemical constituents attached to the atom, *Si* can be formulated to a wide range of refractive indices (between 1.38 to 1.58) [61]. Due to its low modulus and low glass transition temperature (– 50 °C), *Si* is stress relieving over a wide temperature range. It is well known as a dielectric insulator and has high volume resistivity [50]. Moreover, because of hydrophobicity, it has low moisture pick-up in damp-heat environment and in total water immersion [62]. Damp-heat has a negative influence on devices [37, 63], e.g. copper indium gallium selenide *(CIGS)* cells suffer from reduced open circuit voltage (V_{OC}) and fill factor (*FF*) [64]. Low moisture of *Si* uptake is therefore an excellent property for its use as an encapsulant [59].

SILICON NITRIDE (SiN_x): SiN_x thin films can be deposited using radio frequency (RF) PECVD and low frequency (LF) PECVD. However, films deposited using these processes show significant differences. The layers deposited with LF PECVD show lower values of extinction coefficient for the same refractive index values, which means that LF PECVD layers have lower absorption and are more suitable for PV [65]. Fourier transform infrared spectroscopy (FTIR) characterization shows that LF PECVD layers have the highest Si–N bond density at 1.2×10^{23} cm^{-3} [65]. The maximal density of the film deposited by LF PECVD at 360°C is equal 2.6 g/cm^3, which is lower than the value (2.8–3 g/cm^3) required to obtain high efficiency [65]. An efficiency of 14.1% was found with V_{OC} = 590 mV at 360°C for solar cells with SiN_x layer deposited by LF PECVD. The OTR and WVTR for SiN_x films are below the detection limit of MOCON method (0.01 $cm^3\ m^{-2}\ day^{-1}$ and 0.01 $g\ m^{-2}\ day^{-1}$ respectively) [66]. Low stress for these films is also important for encapsulation purpose [67].

The reason for middling behavior of the SiN_x film deposited by RF PECVD may be due to the extent to which the chemical structure of the polymer differs from that of the monomer and the power level used during the deposition. The degree of monomer fragmentation is determined to a large extent by the intensity of the plasma field, with the higher bond dissociation corresponding to the increased magnitude of the RF energy input [68]. Furthermore, there is an increase in the temperature of the substrate associated with higher applied power. Lowering the substrate temperature encourages condensation and adsorption of non-excited gaseous species and subsequent incorporation of an increased number of non-fragmented molecules or slightly fragmented precursors in the growth region of the film [69]. This process of integration of large fragments is driven by the reactive species, which arise as a result of plasma field. In addition, in agreement with a competitive ablation-polymerization concept [70], the respective rates for ablation and polymerization may have differing temperature dependencies and therefore it is possible that lower temperatures may result in a reduction of energetic particle damage [71]. Hence, by choosing appropriate RF power conditions, encapsulation films with material properties tailored to the desired application can be manufactured.

ALUMINIUM OXIDE (Al_2O_3): Atomic layer deposition (ALD) is a promising alternative to PECVD. Encapsulation films have been achieved using Al_2O_3 [55, 72] and Al_2O_3/HfO_2 nanolaminates [73] deposited by this process. H_2O is used as the oxidant in both approaches. However, the films deposited by ALD using H_2O as the oxidant have a high impurity content, particularly of hydrogen [74]. A longer time is also needed during deposition to purge water molecules from the surface of the cell, as water has a high surface affinity owing to its large dipole moment [74, 75]. This problem reduces throughput of the process [76]. In current semiconductor technology, O_3 is the preferred oxidant and higher throughput is gained from O_3-based ALD as the time required for surface reactions and purging of the unreacted surface adsorbed species is much shorter than H_2O-based processes [74-77]. This is due to the high chemical reactivity between trimethylaluminum (TMA) and O_3, meaning that it can be purged more efficiently than H_2O [77]. An O_3–Al_2O_3 film also shows smaller residual hydrogen concentration compared to H_2O–Al_2O_3 films [40, 74]. Only Al_2O_3 is used as the primary barrier layer and no UV-curable epoxy resin film is used as an additional sealant for protecting OPVs from ambient moisture or oxygen. A WVTR of 1.7×10^{-5} g m^{-2} day^{-1} at 38 °C is found by quantitative *Ca* test [55].

The encapsulating ability of Al_2O_3 deposited using both O_3 and H_2O increases with increase in thickness, which is expected [40]. The efficiency of O_3–based ALD for device encapsulation is further highlighted by the fact that 10.2 nm of O_3–Al_2O_3 (120 cycles) offers better encapsulation than 20 nm of H_2O–Al_2O_3 (210 cycles) [40]. A thick film of 200 nm is used for the protection of OPV from ambient conditions and Al_2O_3 layer is deposited using H_2O at a growth rate of 10 nm/h [78]. However, 60% degradation is reported in device efficiency within 100 h, indicating extremely poor encapsulation by the Al_2O_3 layer grown using H_2O. In comparison, a device capped with 18 nm of O_3–Al_2O_3 shows 80% retention of the initial efficiency in over 500 h [78]. ALD also serves as the annealing step and irrespective of the anneal temperature, the O_3–Al_2O_3 layers showed superior encapsulation compared to the H_2O–Al_2O_3 film. Encapsulation by

Al_2O_3 deposited using ALD is further demonstrated by the performance of pentacene/C_{60}–based OPV cells. These cells are found to be stable for 6,000 h in ambient conditions with negligible deterioration in properties [78]. ALD encapsulation process on a pentacene/C_{60} –based PV device was performed at 100 ºC and no negative impact on the device performance was observed, other than changes due to the effect of thermal annealing, which have been reported previously [79].

II.1.5.1.2 ORGANIC MATERIALS

ETHYLENE VINYL ACETATE (EVA)

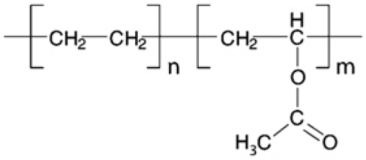

Figure II.7. Chemical structure of EVA

EVA, a copolymer of ethylene and vinyl acetate (Figure II.7), is one of the most widely used encapsulating materials among the single layer encapsulation films available [80]. It offers weather resistance and long-term reliability under long periods of exposure to different elements [81]. EVA has transmission of 91%, a volume resistivity of $0.2 \sim 1.4 \times 10^{16}$ Ω–cm and an adhesion strength of 9–12 N/mm (90º peel). Other advantages are its low cost, dimensional stability and volumetric fill. Therefore, based on the film extrudability and transparency, EVA was used for encapsulation purpose [82].

EUROPIUM DOPED EVA: EVA doped with a single europium (Eu^{3+}) complex whose sensitized region is broadened due to the presence of a co-ligand 4,4$^{/}$ bis(diethylamino) benzophenone (EABP), has been characterized optically and electrically for encapsulation purpose [83]. The Eu^{3+} complex shows an absorption band at 310 nm with full width at half maximum (FWHM) of 46 nm, while the EABP spectrum is centered at 360 nm with a FWHM of about 45 nm. Therefore, neither the organolanthanide complex nor the ketone is able to absorb visible light. But, a ground-state complex formed by EABP and tris[3-(trifluoromethylhydroxymethylene)-*d*-camphorato]europium(III) (Eu(tfc)$_3$) by the interaction of the positively charged Eu^{3+} ion with the electron rich carbonyl group can absorb visible light [83].

Coordinating EABP via its carbonyl group to the lanthanide ion gives rise to stabilization of the very polar energy levels involved. Therefore, doping the PV module encapsulating matrix with Eu(tfc)$_3$–EABP allows the exploitation of a wide portion of the solar spectrum. Moreover, europium doped EVA layers are able to induce down-shifting of photons with wavelengths lower than 460 nm. A 2.9% relative increase of the total power delivered has been observed [83].

ETHYLENE METHYL ACRYLATE (EMA): EMA, a copolymer of ethylene and methyl acrylate, has a potential advantage over EVA because it does not soften to a viscous melt above 70°C and, may not need curing as does EVA to achieve high temperature creep resistance [31]. The key benefits of EMA are its thermal stability, adherence to various substrates, chemical resistance and good mechanical behavior at low temperature [31]. These qualities match with some of the requirements of OPV and therefore used for encapsulation purpose [84].

POLYVINYL BUTYRAL (PVB)

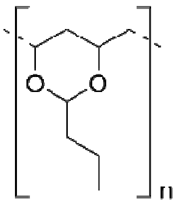

Figure II.8. Chemical structure of PVB

PVB can be used as encapsulation layer which is already widely applied in modern mass production of thin film solar cells [85]. Where EVA is an elastomeric cross-linking material activated by exposure to heat and/or UV light, PVB (Figure II.8) is a thermoplastic product that is non-cross-linking on exposure to heat. As a result, PVB can retain its original chemical composition [86]. The advantages of the film fabricated from PVB are its optical transparency, adhesive properties on glass, solar cells, and other plastics, high bond durability, resistance to heat, UV light and environmental influences and high compatibility with module components [86]. It can strongly reduce the moisture permeation and degradation of CIGS-based solar cell and consequently ensure longer lifetime [87].

THERMOPLASTIC POLYURETHANE (TPU):

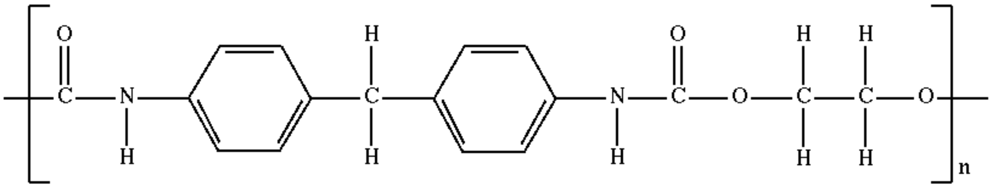

Figure II.9. Chemical structure of Polyurethane

Platilon® hot-melt adhesive films have been made of TPU (Figure II.9) to avoid the problem of time-consuming vacuum lamination. This film is superior to EVA due to the flexibility in bonding with relatively hard materials [88]. TPU films facilitate continuous, vacuum-free processing without cross-linking and emissions. These advantages scale up the productivity in the manufacture of OPV devices. It shows much less UV-induced yellowing and bonds better to substrate than EVA [89]. Several companies such as SunWare Solartechnik GmbH, Bemis Worldwide etc. have introduced TPU encapsulation films, which show improvements over non-encapsulated devices [89].

CYCLIZED PERFLUOROPOLYMER (CYTOP^{TM}): For creating commercially viable encapsulation structures for flexible OPV devices, a commercial polymer *Cytop*^{TM} (Figure II.10) was reported [90]. This polymer is transparent, amorphous, and can be deposited using conventional thin film deposition techniques such as spin coating. It is available as a high viscosity resin with chemical structure shown in Figure II.7. Atomic force microscopy (AFM) analysis shows that spin coating of this resin yields very smooth films with a root mean square roughness of 3.8 Å [90]. Contact angle (CA) analysis defines the material as hydrophobic having a water CA of 110^0. This material provides a good oxygen/water-vapor barrier in lifetime tests of organic light emitting diodes (OLED’s) [91]. OLED's are even more sensitive to oxygen/water-vapor degradation than OPV. *Cytop*^{TM} may therefore provide part of the barrier needed for commercially viable, flexible, printable solar cells [90].

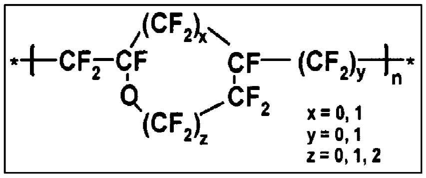

Figure II.10. Molecular structure for *Cytop*^{TM} [91]

II.1.5.1.3 ORGANIC–INORGANIC HYBRID MATERIALS

ORMOCER®(ORM): By using a technology combining organic and inorganic components through the sol–gel method, the organically modified ceramics or ORM is formed [92]. The main characteristic of this type of material is the incorporation of organic groups linked to the inorganic backbone formed by hydrolysis and condensation of alkoxides [93]. The combination of organic and inorganic networks in the ORM can enhance and improve resistance to chemical degradation [94]. *Fraunhofer ISC* (a materials research institute) introduced thin film based on ORM for encapsulation purpose, whose property profile can be varied almost at liberty with the aid of chemical nanotechnology [95].

All transparent materials reflect a certain amount of incident light. Surface structures in the submicron range can help to significantly reduce reflections by producing a smooth change in the refractive index at the surface boundary between air and the substrate. Structured ORM coatings typically reduce the reflection of a glass pane from 8 % to 1 %, thus increasing the transmission from 92 % to 98 % [95]. It has scratch resistance at layer thicknesses of only a few micrometers. It is highly transparent and has some other characteristics such as anti-soiling, antistatic or diffusion-inhibiting properties. OTR is measured below 0.01 $cm^3 m^{-2} day^{-1}$ while the WVTR reaches the value 0.01 $g m^{-2} day^{-1}$. These results are in the range of the necessary barrier requirements for the encapsulation of solar cells [95].

ORMOSIL AEROGEL THIN FILM: In nature, many plants and animals utilize superhydrophobic surfaces with a water CA larger than 150° and a sliding angle (SA) lower than 10° [96-98]. Inspired by this structure, many artificial super hydrophobic surfaces have been produced with a variety of techniques [99-105]. However, simple, low-cost, and large area fabrication of super hydrophobic surfaces, vital for practical applications, is rarely achieved and with a view to achieving this goal, several surfaces have been introduced recently [106-109]. Highly transparent and organically modified silica (ORMOSIL) aerogel thin film is one of them that has good thermal and mechanical stability [106]. ORMOSIL materials show some unique properties, such as flexibility and stability at atmospheric conditions, which cannot be afforded by either organic polymers or glasses alone. Both chemical and physical properties of the resulting surfaces, such as wettability, can be changed by modifying the organic group on the ORMOSIL [110]. Moreover, ORMOSIL aerogel thin films are highly transparent, do not need any pre or post surface treatments and can be applied on a variety of substrates at ambient conditions with common thin film deposition methods [106].

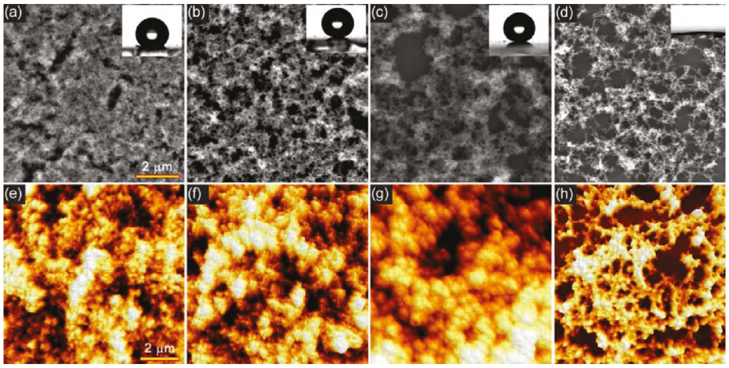

Figure II.11. Surface morphologies of ORMOSIL aerogel films [106]

ORMOSIL aerogel films have highly porous networks (Figure II.11) that provide high chemical and thermal stability, superior aging behavior and can facilitate a very short diffusion pathway for ions. These aerogel thin films contain both micrometer and nanometer scale roughness which provide super hydrophobicity. The films preserve their super hydrophobicity even after annealing at 500°C for 1 hour and also exhibit very high CA of 179.9° [106]. For higher temperatures, the CA starts to decrease and super hydrophilic films with CA less than 5° are obtained at 600°C. The increase in the macro porosity results in higher static CA values. This increase stems from increasing roughness which allows more air to be trapped between the water and the surface [106].

Super hydrophobic coatings must be transparent to be used in OPV cells. However, high surface roughness required for super hydrophobicity lowers the transparency by scattering light [88, 111]. ORMOSIL aerogel thin films are found to have an average surface roughness smaller than 100 nm, resulting in a highly transparent appearance. As a result, this approach is a suitable option for encapsulation of OPV [106].

OTHER ORGANIC MATERIALS: The air and encapsulation induced degradations affect the efficiency of organic thin film transistors (OTFT) and solar cells. To counteract the encapsulation-induced degradations in OTFT, ten types of encapsulating polymers over poly(3-hexylthiophene) (P3HT) are studied [112]. This research on OTFT gives us ideas about the degradation mechanisms and new encapsulation approach that can be applied on OPV. It is found that degradations could be avoided with polymers containing low-polarity functional groups, having poly(vinyl methyl ketone), poly(methyl vinyl ether), poly(methyl methacrylate), and polystyrene. Encapsulating polymers were poly(vinyl methyl ketone) (PVMK), poly(methyl vinyl ether) (PMVE), poly(methyl methacrylate) (PMMA), polystyrene (PS), poly(vinylidene chloride–co–vinyl chloride) (PVDC–co–PVC), poly(vinyl chloride) (PVC), poly(vinylidene fluoride) (PVDF), polyacrylonitride (PAN), poly(vinyl alcohol) (PVA) and poly(vinyl phenol)

(PVP). Of the 10 polymers tested, six polymers, namely PVA, PVP, PAN, PVC, PVDC–co–PVC, and PVDF induced strong p-type doping, i.e., they increased the off current (by 2–4 orders of magnitude), increased the on current (by 2–7 fold), and reduced the on/off ratio (by ~3 orders of magnitude). As a result, the P3HT layer encapsulated with the six doping-inducing polymers essentially becomes conductive, with conductivity rising from the pristine value of 1.1×10^{-5} S/cm to up to 1.6 S/cm [112]. The strong p-type doping by the six polymers was attributable to their electron-withdrawing functional groups. On the other hand, other 4 polymers - PVMK, PMVE, PMMA, and PS did not cause observable degradation [112]. This indicates that the functional groups on these polymers were not inducing charge-displacing interactions with P3HT. This was attributed to the lack of electron-withdrawing group on PS and PMVE [76]. On PVMK and PMMA, although there were the electron withdrawing carbonyl groups, the absence of degradation suggested that the interactions between P3HT and the carbonyl groups may have been hindered by the alkyl groups adjacent to the carbonyl groups [112].

Taking into account the identified sources of degradation, an encapsulation approach is demonstrated [112] which involves using a low-polarity encapsulating polymer (polystyrene) layer to serve as a moisture barrier and to avoid encapsulation-induced degradation. It also includes applying a light-blocking dye to eliminate the effects of oxygen [112]. This approach shows nearly constant device characteristics for >5500 h of storage in the ambient air. This long-term stability is a significant improvement over previously reported results [113-116].

II.1.5.1.4 COMPARISON AMONG SINGLE LAYER ENCAPSULATION MATERIALS

High transparency is found for *Si* polymers in the UV–visible band [59]. It is found down to 250 nm compared to the cutoff of 400 nm for EVA. It requires no additional additives to protect against UV degradation such as those used in other encapsulants like EVA formulations [59]. However, *Si* is very permeable to gas and water vapor and damp heat caused reduction in transmission [62].

Weatherability testing of EVA under UV irradiation and evaluation by FTIR measurements (Figure II.12) [81] shows apparent absorption growth at about 1715 cm^{-1} and 1175 cm^{-1}, representing carbonyl C=O stretching vibration in the rapidly forming ketone structure and C–O vibration respectively [117]. It might be obtained during the H_2O deprivation reaction of the hydroperoxide [118], or formed from the acetaldehyde evolution process in Norrish III photolysis reaction [119]. Such ketone structures are unstable that can lead to molecular decomposition in EVA [81]. Furthermore, adhesion strength can be affected by the processing conditions, damp heat and exposure time.

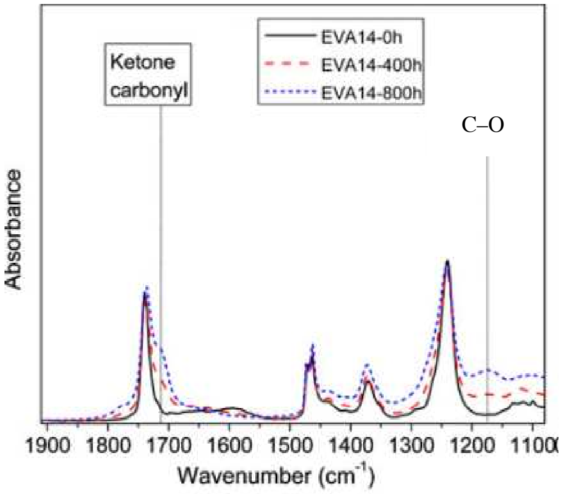

Figure II.12. FTIR spectra of EVA film during UV irradiation [81]

Yellow browning is another problem with the EVA films which leads to large transmission (%T) loss and power loss [80]. Furthermore, EVA softens to a viscous melt above 70°C and, therefore, must be cured (cross-linked) for service temperatures above 70°C [31].

Improvements were monitored for SiO_x and SiN_x encapsulation films over non-encapsulated devices [66]. However, the deposition of the encapsulation structure may cause plasma damage on the devices owing to the high sensitivity of the organic films to radiation, charging and heating [120, 121]. Introducing a buffer layer between the active layer and the barrier structure for reducing the plasma damage is therefore essential [33]. Encapsulation performance of Al_2O_3 is also found to be excellent [73, 78]. However, their relatively slow deposition rate compared to PECVD-based methods makes them more difficult to use in low-cost mass manufacturing processes. EMA and PVB have the same problem as vacuum-bag lamination is needed for the fabrication that is a slow process [31, 86].

II.1.5.2 MULTILAYER THIN FILM ENCAPSULATION

Multilayer films are widely used for encapsulation of OPV devices and often consist of alternating organic and/or inorganic layers [41, 76, 122-126]. Examples of multilayer films include alternating layers of inorganic materials such as SiN_x and SiO_x deposited by PECVD or a combination of Al_2O_3/SiO_x deposited by ALD [76, 127]. This multilayer approach is developed to thwart the defect issues limiting the barrier performance of single-layer encapsulation films. Defects which span the entire thickness of the individual inorganic layers are interrupted by applying multilayer films with alternating materials and do not channel continuously through the encapsulation film structure. This structure creates a path resulting in long effective diffusion pathways, increasing the barrier performance [128].

II.1.5.2.1 INORGANIC MATERIALS

SILICON OXIDE (SiO_x) AND SILICON NITRIDE (SiN_x): A barrier structure consisting of SiO_x and SiN_x films deposited via PECVD has been tested for the encapsulation purpose [127]. The WVTR of the barrier structure is ~3.12×10^{-6} g m^{-2} day^{-1} measured by a calcium test at 25 °C, 40%RH. This encapsulation structure shows less reactivity to water vapor and oxygen than individual SiO_x or SiN_x film [127]. Devices using the encapsulation structure are found to have a relatively low short circuit current density (J_{SC}) of 6.1 mA/cm^2, *FF* of 32% and *PCE* of 0.98% compared to the devices without barrier structure (J_{SC} = 8.2 mA/cm^2, *FF*=37% and *PCE*=1.57%). This performance presents a high potential for the structure to be used for encapsulation purpose of OPV [127].

NITROGEN GAS–PHASE SPACER: Permeation of gases through polymeric barriers is frequently described by the "solution-diffusion" model [129, 130], in which gas molecules dissolve in the barrier and then diffuse down a concentration gradient through the barrier. The total permeation rate is influenced by both the diffusion and the sorption properties of the permeant in the barrier. At steady state, the permeation rate is inversely proportional to the barrier thickness. However, increasing the barrier thickness increases encapsulation cost and to find an alternative encapsulation architecture that increases device lifetime without additional cost, contaminant-free (e.g., pure N_2) gas-phase spacers were inserted between free-standing barrier films in a multilayer structure (Figure II.13 (a)) [131].

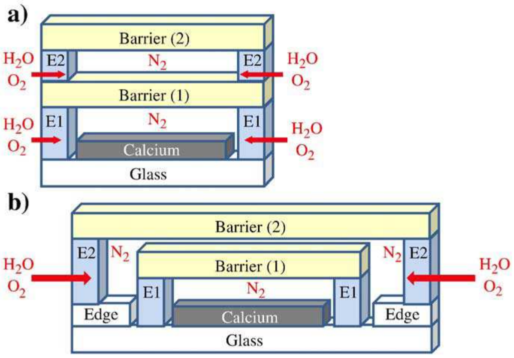

Figure II.13. (a) A calcium film encapsulated with a nitrogen gas-phase spacer between freestanding barrier films (b) Russian Doll encapsulation architecture [132]

The nitrogen spacers act as sinks for permeating H_2O and O_2, delaying establishment of steady-state chemical potential gradients across the downstream barrier layers during the transient regime and thereby reducing permeation rates. A limitation for the barrier performance of the encapsulation architecture (Figure II.13 (a)) is the epoxy (E_1), attaching Barrier (1) to the glass substrate, through which contaminants can diffuse and reach the encapsulated device without ever passing through the high performance barrier material [132]. Although the exposed area (and hence the contaminants flux) of E_1 is much smaller than Barrier (1), inexpensive epoxies are not optimized for barrier performance and so may have substantially higher permeability. As a result, diffusion through the epoxy may be large enough to result in significant flux of permeants through E_1 [132]. This flux may constitute the limiting factor for encapsulation performance. Using an encapsulation architecture that minimizes transport through epoxy layers is therefore desirable.

An encapsulation architecture utilizing a Russian Doll architecture (separating pairs of free-standing barrier films and epoxy seals with nitrogen spacers) (Figure II.13 (b)) is introduced to minimize the problem encountered by the *nitrogen gas-phase spacer* as discussed earlier [132]. Unlike the architecture of Figure II.13 (a), here permeants have to pass through at least two epoxy layers and a nitrogen spacer permeant sink to reach a device. The calcium thin film optical transmission test indicates that this encapsulating structure results in less than 10% calcium degradation after 95,000 min and a WVTR value of 0.00021 g m^{-2} day^{-1}, confirming that this architecture can enable construction of high performance barriers from low-cost materials [132].

TANTALUM–SILICON–OXYGEN (Ta–Si–O)/TANTALUM–SILICON–NITRIDE (Ta–Si–N): With a view to establishing a highly efficient barrier against humidity diffusion, thin films of *Ta–Si–O*/*Ta–Si–N* were investigated [133]. Investigations show that a 10 nm thick *Ta–Si–N* layer deposited onto a *Ta–Si–O* layer reduces CIS solar cell degradation at an accelerated aging test. Transparency is found for *Ta–Si–O* films over the whole CIS absorption region [133]. With increasing reactive gas content, the deposited films become more and more resistive. At the point of target poisoning, the thin-film resistance is changed from an ohmic to an insulating behavior. The electrical breakdown of 200 nm thick *Ta–Si–O* films appears at 6.5 MV/cm and reactively sputtered SiO_2 layers break down at approximately 10 MV/cm. Therefore, *Ta–Si–O* is a good isolator and passes the electrical needs for front diffusion barriers [133]. Reactively sputtered *Ta–Si–N* films are unstable even under low electrical stress. The thin-film capacitor with a *Ta–Si–N* dielectric layer reaches no significant breakdown voltage. The weak field stability of *Ta–Si–N* makes it suitable for using as an additional isolation layer. Altogether, a double-layer encapsulation, consisting of *Ta–Si–O* and *Ta–Si–N*, is able to protect a cell well against degradation in the accelerated aging test. Therefore, such a diffusion barrier is a good option for encapsulation of flexible solar modules [133].

Al_2O_3/SiO_2: Single Al_2O_3 atomic layer deposition (ALD) films on polymers have demonstrated excellent gas diffusion barrier properties [40, 55, 73, 78]. Further improvements can be achieved using multilayers of Al_2O_3 layers with other inorganic layers [76]. Al_2O_3/SiO_2 bilayers (26nm and 60 nm, respectively) can reduce the effective WVTR to 1×10^{-4} g m^{-2} day^{-1}, as opposed to ~1×10^{-3} g m^{-2} day^{-1} for the 26nm thick Al_2O_3 layer [76]. Some corrosion of Al_2O_3 layer was reported due to H_2O, which deteriorates the barrier functionality [75]. By the concept of Al_2O_3/SiO_2 bilayers, it is possible to reduce this corrosion substantially and improve the gas diffusion barrier performance [76].

Al_2O_3/ZrO_2: Nanolaminate films of Al_2O_3/ZrO_2 thin layers have been investigated to counter the drawbacks of Al_2O_3/SiO_2 bilayers [56, 125, 134, 135]. Nanolaminates are composite films comprised of alternating layers of different materials that often imparts unique properties to the films, which have physical properties that are superior to those of the constituent materials [125]. In this structure, amorphous Al_2O_3 sublayers serve as “termination” layers that hinder the formation of extended ZrO_2 crystallites and the ZrO_2 layer is intended to stop the accumulation of unreacted $Al–OH$ species [56]. The denser $ZrAl_xO_y$–aluminate phase that forms at the interfaces of the nanolaminate layer seems to hinder the penetration of moisture through the layer [125]. Experimental results prove that 100 nm and 130nm thick Al_2O_3/ ZrO_2 nanolaminates achieve permeation rates for both water and oxygen that are about one-half and one-fifth the values for 100nm and 130 nm thick Al_2O_3 layers, respectively [56]. A WVTR of 2×10^{-4} g m^{-2} day^{-1} is found for a 30 nm thick moisture barrier with this structure at ambient conditions [125]. The permeation rate is determined to be 1.6×10^{-2} cm^3 m^{-2} day^{-1} for oxygen (OTR) under a controlled environment of 70% humidity and 70°C [56]. Due to these very low permeation rates and the low process temperature, the Al_2O_3/ZrO_2 nanolaminate is able to provide encapsulation for OPV devices [56].

II.1.5.2.2 ORGANIC–INORGANIC HYBRID MATERIALS

NANOCOMPOSITE IV: To increase the gas barrier performances of polymer matrices, fillers (e.g. silica, metal oxide, clay, etc.) are added into them [136-140]. However, gas permeation continues for polymer matrices/fillers and metal alloys are therefore been blended with them to reduce the gas penetration [141]. This lab-made nanocomposite IV is applied for the encapsulation of OPV cells.

Thermal characterization reveals that nanocomposite IV has excellent thermal stability since it has a decomposition temperature larger than 300°C [141]. This is very crucial for the encapsulation of OPV because it can sustain high temperatures and defy the penetration of gas despite the OPV devices liberate much heat when actuated. It also exhibits good gas resistance.

Photoelectric conversion properties and efficiency of 0.42% are found initially in OPV cells without encapsulation [141]. The photoelectric conversion capabilities gradually decay while the actuating time proceeds. This decay is due to the invasion of atmospheric moisture and oxygen into the device, causing corrosion of organic materials and the metal electrode. After being actuated for 48 h, the efficiency reaches 0.016% (decay ratio = 96.2%) [141]. With the encapsulation of nanocomposite IV, the decay ratio is 13.0% and 37.0% when the actuating times are 15 and 48 h, respectively. Along with afore mentioned properties, it also has moderate adhesion strength, low shrinkage and fast curing speed that demonstrate the capability of defying the permeation of oxygen as well as moisture of the air into the device, effectively elongating the lifetime of OPV cells [141].

SiO_x/ORGANOSILICON: Alternating SiO_x and organosilicon layers deposited by PECVD on a poly(ethylene naphthalate) (PEN) substrate are introduced for encapsulation to prolong the lifetime of OPV cells to a greater extent than the organic/inorganic hybrid nanocomposite IV does [142]. SiO_x is produced from a volatile organosilicon precursor under oxidative plasma conditions and organosilicon is deposited using similar organosilicon in non-oxidizing plasma. The final ultra-high barrier consists of five layers, each approximately 100 nm thick, resulting in a total thickness of 500 nm [142]. This coating is transparent having an optical transmission $T >$ 85% over the entire visible spectrum. It also shows good resistance to common organic solvents. In the case of encapsulated OPV cells based on MDMO-PPV devices, V_{OC} remains at about 90% of its initial value after 3,000 hours, as does FF [142].

The 3000 h of device stability achieved by applying encapsulation structure of alternating SiO_x and organosilicon layers is not sufficient for OPV. Developing ultra-high barrier performance encapsulation layer as well as more stable materials for OPV devices is therefore important to extend the cell's lifetime [142]. With a view to this, organosilicon/SiO_x structure is deposited onto the polyethylene terephthalate (PET) substrate by PECVD process [143]. A WVTR of 0.22 g m^{-2} day^{-1} is found for the assembly. By coating 6-pairs of the multilayered structure onto PET, an ultra low WVTR much lower than the MOCON detection limit ($<1\times10^{-2}$ g m^{-2} day^{-1}) is achieved. Such a simple and controllable encapsulation approach is a promising candidate for OPV [143].

SiN_x/PARYLENE: A benefit of SiN_x over oxide or oxynitride as an effective, transparent inorganic barrier coating material is that it does not require reactive oxygen atoms in the deposition process, which could react with the substrate [123]. The OTR and WVTR decrease as much as thousand fold when the coating thickness of SiN_x exceeds 70 nm. An external tensile state of stress in the SiN_x coating may cause the formation of cracks and the cracked film may also debond from the substrate along the interface. One way to further improve the barrier performance is to deposit a smoothing, defect decoupling organic film on top of the inorganic layer. With a view to this SiN_x/parylene multilayered structure is introduced [123]. It results in an improved permeation resistance of the coating as well as an improved resistance to crack formation. After 3000-times cyclic bending, the WVTR and OTR of the two pairs of parylene/SiN_x coatings can be maintained at a level near 0.01 g m^{-2} day^{-1} and 0.1 cm^3 m^{-2} day^{-1}, respectively. The barriers exhibit moisture and oxygen barrier performance below the detection limit of the MOCON instruments [123]. SiN_x/parylene is therefore a good candidate for the encapsulation of OPV [123].

SiO_x/SiN_x/PARYLENE: Inorganic encapsulation films show limited barrier performance due to micro defects [144]. These defects provide easy pathways for moisture and oxygen diffusion, and thus limit the barrier characteristics [145]. The micro defects can easily promulgate to form cracks, which render such flexible films permeable. An organic barrier film with the low internal stress, high transparency, and pinhole-free can be used to suppress the crack elongation. A multilayer encapsulation structure composed of SiO_x, SiN_x and parylene is therefore investigated for permeation barrier applications [124, 145]. After 75 d, the WVTR can reach 2.5×10^{-7} g m^{-2} day^{-1}, as calculated by the calcium test [124]. After being flexed for 5 000 times, the WVTR value almost keeps around 2.1×10^{-6} g m^{-2} day^{-1}. Therefore, the performance of this multilayer barrier structure has a high potential for OPV [145].

II.1.5.2.3 COMPARISON OF MULTILAYER ENCAPSULATION MATERIALS

Russian doll architecture minimizes the problem of diffusion through epoxy layers [132]. However, desired lifetime is not achieved by this approach. Multi-layer structure of *Ta-Si-O* and *Ta-Si-N* is an improvement over Russian doll architecture. These films have an amorphous-like microstructure although they both are grown on crystalline substrates. *Ta-N* films without silicon are slightly crystalline. Tantalum-Oxygen films deposited on native silicon-oxide also grow amorphous-like. In the case of a polycrystalline substrate, the microstructure is reproduced from the substrate so that the *Ta-O* microstructure becomes polycrystalline. The grain boundaries in polycrystalline films are fast diffusion paths for humidity resulting in a significant decrease of the PV cell efficiency. Al_2O_3/SiO_2 films show better efficacy in that sense. However, the deposition temperature needed is 175°C whereas a temperature below 100°C is required for deposition on top of OPV devices [76]. Moreover, larger thicknesses and greater brittleness may cause cracks under the strain of handling and mounting the ALD-coated polymer films. Al_2O_3/ZrO_2, nanocomposite IV and UHB coating are other encapsulants used to solve the encapsulation problems. However, none of them meets the desired lifetime criteria.

II.1.6 SUMMARY OF ENCAPSULATING MATERIALS

Permeation of about two to three orders of magnitude lower than the bare substrate is usually considered satisfactory to ensure encapsulation requirements (Table II.1). It has been shown that the best transparent single-layer barrier performance is achieved for silicon-based dielectric films deposited by PECVD [50]. However, single layer barriers cannot reach permeation levels lower than 1000 times that of bare polymer substrates. Increasing the thickness of a single-layer barrier leads to a non-zero asymptotic value of OTR that is controlled by the number of defects present in the barrier layer. These defects are mainly caused by intrinsic or extrinsic surface roughness [51]. Hence, these nanometer size structural defects account for the limited performance of single-layer gas barriers. Besides, theoretical calculations have shown that the total permeation rate through many small pinholes is much higher than that corresponding to the same total pinhole area combined in a few larger defects [146]. This can be explained by lateral diffusion, and it is of crucial importance when the diameters of the defects are small compared with the thickness of the substrate. It has been proven that deposition of multilayered inorganic films generally improves the barrier performance only slightly. The most common technique used to achieve high performance barriers is based on organic–inorganic multi- layers. However, several constraints on the development and utilization of thin-film encapsulation technologies exist that make their development challenging. A variety of materials have been developed to face these challenges that improve lifetimes and one notable case is Titanium Oxide (TiO_X). It cannot satisfy the encapsulation requirements of organic devices, however, results prove the concept of using thin films as barriers to encapsulate devices. The simplest example of encapsulation is the use of glass plates. This provides the level of oxygen protection required by the industry, but glass creates inflexible devices however. Research also shows that a layer of SiO_XC_Y performs well. Unfortunately, despite being flexible, and resistant to oxygen transmission, this encapsulation must be performed with PECVD process that involves expensive, and complicated vacuum systems. There are many other materials used for the encapsulation purpose, however, in general they cannot fully satisfy the barrier requirements. Some of these materials and methods are summarized below in terms of their WVTR and drawbacks:

Table II.2. Summary of encapsulating materials

Material	Encapsulation type	WVTR (g m^{-2} day^{-1})	Comment
SiN_x	Single layer (inorganic)	< 0.01	Passivation properties should be improved
Al_2O_3	Single layer (inorganic)	1.7×10^{-5}	Permeation governed by nanoscale defects
PVB	Single layer (organic)	50 (at 38°C/100% RH)	Time consuming vacuum lamination Low mechanical strength
ORMOCER®	Single layer (organic-inorganic hybrid)	0.01	Surface roughness Biological disadvantages
SiO_x/SiN_x	Multi-layer (inorganic)	3.12×10^{-6}	High deposition temperature
N_2 gas phase spacer	Multi-layer (inorganic)	2.1×10^{-4}	Lifetime expectancy
Al_2O_3/SiO_2	Multi-layer (inorganic)	1×10^{-4}	High deposition temperature (175ºc) Formation of cracks
Al_2O_3/ZrO_2	Multi-layer (inorganic)	2×10^{-4}	Lifetime expectancy
Organosilicon/SiO_x	Multi-layer (organic-inorganic hybrid)	22×10^{-2}	Formation of defects Degradation of reliability due to residual compressive stress
SiN_x/Parylene	Multi-layer (organic-inorganic hybrid)	1×10^{-2}	Poor adhesion between organic and inorganic layer Durability is dependent on coating thickness
SiO_x/SiN_x/Parylene	Multi-layer (organic-inorganic hybrid)	2.5×10^{-7}	WVTR is dependent on coating thickness Lifetime expectancy

Thin film encapsulation is a critical technology required for the application and commercialization of OPVs. Effective encapsulation to prevent the permeation of water vapor and oxygen, which degrades OPV devices, is key for achieving the reliability and desired lifetimes. The materials applied for this purpose, cannot yet satisfy the encapsulation requirements discussed in this chapter. Hence, new materials are needed which will satisfy the encapsulation requirements and achieve the reliability and lifetime required.

Optimizing the dimension of individual films or replacing some of the constituent films with others deposited by different processes can be considered as an alternative based on the encapsulation structures discussed in this chapter. Further study for reducing processing time and steps is required. Efforts to improve the quality of films should also be addressed before adapting these technologies. In addition to reducing processing steps and time, studies concerning the reliable and continuous yield of encapsulation processes should be performed. In summary, high quality encapsulation layers are critical for improving the life span of OPV devices, and further research is needed to improve the quality of materials suitable for encapsulation layers.

II.2 FUNDAMENTALS OF SURFACE MODIFICATION AND PLASMA POLYMERIZATION

The fundamentals of surface modification and plasma polymerization process have been investigated extensively in the past [147-154]. A complete coverage of this topic would by far exceed the scope of this work. Therefore, only the most relevant concepts and some basic ideas are introduced in this section. Emphasis is placed on fundamentals that are relevant for the applied process within this work.

II.2.1 SURFACE MODIFICATION TECHNIQUES

In recent years, an increased trend in replacing traditional materials such as glass, metals, and paper with polymeric materials is noticeable in various applications [155]. Comparability of physical and chemical characteristics of polymers to those of conventional materials and their relatively low cost are the primary reasons for this increased trend. However, most polymeric surfaces do not possess specific surface properties needed in various applications. They are inert, hydrophobic in nature, and usually have a low surface energy [156]. Therefore, their surfaces need to be treated and modified to obtain polymers with desired surface properties in various instances [44].

Surface treatments can serve different purposes such as improving adhesion characteristics, increasing hydrophobicity, introducing special functional groups at a surface, or modifying the surface morphology, and surface deposition [157]. Surface modification of polymers can be accomplished by either chemical or physical methods. However, physical methods can provide more precise surface modification without the requirement of rigorous process control than chemical process does. Ease and precise controllability of physical methods eliminates harsh surface roughening, surface damage, and improper surface modification problems. In addition, they are environmentally safe and clean processes because no chemical solution is involved in physical methods, and thereby there is no disposal of the waste liquids. Physical surface modification methods range from simple flame and corona treatments to more complicated and advanced techniques such as UV, γ–ray, electron beam irradiations, ion beam, plasma, and laser treatments [158]. Some of these physical surface modification techniques will be discussed briefly in the next section.

II.2.1.1 PHYSICAL SURFACE MODIFICATION METHODS

A. FLAME TREATMENT

The purpose of flame treatment is to introduce oxygen-containing polar groups on surfaces to improve their printability, wettability, and adhesion [159]. The formation of oxygen-containing polar groups is responsible for the enhanced printability, wettability, and adhesion. The high flame temperature (1000-2000 °C) and reaction with excited species in the flame, basically leads to an increased oxygen concentration at the treated surface.

B. CORONA DISCHARGE TREATMENT

Corona discharges are widely used in surface modification of polymers to enhance the adhesion [158]. A corona discharge (atmospheric pressure plasma) is produced when air is ionized by a high electric field. Voltage and frequency of electromagnetic field, the compositions of gas atmosphere, corona exposure time, etc. are important factors that require precise control to obtain polymer films with good adhesion properties [160].

Corona and flame treatment processes can be used in continuous operation and the required equipment is very simple and cost effective. However, both treatments are carried out in open air that often makes it difficult to control the uniformity or chemical nature of the modification, due to variations in ambient conditions such as temperature and humidity or contaminations.

C. UV TREATMENT

Surface modification of polymers with UV treatment first began in the electronics industry [161]. The principle of this treatment is based on photons (high energy species) that are used to activate many chemical reactions. These reactions generally occur in the presence of an initiator or a sensitizer that absorbs UV irradiation and it is excited to a short lifetime singlet state that rapidly transforms to a more stable triplet state. The initiator in its triplet state can abstract hydrogen from the polymer surface and create active sides for grafting. If a grafting monomer is supplied in the medium, graft polymerization occurs at the interface between the polymer and the surrounding medium. Bulk properties of polymers are not altered at the end of this process because of the absorbance of UV irradiation by the initiator, [162]. The main advantage of UV irradiation is the low cost of equipment and the process with a high selectivity of the photo initiator. In addition, UV treatments are fast, non-polluting processes, suitable for heat-sensitive polymers and require less space. However, the interference due to the presence of pigments in polymers or coatings is the major limitation of this process as pigments also absorb and scatter UV radiation to some degree.

D. γ–RAY TREATMENT

Gamma-ray treatments modify polymer surfaces via a mechanism of free radical formation similar to that occurring in UV treatment. Generally, γ–ray treatments are used for cross-linking of polymeric coatings and formation of thin polymeric films with desirable surface characteristics. This process increases the adhesion and modifies the mechanical properties of polymers.

E. ELECTRON BEAM TREATMENT

The basic principle of electron beam treatments is based on accelerated electrons, which carry high amount of energy, causing excitation or ionization of molecules. This process induces the formation of some functional species that can be deposited on the surface of electron beam-treated polymers. Electron beam treatments do not require photo–initiators, unlike UV treatments and electron beams can be focused or directed onto materials to be cured. However, this type of treatment is more expensive, needs more space and more stringent safety precautions than UV treatments.

F. PLASMA TREATMENT

Flame treatment and corona discharge are both based on the formation of plasma. However, plasma treatment will be referred to in this thesis as the modification of a surface with a non-polymerizable gas in a vacuum system.

The plasma is a partially ionized gas that is a mixture of electrons, negatively and positively charged particles, and neutral atoms and molecules [153]. Plasmas have been described as the fourth state of matter, which is highly activated compared to solid, liquid or gas state. It is typically obtained by exciting a gas or vapor into high energetic states by RF, microwave, alternating current (AC) or direct current (DC) glow discharges, as well as by the electrons of a hot filament discharge. The existence of diverse plasma techniques and varied ways of generation allows for plasma modification methods to be adapted to any kind of material and specific requirements.

Plasma can be divided into three major groups depending on the type of gas used to create the plasma: chemically non-reactive plasma, chemically reactive plasma and polymer-forming plasma. Chemically non-reactive types of plasma are those of monoatomic inert gases (Argon or Neon) that can ionize other molecules or sputter materials but are not consumed in chemical reactions. Chemically reactive plasmas use inorganic or organic molecular gases that are chemically reactive but form no deposit on the substrate, like O_2 or CO. These kinds of gases are able to cross-link, incorporate oxygen or modify the surfaces. Polymer-forming plasmas are chemically reactive and form a solid polymeric deposit [153].

Based on the above mentioned plasma classification (by the type of gas), different kinds of plasma processes can be used to modify the surfaces. Physical sputtering of materials is one of these processes that is based on a non–reactive gas in the plasma phase. This sputtering is mainly used as cleaning process on glass and ceramics [163]. Chemical etching is another plasma process that is widely used in electronics fabrication. This process involves the chemical reaction of the excited species with the surface elements, such as oxidation by O_2 plasma. This process can modify the surface with high degree of cross-linking (in the case of polymeric surfaces), or changes of the hydrophobicity of the surfaces by changing their chemical nature [164]. Plasma deposition processes include polymerization, grafting or plasma spraying [163]. The plasma polymerization is explained in detail in section II.2.2 as it was the method used to fabricate insulating polymer-like thin films throughout the work of this thesis.

II.2.2 PLASMA POLYMERIZATION

Plasma polymerization (plasma deposition or often referred to as PECVD) has a long history, dating as early as 1796 [165]. It was not until the 19th century that plasma deposits gained significant interest and the field of plasma deposition received attention [166, 167]. It is an inexpensive technique that can be used to control the fabrication of polymer thin films and their properties by varying the process parameters (e.g. pressure, applied current, monomer flow rate and deposition time) [168]. Being a low-temperature process, non-equilibrium plasma polymerized films are smooth, insoluble, pinhole-free, chemically inert, thermally stable and cross-linked [153, 169-171]. Their chemical, physical and optoelectronic properties can be tailored to suit a desired application by controlling the retention of original monomer functionality, degree of cross-linking, and branching [172]. This low-cost ‘green’ process has been used to fabricate environmentally friendly insulating thin films from a number of naturally occurring non-synthetic monomers, such as linalyl acetate and terpinen-4-ol [173, 174]. Current understanding of the processes and mechanisms involved in PECVD, their relationship with internal system characteristics and external experimental variables and how these relate to the characteristics of the deposited thin films are discussed in this section.

II.2.2.1 FUNDAMENTALS OF PLASMA POLYMERIZATION

Modeling the internal mechanisms involved in plasma polymerization is complex, due to the difficulty of reconciling observed film properties with internal reaction parameters. The same process can remove material from a substrate, or deposit material onto a substrate, i.e. the process can both etch materials *and* form a plasma product on exposed surfaces, depending on reaction parameters [175]. Depending on the reactor type, process variables and feed gas, the properties of resultant thin films therefore vary drastically. Moreover, until recently, the ability to accurately measure properties of the plasma discharge had been significantly limited; measurement of the reactive species involved and density, temperature and source of electrons was difficult, if not impossible. These factors made the task of developing a description of the plasma deposition process difficult.

The key factor in any plasma is the dynamics of electrons, typically created through the ionization of feed gases and their dissociated products [11]. When an electric field is applied, the electrons gain energy according to Newton's law [153],

$$\mathrm{a} = \frac{\mathrm{q}}{\mathrm{m_e}}\mathrm{E} \tag{II.7}$$

where a is the acceleration of the electron, q is its electric charge, m_e is its mass and E is the electric field. Three different types of collisions can occur between an electron and an atom, depending on the energy K that is transferred to an electron in the atom:

1. $K = 0$. The electrons in the atom remain in the ground state. The collision is elastic, and causes no change in the structure of the atom.
2. $0 < K < qV_i$, where V_i is the ionization potential of the atom. An electron in the atom is excited to a higher energy level, but returns to the ground state in a short time, generally releasing the gained energy through collisional or radiative processes. The collision is referred to as an inelastic process.
3. $K > qV_i$. The atom is ionized by electron impact, and becomes positive with charge $+q$, ejecting a secondary electron, which then contributes to other electron induced processes in the plasma.

Between the energy level of the ground state and that of the ionized state, a number of other energy levels can exist. An electron in an atom that receives energy from a primary electron can jump to a higher energy level. However, after a short period of time (of the order of 10^{-8} s), it returns to lower energy levels or to the ground state. The electron's excess energy is thus released e.g. by emission of a photon, or via collisional deexcitation. When an electron returns from energy level E_m to E_n via photon emission (m and n represents higher energy level and ground state respectively), the frequency v of the photon is given by:

$$\mathrm{hv} = \mathrm{E_m} - \mathrm{E_n} \tag{II.8}$$

where h is Plank's constant.

The temperature of colliding species plays an important role on the collision processes occurring in a glow discharge. The electron temperature T_e in a plasma is often approximated by by [176]:

$$\mathrm{T_e} = \left(\frac{\mathrm{e}}{\mathrm{k}}\right)\left(\frac{\mathrm{E}\lambda_\mathrm{e}}{2\sqrt{2}}\right)\left(\frac{\mathrm{m_m}}{\mathrm{m_e}}\right)^{1/2}\left(\frac{\pi}{6}\right)^{1/4} \tag{II.9}$$

in which k is the Boltzmann constant, λ_e the mean free path of electrons, and m_m the mass of particles (neutral atoms and molecules). Since the ratio of m_m/m_e is very high, the electron temperature in a low pressure plasma is extremely high (e.g. on the order of 10^4 K). Because ions have roughly the same mass as the corresponding neutral atoms and molecules, they lose most of their kinetic energy in collisions with molecules. The ion temperature T_i is therefore much lower than T_e (in the range of 300-1000 K), and it is only slightly higher than the temperature of molecules T_m (~ 300 K) [153].

II.2.2.2 TYPES OF COLLISIONS

A number of different collision processes occur in a glow discharge, including ionization, excitation, dissociation and attachment [159]. Ionization is an essential step in creating and sustaining a plasma, but is not necessarily the primary step in initiating plasma polymerization [153]. The ionization of an atom "M" for example can be visualized as follows:

$$\mathrm{M} + \mathrm{e}^- \rightarrow \mathrm{M}^+ + 2\mathrm{e}^- \tag{Ionization}$$

A positive ion and two electrons are produced in this reaction. The two electrons are accelerated by the electric field, and can produce further ionization. Electrons in the ground state can also jump to higher energy levels (excitation), without resulting in ionization:

$\mathrm{M} + \mathrm{e}^- \rightarrow \mathrm{M}^* + \mathrm{e}^-$ (Excitation)

After a very short period of time the electron returns to a lower energy level, or returns to the ground state by radiated decay (de–excitation):

$\mathrm{M}^* \rightarrow \mathrm{M} + \mathrm{h}\nu$ (De-excitation)

Some excited states, however, have much higher stability than others, and have lifetimes of 1 ms or longer. Such a state is called a metastable state [152]. The metastable atom returns to the ground state upon collision, but transfers the excess energy to the colliding atom. A metastable atom can also be ionized by electron impact directly. Negative ions (F^-, Cl^-, Br^-, I^-, O^- and O_2^-) can also be produced in a glow discharge, if a molecule captures a free electron.

Collisions between charged species take place in ionized gas as well. However, these collisions do not play an important role in our processes, as our plasmas are only partially ionized, and contain far more neutral species than the charged ones. An example of such a collision is recombination:

$\mathrm{Ar}^+ + \mathrm{e}^- \rightarrow \mathrm{Ar}$ (Electron–ion recombination)

$\mathrm{O}^- + \mathrm{Ar}^+ \rightarrow \mathrm{O} + \mathrm{Ar}$ (Ion–ion recombination)

Recombination also occurs at the surface of the reactor. Collisions of electrons with the reactor wall charge the surface negatively, which attracts positive ions that neutralize the charge. In this reaction the energy gained in the ionization process is released, and absorbed by the surface in the form of thermal energy [153].

II.2.2.3 REACTION PATHWAY OF PLASMA DEPOSITION OF THIN FILMS

Monomer units, monomer fragments, ions, radicals, electrons and photons are present in the gas phase after the formation of the active species. Recombination of radicals is the main contributor to the increase of molecular weight of the material, i.e. the growth mechanism is considered to be a radical dominated mechanism [177]. This can happen in both the gas phase or at the substrate surface by the recombination of adsorbed species as mentioned in section II.2.2.2. ‘Powder-like’ deposits may be produced due to the formation of a polymer in the gas phase at higher pressures [178]. Recombination reactions with adsorbed species at the substrate surface are therefore preferred. The bombardment of adsorbed particles and reaction products at the surface of a substrate by the charged active species in the gas phase is another important consideration. This bombardment is caused by materials exposed to the plasma which in turn results in the attraction of charged particles to the surface. Ion and photon bombardment causes ablation, or sputtering of the deposited film back into the gas phase that is also associated with the formation of radical products in the bulk of the material [175, 179]. Bombardment of the bulk film by active species is also partially responsible for the crosslinking and insolubility observed in many plasma deposited films, for the high concentration of radicals embedded in the film, and some of the aging reactions.

The complex mechanisms of plasma deposition and reaction pathways include the contributions of several factors:

1. Initial kinetic reactions to form reactive species.
2. Interaction of reactive species via radical growth reactions in the gas phase and at the surface.
3. Bombardment of surfaces by active species.

These results in ablation of deposited species back into the gas phase. This is outlined in Figure II.14 [177]:

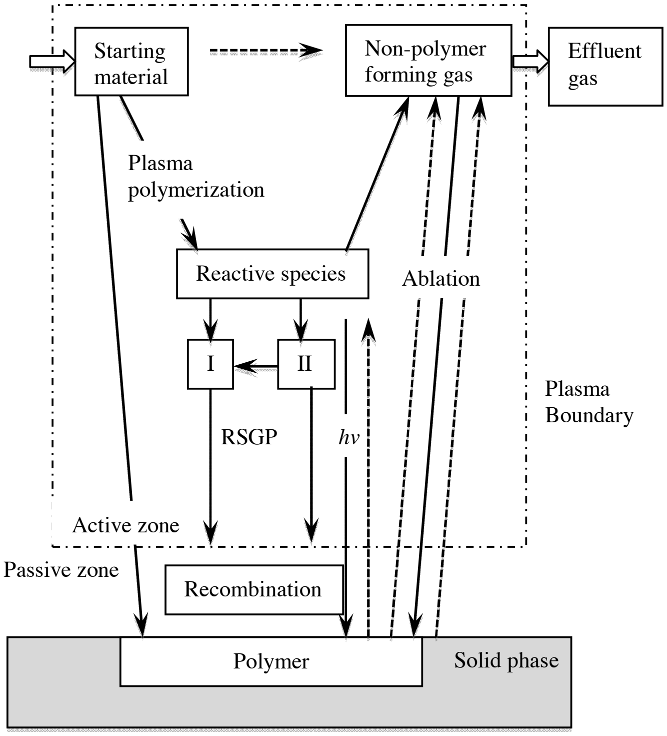

Figure II.14. Plasma deposition process [153]

The processes in the recombination and chemical reaction steps can be explained by the Rapid Step Growth Polymerization (RSGP) mechanism, proposed by Yasuda [179]. It is assumed that radical formation is taking place within the gas phase in the active zone (bulk plasma and plasma/sheath boundary region) through which the gas particles (monomers and reactive gases) travel, and then enter a passive zone (plasma sheath and surface growth region) yielding recombination and stable products, such as deposition (concept of chemical quasi-equilibrium) [177]. As schematically shown in Figure II.14, the recombination of reactive species and reactivation of reaction products determine the plasma polymerization. The reactive species are mainly radicals, where cycle I (Figure II.15) consists of reactions between reactive species and a single reactive site. *M* (Figure II.15) can be either the original monomer molecule, or any of the dissociation products, including atoms. The reactive species are denoted here as mono–functional (*M•*), or di–functional (*•M•*) free radicals, but other activated species should also be considered in the reaction mechanism. In cycle I, the reaction products from mono–functional activated species are repeatedly activated. Cycle II proceeds through the reaction of di–functional radicals with other species.

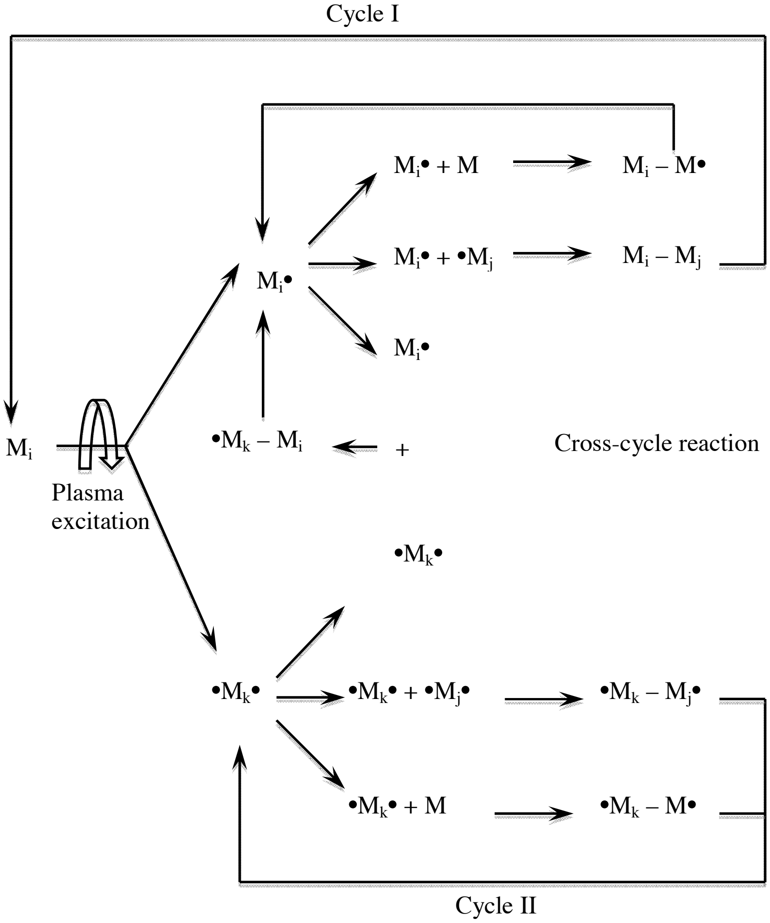

Figure II.15. Schematic diagram of the RSGP mechanism [153]

Cross-cycle reactions from II to I can also occur [180]. Furthermore, the surface takes part in plasma polymerization by radical sites, third-body reactions, and etching processes that lead to ablation and re-deposition. Hence, a plasma polymer typically results from the competition between etching and deposition processes and it has a more or less cross-linked structure, depending on the plasma species present during the film growth. The growth via cycle I requires the reactivation of the products of reaction, while cycle II can proceed as long as divalent reactive species or monomers with double and triple bond exist. Repeating steps via both cycles, the species vary in size, leading to a deposit in the substrate surface. The kinetic chain length expresses the number of how many times the cycles repeat before a species deposits. It is a measure of the number of monomer units that are added to the polymer chain by one initiating reaction before termination of the chain occurs, and increases with monomer concentration and decreases with reactive species concentration. As the concentration of monomer units is quite low in a plasma system, given the tendency for the monomer to dissociate into radical fragments, the concentration of reactive species is very high and very short kinetic chain lengths occur [178]. The reactions therefore begin and terminate quickly and deposition occurs in a series of small steps, resulting in a film of very short, branched, randomly terminated and cross–linked polymer chains.

The RSGP mechanism describes reactions between reactive species in a generalized sense; above the reactive species were considered to be radical monomer fragments, however nothing prevents these reactive species from being ionic, for example. As well as this the location of the reactions are not specified, only the reactions between reactive species. Thus RSGP can apply to gas phase, plasma sheath and surface reactions.

II.2.2.4 GENERAL CONTROL PARAMETERS

By comparison of different reactor geometries, reactor-specific particularities can be revealed, which allows one to select the appropriate plasma reactor set-up depending on the required application [177]. However, different other requirements and influencing factors have to be taken into account that will influence the behavior of the reactions and the plasma deposition. These parameters are: the geometry of the reactor [181], substrate temperature, influence of energetic particles, the monomer [177], influence of carrier/reactive gases, the flow rate of the monomer through the system [182], the power delivered to the system [183, 184] and the gas pressure [177, 185]. All of these factors have been shown to significantly influence the properties of resulting films [177].

INFLUENCE OF REACTOR GEOMETRY

Use of different geometry reactors while maintaining other parameters of the deposition constant resulted in different behavior of amorphous hydrocarbon (a–C:H) thin films deposited from tetramethylsilane (TMS) and hexamethyldisiloxane (HMDSO) monomers [181]. Hegemann *et al* further investigated the significance of reactor geometry on the behavior of films deposited from methane and HMDSO, and ascribed the different behaviors to the change in volume which the plasma occupied [186].

INFLUENCE OF SUBSTRATE TEMPERATURE

During plasma processing, the growth rate depends only on the monomer supply at relatively low substrate temperatures, while for elevated temperatures, the monomer coverage is the limiting factor for the quantity of the layer being deposited [187]. The deposition rate can therefore be considered to be constant within a temperature range close to the room temperature, and decreases with further increasing the temperature, due to ion interaction during the growth of the film [177].

INFLUENCE OF ENERGETIC PARTICLES

As mentioned before, energetic particles might play a dominant role in plasma deposition. Potential drops (plasma sheaths) are obtained near material surfaces depending on the reactor design and external parameters that accelerate ions and influence the growing of plasma films [177]. Increasing energy input yields higher energetic ion bombardment that causes higher plasma dissociation and contributes to increased generation rate of nucleation sites on the film surface that in turn increases the deposition rate. The energetic particle interactions can also influence the absolute deposition rates and film characteristics, such as density, material microstructure, morphology, as well as optical, electrical, and mechanical properties [177].

INFLUENCE OF MONOMER

The influence of monomer on the resultant thin film properties was demonstrated through the investigation of films fabricated using isomeric monomers by Denis *et al* [188]. No compositional differences were present between the monomers in this study; only the molecular structure was varied. Differences in bond dissociation energies in the different isomers caused the differences in the chemical composition of the films. Differences in the chemical composition of the plasma gas (i. e. differences induced by the monomer) can induce substantial differences in the properties of resulting films [177].

INFLUENCE OF CARRIER/REACTIVE GASES

The addition of non-polymerizable gases such as inert (He, Ar, etc.) and reactive (O_2, N_2, etc.) gases to monomers during plasma polymerization might have a strong influence on the film growth mechanism. Hegemann *et. al.* found that a large part of the energy input is consumed by the reactive gas oxygen that contributes to the film deposition via reactions with oxygen radicals and incorporation into the growing film [186]. It was also found that the addition of inert gases, such as Ar and He, showed a negligible effect (physical interactions) on the deposition rate, and hence on the plasma polymerization mechanism. They can be considered as carrier gases. However, reactive gases showed a more distinct influence that proves their increased contribution to film formation by plasma chemical processes.

INFLUENCE OF MONOMER FLOW RATE

The dependence of gas flow rate on the deposition rate of specific surface material varies from plasma reactor to plasma reactor. However, below a critical flow rate, there is an inadequate supply of reactant to be deposited on the surface material. A small increase in flow rate can therefore rapidly increase the deposition rate.

As the flow rate is increased, the product species are flushed away and thus subjected to less dissociation and recombination reaction in the plasma [177, 182]. However, the initial reactant gas is less utilized. Use of the precursor will increase as the input power is increased [189]. If the flow rate is further increased maintaining a constant pressure, it is possible that the active species produced in the plasma can be pumped away before they can react.

INFLUENCE OF RF POWER INPUT

At constant pressure, increasing the power input into the plasma can raise the plasma density. Applied potential will therefore increase, particularly at the lower pressures [190]. It will also increase the potential across the ion sheath raising the ion bombardment energy. The rate of formation of other plasma products such as free radicals also increases with increase in power input. However, any polymer condensation from heavy free radicals will be offset by the higher ion bombardment energy.

The increase in ion bombardment energy by increasing RF power input could make the ion bombardment, at the surface, a more probable reaction for inducing chemical change by bond rupture or damage. There will also be an increase in ion density that can increase the deposition rate on the surface. An increase in ion bombardment energy may also have an effect on surrounding atoms in the area of bombardment, which can lower the activation energy and increase the rate of reaction thus increasing the deposition rate [183].

INFLUENCE OF GAS PRESSURE

The mean free path of the plasma components is reduced as the gas pressure is raised [177]. An increase in producing more radicals and ions (depending on the electron temperature and the species in the system) is therefore observed that can have several effects. It can increase the deposition rate by raising the ion or free radical concentration at the surface [177]. Free radicals can recombine with each other forming higher molecular weight species. These species can also fragment and recombine eventually forming high molecular weight condensed polymers on surfaces. Such an event is more probable at higher pressures, and with long resident times for free radicals of heavy mass.

Ion concentration initially increases with the increase of gas pressure and the impedance of the plasma may therefore fall resulting in a lower applied potential at a given power input [185]. At the ion sheath, the ion bombardment energy will fall with the decrease in sheath potential caused by the reduction of applied potential to the plasma. Thus polymer may grow on an exposed surface as the arriving ions have lower energy. Also the ion energy may be too low to induce chemical reactions that need for ion bombardment.

II.2.2.5 RELATIONSHIP BETWEEN CONTROL PAPRAMETERS AND FILM PROPERTIES

A decrease in monomer flow rate results in a larger residence time and hence an increase in the fragmentation of the monomer [177, 182]. In a similar manner, power delivered to the reaction relates to the energy delivered to monomer molecules, resulting in increased monomer fragmentation [183] and change in film properties. The pressure influences the deposition indirectly by influencing the plasma volume and the distribution of reactive species in this volume [185]. All of these parameters interact in complex and unpredictable ways. In an attempt to relate the deposition conditions and film properties through a single parameter, the composite parameter, W/FM was developed, where W is the power absorbed by the plasma in W, F is the flow rate of the monomer in mol s^{-1} and M is the molecular mass of the monomer in kg mol^{-1}. As the parameter M is constant for a given monomer, the composite parameter is often reduced to W/F.

The W/FM parameter is defined as an apparent input energy of the plasma per the unit of monomer molecule in plasma polymerization. In other words, this parameter means that how much energy is invested in the fragmentation process of monomer molecules [181]. It is considered to be proportional to the concentration of activated species in the plasma [191]. This has been experimentally investigated by monitoring the composition of the plasma discharge as a function of W/FM by several research groups [183, 188, 192, 193]. In a thiophene discharge subject to variation in the parameter W/FM, an increase in the number of monomer molecules becoming fragmented was found [193], which indicates the formation of more reaction products in the plasma i.e. N_2^-, CH, H and O. A decrease in dc conductivity was also found due to this increased monomer fragmentation induced by higher power density. Similar behaviors were observed by Denis *et al* who synthesized plasma polymer films from several amine precursors in continuous wave and pulsed wave modes under fixed flow rate, varying power conditions [188, 192]. These investigations suggest as the value of W/FM increases: a) a decrease of the primary monomer concentration in the resultant films and b) an increase of the degree of cross–linking. Additionally, it was shown that a critical power could be reached, beyond which the differences in monomer structure have less influence over plasma properties, due to their complete fragmentation. Below this threshold however, differences in the plasma chemistry were related to differences in the bonding energies of the monomers. Changing W/FM can therefore allow for selectivity in the degree to which the monomers are fragmented. These examples explicitly relate the composite parameter, plasma chemistry and film properties. Numerous other studies demonstrate that plasma polymerization covers a broad range of film properties, from swellable, hydrogel-like coatings that retain a significant proportion of monomer groups of the precursor (e.g. acrylic-like) towards more cross-linked, hard coatings (e.g. SiO_x) depending on energy input and fragmentation [169, 181, 191, 194-196].

Plasma polymerization is governed by the energy invested per particle of the gas mixture during the flow through the active plasma zone (according to the concept of chemical quasi-equilibrium) [177]. The governing reaction parameter is:

$$R = \frac{W\tau_{act}}{pV_{act}} \tag{II.10}$$

where W is the absorbed energy, τ_{act} is the residence time within the active (plasma) zone, p is the pressure, and V_{act} is the volume of the active (plasma) zone. With $\tau_{act} = pV_{act}/p_0F$ (p_0 =

pressure at standard conditions, F = gas flow), the reaction parameter R is proportional to the power input per flow W/F with respect to the active plasma zone. Following this approach, the growth rate of the thin films can be related to the controlling parameter W/F through the relation:

$$\frac{R_m}{F} = G\exp\left(\frac{-E_a}{W/F}\right) \tag{II.11}$$

where G is a reactor dependent geometry factor, R_m is the rate of film growth and E_a is the (apparent) activation energy corresponding to the monomer used [177]. Such a relationship is desirable as it relates the controlling parameters W and F to an immediately measurable internal parameter, the deposition rate, which can be monitored *in situ* and allow more direct process control without necessitating knowledge of less tangible parameters such as electron energy distribution functions, or precise gas phase chemical compositions. However, there are some shortcomings associated with this model; most notably that while geometry and pressure influence the behavior of the deposition, they are not explicitly embedded in Eq. II.11 [197-199]. This is addressed in part by the geometry factor, G and by modification of Eq. II.11 to include a similarity parameter, S. First, the real power delivered to the plasma zone contributing to film deposition should be regarded. S can therefore be scaled by the expansion of the active plasma zone d_{act} above the electrode area A_{dep} to the total discharge volume V_{dis}, whereby the residence time of the monomer in the active plasma zone is regarded:

$$S = \frac{W}{F'}\frac{A_{dep}d_{act}}{V_{dis}} \tag{II.12}$$

Second, the real flow F′ that contributes to film deposition should be scaled by the volume between gas inlet and electrode area $A_{dep}d_{gas}$ per total volume V_{gas} where the gas is flowing, which finally leads to

$$S = \frac{W}{F}\frac{d_{act}V_{gas}}{d_{gas}V_{dis}} \tag{II.13}$$

There are still some issues with the use of S, particularly for non-parallel plate reactors, or conditions where precise determination of the plasma volume is difficult [198].

Based on this approach and the determined activation energy parameter, different regions of growth kinetics can be identified within a system. In the monomer deficient (energy sufficient) region, the monomer flow rate is typically low and the power level is large, resulting in a high energy per molecule and complete dissociation of molecular bonds [169]. Increasing the RF power does not therefore increase the deposition rate, as maximum fragmentation has been reached. The deposition rate will rather decrease due to the increased effects of sputtering and ablation [191]. However, deposition rate can be increased by increasing the flow rate of the monomer (or alternatively the applied energy is decreased) i.e., entering the monomer sufficient (energy deficient) region. This insufficient energy cannot completely fragment the large number of monomer molecules present in the gas phase. Increasing the monomer flow rate therefore results in a decrease in deposition rate due to the decrease of the degree of monomer fragmentation. These different regions are often associated with different film properties [181, 191].

Generally it is found that the degree of monomer fragmentation and crosslinking directly influences film properties beyond simply the chemical properties and are also controlled by W/F parameter. Many studies examine the relationship between W/F and morphological, optical, surface and electrical properties of thin films. For fabrication of very hard a-C:H thin films, high composite parameter conditions are often cited as necessary [181, 200]. This establishes a relationship between W/F and film hardness, likely due to the underlying increase in relative carbon concentration, crosslinking and film density [201]. In many cases, surface roughness is found to decrease with increasing RF power [202, 203]. However, in cases of very high W/F values, roughness may increase, i.e., for plasma deposited cyanopyridine thin films, roughness increased from 0.43 nm to 3.63 nm, when the parameter *W* varied between 3 W and 60 W [169]. Increasing roughness also corresponds to significant changes in surface topography [191].

Optical properties of thin films change with variation in monomer retention and crosslinking. For example, changes in absorption and transmittance spectra due to differences in chemical functionality [184, 204] and increase in refractive index with W/F in plasma deposited thin films due to an increase in their density are often found [201]. In general, the optical properties of thin films deposited using PECVD are strongly dependent on the W/F parameter [205-207], through a combination of the dependence of the optical properties on film morphology, structure and chemical functionality, and the influence of W/F and monomer fragmentation over these properties.

Surface properties depend on the power density that is governed in part by changes in surface chemistry [208]. Thiophene and ethylcyclohexane deposition and a-C:H films, for example shows significant dependence of CA and hence surface energy on the deposition parameter [181, 208]. For linalyl acetate thin films [209], it was found that as the power density increased, the polar contribution to the total surface energy decreased while the dispersive component increased, though the total surface free energy remained relatively constant. The decrease in the polar component of surface energy was again attributed to the reduction in the more polar oxygen functionalities at the surface observed in XPS measurements. No significant trend was observed in the solubility of the material in various solvents as a function of RF power; films deposited at all power densities were shown to be insoluble in all liquids investigated [209]. This was attributed to the increase in crosslinking of the plasma deposited layers, which typically results in films that are insoluble or less soluble in many common solvents [183, 210]. However, it is possible to decrease the degree of fragmentation and crosslinking sufficiently to result in films, which are soluble, generally through use of very low W/F conditions or pulsed plasma systems [175, 198, 211].

The W/F parameter has also been found to influence the electrical properties of thin films, i.e., modify the conductivity, breakdown capacity and permittivity of thin films [173, 184, 193, 204, 208, 212]. For linalyl acetate thin films [173, 213, 214], the dc conductivity was found to decrease was power density increased and similar trend was observed with permittivity. The reduction in permittivity at higher RF energies is attributed to the reduction in more polar oxygen functionalities, while the decrease in conductivity is attributed to the increase in crosslinking in samples fabricated in higher energy conditions. Thiophene films [193] shows similar trend as conductivity decreases significantly (two orders of magnitude) as power density increases. Electrical properties of thin films are therefore implicitly linked to W/F parameter.

II.3 CONCLUSION

OPV was overviewed with a specific focus on the lifetime and reliability of the devices. It was found that thin film encapsulation is a critical technology required for the application and commercialization of OPVs. Effective encapsulation to prevent the permeation of water vapor and oxygen, which degrades OPV devices, is key for achieving the reliability and desired lifetimes. The materials that are currently applied for this purpose cannot satisfy the encapsulation requirements discussed in this chapter. Hence, new materials are needed which will satisfy the encapsulation requirements and achieve the reliability and lifetime required.

Plasma deposited thin films were found to possess a wide variety of tunable optical, chemical, topographical and electrical properties. These properties were found to be dependent on various deposition parameters (i.e., the deposition chamber in use, the monomer, system pressure, monomer flow rate, deposition power etc.). The fragmentation of the monomer induced during the reaction was shown to be the factor of primary importance in controlling the resulting thin film properties, and the degree of fragmentation related to the controlling parameter W/FM.

REFERENCES

[1] N. Grossiord, J. M. Kroon, R. Andriessen, and P. W. M. Blom, "Degradation mechanisms in organic photovoltaic devices," *Organic Electronics,* vol. 13, pp. 432-456, 2012.

[2] B. Christoph J, "Organic photovoltaics: technology and market," *Solar Energy Materials and Solar Cells,* vol. 83, pp. 273-292, 2004.

[3] H. Spanggaard and F. C. Krebs, "A brief history of the development of organic and polymeric photovoltaics," *Solar Energy Materials and Solar Cells,* vol. 83, pp. 125-146, 2004.

[4] N. S. Sariciftci, L. Smilowitz, A. J. Heeger, and F. Wudl, "Photoinduced Electron Transfer from a Conducting Polymer to Buckminsterfullerene," *Science,* vol. 258, pp. 1474-1476, November 27, 1992 1992.

[5] H. GmbH. (Dec 22). *Heliatek consolidates its technology leadership by establishing a new world record for organic solar technology with a cell efficiency of 12%.*

[6] J. Schmidtke, "Commercial status of thin-film photovoltaic devices and materials," *Opt. Express,* vol. 18, pp. A477-A486, 2010.

[7] G. Conibeer, "Third-generation photovoltaics," *Materials Today,* vol. 10, pp. 42-50, 2007.

[8] C. H. Peters, I. T. Sachs-Quintana, J. P. Kastrop, S. Beaupré, M. Leclerc, and M. D. McGehee, "High Efficiency Polymer Solar Cells with Long Operating Lifetimes," *Advanced Energy Materials,* vol. 1, pp. 491-494, 2011.

[9] C.-S. Ho, C.-S. Lee, W.-C. Hsu, C.-Y. Lin, Y.-N. Lai, and C.-W. Wang, "Efficiency improvements in single-heterojunction organic photovoltaic cells by insertion of wide-bandgap electron-blocking layers," *Solid-State Electronics,* vol. 76, pp. 101-103, 2012.

[10] S. E. Shaheen, C. J. Brabec, N. S. Sariciftci, F. Padinger, T. Fromherz, and J. C. Hummelen, "2.5% efficient organic plastic solar cells," *Applied Physics Letters,* vol. 78, p. 3, 2001.

[11] P. Schilinsky, C. Waldauf, and C. J. Brabec, "Recombination and loss analysis in polythiophene based bulk heterojunction photodetectors," *Applied Physics Letters,* vol. 81, pp. 3885-3887, Nov 2002.

[12] M. Jørgensen, K. Norrman, and F. C. Krebs, "Stability/degradation of polymer solar cells," *Solar Energy Materials and Solar Cells,* vol. 92, pp. 686-714, 2008.

[13] T. Jeranko, H. Tributsch, N. S. Sariciftci, and J. C. Hummelen, "Patterns of efficiency and degradation of composite polymer solar cells," *Solar Energy Materials and Solar Cells,* vol. 83, pp. 247-262, 2004.

[14] K. Bazaka and M. V. Jacob, "Post-deposition ageing reactions of plasma derived

polyterpenol thin films," *Polymer Degradation and Stability,* vol. 95, pp. 1123-1128, 2010.

[15] H. Neugebauer, C. J. Brabec, J. C. Hummelen, R. A. J. Janssen, and N. S. Sariciftci, "Stability studies and degradation analysis of plastic solar cell materials by FTIR spectroscopy," *Synthetic Metals,* vol. 102, pp. 1002-1003, 1999.

[16] N. Chawdhury, A. Köhler, M. G. Harrison, D. H. Hwang, A. B. Holmes, and R. H. Friend, "The effects of H_2O and O_2 on the photocurrent spectra of MEH-PPV," *Synthetic Metals,* vol. 102, pp. 871-872, 1999.

[17] B. M. Henry, F. Dinelli, K. Y. Zhao, C. R. M. Grovenor, O. V. Kolosov, G. A. D. Briggs, A. P. Roberts, R. S. Kumar, and R. P. Howson, "A microstructural study of transparent metal oxide gas barrier films," *Thin Solid Films,* vol. 355–356, pp. 500-505, 1999.

[18] A. G. Erlat, B. M. Henry, J. J. Ingram, D. B. Mountain, A. McGuigan, R. P. Howson, C. R. M. Grovenor, G. A. D. Briggs, and Y. Tsukahara, "Characterisation of aluminium oxynitride gas barrier films," *Thin Solid Films,* vol. 388, pp. 78-86, 2001.

[19] M. Yanaka, B. M. Henry, A. P. Roberts, C. R. M. Grovenor, G. A. D. Briggs, A. P. Sutton, T. Miyamoto, Y. Tsukahara, N. Takeda, and R. J. Chater, "How cracks in SiO_x-coated polyester films affect gas permeation," *Thin Solid Films,* vol. 397, pp. 176-185, 2001.

[20] A. P. Roberts, B. M. Henry, A. P. Sutton, C. R. M. Grovenor, G. A. D. Briggs, T. Miyamoto, M. Kano, Y. Tsukahara, and M. Yanaka, "Gas permeation in silicon-oxide/polymer (SiO_x/PET) barrier films: role of the oxide lattice, nano-defects and macro-defects," *Journal of Membrane Science,* vol. 208, pp. 75-88, 2002.

[21] A. G. Erlat, B. M. Henry, C. R. M. Grovenor, A. G. D. Briggs, R. J. Chater, and Y. Tsukahara, "Mechanism of Water Vapor Transport through PET/AlO_xN_y Gas Barrier Films," *The Journal of Physical Chemistry B,* vol. 108, pp. 883-890, 2004/01/01 2003.

[22] K. Norrman and F. C. Krebs, "Photodegradation of poly(ether sulphone) Part 2. Wavelength and atmosphere dependence," *Surface and Interface Analysis,* vol. 36, pp. 1542-1549, 2004.

[23] K. Norrman, N. B. Larsen, and F. C. Krebs, "Lifetimes of organic photovoltaics: Combining chemical and physical characterisation techniques to study degradation mechanisms," *Solar Energy Materials and Solar Cells,* vol. 90, pp. 2793-2814, 2006.

[24] M. Lira-Cantu, K. Norrman, J. W. Andreasen, and F. C. Krebs, "Oxygen Release and Exchange in Niobium Oxide MEHPPV Hybrid Solar Cells," *Chemistry of Materials,* vol. 18, pp. 5684-5690, 2006/11/01 2006.

[25] M. O. Reese, M. S. White, G. Rumbles, D. S. Ginley, and S. E. Shaheen, "Optimal negative electrodes for poly(3-hexylthiophene): 6,6 -phenyl C61-butyric acid methyl ester bulk heterojunction photovoltaic devices," *Applied Physics Letters,* vol. 92, Feb 2008.

[26] M. T. Lloyd, D. C. Olson, P. Lu, E. Fang, D. L. Moore, M. S. White, M. O. Reese, D. S. Ginley, and J. W. P. Hsu, "Impact of contact evolution on the shelf life of organic solar

cells," *Journal of Materials Chemistry,* vol. 19, pp. 7638-7642, 2009.

[27] B. Paci, A. Generosi, V. R. Albertini, P. Perfetti, R. de Bettignies, J. Leroy, M. Firon, and C. Sentein, "Controlling photoinduced degradation in plastic photovoltaic cells: A time-resolved energy dispersive x-ray reflectometry study," *Applied Physics Letters,* vol. 89, pp. 043507-3, 2006.

[28] B. Paci, A. Generosi, V. R. Albertini, P. Perfetti, R. de Bettignies, M. Firon, J. Leroy, and C. Sentein, "In situ energy dispersive x-ray reflectometry measurements on organic solar cells upon working," *Applied Physics Letters,* vol. 87, pp. 194110-3, 2005.

[29] M. O. Reese, A. J. Morfa, M. S. White, N. Kopidakis, S. E. Shaheen, G. Rumbles, and D. S. Ginley, "Pathways for the degradation of organic photovoltaic P3HT:PCBM based devices," *Solar Energy Materials and Solar Cells,* vol. 92, pp. 746-752, 2008.

[30] F. C. Krebs, J. E. Carlé, N. Cruys-Bagger, M. Andersen, M. R. Lilliedal, M. A. Hammond, and S. Hvidt, "Lifetimes of organic photovoltaics: photochemistry, atmosphere effects and barrier layers in ITO-MEHPPV:PCBM-aluminium devices," *Solar Energy Materials and Solar Cells,* vol. 86, pp. 499-516, 2005.

[31] E. Cuddihy, C. Coulbert, A. Gupta, and R. Liang, "Electricity from photovoltaic solar cells: Flat-Plate Solar Array Project final report. Volume VII: Module encapsulation," Jet Propulsion Laboratory1986.

[32] Cunha LG, Alonso RC, Santos PH, and S. MA., "Comparative study of the surface roughness of Ormocer-based and conventional composites.," *J Appl Oral Sci,* vol. 11, pp. 348-53, 2003.

[33] T.-N. Chen, D.-S. Wuu, C.-Y. Lin, C.-C. Wu, and R.-H. Horng, "Thermal effects and plasma damage upon encapsulation of polymer solar cells," *Thin Solid Films,* vol. 517, pp. 4179-4183, 2009.

[34] F. Ramsteiner, T. Jaworek, M. Weber, and S. Forster, "Scratch resistance and embrittlement of coated polymers," *Polymer Testing,* vol. 22, pp. 439-451, 2003.

[35] B. Fayolle, E. Richaud, X. Colin, and J. Verdu, "Review: degradation-induced embrittlement in semi-crystalline polymers having their amorphous phase in rubbery state," *Journal of Materials Science,* vol. 43, pp. 6999-7012, 2008/11/01 2008.

[36] L. Roliand and L. J. Broutman, "Surface embrittlement of ductile polymers: A fracture mechanics analysis," *Polymer Engineering & Science,* vol. 25, pp. 207-211, 1985.

[37] Z. Xiong, T. M. Walsh, and A. G. Aberle, "PV module durability testing under high voltage biased damp heat conditions," *Energy Procedia,* vol. 8, pp. 384-389, 2011.

[38] A. Tapponnier, I. Biaggio, and P. Gunter, "Ultrapure C_{60} field-effect transistors and the effects of oxygen exposure," *Applied Physics Letters,* vol. 86, pp. 112114-3, 2005.

[39] P. E. Burrows, V. Bulovic, S. R. Forrest, L. S. Sapochak, D. M. McCarty, and M. E. Thompson, "Reliability and degradation of organic light emitting devices," *Applied Physics*

Letters, vol. 65, pp. 2922-2924, 1994.

[40] S. Sarkar, J. H. Culp, J. T. Whyland, M. Garvan, and V. Misra, "Encapsulation of organic solar cells with ultrathin barrier layers deposited by ozone-based atomic layer deposition," *Organic Electronics,* vol. 11, pp. 1896-1900, 2010.

[41] N. Kim, W. J. Potscavage Jr, A. Sundaramoothi, C. Henderson, B. Kippelen, and S. Graham, "A correlation study between barrier film performance and shelf lifetime of encapsulated organic solar cells," *Solar Energy Materials and Solar Cells,* vol. 101, pp. 140-146, 2012.

[42] S. Cros, R. de Bettignies, S. Berson, S. Bailly, P. Maisse, N. Lemaitre, and S. Guillerez, "Definition of encapsulation barrier requirements: A method applied to organic solar cells," *Solar Energy Materials and Solar Cells,* vol. 95, pp. S65-S69, 2011.

[43] Q. Mao, C. J. Fell, and A. D. Scully, "Self-assembled nano-phase particles for enhanced oxygen barrier coatings on polymeric materials," *Progress in Organic Coatings,* vol. 76, pp. 51-59, 2013.

[44] J. Ahmad, K. Bazaka, L. J. Anderson, R. D. White, and M. V. Jacob, "Materials and methods for encapsulation of OPV: A review," *Renewable and Sustainable Energy Reviews,* vol. 27, pp. 104-117, 2013.

[45] M. Hanika, H. C. Langowski, U. Moosheimer, and W. Peukert, "Inorganic Layers on Polymeric Films – Influence of Defects and Morphology on Barrier Properties," *Chemical Engineering & Technology,* vol. 26, pp. 605-614, 2003.

[46] G. L. Graff, R. E. Williford, and P. E. Burrows, "Mechanisms of vapor permeation through multilayer barrier films: Lag time versus equilibrium permeation," *Journal of Applied Physics,* vol. 96, pp. 1840-1849, 2004.

[47] Y. G. Tropsha and N. G. Harvey, "Activated Rate Theory Treatment of Oxygen and Water Transport through Silicon Oxide/Poly(ethylene terephthalate) Composite Barrier Structures," *The Journal of Physical Chemistry B,* vol. 101, pp. 2259-2266, 1997/03/01 1997.

[48] A. G. Erlat, R. J. Spontak, R. P. Clarke, T. C. Robinson, P. D. Haaland, Y. Tropsha, N. G. Harvey, and E. A. Vogler, "SiO_x Gas Barrier Coatings on Polymer Substrates: Morphology and Gas Transport Considerations," *The Journal of Physical Chemistry B,* vol. 103, pp. 6047-6055, 1999/07/01 1999.

[49] R. H. Doremus, *Glass science*: Wiley, 1973.

[50] A. S. d. S. Sobrinho, M. Latreche, G. Czeremuszkin, J. E. Klemberg-Sapieha, and M. R. Wertheimer, "Transparent barrier coatings on polyethylene terephthalate by single- and dual-frequency plasma-enhanced chemical vapor deposition," *Journal of Vacuum Science & Technology A: Vacuum, Surfaces, and Films,* vol. 16, pp. 3190-3198, 1998.

[51] A. S. da Silva Sobrinho, G. Czeremuszkin, M. Latrèche, G. Dennler, and M. R. Wertheimer, "A study of defects in ultra-thin transparent coatings on polymers," *Surface and*

Coatings Technology, vol. 116–119, pp. 1204-1210, 1999.

[52] A. S. da Silva Sobrinho, G. Czeremuszkin, M. Latrèche, and M. R. Wertheimer, "Defect-permeation correlation for ultrathin transparent barrier coatings on polymers," *Journal of Vacuum Science & Technology A,* vol. 18, pp. 149-157, 2000.

[53] E. H. H. Jamieson and A. H. Windle, "Structure and oxygen-barrier properties of metallized polymer film," *Journal of Materials Science,* vol. 18, pp. 64-80, 1983/01/01 1983.

[54] W. G. Perkins and D. R. Begeal, "Diffusion and Permeation of He, Ne, Ar, Kr, and D2 through Silicon Oxide Thin Films," *The Journal of Chemical Physics,* vol. 54, pp. 1683-1694, 1971.

[55] P. F. Carcia, R. S. McLean, M. H. Reilly, M. D. Groner, and S. M. George, "Ca test of Al_2O_3 gas diffusion barriers grown by atomic layer deposition on polymers," *Applied Physics Letters,* vol. 89, pp. 031915-3, 2006.

[56] J. Meyer, P. Görrn, F. Bertram, S. Hamwi, T. Winkler, H.-H. Johannes, T. Weimann, P. Hinze, T. Riedl, and W. Kowalsky, " Al_2O_3/ZrO_2 Nanolaminates as Ultrahigh Gas-Diffusion Barriers – A Strategy for Reliable Encapsulation of Organic Electronics," *Advanced Materials,* vol. 21, pp. 1845-1849, 2009.

[57] J. Crank, *The mathematics of diffusion / by J. Crank*. Oxford [England]: Clarendon Press, 1975.

[58] S. K. Park, J. Oh, C. S. Hwang, J. Lee, Y. S. Yang, H. Y. Chu, and K. Y. Kang, "Ultra Thin Film Encapsulation of OLED on Plastic Substrate," *ETRI Journal,* vol. 27, pp. 545-550, 2005.

[59] B. Ketola, K. R. McIntosh, A. Norris, and M. K. Tomalia, "Silicones for Photovoltaic Encapsulation," in *23rd European Photovoltaic Solar Energy Conference*, 2008, pp. 2969 - 2973.

[60] B. Ketola, C. Shirk, P. Griffith, and G. Bunea, "Demonstration of the Benefits of Silicone Encapsulation of PV Modules in a Large Scale Outdoor Array," presented at the 5th World Conference on Photovoltaic Energy Conversion, Valencia, Spain, 2010.

[61] V. V. Iyengar, B. K. Nayak, and M. C. Gupta, "Optical properties of silicon light trapping structures for photovoltaics," *Solar Energy Materials and Solar Cells,* vol. 94, pp. 2251-2257, 2010.

[62] K. R. McIntosh, N. E. Powell, A. W. Norris, J. N. Cotsell, and B. M. Ketola, "The effect of damp-heat and UV aging tests on the optical properties of silicone and EVA encapsulants," *Progress in Photovoltaics: Research and Applications,* vol. 19, pp. 294-300, 2011.

[63] C. Deibel, V. Dyakonov, J. Parisi, J. Palm, S. Zweigart, and F. Karg, "Influence of damp heat testing on the electrical characteristics of $Cu(In,Ga)(S,Se)_2$ solar cells," *Thin Solid Films,* vol. 403–404, pp. 325-330, 2002.

[64] B. Selin Tosun, R. K. Feist, A. Gunawan, K. Andre Mkhoyan, S. A. Campbell, and E. S. Aydil, "Improving the damp-heat stability of copper indium gallium diselenide solar cells with a semicrystalline tin dioxide overlayer," *Solar Energy Materials and Solar Cells,* vol. 101, pp. 270-276, 2012.

[65] M. Lipiñski*, "Silicon nitride for photovoltaic application," *Archives of Materials Science and Engineering,* vol. 46, pp. 69-87, 01.12.2010 2010.

[66] A. Masuda, H. Umemoto, and H. Matsumura, "Various applications of silicon nitride by catalytic chemical vapor deposition for coating, passivation and insulating films," *Thin Solid Films,* vol. 501, pp. 149-153, 2006.

[67] M. Takano, T. Niki, A. Heya, T. Osono, Y. Yonezawa, T. Minamikawa, S. Muroi, S. Minami, A. Masuda, H. Umemoto, and H. Matsumura, "Preparation of Low-Stress SiNx Films by Catalytic Chemical Vapor Deposition at Low Temperatures," *Japanese Journal of Applied Physics,* vol. 44, pp. 4098-4102, 2005.

[68] X.-Y. Zhao, M.-Z. Wang, B.-Z. Zhang, and L. Mao, "Synthesis, characterization and nonlinear optical properties of plasma-prepared poly(4-biphenylcarbonitrile) thin films," *Polymer International,* vol. 56, pp. 630-634, 2007.

[69] G. P. Lopez and B. D. Ratner, "Substrate temperature effects on film chemistry in plasma deposition of organics. I. Nonpolymerizable precursors," *Langmuir,* vol. 7, pp. 766-773, 1991/04/01 1991.

[70] H. Yasuda, "New insights into aging phenomena from plasma chemistry," *Nuclear Instruments and Methods in Physics Research Section A: Accelerators, Spectrometers, Detectors and Associated Equipment,* vol. 515, pp. 15-30, 2003.

[71] T. B. Casserly and K. K. Gleason, "Effect of Substrate Temperature on the Plasma Polymerization of Poly(methyl methacrylate)," *Chemical Vapor Deposition,* vol. 12, pp. 59-66, 2006.

[72] S.-H. K. Park, J. Oh, C.-S. Hwang, J.-I. Lee, Y. S. Yang, and H. Y. Chu "Ultrathin Film Encapsulation of an OLED by ALD," *Electrochemical and Solid-State Letters,* vol. 8, pp. H21-H23, January 1, 2005 2005.

[73] C.-Y. Chang, C.-T. Chou, Y.-J. Lee, M.-J. Chen, and F.-Y. Tsai, "Thin-film encapsulation of polymer-based bulk-heterojunction photovoltaic cells by atomic layer deposition," *Organic Electronics,* vol. 10, pp. 1300-1306, 2009.

[74] S. K. Kim, S. W. Lee, C. S. Hwang, Y.-S. Min, J. Y. Won, and J. Jeong, "Low Temperature (< 100 ° C) Deposition of Aluminum Oxide Thin Films by ALD with O_3 as Oxidant," *Journal of The Electrochemical Society,* vol. 153, pp. F69-F76, January 1, 2006 2006.

[75] M. Rose, J. Niinistö, I. Endler, J. W. Bartha, P. Kücher, and M. Ritala, "In Situ Reaction Mechanism Studies on Ozone-Based Atomic Layer Deposition of Al_2O_3 and HfO_2," *ACS Applied Materials & Interfaces,* vol. 2, pp. 347-350, 2010/02/24 2010.

[76] A. A. Dameron, S. D. Davidson, B. B. Burton, P. F. Carcia, R. S. McLean, and S. M. George, "Gas Diffusion Barriers on Polymers Using Multilayers Fabricated by Al_2O_3 and Rapid SiO_2 Atomic Layer Deposition," *The Journal of Physical Chemistry C,* vol. 112, pp. 4573-4580, 2008/03/01 2008.

[77] J. B. Kim, D. R. Kwon, K. Chakrabarti, C. Lee, K. Y. Oh, and J. H. Lee, "Improvement in Al_2O_3 dielectric behavior by using ozone as an oxidant for the atomic layer deposition technique," *Journal of Applied Physics,* vol. 92, pp. 6739-6742, 2002.

[78] W. J. Potscavage, S. Yoo, B. Domercq, and B. Kippelenb, "Encapsulation of pentacene/C_{60} organic solar cells with Al2O3 deposited by atomic layer deposition," *APPLIED PHYSICS LETTERS,* vol. 90, 2007.

[79] S. Yoo, W. J. Potscavage Jr, B. Domercq, S.-H. Han, T.-D. Li, S. C. Jones, R. Szoszkiewicz, D. Levi, E. Riedo, S. R. Marder, and B. Kippelen, "Analysis of improved photovoltaic properties of pentacene/C_{60} organic solar cells: Effects of exciton blocking layer thickness and thermal annealing," *Solid-State Electronics,* vol. 51, pp. 1367-1375, 2007.

[80] J. Schlothauer, S. Jungwirth, M. Köhl, and B. Röder, "Degradation of the encapsulant polymer in outdoor weathered photovoltaic modules: Spatially resolved inspection of EVA ageing by fluorescence and correlation to electroluminescence," *Solar Energy Materials and Solar Cells,* vol. 102, pp. 75-85, 2012.

[81] J. Jin, S. Chen, and J. Zhang, "Investigation of UV aging influences on the crystallization of ethylene-vinyl acetate copolymer via successive self-nucleation and annealing treatment," *Journal of Polymer Research,* vol. 17, pp. 827-836, 2010.

[82] E. E. van Dyk, A. Audouard, E. L. Meyer, and C. D. Woolard, "Investigation of the degradation of a thin-film hydrogenated amorphous silicon photovoltaic module," *Solar Energy Materials and Solar Cells,* vol. 91, pp. 167-173, 2007.

[83] A. Le Donne, M. Dilda, M. Crippa, M. Acciarri, and S. Binetti, "Rare earth organic complexes as down-shifters to improve Si-based solar cell efficiency," *Optical Materials,* vol. 33, pp. 1012-1014, 2011.

[84] R. A. Hayes, G. M. Lenges, and S. C. Pesek, "Low modulus solar cell encapsulant sheets with enhanced stability and adhesion," May 1, 2012, 2012.

[85] J. Yin, H. Zhu, Y. Wang, Z. Wang, J. Gao, Y. Mai, Y. Ma, M. Wan, and Y. Huang, "A study of ZnO:B films for thin film silicon solar cells," *Applied Surface Science,* vol. 259, pp. 758-763, 2012.

[86] K. E. GmbH, "Photovoltaic Module Encapsulation- Advanced solar solutions with PVB film," vol. 09/2010, ed, 2010.

[87] A. Bonucci, S. Rondena, A. Gallitognotta, P. Gallina, O. Salomon, W. Wischmann, and S. Hiss, "Thin-film CIGS PV modules with more than 3000h damp heat stability: Breakthrough time property of the B-Dry® edge sealant and its characterization," *Solar Energy Materials and*

Solar Cells, vol. 98, pp. 398-403, 2012.

[88] C. Bayer Material Science AG. (2010). *Encapsulation of solar cells by hot-melt adhesive films made of thermoplastic polyurethane*.

[89] J. H. Schut. (2009) Shining opportunities in solar films. *Plastics Technology*.

[90] G. Rowell, "Identification and Suppression of Instabilities in Cytop$^{\text{TM}}$ films for Encapsulation of Organic Photovoltaic Devices," Bachelor of Science Dissertation, Physics, University of California, 2009.

[91] J. Granstrom, J. S. Swensen, J. S. Moon, G. Rowell, J. Yuen, and A. J. Heeger, "Encapsulation of organic light-emitting devices using a perfluorinated polymer," *Applied Physics Letters,* vol. 93, pp. 193304-3, 2008.

[92] L. M. Cavalcante, L. F. J. Schneider, M. Hammad, D. C. Watts, and N. Silikas, "Degradation resistance of ormocer and dimethacrylate-based matrices with different filler contents," *Journal of Dentistry,* vol. 40, pp. 86-90, 2012.

[93] H. Wolter, W. Storch, and H. Ott, "New Inorganic/Organic Copolymers (Ormocer®s) for Dental Applications," *MRS Online Proceedings Library,* vol. 346, 1994.

[94] L. M. Cavalcante, L. F. J. Schneider, N. Silikas, and D. C. Watts, "Surface integrity of solvent-challenged ormocer-matrix composite," *Dental Materials,* vol. 27, pp. 173-179, 2011.

[95] F. ISC. (2008, 28.08.2008). *Flexible polymer barrier films for the encapsulation of solar cells*.

[96] Q. F. Xu, J. N. Wang, and K. D. Sanderson, "Organic–Inorganic Composite Nanocoatings with Superhydrophobicity, Good Transparency, and Thermal Stability," *ACS Nano,* vol. 4, pp. 2201-2209, 2010.

[97] X.-M. Li, D. Reinhoudt, and M. Crego-Calama, "What do we need for a superhydrophobic surface? A review on the recent progress in the preparation of superhydrophobic surfaces," *Chemical Society Reviews,* vol. 36, pp. 1350-1368, 2007.

[98] P. Gould, "Smart, clean surfaces," *Materials Today,* vol. 6, pp. 44-48, 2003.

[99] P. M. Barkhudarov, P. B. Shah, E. B. Watkins, D. A. Doshi, C. J. Brinker, and J. Majewski, "Corrosion inhibition using superhydrophobic films," *Corrosion Science,* vol. 50, pp. 897-902, 2008.

[100] M. Hikita, K. Tanaka, T. Nakamura, T. Kajiyama, and A. Takahara, "Super-Liquid-Repellent Surfaces Prepared by Colloidal Silica Nanoparticles Covered with Fluoroalkyl Groups," *Langmuir,* vol. 21, pp. 7299-7302, 2005/08/01 2005.

[101] H. M. Shang, Y. Wang, K. Takahashi, and G. Z. Cao, "Nanostructured superhydrophobic surfaces," *Journal of Material Science,* vol. 40, pp. 3587-3591, 2005.

[102] S. S. Latthe, H. Imai, V. Ganesan, and A. Venkateswara Rao, "Porous superhydrophobic silica films by sol–gel process," *Microporous and Mesoporous Materials,* vol. 130, pp. 115-121, 2010.

[103] R. Chen, X. Zhang, Z. Su, R. Gong, X. Ge, H. Zhang, and C. Wang, "Perfectly Hydrophobic Silicone Nanofiber Coatings: Preparation from Methyltrialkoxysilanes and Use as Water-Collecting Substrate," *The Journal of Physical Chemistry C,* vol. 113, pp. 8350-8356, 2009/05/14 2009.

[104] X. Liu and J. He, "One-Step Hydrothermal Creation of Hierarchical Microstructures toward Superhydrophilic and Superhydrophobic Surfaces," *Langmuir,* vol. 25, pp. 11822-11826, 2009/10/06 2009.

[105] B. Balu, V. Breedveld, and D. W. Hess, "Fabrication of “Roll-off” and “Sticky” Superhydrophobic Cellulose Surfaces via Plasma Processing," *Langmuir,* vol. 24, pp. 4785-4790, 2008/05/01 2008.

[106] H. Budunoglu, A. Yildirim, M. O. Guler, and M. Bayindir, "Highly Transparent, Flexible, and Thermally Stable Superhydrophobic ORMOSIL Aerogel Thin Films," *ACS Applied Materials & Interfaces,* vol. 3, pp. 539-545, 2011.

[107] T. T. Isimjan, T. Wang, and S. Rohani, "A novel method to prepare superhydrophobic, UV resistance and anti-corrosion steel surface," *Chemical Engineering Journal,* vol. 210, pp. 182-187, 2012.

[108] Y. Fan, C. Li, Z. Chen, and H. Chen, "Study on fabrication of the superhydrophobic sol–gel films based on copper wafer and its anti-corrosive properties," *Applied Surface Science,* vol. 258, pp. 6531-6536, 2012.

[109] L. D. Zhang, W. L. Liu, W. H. Xu, J. S. Yao, L. Zhao, X. Q. Wang, and Y. Z. Wu, "Synthesis and characterization of superhydrophobic and superparamagnetic film based on maghemite–polystyrene composite nanoparticles," *Applied Surface Science,* vol. 259, pp. 719-725, 2012.

[110] M. Pagliaro, R. Ciriminna, and G. Palmisano, "Silica-based hybrid coatings," *Journal of Materials Chemistry,* vol. 19, pp. 3116-3126, 2009.

[111] H. Yabu and M. Shimomura, "Single-Step Fabrication of Transparent Superhydrophobic Porous Polymer Films," *Chemistry of Materials,* vol. 17, pp. 5231-5234, 2005/10/01 2005.

[112] Y. Fu and F.-Y. Tsai, "Air-stable polymer organic thin-film transistors by solution-processed encapsulation," *Organic Electronics,* vol. 12, pp. 179-184, 2011.

[113] S. Ferrari, F. Perissinotti, E. Peron, L. Fumagalli, D. Natali, and M. Sampietro, "Atomic layer deposited Al_2O_3 as a capping layer for polymer based transistors," *Organic Electronics,* vol. 8, pp. 407-414, 2007.

[114] Y. Fu, C. Lin, and F.-Y. Tsai, "High field-effect mobility from poly(3-hexylthiophene) thin-film transistors by solvent–vapor-induced reflow," *Organic Electronics,* vol. 10, pp. 883-888, 2009.

[115] S. P. Tiwari, P. Srinivas, S. Shriram, N. S. Kale, S. G. Mhaisalkar, and V. Ramgopal

Rao, "Organic FETs with HWCVD silicon nitride as a passivation layer and gate dielectric," *Thin Solid Films,* vol. 516, pp. 770-772, 2008.

[116] K. S. Ong, G. C. R. Raymond, E. Ou, Z. Zheng, and D. L. M. Ying, "Interfacial and mechanical studies of a composite Ag–IZO–PEN barrier film for effective encapsulation of organic TFT," *Organic Electronics,* vol. 11, pp. 463-466, 2010.

[117] N. S. Allen, M. Edge, M. Mohammadian, and K. Jones, "Physicochemical aspects of the environmental degradation of poly(ethylene terephthalate)," *Polymer Degradation and Stability,* vol. 43, pp. 229-237, 1994.

[118] M. Çopuroğlu and M. Şen, "A comparative study of UV aging characteristics of poly(ethylene-co-vinyl acetate) and poly(ethylene-co-vinyl acetate)/carbon black mixture," *Polymers for Advanced Technologies,* vol. 16, pp. 61-66, 2005.

[119] M. Çopuroğlu and M. Şen, "A comparative study of thermal ageing characteristics of poly(ethylene-co-vinyl acetate) and poly(ethylene-co-vinyl acetate)/carbon black mixture," *Polymers for Advanced Technologies,* vol. 15, pp. 393-399, 2004.

[120] W. Ma, C. Yang, X. Gong, K. Lee, and A. J. Heeger, "Thermally Stable, Efficient Polymer Solar Cells with Nanoscale Control of the Interpenetrating Network Morphology," *Advanced Functional Materials,* vol. 15, pp. 1617-1622, 2005.

[121] H.-K. Kim, D. G. Kim, K. S. Lee, M. S. Huh, S. H. Jeong, K. I. Kim, and T.-Y. Seong, "Plasma damage-free sputtering of indium tin oxide cathode layers for top-emitting organic light-emitting diodes," *Applied Physics Letters,* vol. 86, pp. 183503-3, 2005.

[122] N. Kim, "Fabrication and characterization of thin-film encapsulation for organic electronics," PhD Dissertation, Mechanical Engineering, Georgia Institute of Technology, Georgia, 2009.

[123] C. C. Chiang, D. S. Wuu, H. B. Lin, Y. P. Chen, T. N. Chen, Y. C. Lin, C. C. Wu, W. C. Chen, T. H. Jaw, and R. H. Horng, "Deposition and permeation properties of SiN_X/parylene multilayers on polymeric substrates," *Surface and Coatings Technology,* vol. 200, pp. 5843-5848, 2006.

[124] T.-N. Chen, D.-S. Wuu, C.-C. Wu, C.-C. Chiang, Y.-P. Chen, and R.-H. Horng, "Improvements of Permeation Barrier Coatings Using Encapsulated Parylene Interlayers for Flexible Electronic Applications," *Plasma Processes and Polymers,* vol. 4, pp. 180-185, 2007.

[125] S.-W. Seo, E. Jung, H. Chae, and S. M. Cho, "Optimization of Al2O3 Al_2O_3/ZrO_2 nanolaminate structure for thin-film encapsulation of OLEDs," *Organic Electronics,* vol. 13, pp. 2436-2441, 2012.

[126] D.-w. Choi, S.-J. Kim, J. H. Lee, K.-B. Chung, and J.-S. Park, "A study of thin film encapsulation on polymer substrate using low temperature hybrid ZnO/Al_2O_3 layers atomic layer deposition," *Current Applied Physics,* vol. 12, Supplement 2, pp. S19-S23, 2012.

[127] T. N. Chen, D. S. Wuu, C. C. Wu, C. C. Chiang, Y. P. Chen, and R. H. Horng, "High-

Performance Transparent Barrier Films of SiO_x /SiN_x Stacks on Flexible Polymer Substrates," *Journal of The Electrochemical Society,* vol. 153, pp. F244-F248, January 1, 2006 2006.

[128] J. D. Affinito, M. E. Gross, C. A. Coronado, G. L. Graff, I. N. Greenwell, and P. M. Martin, "A new method for fabricating transparent barrier layers," *Thin Solid Films,* vol. 290–291, pp. 63-67, 1996.

[129] J. G. Wijmans and R. W. Baker, "The solution-diffusion model: a review," *Journal of Membrane Science,* vol. 107, pp. 1-21, 1995.

[130] M. S. Hedenqvist and U. W. Gedde, "Prediction of permeability of laminate films; new methods for ultra-thin layers and systems with solute-concentration-dependent diffusivity," *Packaging Technology and Science,* vol. 12, pp. 131-141, 1999.

[131] J. Granstrom, M. Villet, T. Chatterjee, J. A. Gerbec, E. Jerkunica, and A. Roy, "Multilayer barrier films comprising nitrogen spacers between free-standing barrier layers," *Applied Physics Letters,* vol. 95, pp. 093306-3, 2009.

[132] J. Granstrom, M. Gällstedt, M. Villet, J. S. Moon, and T. Chatterjee, "High performance encapsulation structures utilizing Russian Doll architectures," *Thin Solid Films,* vol. 518, pp. 5282-5287, 2010.

[133] H. Heuer, C. Wenzel, D. Herrmann, R. Hübner, Z. L. Zhang, and J. W. Bartha, "Thin tantalum-silicon-oxygen/tantalum-silicon-nitrogen films as high-efficiency humidity diffusion barriers for solar cell encapsulation," *Thin Solid Films,* vol. 515, pp. 1612-1617, 2006.

[134] J. Meyer, H. Schmidt, W. Kowalsky, T. Riedl, and A. Kahn, "The origin of low water vapor transmission rates through Al_2O_3/ZrO_2 nanolaminate gas-diffusion barriers grown by atomic layer deposition," *Applied Physics Letters,* vol. 96, pp. 243308-3, 2010.

[135] J. Meyer, D. Schneidenbach, T. Winkler, S. Hamwi, T. Weimann, P. Hinze, S. Ammermann, H. H. Johannes, T. Riedl, and W. Kowalsky, "Reliable thin film encapsulation for organic light emitting diodes grown by low-temperature atomic layer deposition," *Applied Physics Letters,* vol. 94, pp. 233305-3, 2009.

[136] M. Alexandre and P. Dubois, "Polymer-layered silicate nanocomposites: preparation, properties and uses of a new class of materials," *Materials Science and Engineering: R: Reports,* vol. 28, pp. 1-63, 2000.

[137] S. Takahashi, H. A. Goldberg, C. A. Feeney, D. P. Karim, M. Farrell, K. O'Leary, and D. R. Paul, "Gas barrier properties of butyl rubber/vermiculite nanocomposite coatings," *Polymer,* vol. 47, pp. 3083-3093, 2006.

[138] M. Frounchi, S. Dadbin, Z. Salehpour, and M. Noferesti, "Gas barrier properties of PP/EPDM blend nanocomposites," *Journal of Membrane Science,* vol. 282, pp. 142-148, 2006.

[139] T. Ogasawara, Y. Ishida, T. Ishikawa, T. Aoki, and T. Ogura, "Helium gas permeability of montmorillonite/epoxy nanocomposites," *Composites Part A: Applied Science and Manufacturing,* vol. 37, pp. 2236-2240, 2006.

[140] E. Picard, A. Vermogen, J. F. Gérard, and E. Espuche, "Barrier properties of nylon 6-montmorillonite nanocomposite membranes prepared by melt blending: Influence of the clay content and dispersion state: Consequences on modelling," *Journal of Membrane Science,* vol. 292, pp. 133-144, 2007.

[141] C.-M. Chen, M.-H. Chung, T.-E. Hsieh, M. O. Liu, J.-L. Lin, W.-P. Chu, R.-M. Tang, Y.-S. Tsai, and F.-S. Juang, "Synthesis, thermal characterization, and gas barrier properties of UV curable organic/inorganic hybrid nanocomposites with metal alloys and their application for encapsulation of organic solar cells," *Composites Science and Technology,* vol. 68, pp. 3041-3046, 2008.

[142] G. Dennler, C. Lungenschmied, H. Neugebauer, N. S. Sariciftci, M. Latrèche, G. Czeremuszkin, and M. R. Wertheimer, "A new encapsulation solution for flexible organic solar cells," *Thin Solid Films,* vol. 511-512, pp. 349-353, 2006.

[143] C.-Y. Wu, R.-M. Liao, L.-W. Lai, M.-S. Jeng, and D.-S. Liu, "Organosilicon/silicon oxide gas barrier structure encapsulated flexible plastic substrate by using plasma-enhanced chemical vapor deposition," *Surface and Coatings Technology,* vol. 206, pp. 4685-4691, 2012.

[144] M. Schaepkens, T. W. Kim, A. G. Erlat, M. Yan, K. W. Flanagan, C. M. Heller, and P. A. McConnelee, "Ultrahigh barrier coating deposition on polycarbonate substrates," *Journal of Vacuum Science & Technology A: Vacuum, Surfaces, and Films,* vol. 22, pp. 1716-1722, 2004.

[145] E. Lay, D.-S. Wuu, S.-Y. Lo, R.-H. Horng, H.-F. Wei, L.-Y. Jiang, H.-U. Lee, and Y.-Y. Chang, "Permeation barrier coatings by inductively coupled plasma CVD on polycarbonate substrates for flexible electronic applications," *Surface and Coatings Technology,* vol. 205, pp. 4267-4273, 2011.

[146] G. Rossi and M. Nulman, "Effect of local flaws in polymeric permeation reducing barriers," *Journal of Applied Physics,* vol. 74, pp. 5471-5475, 1993.

[147] K. Ostrikov, E. C. Neyts, and M. Meyyappan, "Plasma nanoscience: from nano-solids in plasmas to nano-plasmas in solids," *Advances in Physics,* vol. 62, pp. 113-224, 2013/04/01 2013.

[148] A. Michelmore, D. A. Steele, D. E. Robinson, J. D. Whittle, and R. D. Short, "The link between mechanisms of deposition and the physico-chemical properties of plasma polymer films," *Soft Matter,* vol. 9, pp. 6167-6175, 2013.

[149] A. Michelmore, C. Charles, R. W. Boswell, R. D. Short, and J. D. Whittle, "Defining Plasma Polymerization: New Insight Into What We Should Be Measuring," *ACS Applied Materials & Interfaces,* vol. 5, pp. 5387-5391, 2013/06/26 2013.

[150] J. D. Whittle, D. A. Steele, and R. D. Short, "Reconciling the Physical and Chemical Environments of Plasma: A Commentary on “Mechanisms of Plasma Polymerisation – Reviewed from a Chemical Point of View”," *Plasma Processes and Polymers,* vol. 9, pp. 840-843, 2012.

[151] H. Biederman and D. Slavinska, "Plasma polymer films and their future prospects," *Surface and Coatings Technology,* vol. 125, pp. 371-376, 2000.

[152] H. Biederman and Y. Osada, *Plasma Polymerization Processes*: Elsevier Science, 1992.

[153] H. Yasuda, "Plasma Polymerization," *Academic Press, New York,* 1985.

[154] K. Bazaka, M. V. Jacob, R. J. Crawford, and E. P. Ivanova, "Plasma-assisted surface modification of organic biopolymers to prevent bacterial attachment," *Acta Biomaterialia,* vol. 7, pp. 2015-2028, 2011.

[155] M. Marquez, B. P. Grady, and I. Robb, "Different methods for surface modification of hydrophilic particulates with polymers," *Colloids and Surfaces A: Physicochemical and Engineering Aspects,* vol. 266, pp. 18-31, 2005.

[156] M. Jafari and D. Dorranian, "Surface modification of PMMA polymer in the interaction with oxygen–argon RF plasma," *Journal of Theoritical and Applied Physics,* vol. 5, pp. 59-66, 2009.

[157] G. Reiners, "Polymer surface modification: Relevance to adhesion. Ed.: K. L. Mittal, 547 Seiten, 337 Abbildungen, 79 Tabellen, VSP BV 1996, 3700 AH Zeist, The Netherlands, DM 177,00 ISBN 90-6764-201-0," *Materials and Corrosion,* vol. 47, pp. 656-656, 1996.

[158] M. Ozdemir, C. U. Yurteri, and H. Sadikoglu, "Physical Polymer Surface Modification Methods and Applications in Food Packaging Polymers," *Critical Reviews in Food Science and Nutrition,* vol. 39, pp. 457-477, 1999/07/01 1999.

[159] R. A. Pethrick, "Polymer surface modification and characterization, edited by Chi-Ming Chan. Carl Hanser Verlag, Munich, Vienna, New York, 1993. *Polymer International,* vol. 37, pp. 84-84, 1995.

[160] D. Briggs, C. R. Kendall, A. R. Blythe, and A. B. Wootton, "Electrical discharge treatment of polypropylene film," *Polymer,* vol. 24, pp. 47-52, 1983.

[161] M. Ozdemir and H. Sadikoglu, "A new and emerging technology: Laser-induced surface modification of polymers," *Trends in Food Science & Technology,* vol. 9, pp. 159-167, 1998.

[162] K. Allmér, A. Hult, and B. Rånby, "Surface modification of polymers. II. Grafting with glycidyl acrylates and the reactions of the grafted surfaces with amines," *Journal of Polymer Science Part A: Polymer Chemistry,* vol. 27, pp. 1641-1652, 1989.

[163] P. K. Chu, J. Y. Chen, L. P. Wang, and N. Huang, "Plasma-surface modification of biomaterials," *Materials Science and Engineering: R: Reports,* vol. 36, pp. 143-206, 2002.

[164] F. Arefi-Khonsari, M. Tatoulian, F. Bretagnol, O. Bouloussa, and F. Rondelez, "Processing of polymers by plasma technologies," *Surface and Coatings Technology,* vol. 200, pp. 14-20, 2005.

[165] D. Bondt, T. Paets Van, and Lauwerenburg, *Cited in: J. Fourcroy, Ann. Chem.,* vol. 2, 58, 1796.

[166] J. Goodman, "The formation of thin polymer films in the gas discharge," *Journal of Polymer Science,* vol. 44, pp. 551-552, 1960.

[167] M. P. v. Wilde, "Vermischte Mittheilungen," *Berichte der deutschen chemischen Gesellschaft,* vol. 7, pp. 352-357, 1874.

[168] T. Ong, L. Xu, T. A. van der Laan, S. Xu, and K. Ostrikov, "Plasma-aided hydrogenation and Al-doping: Increasing the conductivity and optical transparency of ZnO transparent conducting oxide," *Applied Surface Science,* vol. 257, pp. 9986-9990, 2011.

[169] X. Hu, X. Zhao, A. Uddin, and C. B. Lee, "Preparation, characterization and electronic and optical properties of plasma-polymerized nitriles," *Thin Solid Films,* vol. 477, pp. 81-87, 2005.

[170] A. Arias-Durán, L. Giuliani, N. B. D. Accorso, D. Grondona, and S. Goyanes, "Thin films of polymerized acetylene by RF discharge and its benzene absorption ability," *Surface and Coatings Technology,* vol. 216, pp. 185-190, 2013.

[171] K. D. Anderson, R. B. Weber, M. E. McConney, H. Jiang, T. J. Bunning, and V. V. Tsukruk, "Responsive plasma polymerized ultrathin nanocomposite films," *Polymer,* vol. 53, pp. 4686-4693, 2012.

[172] H. Biederman, "Nanocomposites and nanostructures based on plasma polymers," *Surface and Coatings Technology,* vol. 205, Supplement 2, pp. S10-S14, 2011.

[173] L. J. Anderson and M. V. Jacob, "Electrical characterisations of plasma polyermised linalyl acetate," *Materials Science and Engineering: B,* vol. 177, pp. 311-315, 2012.

[174] M. V. Jacob, K. Bazaka, M. Weis, D. Taguchi, T. Manaka, and M. Iwamoto, "Fabrication and characterization of polyterpenol as an insulating layer and incorporated organic field effect transistor," *Thin Solid Films,* vol. 518, pp. 6123-6129, 2010.

[175] H. Yasuda and T. Yasuda, "The competitive ablation and polymerization (CAP) principle and the plasma sensitivity of elements in plasma polymerization and treatment," *Journal of Polymer Science Part A: Polymer Chemistry,* vol. 38, pp. 943-953, 2000.

[176] R. A. Pethrick, "Book review: Plasma surface modification and plasma polymerization N. Inagaki. Technomic Publishing, Basel, 1995. pp. xi+265, price SFr181.00. ISBN 1-56676-337-1," *Polymer International,* vol. 44, pp. 114-114, 1997.

[177] D. Hegemann, M. M. Hossain, E. Körner, and D. J. Balazs, "Macroscopic Description of Plasma Polymerization," *Plasma Processes and Polymers,* vol. 4, pp. 229-238, 2007.

[178] J. Friedrich, "Mechanisms of Plasma Polymerization – Reviewed from a Chemical Point of View," *Plasma Processes and Polymers,* vol. 8, pp. 783-802, 2011.

[179] H. Yasuda and Q. Yu, "Creation of polymerizable species in plasma polymerization," *Plasma Chemistry and Plasma Processing,* vol. 24, pp. 325-351, 2004.

[180] H. Yasuda, *Luminous chemical vapor deposition and interface engineering*. New York: Marcel Dekker, 2005.

[181] C. Corbella, I. Bialuch, M. Kleinschmidt, and K. Bewilogua, "Up-scaling the production of modified a-C:H coatings in the framework of plasma polymerization processes," *Solid State Sciences,* vol. 11, pp. 1768-1772, 2009.

[182] L.-g. Wu, C.-l. Zhu, and M. Liu, "Study on plasma polymerization of 1.1.1-trifluoroethane: deposition and structure of plasma polymer films," *Desalination,* vol. 192, pp. 234-240, 2006.

[183] A. J. Choudhury, J. Chutia, S. A. Barve, H. Kakati, A. R. Pal, Jagannath, N. Mithal, R. Kishore, M. Pandey, and D. S. Patil, "Studies of physical and chemical properties of styrene-based plasma polymer films deposited by radiofrequency Ar/styrene glow discharge," *Progress in Organic Coatings,* vol. 70, pp. 75-82, 2011.

[184] K. Hosono, I. Matsubara, N. Murayama, W. Shin, and N. Izu, "Effects of discharge power on the structure and electrical properties of plasma polymerized polypyrrole films," *Materials Letters,* vol. 58, pp. 1371-1374, 2004.

[185] L. Ledernez, H. Yasuda, F. Olcaytug, F. Gemetz, and G. Urban, "Pressure Dependence of Plasma Polymerization of Methane at Constant W/FM," *Plasma Processes and Polymers,* vol. 4, pp. S794-S796, 2007.

[186] D. Hegemann, U. Schütz, and A. Fischer, "Macroscopic plasma-chemical approach to plasma polymerization of HMDSO and CH4," *Surface and Coatings Technology,* vol. 200, pp. 458-462, 2005.

[187] H. Kersten, H. Deutsch, H. Steffen, G. M. W. Kroesen, and R. Hippler, "The energy balance at substrate surfaces during plasma processing," *Vacuum,* vol. 63, pp. 385-431, 2001.

[188] L. Denis, P. Marsal, Y. Olivier, T. Godfroid, R. Lazzaroni, M. Hecq, J. Cornil, and R. Snyders, "Deposition of Functional Organic Thin Films by Pulsed Plasma Polymerization: A Joint Theoretical and Experimental Study," *Plasma Processes and Polymers,* vol. 7, pp. 172-181, 2010.

[189] B. N. Chapman and V. J. Minkiewicz, *J. Vac. Sci. and Tech.,* vol. 15, 1978.

[190] R. A. Morgan, "The rf voltage/current characteristics and related de negative bias properties of an electrotech flat bed plasma etcher," *Vacuum,* vol. 32, pp. 297-303, 1982.

[191] N. D. Tran, N. K. Dutta, and N. R. Choudhury, "Plasma-polymerized perfluoro(methylcyclohexane) coating on ethylene propylene diene elastomer surface: Effect of plasma processing condition on the deposition kinetics, morphology and surface energy of the film," *Thin Solid Films,* vol. 491, pp. 123-132, 2005.

[192] L. Denis, D. Cossement, T. Godfroid, F. Renaux, C. Bittencourt, R. Snyders, and M. Hecq, "Synthesis of Allylamine Plasma Polymer Films: Correlation between Plasma Diagnostic and Film Characteristics," *Plasma Processes and Polymers,* vol. 6, pp. 199-208, 2009.

[193] A. Kiesow and A. Heilmann, "Deposition and properties of plasma polymer films made from thiophenes," *Thin Solid Films,* vol. 343–344, pp. 338-341, 1999.

[194] Y. Martin, D. Boutin, and P. Vermette, "Study of the effect of process parameters for n-heptylamine plasma polymerization on final layer properties," *Thin Solid Films,* vol. 515, pp. 6844-6852, 2007.

[195] C. L. Chapman, D. Bhattacharyya, R. C. Eberhart, R. B. Timmons, and C.-J. Chuong, "Plasma polymer thin film depositions to regulate gas permeability through nanoporous track etched membranes," *Journal of Membrane Science,* vol. 318, pp. 137-144, 2008.

[196] C. Corbella, "Upscaling plasma deposition: The influence of technological parameters," *Surface and Coatings Technology,* vol. 242, pp. 237-245, 2014.

[197] M. C. M. van de Sanden, "Views on Macroscopic Kinetics of Plasma Polymerization: Acrylic Acid Revisited," *Plasma Processes and Polymers,* vol. 7, pp. 887-888, 2010.

[198] A. von Keudell and J. Benedikt, "A Physicist's Perspective on "Views on Macroscopic Kinetics of Plasma Polymerisation"," *Plasma Processes and Polymers,* vol. 7, pp. 376-379, 2010.

[199] H. Biederman and O. Kylián, "Some Remarks to Macroscopic Kinetics of Plasma Polymerization," *Plasma Processes and Polymers,* vol. 8, pp. 475-477, 2011.

[200] D. Hegemann, H. Brunner, and C. Oehr, "Evaluation of deposition conditions to design plasma coatings like SiO_x and a-C:H on polymers," *Surface and Coatings Technology,* vol. 174–175, pp. 253-260, 2003.

[201] R. Prikryl, V. Cech, L. Zajickova, J. Vanek, S. Behzadi, and F. R. Jones, "Mechanical and optical properties of plasma-polymerized vinyltriethoxysilane," *Surface and Coatings Technology,* vol. 200, pp. 468-471, 2005.

[202] K. Bazaka and M. V. Jacob, "Nanotribological and nanomechanical properties of plasma-polymerized polyterpenol thin films," *Journal of Materials Research,* vol. 26, pp. 2952-2961, 2011.

[203] L. Anderson, M. Jacob, M. Barra, F. Di Girolamo, and A. Cassinese, "Effect of a plasma polymerised linalyl acetate dielectric on the optical and morphological properties of an n-type organic semiconductor," *Applied Physics A: Materials Science & Processing,* vol. 105, pp. 95-102, 2011.

[204] I. S. Bae, C. K. Jung, S. J. Cho, Y. H. Song, and J. H. Boo, "A comparative study of plasma polymerized organic thin films on their electrical and optical properties," *Journal of Alloys and Compounds,* vol. 449, pp. 393-396, 2008.

[205] M. C. Kim, S. H. Cho, J. G. Han, B. Y. Hong, Y. J. Kim, S. H. Yang, and J. H. Boo, "High-rate deposition of plasma polymerized thin films using PECVD method and characterization of their optical properties," *Surface and Coatings Technology,* vol. 169–170, pp. 595-599, 2003.

[206] C. D. Easton and M. V. Jacob, "Optical characterisation of radio frequency plasma polymerised Lavandula angustifolia essential oil thin films," *Thin Solid Films,* vol. 517, pp. 4402-4407, 2009.

[207] J. Ahmad, K. Bazaka, and M. Jacob, "Optical and Surface Characterization of Radio Frequency Plasma Polymerized 1-Isopropyl-4-Methyl-1,4-Cyclohexadiene Thin Films," *Electronics,* vol. 3, pp. 266-281, 2014.

[208] I. S. Bae, C. K. Jung, S. H. Jeong, S. J. Cho, Y. J. Yu, J. G. Kim, and J. H. Boo, "Comparison of their electrical, optical, and electrochemical properties of as-grown plasma polymerized organic thin films by PECVD," *Thin Solid Films,* vol. 515, pp. 407-410, 2006.

[209] L. Anderson, C. Easton, and M. Jacob, "Compatibility of plasma-deposited linalyl acetate thin films with organic electronic device fabrication techniques," *Journal of Materials Science,* vol. 48, pp. 4851-4859, 2013/07/01 2013.

[210] J. Ahmad, K. Bazaka, M. Oelgemöller, and M. V. Jacob, "Wetting, solubility and chemical characteristics of plasma polymerized 1-isopropyl-4-methyl-1,4-cyclohexadiene thin films," *Coatings,* vol. 4, pp. 527-552, 2014

[211] D. Hegemann, E. Körner, and S. Guimond, "Plasma Polymerization of Acrylic Acid Revisited," *Plasma Processes and Polymers,* vol. 6, pp. 246-254, 2009.

[212] K. Bazaka, M. V. Jacob, D. Taguchi, T. Manaka, and M. Iwamoto, "Investigation of interfacial charging and discharging in double-layer pentacene-based metal-insulator-metal device with polyterpenol blocking layer using electric field induced second harmonic generation," *Chemical Physics Letters,* vol. 503, pp. 105-111, 2011.

[213] L. Anderson and M. Jacob, "Microwave characterization of a novel, environmentally friendly, plasma polymerized organic thin film," *Physics Procedia,* vol. 14, pp. 87-90, 2011.

[214] L. J. Anderson and M. V. Jacob, "Temperature dependent electrical impedance spectroscopy measurements of plasma enhanced chemical vapour deposited linalyl acetate thin films," *Thin Solid Films,* vol. 5347, pp. 452-458, 2013.

CHAPTER III

MATERIALS AND METHODOLOGY

The main goal of this chapter is to provide details of the experimental methods used in this dissertation work. It starts with various fabrication techniques for thin films including detailed process parameters. PECVD process was used for thin film fabrication. Detailed characterization procedures of the thin films are also explained in this chapter.

Section III.1 gives a succinct overview of the thin film fabrication procedure using PECVD process. Metal deposition process using thermal evaporation is also briefly discussed in this section.

Section III.2 details the most important techniques that have been used to characterize the plasma polymers in this research.

III.1 THIN FILM FABRICATION

III.1.1 PLASMA ENHANCED CHEMICAL VAPOR DEPOSITION (PECVD)

PECVD is one of the techniques that allows for industrial-scale deposition of good quality thin films with good adhesion [1]. One of the main advantages of PECVD is the availability of low temperature deposition compared to other chemical vapor deposition (CVD) methods, such as thermally driven CVD (700 °C to 900 °C). This lower temperature capability is very attractive for application to the encapsulation of both organic electronics and flexible electronics because the intrinsic properties of organic materials and polymer substrates for flexible electronics limit the maximum processing temperature (preferably below 100 °C, maximum limit ~ 130 °C) [2].

Plasma is usually created by an electric glow discharge that can be generated by the transfer of power from an electric field to electrons [3]. In a *direct current* (DC) glow discharge, this can be established by passing a DC electric current through a gas under low pressure. The positive ions are bombarded to the cathode that results in the generation of secondary electrons. These electrons are accelerated away from the cathode until they gain sufficient energy to ionize the gas molecules or atoms that collide with the electrons [3, 4]. In *alternating current* (AC) glow discharges, the mechanism depends on the frequency of the alternation. At low frequencies, the system can be looked upon as a DC glow discharge with alternating polarity. Upon increasing the frequency of the applied voltage, positive ions become immobile and at frequencies above 500 kHz, the loss of charged particles from the system is reduced significantly. Regeneration of electrons and ions occurs within the body of the plasma through collisions of electrons with gas molecules. In RF plasma (13.56 MHz) therefore, no contact between the electrodes and the plasma is required. The plasma can be initiated and sustained by external electrodes, at a much lower voltage than is required for maintaining a DC glow discharges [5]. RF plasma polymerization is therefore used to fabricate polymer thin films throughout the work of this thesis.

The RF plasma polymerization process is usually achieved by means of the two types of reactor: a bell-jar type reactor and a tubular-type reactor [6]. Bell-jar type reactor has internal parallel-plate metal electrodes; and tubular-type reactor has an external coil or ring electrodes for excitation by RF discharge [6]. In this work, plasma deposition of organic thin films was performed in a custom build, glass chamber on a variety of substrates using a variety of power densities. To ensure reproducibility of results, samples were fabricated under identical fabrication conditions in all instances, and the only parameter that changed was the power delivered to the reaction chamber.

III.1.1.1 PRE-DEPOSITION TREATMENT

The pre-deposition treatment plays an important role in achieving the desired deposition parameters, and in obtaining good quality plasma polymer thin films. As the plasma polymerization occurs in low temperature and low-pressure environment, obtaining a low pressure within the reactor chamber is one of the most important pre-deposition conditions. A vacuum pump was used to continually reduce the pressure of the chamber until the capacity of the pump is reached, as long as there is no supply to the molecules of the gas. Eventually the system will reach a steady state point and the pressure will remain constant before the ideal pressure for plasma polymerization is reached.

In this research work, different substrates were used depending on the type of study to be accomplished. However glass microscope slides were the most common substrate, utilized in the majority of experiments. A cleaning treatment prior to deposition was performed for all substrates to ensure a surface free of contamination.

Cleaning treatment started with the substrates placed in a sonicator of doubly–distilled warm water and Extran for thirty minutes. Ultrasonic cleaning enables the cleaning of macro and micro scale contaminates without manually scrubbing them. The ultrasonic cleaner used in this project is the Soniclean 160HT. Following this ultrasonic cleaning treatment, acetone and isopropanol were used to sequentially rinse the substrates to further clean the surface and dried in air. All substrates were stored in a closed container, in otherwise ambient conditions.

III.1.1.2 THIN FILM DEPOSITION PROCESS

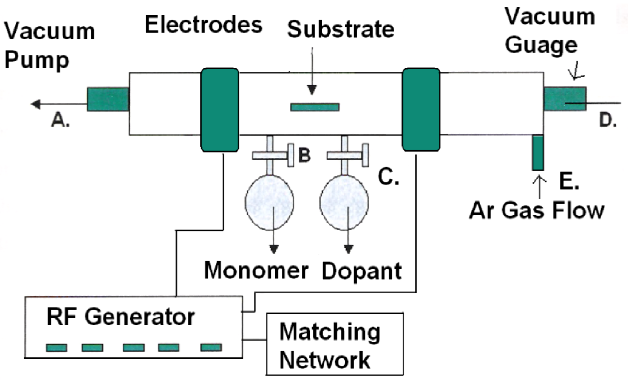

Figure III.1. Schematic diagram of thin film deposition arrangement

Thin film deposition was performed using a custom built, glass RF reaction chamber (figure

III.1), 0.75 m in length with an inner diameter of 0.055 m (approximate volume of 0.0018 m3). Two removable caps are at the two ends of the chamber. One of these end caps includes two inlets, one of which is used to introduce inert gas (generally *Ar*) to the system, and the other to monitor system pressure. An outlet to a vacuum pump is present on the second end cap to evacuate the system to suitable pressures. The monomer flow rate is kept constant via a vacuum stopcock on the monomer inlet and the system pressure is monitored via a vacuum gauge. RF power is delivered to the system via an ENI RF generator at 13.56 MHz through a matching network and capacitively coupled external copper electrodes.

The RF input power was controlled and varied between 10 W and 75 W for the investigations in this work. Above 75 W the strength of the field began to interfere with sensitive electronics in the proximity of the system (such as the vacuum gauge) and overheat the matching network. To ensure accurate pressure readings and correct operation of the matching network, 75 W was the highest power used in any study. The capacitively coupled external copper electrodes were placed 0.13 m from the monomer inlet and 0.1 m apart. Uniformity of the RF discharge was the determinant of this electrode configuration and the corresponding uniformity of resulting thin films for the particular reaction chamber was utilized throughout this work.

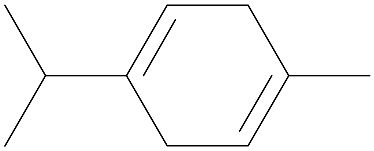

Figure III.2. Chemical structure of γ-terpinene

For deposition of pp–GT thin films, 10 mL of monomer (in all cases, γ-terpinene purchased from Australian Botanical Products Pty. Ltd., Australia) was used without further purification. The monomer flow rate was kept constant via a vacuum stopcock, and estimated using the following relation [7]:

$$F = 16172\frac{V}{T}\frac{dp}{dt} \qquad \text{(III.1)}$$

where *F* is the flow rate (cm^3 min^{-1}), *T* the temperature (295 K), *V* the volume of the chamber (1.8 L), *p* the pressure (mbar) and *t* time (s). The rate of change of pressure with respect to time for the monomer was evaluated in two steps: first, all inlets/outlets to the system were closed and the pressure of the system (evacuated to a stable starting pressure) was measured every 10 seconds for 120 seconds to establish a baseline leakage rate for the system. This process was repeated with the monomer inlet open after the base pressure had been reached. The value *dp/dt* was determined by subtracting the leakage pressure change from the pressure change when the monomer inlet was open, plotting this value against time and taking a linear regression. The gradient was then equal to *dp/dt* and corresponded to an increase in pressure of approximately 2.23×10^{-3} mbar every 10 seconds. Substitution into Eq. III.1 gives the estimated monomer flow rate to be 1.57 cm^3 min^{-1} for this system.

Synthesis of pp–GT films with consistent and repeatable properties followed the steps mentioned below:

1. The reaction chamber and substrates were cleaned using the cleaning treatments mentioned earlier. This ensured that the substrate surfaces and reaction chamber were free of contaminants that could affect the plasma polymer thin film deposition. The reactor was routinely cleaned as thin films form on all surfaces exposed to both the RF field and monomer.
2. The reaction chamber was connected to the vacuum pump, pressure gauge and gas (*Ar*) inlet.
3. Vacuum grease was applied to the joints and all the valves were turned off.
4. Vacuum pump was turned on and the plasma chamber was evacuated to a low pressure, evaporating residual alcohols left in the chamber from the cleaning treatment. The external electrodes and power source were connected to the chamber as previously outlined.
5. RF glow at a power of 25 W was initiated at low pressure (~100 micron) and the apparatus left for approximately 60 minutes. This RF field further cleaned the interior surface of the reaction chamber and further removed contaminants remaining from the cleaning treatment due to etching effects without the presence of a monomer. After 60 minutes the RF input was stopped and the system was exposed to atmosphere.
6. The system was again evacuated to low pressure (~200 micron) and 10 mL of γ-terpinene monomer was placed into the flask and the monomer inlet was opened. This caused the monomer to degas, and matched the pressure of the monomer inlet to that of the tube during deposition, such that sudden increases in pressure did not occur when the monomer inlet was opened during the deposition of pp–GT thin films. No substrate was in the reactor at this time so that its surface was not exposed to contamination in the form of monomer vapor.
7. The chamber was exposed to atmosphere again and a substrate was placed between the two electrodes. The tube was partially evacuated and *Ar* passed through the system for 60 seconds to ensure an O_2 free surface.

8. When the chamber reached a pressure of ~100 micron, RF glow was initiated, causing a sharp rise in pressure.
9. Once the pressure had reached ~150 micron, the monomer inlet was opened, beginning the deposition of pp–GT thin film.
10. The deposition was allowed to continue for a predetermined amount of time depending on several factors. As discussed in the literature review, the deposition time is the variable, which most fundamentally determines the thickness of the final pp–GT film, with increased deposition time resulting in thicker samples. RF power of the discharge also influences the film thickness, and in the monomer sufficient regime, higher powers result in thicker films. This behavior was confirmed for γ-terpinene monomer and deposition used throughout this thesis.
11. When the deposition was complete, the monomer inlet was closed and the RF glow extinguished. The sample was left under vacuum for a minute, then removed and stored in a closed box in otherwise ambient conditions.

III.1.2 THERMAL EVAPORATION OF METALS

Investigating the electrical behavior of pp–GT thin films required the deposition of metallic layers to provide a conducting surface. Thermal evaporation technique was used to deposit metal in a Hivac thermal evaporation unit.

All substrates underwent cleaning procedure prior to being placed inside the thermal evaporation unit. High purity *Al* wire was placed within the alumina-coated tungsten boat and the system evacuated to a pressure of 0.2 mbar. At this pressure, the plasma source was initiated to further clean the substrates for one minute. When the pressure reached a base pressure of ~10^{-5} mbar, a high current was passed until the metal changed phase. After the metal melted (~30 seconds), the shutter was removed from between the boat and substrates to enable deposition. The deposition was continued until the entire length of wire in the boat had evaporated; then the shutter was closed while any remaining residue was burned off the boat so that it was clean for the next deposition.

For metal–insulator–metal (MIM) structures on standard glass substrates (25 mm x 75 mm), pp–GT thin films were fabricated over the metal layer already deposited. To define electrode structure a shadow mask was used, where a physical layer was placed over the portion of the substrate that does not define the electrode. Samples were fabricated in such a way that there were two devices on each substrate. The top electrode was 5 mm x 10 mm and defined by the shadow mask. Following deposition, samples were stored under vacuum until the next fabrication step was performed, in order to prevent oxidization and degradation of the deposited metallic layers.

Deposition of metallic electrodes often required a final step before devices were ready for use. It was necessary to attach copper wires to the electrodes on the device to interface with any other electronic or measurement device. This was achieved using *Ag* paste (CircuitWorks two–part silver conductive epoxy) to bond the wire to the surface of the electrode.

III.2 CHARACTERIZATION METHODS

From the literature review, it was found that various properties of plasma polymer thin films are commonly investigated, due to their fundamental importance to applications, improved understanding of other material properties and influence of these characteristics over interactions with other materials and processes. These are the optical, topographical and properties and were a subject of investigation in this thesis. In this section, the techniques that have been used to characterize pp–GT are briefly discussed.

III.2.1 MASS SPECTROSCOPY

Plasma polymer thin films have the potential to provide a diverse range of surface properties. This has led to their application in areas as diverse as encapsulation coatings [8, 9], biomaterials [10], electronics [11] and nanotechnology [12]. In practice, plasma polymers are synthesized with reference to monomer flow rate, discharge power, and chamber pressure. These parameters provide sufficient control over the deposition process required for many applications. However, a better understanding of the processes occurring during deposition and the mechanisms of film formation are required to expand the extent of opportunities that plasma polymer films provide [13]. Mass spectrometry has been identified as a useful tool for this purpose that derives a mechanistic understanding of the chemistry of the plasma phase. It may be used to determine the spectrum of both neutral and ionic species in the plasma. The technique relies on separating species based on their mass-to-charge (m/z) ratio by applying an electric field.

For neutral species, after entering the instrument via a small orifice, molecules (or atoms) are converted to ions by electron impact (typically at 70 eV) [14]. Ions are then subjected to an electric field in an analyzer, which mass selects the species, which are then measured by a detector in the form of a current and the signal is converted to a mass spectrum. This spectrum is used to determine the elemental or isotopic signature of a sample, the masses of particles and of molecules, and to elucidate the chemical structures of molecules through a characteristic fragmentation pattern. Based on this technique, the role of ions in plasma polymerization of γ-terpinene is assessed in this thesis. Ion flux is measured as a function of input power. Ion energy, neutral and positive ion mass spectra and film deposition rate are simultaneously monitored.

III.2.2 SPECTROSCOPIC ELLIPSOMETRY

The refractive index (*n*) and extinction coefficient (*k*) of a plasma polymer can derive the material's interaction with light. Variable Angle Spectroscopic Ellipsometry (VASE) is a powerful technique to measure these parameters for research on new materials and processes and used therefore in this thesis.

VASE is a technique, which measures a change in polarization as light reflects or transmits from a material structure. The polarization change is represented as an amplitude ratio, Ψ, and the phase difference, Δ:

$$\rho = \frac{r_p}{r_s} = \tan(\Psi) e^{i\Delta} \qquad \text{(III.2)}$$

where ρ is the complex reflectance ratio, r_p and r_s denote the amplitude of *p*- and *s*- polarized reflected light normalized to their initial values.

After the data are acquired covering the desired spectral range and angles of incidence, a model for the optical structure is constructed. For example, this may include a substrate and a single film on top, or substrate plus film with roughness on top. The model is then used to calculate the predicted response from Fresnel's equations that describe each material with thickness and optical constants. If these values are not known, an estimate is given for the purpose of the preliminary calculation. The calculated values are compared to experimental data. Any unknown material properties can then be varied to improve the match between experiment and calculation. Finding the best match is typically achieved through regression. An estimator, like the Mean Squared Error (MSE), is used to quantify the difference between curves. The unknown parameters are allowed to vary until the minimum MSE is reached.

$$\mathrm{MSE} = \sqrt{\frac{1}{2N-M}\sum_{i=1}^{N}\left[\left(\frac{\Psi_i^{mod}-\Psi_i^{exp}}{\sigma_{\Psi,i}^{exp}}\right)^2 + \left(\frac{\Delta_i^{mod}-\Delta_i^{exp}}{\sigma_{\Delta,i}^{exp}}\right)^2\right]} \qquad \text{(III.3)}$$

where N is the number of measured Ψ, Δ pairs and M is the number of real valued fit parameters. The Levenberg-Marquardt algorithm is used to perform the optimization and is described elsewhere [15]. All analysis of ellipsometry data was performed in the WVASE32 software, which was packaged with the J.A. Woollam Co., Inc. VASE used for data acquisition. This software package implemented the optimization algorithm; however, checks for uniqueness of fits and a true global minimum were performed on results from all data analyses.

A typical example of the fitting process for a pp–GT sample deposited on a glass substrate is presented below. Unless otherwise noted, this procedure has been used for the analysis of all ellipsometry data presented in this thesis, and is relevant to all experiments and analysis presented, as it was how sample thickness was determined in all cases.

III.2.2.1 ELLIPSOMETRIC ANALYSIS OF A pp–GT SAMPLE

Ellipsometric analysis of a pp–GT sample has been carried on across the measured spectrum of 200 nm – 1000 nm and angles of 55° - 65° to ensure measurement about the Brewster angle, which reduces sensitivity of the data to noise and systematic errors [15]. Figure III.3 shows the typical measured amplitude ratio, Ψ, and the phase difference, Δ values.

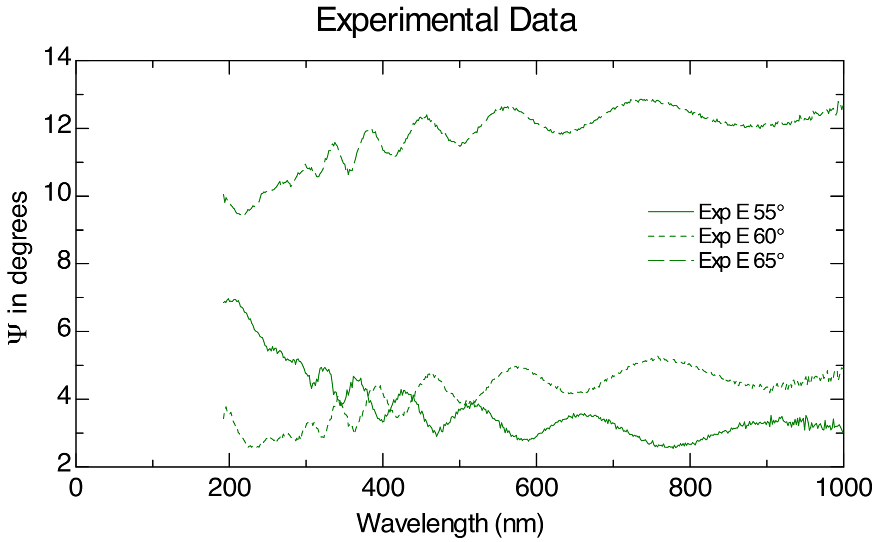

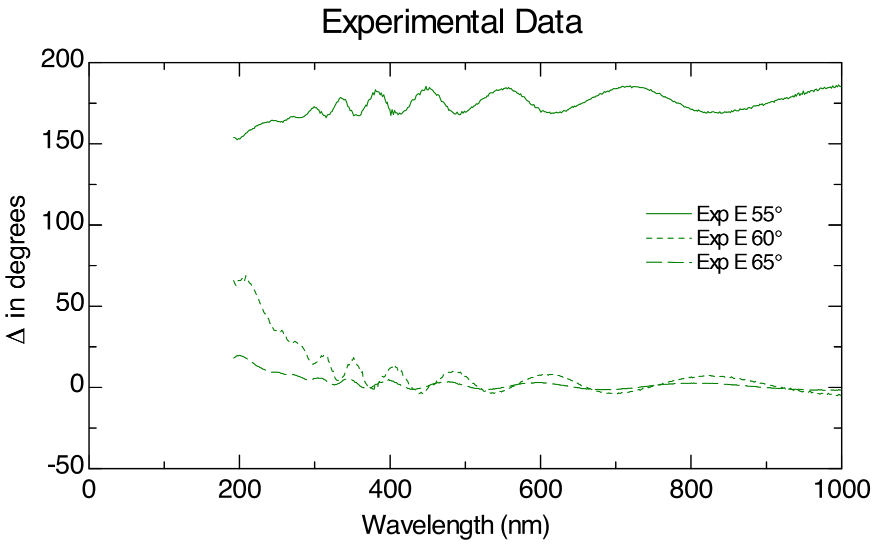

Figure III.3. Experimental Ψ and Δ data

For pp–GT, an optically transparent glass microscopy slide was used as the substrate, and a layer was added to the model that describes the optical properties of this slide.

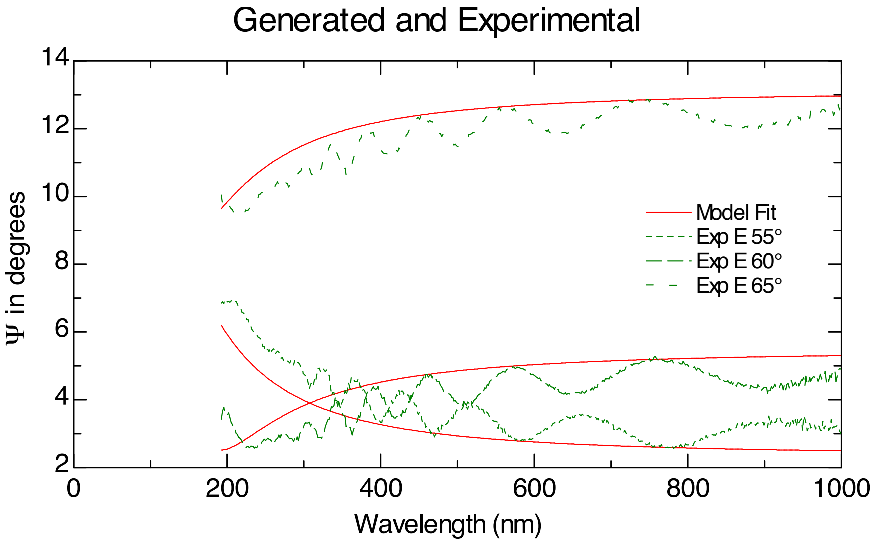

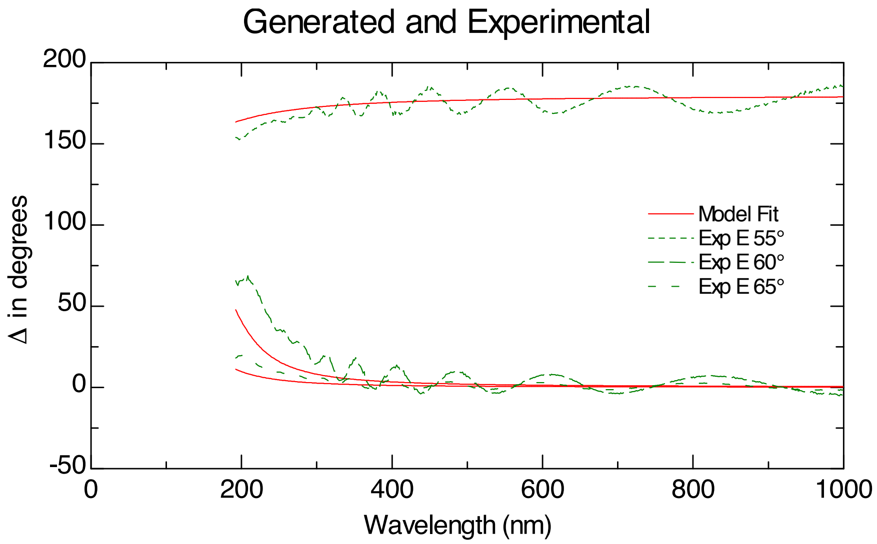

Figure III.4. Experimental and modelled Ψ and Δ data after inclusion of a substrate layer

Figure III.4 shows the experimental and modeled Ψ and Δ data after inclusion of a substrate layer. This reveals that a model including only a substrate is insufficient to adequately describe the experimentally obtained data. An optical model of the thin film must therefore be determined. pp–GT thin films are optically transparent and non-absorbing in the visible spectral range and hence their extinction coefficient tends to zero as wavelengths become longer. Such behavior is well modeled by a Cauchy layer, described mathematically as [15]:

$$\tilde{n}(\lambda) = A + \frac{B}{\lambda^2} + \frac{C}{\lambda^4} + j\alpha \exp\left(\beta\left(12400\left[\frac{1}{\lambda} - \frac{1}{\gamma}\right]\right)\right) \quad \text{(III.4)}$$

where A, B and C are parameters that describe the refractive index of the layer and α, β and γ are the extinction coefficient amplitude, exponent factor and band edge respectively, which describe the extinction coefficient of the layer, modeled as an exponential absorption tail.

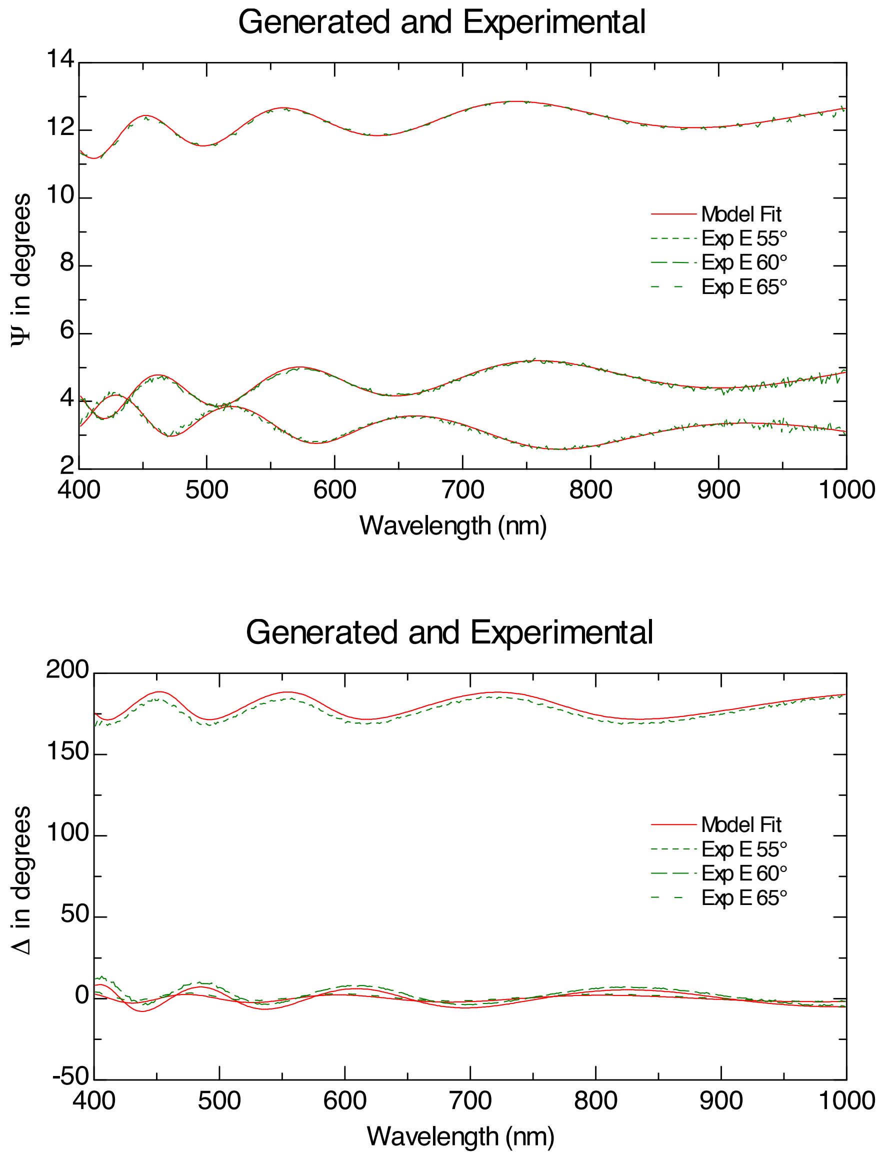

Figure III.5. Result of fitting Cauchy layer refractive index parameters and film thickness to experimental Ψ and Δ data at high wavelengths

Figure III.5 shows the modeled system from fitting A, B and C parameters to experimental data at high wavelengths. As C is the coefficient of a λ^{-4} term, if the band edge γ occurs at higher wavelengths, as was the case here, it is typical for the model to show minimal sensitivity to the parameter and be left out of fitting entirely [15, 16].

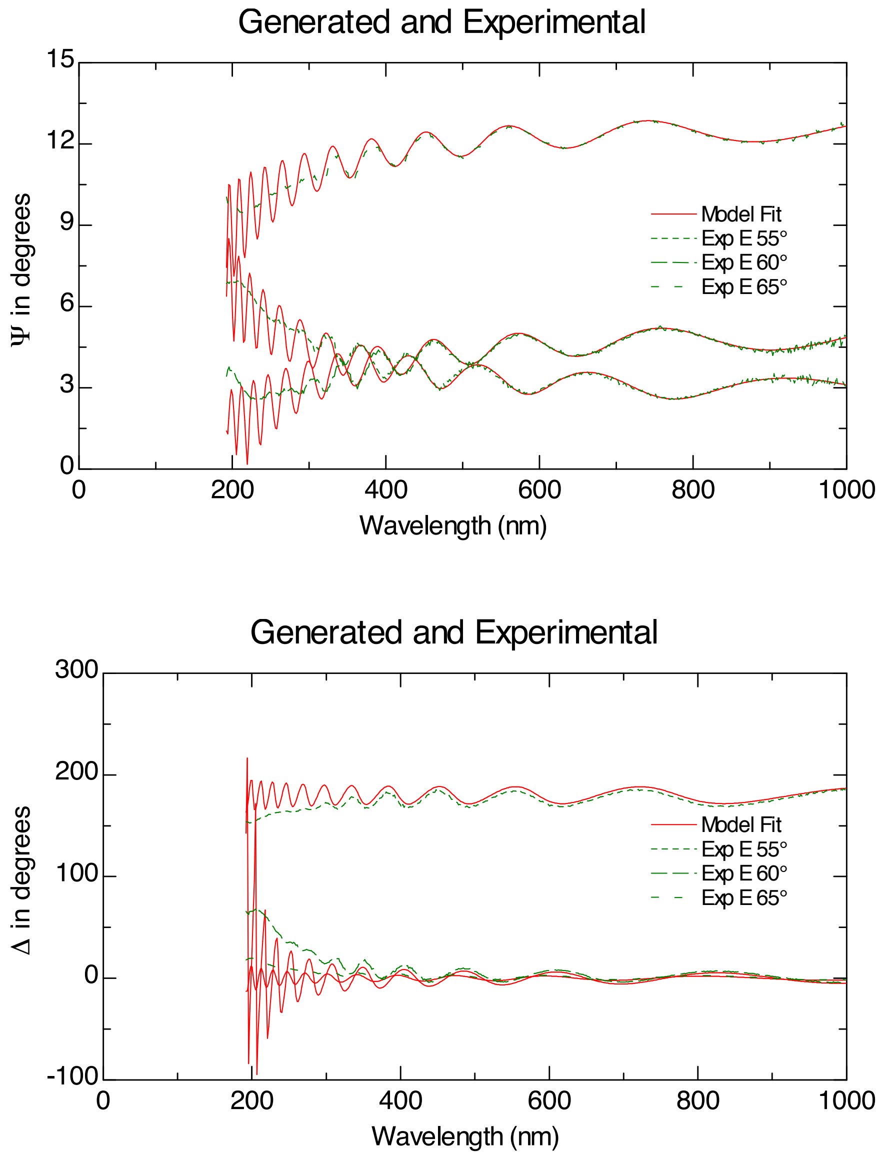

Figure III.6. Modelled Ψ and Δ data across entire spectrum

Figure III.6 shows the result of modeled Ψ and Δ data across entire spectrum. While the model adequately describes experimental data above approximately 400 nm, below this point the model loses accuracy. This is because of the zero extinction coefficient across the entire spectrum. However, in reality, absorption in the UV region takes place.

Figure III.7 shows the improved model across all wavelengths by fitting the extinction coefficient parameters α, β and γ at low wavelengths while leaving A, B and C fixed at their initial estimates. Replacing the Cauchy description of pp–GT with a General Oscillator description, makes further improvements to the model.

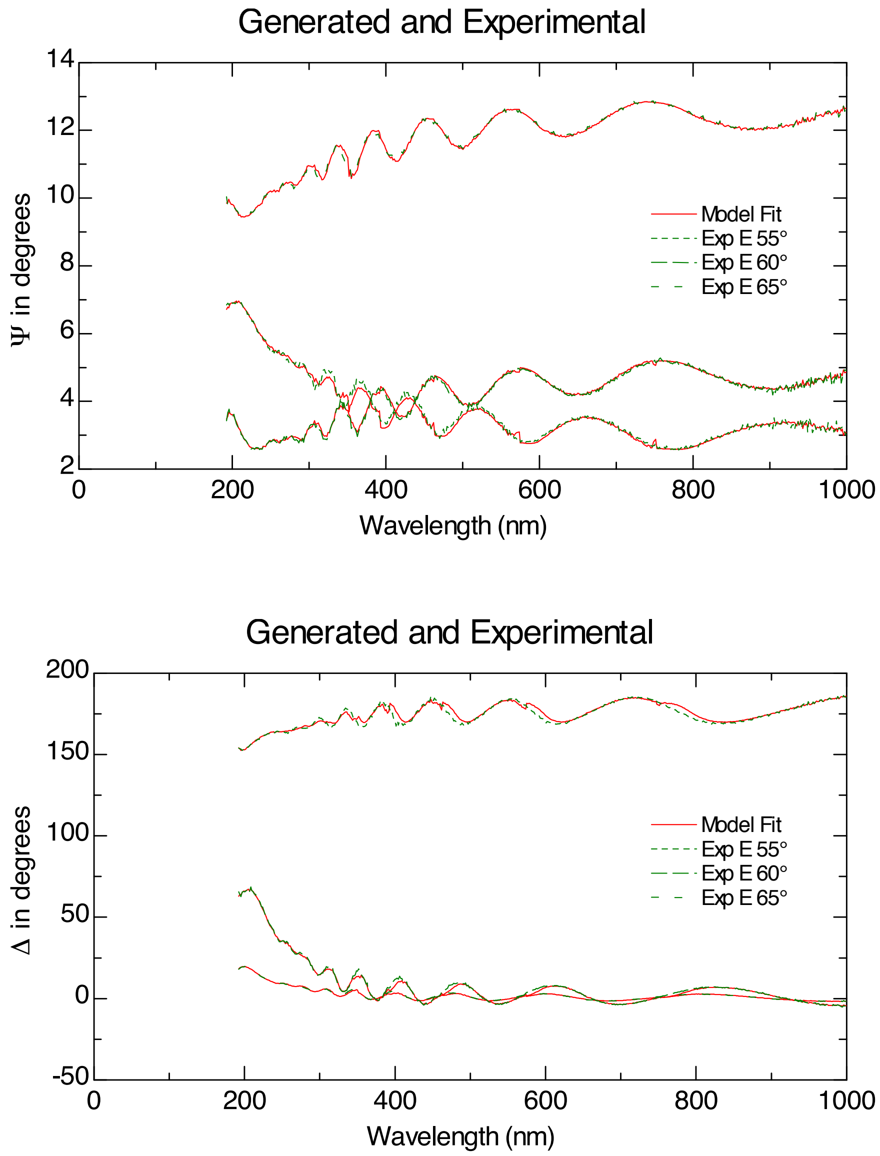

Figure III.7. Experimental model to Ψ and Δ data after fitting for extinction coefficient parameters α, β and γ

III.2.2.2 GENERAL OSCILLATOR MODELS

The general oscillator model with generalized parameters, which model the absorption features of the material, replaces the Cauchy description of the optical constants of the layer of interest. The refractive index is then obtained by exploiting the Kramers-Kronig (KK) consistency of the dielectric function. Depending on the characteristic shape of the material's dispersion behavior, different oscillator models are required. The shape of the absorption depends on the physical source of the absorption in the material, and hence correct choice in oscillator can properly model the experimental data and determine the optical properties of the thin film.

In amorphous materials, absorption occurs at distributed resonant frequencies and the width of the absorption features is Gaussian in nature. Gaussian oscillators are therefore useful to capture the features present and inform further fitting efforts, if little is known about the physical and chemical characteristics of the material and simplifying assumptions cannot immediately be made [16]. As mentioned earlier, plasma deposited thin films are generally amorphous in nature, and hence the assumption of absorption bands with a Gaussian shape is a reasonable starting point. The Gaussian oscillator describes the real (ε_1) and imaginary (ε_2) components of the complex dielectric function, $\varepsilon_c(E)$, where E is the photon energy (related to wavelength, λ, and frequency, f) as [15]:

$$\varepsilon_2(E) = A.\left(\exp\left[-\left(\frac{E-E_a}{\sigma}\right)^2\right] - \exp\left[-\left(\frac{E+E_a}{\sigma}\right)^2\right]\right) \quad \text{(III.5)}$$

$$\varepsilon_1 = \frac{2}{\pi} P \int_0^{\infty} \frac{\xi \varepsilon_2(\xi)}{\xi^2 - E^2} d\xi \quad \text{(III.6)}$$

$$\sigma = \frac{B_r}{2\sqrt{\ln(2)}} \quad \text{(III.7)}$$

where A is the amplitude, E_a the center energy and B_r the broadening of the absorption peak, which become the fit parameters of the model, rather than the optical constants themselves. Eq. III.8 provides the relationship between ε_2 *(E)* and ε_1 *(E)* via the KK transform.

In the case of pp–GT thin films, optical properties of the previously modeled Cauchy layer are used as the starting point for modeling the material's optical properties with a single Gaussian oscillator. The oscillator’s parameters are selected as optimization variables and a fit is performed. After fitting the oscillator parameters to the initial guess provided from the Cauchy layer, the thickness is chosen as a fit parameter, and the thickness and oscillators variables are optimized to provide the best fit to the experimental data.

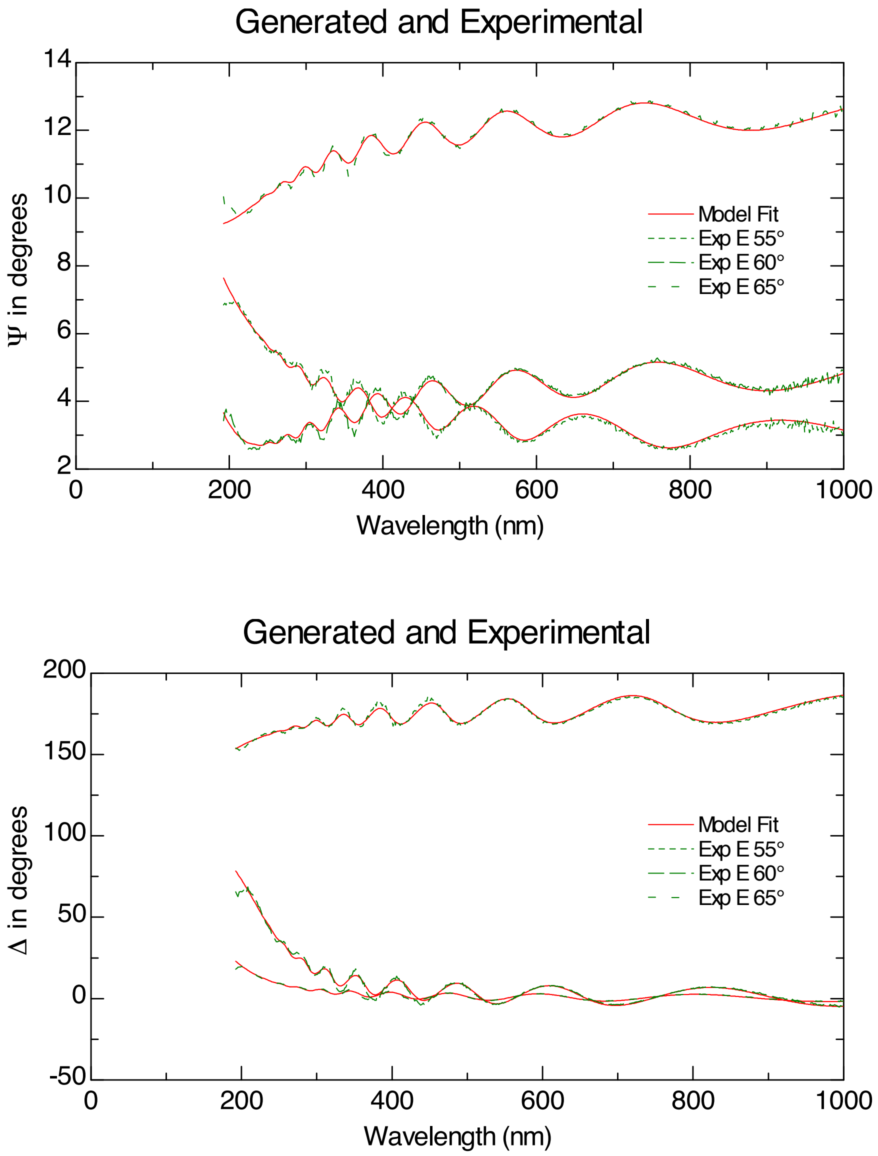

Figure III.8. Experimental and modelled Ψ and Δ data after fitting with general oscillator parameters

Figure III.8 shows the result of the fitting of the Gaussian oscillator parameters and thickness of the layer to experimental data. The optical profile of the sample is shown in Figure III.9.

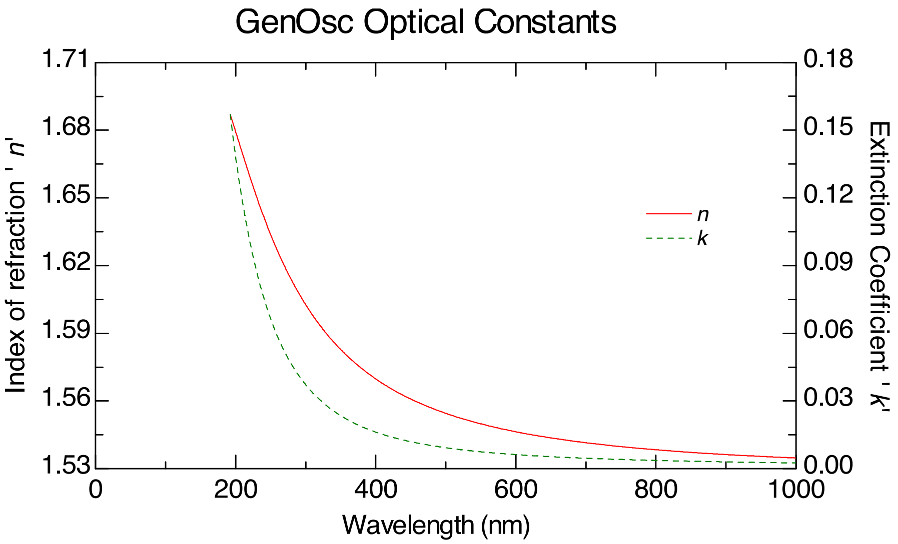

Figure III.9. Optical properties of general oscillator model

III.2.3 ULTRAVIOLET–VISIBLE (UV-Vis) SPECTROSCOPY

Ultraviolet–visible spectroscopy or spectrophotometry (UV–Vis) refers to absorption spectroscopy or reflectance spectroscopy in the UV spectral region. The instrument used in UV–Vis spectroscopy is called an UV–Vis spectrophotometer. It measures the intensity of light passing through a sample (I), and compares it to the intensity of light before it passes through the sample (I_0). The ratio I/I_0 is called the *transmittance*, and is usually expressed as a percentage (%T). UV–Vis spectroscopy is used to measure the transmittance of pp–GT samples throughout this research work. The absorbance, A, is based on the transmittance:

$$A = -\log\left(\%\frac{T}{100}\%\right) \tag{III.8}$$

The UV-visible spectrophotometer is also used to determine the nature of the optical transitions for pp–GT. The optical absorption coefficient data are obtained from UV–Vis spectroscopy measurements. The optical absorption dependence of photon energy is expressed by the following relationship [17]:

$$\alpha h\nu = A(h\nu - E_g)^m \tag{III.9}$$

where A is an energy-independent constant, E_g is the optical band gap and m is a constant which is connected to the density-of-states distribution in the transport gap in the band tails and thus determines the type of transition (m = 1/2 and 3/2 for direct allowed and forbidden transitions, respectively, m = 2 and 3 for indirect allowed and forbidden transitions, respectively) [17].

The optical absorption coefficient data obtained from UV–Vis spectroscopy measurements are converted to a Tauc plot using a MATLAB program. In that curve, a value of m is employed that provides the most linear plot, indicating the suitable optical transition.

III.2.4 ATOMIC FORCE MICROSCOPY (AFM)

Atomic force microscopy (AFM), in which a sharp probe is employed for profiling surfaces has developed into an invaluable multi-disciplinary technique for advanced characterization of plasma polymer materials [18]. It was used in this research work because it can provide three-dimensional high-resolution images of the surface ultrastructure with molecular resolution, in real time, under physiological conditions, and with minimal sample preparation.

The primary modes of operation are contact and dynamic mode. Because the measurement of the contact mode is prone to noise and drift, low stiffness cantilevers are used. However, a drawback of contact mode AFM is the destruction of fragile objects on the sample. This can be avoided by using the tapping mode, whereby the cantilever is vibrated at its resonance frequency. Tip-sample interaction forces modify the oscillation amplitude, phase, and resonance frequency; these changes in oscillation with respect to the external reference oscillation provide information about the sample's characteristics [19].

AFM measurements can be made on almost all surfaces, conducting, non-conducting, organic, and inorganic surfaces. Single-molecular elongation of polymer chains can also be observed using this technique [20]. In this work, the surface morphology and roughness of the pp–GT films were studied using AFM at ambient pressure and room temperature. The topographic images were obtained in the tapping mode.

III.2.4.1 NANOINDENTATION

For more than a century, researchers have acknowledged that surface contacts between materials are highly dependent on their mechanical properties [21]. To measure these properties from a contact of known geometry, many different indentation tests have been developed in the past two decades. However, due to the development of new sensors and actuators instrumented indentation, also known as depth-sensing indentation or nanoindentation, is now increasingly being used to probe the mechanical response of materials from metals and ceramics to polymeric materials [22]. The additional levels of control, sensitivity, and data acquisition offered by this technique have resulted the measurement of hardness and elastic modulus [23] of materials of interest very easy [22]. This technique was used in this research work to investigate the mechanical properties of pp–GT deposited under different RF power conditions. The elastic modulus and hardness were calculated from the elastic contact stiffness (*s*).

III.2.5 FOURIER TRANSFORM INFRARED (FTIR) SPECTROSCOPY

Infrared spectroscopy is the study of the interaction of infrared light with matter. It is used for material characterization because of the fact that the chemical bonds in a material have specific frequencies at which they vibrate corresponding to their energy levels. The shape of the molecular potential energy surfaces, the masses of the atoms and eventually by the associated vibronic coupling, determines the resonance or vibrational frequencies. From these vibrational frequencies, chemical bonds in the material can be determined.

The chemical composition of pp–GT thin films was characterized using FTIR in this thesis. The advantages of this mode are the high signal-to-noise ratios, i.e. the spectrum quality, and the universality.

III.2.6 CONTACT ANGLE (CA) GONIOMETRY

The CA of liquids on solids are widely used to predict wetting and adhesion properties of these solids by calculating their solid–vapor surface tension [24, 25]. The hydrophobicity/ hydrophilicity of a solid surface is usually expressed in terms of wettability that can be quantified by CA measurements.

CA measurement is a simple and convenient method to determine the surface wettability. CAs are not only influenced by the interfacial tensions but also by other phenomena, i.e. roughness, chemical heterogeneity, sorption layers, molecular orientation, swelling, and partial solution of the polymer or low-molecular constituents in the polymeric material [26]. There are two kinds of techniques to measure contact angle, i.e., static and dynamic. Both the methods were used in the present work to characterize pp–GT thin films using the sessile drop technique.

III.2.7 X–RAY PHOTOELECTRON SPECTROSCOPY (XPS)

XPS is an ideal technique used for surface analysis and it possess the following attributes: quantitative atomic identification, chemical sensitivity, sampling depth variability from about 0.2 to 10 nm depending on the material, and it is insensitive to surface roughness [27]. This technique, also known as Electrochemical Spectroscopy for Chemical Analysis (ESCA), involves the irradiation of a sample in a vacuum with soft X-rays and the energy analysis of photo–emitted electrons which are generated close to the sample surface. The interaction between the X-ray photon and an inner-shell electron causes a complete transfer of the photon energy to an electron. This electron then has enough energy to leave the atom and escape from the surface (photoelectron) [28]. The binding energy E_b of the inner-shell electron can be calculated from the difference between the known X-ray photon energy hv, and the kinetic energy E_k of the photoelectron, which is measured by an electron energy analyzer:

$$\mathrm{E_b} = \mathrm{hv} - \mathrm{E_k} \tag{III.10}$$

In order for electrons to reach the analyzer without being scattered by residual gas molecules, an ultra high vacuum (1.33×10^{-9} mbar) is used [29]. The electron energy analyzer measures the binding energy (BE) of a particular shell of an atom, which is then plotted as intensity (counts/second) *vs*. binding energy, known as the XPS spectrum. In this work, the chemical surface composition of the pp–GT thin films fabricated at different RF power levels was investigated by XPS.

III.2.8 ELECTRICAL CHARACTERIZATION

Electrical characterization of a material requires determination of some fundamental properties, *i.e.*, its electrical resistivity, complex dielectric function etc. From a physical perspective, understanding the material's charge transport properties may assist in optimizations in future work. In this thesis, the electrical properties of pp–GT thin films were divided into two frequency regimes; the dc and ac frequency regions, each associated with a different measurement and analysis technique. Here, ac is defined as any applied signal with a frequency of greater than 0 Hz and less than 1 MHz, frequencies between 1 MHz and 1 GHz are considered RF (though not explicitly considered here). In the dc region, current density *vs*. voltage (J–V) curves were used to determine the material resistivity, dielectric strength, and low frequency dielectric constant and charge transport mechanism. Impedance spectroscopy (IS) measurements were used in the ac region to determine the dielectric function of the material as well as its ac resistivity characteristics.

A material's conductivity is determined through analysis of its characteristic *J–V* curves. As well as this, the mechanism of charge transport through the material can be understood, and from this the material's dielectric constant and/or carrier mobility found. These properties are all necessary to understand the material's usefulness as an insulating layer; the expected leakage current density through the material at an applied voltage and the limits of its operating range must be known so that proper design can be performed.

Subsequent to the presentation and analysis of the dc properties, the results of IS measurements in the ac region are given. IS measures the impedance of a device across a range of frequencies, from which other parameters such as capacitance, loss and quality factor (Q) are derived. Combining these measurements with the device geometry, the complex dielectric function of the insulating layer was derived. The real part of the complex dielectric function gives the relative permittivity or dielectric constant (*k*) of the material and describes how a material stores charge under an applied electric field. This property determines the capacitive behavior of the material and allows the classification of the material as low-, moderate- or high-*k*. The imaginary part of the complex dielectric function gives information about a material's dielectric losses. These losses may be induced by conduction losses in the material as well as relaxation losses and resonance effects [213-215].

Permittivity is a frequency dependent property and it is important to know the range over which it can be expected to vary. Some materials may display high-*k* characteristics in one frequency region and low-*k* characteristics in another, while others may maintain a relatively constant value of permittivity across the entire frequency spectrum. Knowledge of the complex permittivity over as wide of a frequency range as possible is therefore important in electronic applications of a material.

In this work, the electrical properties of pp–GT thin films are investigated. The results were then used as the basis of further investigations into the dependence of these properties on deposition conditions, applied field, frequency and temperature. These results provide a means of optimizing the deposition conditions for application specific outcomes. Interpretation of this data also provided a deeper understanding of the material’s structure through analysis of temperature dependent dielectric relaxation features. Furthermore, the results presented were used to further examine potential application as encapsulating material for electronic devices.

III.2.9 STABILITY STUDY

Organic polymer thin films deposited by means of plasma polymerization hold the prospects of combining advantageous properties of the precursor, with the attractive features offered by plasma polymerized thin films, such as high adhesion to substrate and surface uniformity, and have been discussed by many authors [24, 30-32]. The practical implementation of plasma polymer materials will be influenced by the extent to which a polymer film's properties deteriorate or change under ambient environment or when subjected to extreme environmental conditions, such as annealing [30]. High material stability is essential for applications where the original properties are to be maintained during the intended lifetime of the device. On the other hand, a low point of thermal decomposition and low retention rate are a critical characteristic for encapsulating materials, which are used for OPV devices.

In this work, the stability and thermal degradation of polymer thin films derived from organic γ-terpinene monomer is examined. The effect of deposition RF power on the stability of the polymer films is scrutinized. Photo–degradation study is also carried out through UV/visible exposure using solar simulator with intention to use these films in OPVs, especially as encapsulation coatings and insulating layers in flexible electronics.

III.3 CONCLUSION

In this chapter, a methodology to meet the identified research objectives of the project has been detailed. Materials and methods used to fabricate pp–GT thin films and metals were provided in this chapter. The methodology section provides an outline for the measurements performed, the results they provided, and the way in which they satisfied the project goals. In addition, this methodology addressed the issue of consistency in deposition, measurement and analysis and details the steps taken to ensure accurate and reproducible fabrication of samples.

REFERENCES

[1] D. S. Wuu, W. C. Lo, C. C. Chiang, H. B. Lin, L. S. Chang, R. H. Horng, C. L. Huang, and Y. J. Gao, "Plasma-deposited silicon oxide barrier films on polyethersulfone substrates: temperature and thickness effects," *Surface and Coatings Technology,* vol. 197, pp. 253-259, 2005.

[2] A. P. Ghosh, L. J. Gerenser, C. M. Jarman, and J. E. Fornalik, "Thin-film encapsulation of organic light-emitting devices," *Applied Physics Letters,* vol. 86, pp. -, 2005.

[3] H. Yasuda, "Plasma Polymerization," *Academic Press, New York,* 1985.

[4] M. Strobel, C. Dunatov, J. M. Strobel, C. S. Lyons, S. J. Perron, and M. C. Morgen, "Low-molecular-weight materials on corona-treated polypropylene," *Journal of Adhesion Science and Technology,* vol. 3, pp. 321-335, 1989/01/01 1989.

[5] R. A. Pethrick, "Polymer surface modification and characterization, edited by Chi-Ming Chan. Carl Hanser Verlag, Munich, Vienna, New York, *Polymer International,* vol. 37, pp. 84-84, 1995.

[6] H. Biederman and D. Slavinska, "Plasma polymer films and their future prospects," *Surface and Coatings Technology,* vol. 125, pp. 371-376, 2000.

[7] A. Hiratsuka and I. Karube, "Plasma polymerized films for sensor devices," *Electroanalysis,* vol. 12, pp. 695-702, 2000.

[8] H. Yasuda, "Plasma polymerization for protective coatings and composite membranes," *Journal of Membrane Science,* vol. 18, pp. 273-284, 1984.

[9] L. Prager, U. Helmstedt, H. Herrnberger, O. Kahle, F. Kita, M. Münch, A. Pender, A. Prager, J. W. Gerlach, and M. Stasiak, "Photochemical approach to high-barrier films for the encapsulation of flexible laminary electronic devices," *Thin Solid Films,* vol. 570, Part A, pp. 87-95, 2014.

[10] K. S. Siow, L. Britcher, S. Kumar, and H. J. Griesser, "Plasma Methods for the Generation of Chemically Reactive Surfaces for Biomolecule Immobilization and Cell Colonization - A Review," *Plasma Processes and Polymers,* vol. 3, pp. 392-418, 2006.

[11] L. J. Anderson and M. V. Jacob, "Effect of RF power on the optical and morphological properties of RF plasma polymerised linalyl acetate thin films," *Applied Surface Science,* vol. 256, pp. 3293-3298, 2010.

[12] Y. Liu, C. Jia, Z. Wan, X. Weng, J. Xie, and L. Deng, "Electrochemical and electrochromic properties of novel nanoporous NiO/V_2O_5 hybrid film," *Solar Energy Materials and Solar Cells,* vol. 132, pp. 467-475, 2015.

[13] J. D. Whittle, R. D. Short, D. A. Steele, J. W. Bradley, P. M. Bryant, F. Jan, H. Biederman, A. A. Serov, A. Choukurov, A. L. Hook, W. A. Ciridon, G. Ceccone, D. Hegemann, E. Körner, and A. Michelmore, "Variability in Plasma Polymerization Processes – An International Round-Robin Study," *Plasma Processes and Polymers,* vol. 10, pp. 767-778, 2013.

[14] A. Michelmore, D. A. Steele, J. D. Whittle, J. W. Bradley, and R. D. Short, "Nanoscale deposition of chemically functionalised films via plasma polymerisation," *RSC Advances,* vol. 3, pp. 13540-13557, 2013.

[15] J. A. W. Co. Guide to Using WVASE32.

[16] H. Fujiwara, *Spectroscopic Ellipsometry: Principles and Applications*. Chicester: John Wiley and Sons Ltd, 2007.

[17] Z. Z. You and G. J. Hua, "Refractive index, optical bandgap and oscillator parameters of organic films deposited by vacuum evaporation technique," *Vacuum,* vol. 83, pp. 984-988, 2009.

[18] G. Binnig, C. F. Quate, and C. Gerber, "Atomic Force Microscope," *Physical Review Letters,* vol. 56, pp. 930-933, 1986.

[19] P. Hinterdorfer and Y. F. Dufrene, "Detection and localization of single molecular recognition events using atomic force microscopy," *Nat Meth,* vol. 3, pp. 347-355, 2006.

[20] T. Mori, A. Hirose, T. Hagiwara, M. Ohtsuka, Y. Kakuta, K. Kimata, and Y. Okahata, "Single-Molecular Enzymatic Elongation of Hyaluronan Polymers Visualized by High-Speed Atomic Force Microscopy," *Journal of the American Chemical Society,* vol. 134, pp. 20254-20257, 2012/12/19 2012.

[21] K. L. Johnson, *Contact Mechanics*, 1st ed. ed. Cambridge: Cambridge University Press, 1985.

[22] C. A. Schuh, "Nanoindentation studies of materials," *Materials Today,* vol. 9, pp. 32-40, 2006.

[23] W. C. Oliver and G. M. Pharr, "An improved technique for determining hardness and elastic modulus using load and displacement sensing indentation experiments," *Journal of Materials Research,* vol. 7, pp. 1564-1583, 1992.

[24] J. Ahmad, K. Bazaka, M. Oelgemöller, and M. V. Jacob, "Wetting, solubility and chemical characteristics of plasma polymerized 1-isopropyl-4-methyl-1,4-cyclohexadiene thin films," *Coatings,* vol. 4, pp. 527-552, 2014

[25] Y. Yuan and T. R. Lee, "Contact Angle and Wetting Properties," in *Surface Science Techniques*. vol. 51, G. Bracco and B. Holst, Eds., ed: Springer Berlin Heidelberg, 2013, pp. 3-34.

[26] P. Atkins and Paula, J. de, *Physical Chemistry*, 7th ed. ed. UK: Oxford University Press, 2001.

[27] D. Briggs, *Surface Analysis of Polymers by XPS and Static SIMS* Cambridge: Cambridge University Press, 1998.

[28] M. R. Alexander, R. D. Short, F. R. Jones, M. Stollenwerk, J. Zabold, and W. Michaeli, "An X-ray photoelectron spectroscopic investigation into the chemical structure of deposits formed from hexamethyldisiloxane/ oxygen plasmas," *Journal of Materials Science,* vol. 31, pp. 1879-1885, 1996.

[29] J. F. Watts and J. Wolstenholme, *An Introduction to Surface Analysis by XPS and AES*. West Sussex, England: Wiley & Sons, 2003.

[30] K. Bazaka and M. V. Jacob, "Post-deposition ageing reactions of plasma derived polyterpenol thin films," *Polymer Degradation and Stability,* vol. 95, pp. 1123-1128, 2010.

[31] L. Anderson, C. Easton, and M. Jacob, "Compatibility of plasma-deposited linalyl acetate thin films with organic electronic device fabrication techniques," *Journal of Materials Science,* vol. 48, pp. 4851-4859, 2013.

[32] M. Berggren and A. Richter-Dahlfors, "Organic bioelectronics," *Advanced Materials,* vol. 19, pp. 3201-3213, 2007.

CHAPTER IV

ELEMENTAL DISTRIBUTION WITH MASS SPECTROSCOPY

Understanding the polymerization mechanism of a precursor is indispensable to enhance the requisite material properties. In-situ mass spectroscopy is used in this study to understand the RF plasma polymerization of γ-terpinene at different RF powers. The results reported in this chapter enables to comprehend the relationship between the degree of incorporation of oxygen and the rate of deposition with the input RF power. The outcomes of these studies are reported in *Ahmad, J., Bazaka, K., Whittle, J., Michelmore, A. and Jacob, M. V. (2014) Structural Characterization of γ-Terpinene Thin Films Using Mass Spectroscopy and X-ray Photoelectron Spectroscopy. Plasma Processes and Polymers. doi: 10.1002/ppap. 201400220.*

STRUCTURAL CHARACTERIZATION OF γ-TERPINENE THIN FILMS USING MASS SPECTROSCOPY

Plasma Polymer thin films have the capability to provide a diverse range of optical, physical, mechanical and surface properties [1-6] suitable for applications in many areas such as biomaterials [7], electronics [8], protective coatings [9], and nanotechnology. Plasma polymerization can reform natural products, such as honey, into graphenes [10]. It is also a well-known method for the dry deposition of thin polymeric films [6, 11, 12]. It is also an environmentally friendly method because it is typically solvent-free and self-contained (reducing the problem of waste management and environmental pollution) [13]. The attractiveness of plasma polymerization is its ability to generate ultrathin films with good adhesion to many commonly used substrates and alter certain properties of the films by changing plasma parameters such as monomer flow rate, pressure in the chamber, deposition time and power [9]. These polymer thin films are generally pinhole-free and conformal with the substrate geometry [13]. Their properties are often unique and unobtainable by other polymerization techniques [14]. The films are usually prepared in low-temperature plasmas from a hydrocarbon precursor gas, which is dissociated and ionized in the discharge [15]. Ions and radicals formed in the gas phase impinge on the substrates and lead to film growth [15]. From the industrial perspective, plasma polymerization and plasma processes, in general, are attractive as they are relatively energy and material efficient [13].

During the modification of surface chemistry using plasma thin film deposition process, complex chemical reactions occur under the influence of the monomer, the substrate and the process conditions [16, 17]. Plasma contains a range of species including ions, neutrals, electrons, excited species, and photons [18-20]. Free electrons are produced and heated by the application of RF power. The ability of electrons to break bonds that gives rise to radicals, ions and more electrons is of critical importance to the ignition and maintenance of the plasma. The electron energy required for dissociation of chemical species is usually around 3–5 eV, and the ionization energy is of the order of 10 eV [20]. For plasmas of organic monomers, fragmentation of the monomer takes place during these dissociation collisions and low molecular weight species are formed. Radicals (neutral species) remain at or near ambient temperature due to the fact that they do not gain energy from the applied RF power. However, they are highly reactive and higher energy collisions with electrons can result in some kinetic energy being transferred from the electron to the neutral molecule [21]. An electron in the molecule therefore gets excited to a higher energy orbit. Excited molecules are inherently unstable, and the electron will quickly fall back to its initial (ground) state in either one or more transition steps accompanied by emission of photons [20]. The atomic and molecular surface constituents emission is also observed as neutral particles or as positive or negative secondary ions [22]. High-energy collisions between electrons and molecules usually create ions that result in ionization of the molecules and liberation of secondary electrons. Once the various species mentioned above have been initiated in the plasma, reactions may take place between these species. The reactions involving ions occur in the plasma phase, leading to molecular rearrangements that manifest themselves in the plasma polymer formed on a surface [20]. However, despite widespread uses and the vast body of literature related to the chemical composition during plasma polymerization [23, 24], a comprehensive description of the state of the plasma is difficult and requires a great deal of information [25]. The mechanisms involved also raise the question of where the polymer forms: in the plasma or at the plasma/polymer interface, or a combination of both.

Over the last decade, our group investigated plasma-assisted fabrication of functional thin solid films for naturally occurring aromatic hydrocarbons, specifically essential oils and their individual constituents. These films display a range of attractive optical, electrical, and biological properties and can be used as an environmentally friendly alternative to materials derived from synthetic sources in electronics and biomedical applications. The properties vary as a function of precursor chemical structure and deposition conditions, in particular RF power. In this chapter, we investigate the link between deposition mechanism and physical properties of the film fabricated from one such essential oil-derived hydrocarbon under different RF power regimes. The test precursor γ-terpinene, also known as 1-isopropyl-4-methyl-1,4-cyclohexadiene, is an isomeric hydrocarbon isolated directly from *Melaleuca alternifolia* and several other essential oils by means of distillation [26-28]. This chapter primarily aims to assess the role of ions in plasma polymerization of γ-terpinene. Ion flux is measured as a function of input power. Ion energy, neutral and positive ion mass spectra and film deposition rate are simultaneously monitored.

IV.1 EXPERIMENTAL

IV.1.1 PLASMA SYSTEM

The pp–GT thin film samples were fabricated on silicon wafer inside the plasma chamber at 10, 25 and 50 W RF power. The chamber consisted of a 0.25 m steel cylinder with an internal diameter of 0.3 m. Silicon wafer substrates were cleaned with ethanol and acetone, and then dried under a stream of dry nitrogen. The substrates were then placed in the centre of the bottom (ground) electrode. The chamber was evacuated to a base pressure of $<2 \times 10^{-2}$ Pa. RF power at 13.56 MHz was applied to an internal electrode of 0.28 m diameter via a coaxial power supply (RFG050-13) with a matching network (AMN 150R). The ion flux to the RF electrode was measured using an Impedans OctIV ion flux probe (Impedans, Dublin) placed in series between the matching network and the RF electrode. The deposition rate was determined using a Sycon Instruments (USA) Quartz Crystal Microbalance (QCM) using a 6 MHz gold crystal with a diameter of 7 mm placed in the center of the bottom electrode. The thickness of selected samples was measured by NT-MDT NTEGRA Atomic Force Microscope (AFM) operating in semi-contact (tapping) mode, using (NSG03, NT-MDT) cantilevers with a spring constant of 11 N/m, tip radius of curvature of 10 nm, aspect ratio of 10:1 and resonance frequency of 150 KHz. After deposition of the film, the surface was scratched with a scalpel blade, and the thickness of the film measured by scanning a 50 × 50 μm image of the scratch at 1 Hz. The film thickness was then taken as the average of 5 points along the scratch.

IV.1.2 PLASMA MASS SPECTRA

Hiden Analytical Ltd. EQP 1000 quadrupole mass spectrometer was operated in residual gas analysis (RGA) and positive ion mode to acquire spectra. Sampling took place via a grounded 100 μm entrance orifice through which the system is differentially pumped using a turbomolecular pump to keep the internal pressure below 8×10^{-4} Pa during acquisition. The spectrometer was tuned at an m/z equal to the protonated monomer. All spectra were normalized for instrument transmission by assuming the intensity of the peaks was proportional to 1/m, as advised by the manufacturer. The ion energy distribution at various RF powers was also measured for the protonated monomer.

IV.2 RESULTS AND DISCUSSION

IV.2.1 DEPOSITION RATE AND ION FLUX

Table IV.1. Comparison of total mass deposition rates γ-terpinene plasmas

Power (W)	P/Φ	Mass deposition rate ($\mu g m^{-2} s^{-1}$)
5	1.32	12.83
10	2.63	19.2
25	6.58	39.52
50	13.16	68

The P/Φ (power/flow rate) ratio is widely quoted as the most important parameter while describing the plasma [24]. Within narrow limits, it is reasonable to assume that plasma polymers fabricated at the same P/Φ, but using different P and Φ values will be the same [29]. In this study, obtaining identical values of P/Φ when measuring the ion flux and mass deposition rates and acquiring the mass spectra was not possible. However, close values were obtained and these data are presented in Table IV.1.

The mass deposition rate of γ-terpinene from the plasma was determined by in situ monitoring using a QCM. The deposition rate as a function of RF power is shown in Figure IV.1. This technique showed an almost linear increase of the deposition rate with plasma power (Figure IV.1). This is commonly observed for other monomer systems too [30, 31]. The linearity demonstrates the stability of the plasma and of the deposition process.

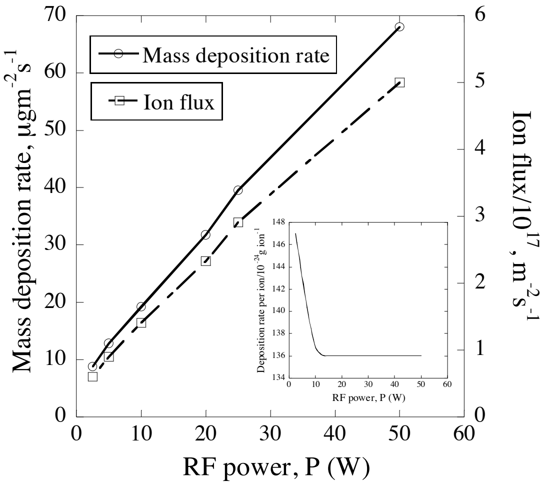

Figure IV.1. Mass deposition rate, ion flux and deposition rate per ion from plasma of γ-terpinene *vs.* plasma power, *P*

The mass deposition rate data in Figure IV.1 can be compared with the calculated ion mass fluxes. For a collision less sheath, the ion flux is usually given by [32]:

$$\Gamma_i = 0.61 n_i \sqrt{\frac{kT_e}{m}} \qquad \text{(IV.1)}$$

where n_i is the ion density, k is Boltzmann's constant, T_e is the electron temperature, and m is the ion mass, so the ion flux is proportional to the ion density and electron temperature. Figure IV.1 also shows the power dependence of ion flux. The ion flux at 10W RF power is estimated to be 1.41×10^{17} m^{-2}s^{-1} and this increases linearly with RF power.

The deposition rate per ion was obtained by division of the deposition rate by the ion flux. However, a crude linear extrapolation, assuming zero ion flux at P = 0W, was employed, as the experimental configuration employed to record the ion flux did not allow measurements to be recorded below 1W. Deposition rate per ion *vs*. plasma power is depicted in the inset of Figure IV.1. It shows that, as P increases, the deposition rate per ion decreases rapidly over the interval (P = 1–10 W). At the end of this interval, the deposition rate per ion is comparable to what we would expect if the deposition were entirely accounted for by the monomeric ion (1.36×10^{-22} g/ monomer ion). Figure IV.1 illustrates the point that at $P < 10$W, there is insufficient ion mass flux to account for all the deposits, even when the increased mass of the average ion is taken into account. The functionalized nature of the low P deposits suggest that monomer structure is retained, a view supported in a study of acrylic acid plasma polymer by Alexander and Duc [33]. This result leads to the suggestion that ions on arrival at the surface promote the grafting of neutral monomer. The trend in Figure IV.1 would then be in part a reflection of the decrease in the concentration of 'intact' monomer (in the plasma) with *power*.

IV.2.2 ION ENERGY

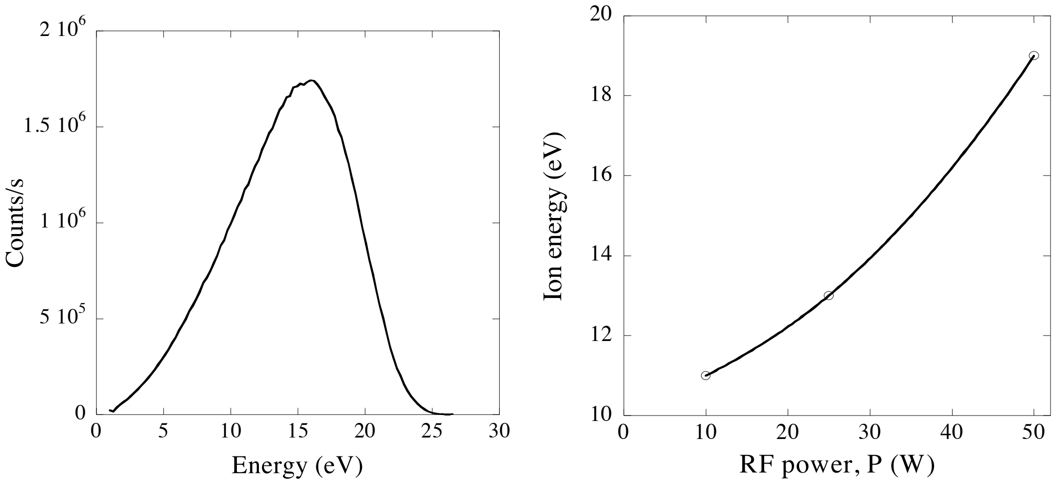

Figure IV.2. Ion energy distribution arriving at a grounded surface in 50W γ-terpinene plasma and the trend in ion energy with RF power, P

Figure IV.2 shows a plot of the ion energy distribution of the *m/z* 136 signal arriving to a grounded surface in 50W γ-terpinene plasma. The Figure shows that the ion energy distribution is centred at ~16eV. The energy distribution is of the expected form, where the "peak" ion energy corresponds to ions accelerated across the plasma pre-sheath and sheath without collision (and hence without any loss of energy) [19].

Figure IV.2 also shows the peak energy of ions arriving at the grounded mass spectrometer orifice at different RF power. By increasing RF power, the ion energy increased from around 15eV at 5W power, to a maximum of 25eV at 50W RF power. These ion energies suggest that sufficient energy is available during ion impact to break chemical bonds and initiate new chemical reactions (typical bond dissociation energies for C—H, C—C, C—O, and O—H bonds are in the range from 3.6 to 4.8 eV).

IV.2.3 MASS SPECTRA

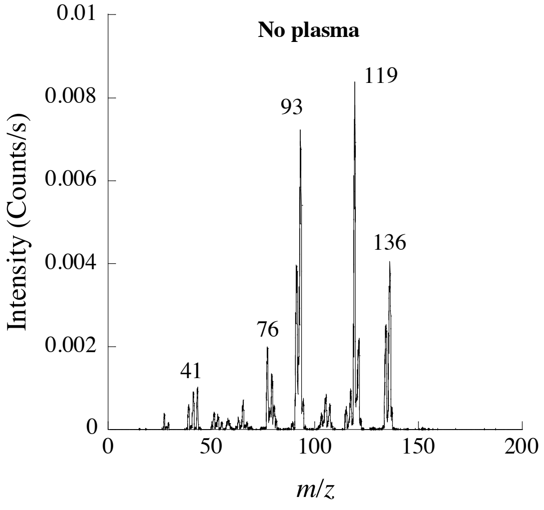

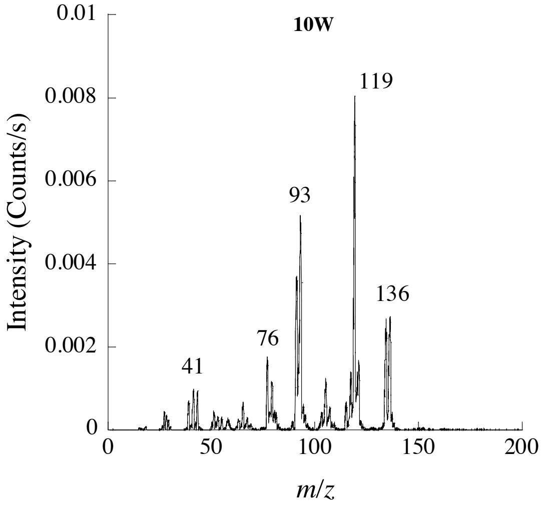

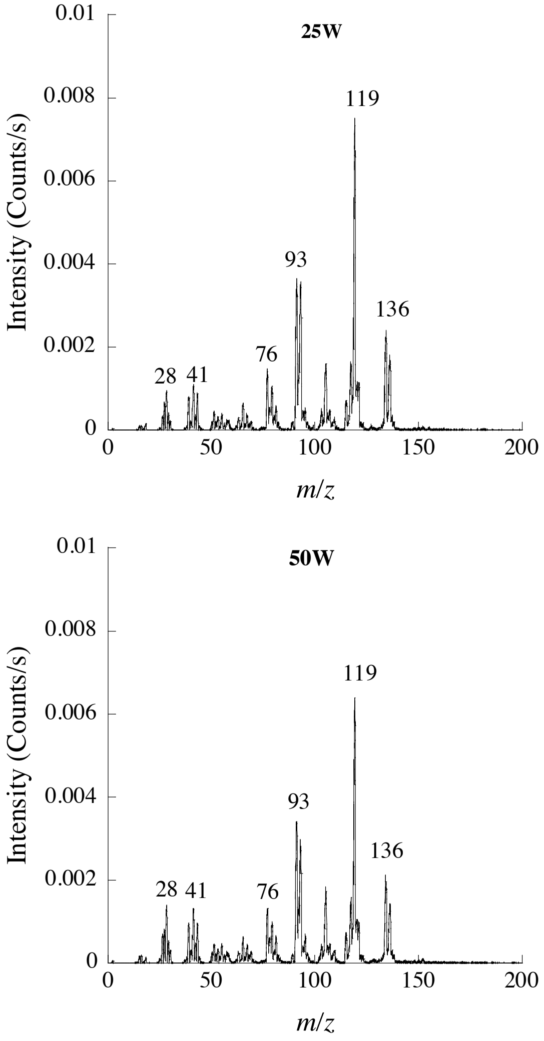

Figure IV.3. Corrected Mass spectra of neutral species at no plasma and different γ-terpinene plasmas

Typical electron impact mass spectra of neutral species of γ-terpinene at 1 Pa (flow rate of 3.8 sccm) and power of 10, 25, and 50 W are shown in Figure IV.3. As advised by the manufacturer of the mass spectrometer, the mass spectra were corrected using $I_{real} = I_{measured} \times m$. Each intensity data point was multiplied by the mass at which it was recorded, and the area beneath the entire spectrum was normalized. In the absence of plasma, the base mass signal is located at 119 m/z (Figure IV.3). However, various lower molecular weight fractions are also detectable. The dominant species (based on peak intensity) in plasma of γ-terpinene correspond to the monomer $[M^{\bullet +}]$ (136 m/z), $C_{10}H_{13}^+$ (133 m/z), $C_9H_{11}^+$ (119 m/z) and $C_7H_9^+$ (93 m/z).

The relative intensities of the neutral species were changed with RF power (Figure IV.3). When plasma is ignited the relative intensity of intact monomer peak (e.g. 136 m/z) and fragment peaks (e.g. 119, 93 m/z) decreases. Same phenomenon has also been observed by Hazrati et. *al*. in case of ethanol [6]. At 10W, the dominant peak in the γ-terpinene mass spectra appears to be at 119 m/z, which corresponds to $C_9H_{11}^+$. The situation does not change at 25 and 50 W whereas for ethanol, the most intense peak changes its appearance from 31 *m/z* to 28 *m/z* (from 2 W to 32 W) [6]. Overall, increasing plasma power leads to reduction of the intensity of the peaks at 136, 133, 119, 93, 91, 78, 76, 64 and 43 m/z and increase in the peaks intensity at 104, 57, 41, 38, 27 and 28 m/z (Figure IV.3). Consistent with published studies on mass spectroscopy characterization of plasma of other monomers there are no significant peaks observed with m/z higher than the mass of the monomer (m/z 136) [30]. Higher mass peaks with very low intensity did appear at higher powers, which are attributed to ablation of polymeric material within the spectrometer [6, 30].

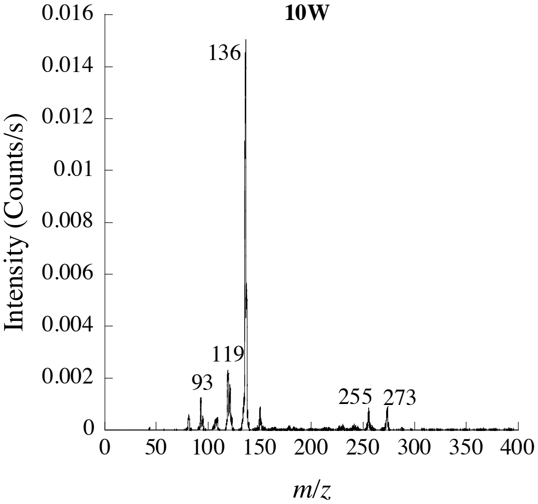

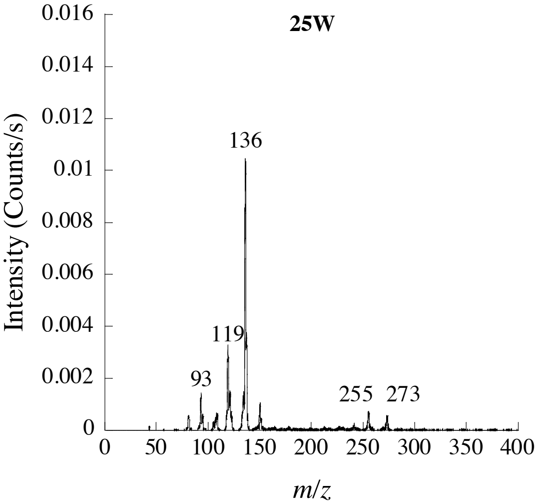

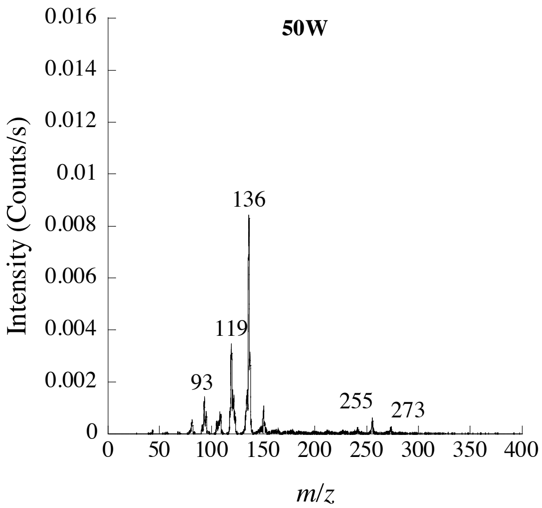

Figure IV.4. Corrected Positive ion mass spectrum of γ-terpinene plasmas

Figure IV.4 shows mass spectra taken in positive ion mode at plasma powers of 10, 25 and 50 W. At each power, the ion optics was retuned to maximize the signal of the molecular ion by acquiring the ion energy distribution, and determining the maximum ion energy intensity (corresponding to ions arriving at the spectrometer orifice without having undergone any collisions). The dominant feature for all plasmas was the peak at *m*/*z* 136, which corresponds to the $M^{\bullet+}$ ($C_{10}H_{16}^{\bullet+}$) ion. The peak at *m*/*z* 273 corresponds to a dimer $[2M+H]^+$, whereas the protonated molecule $[M+H]^+$ at *m*/*z* 137 was also found in the mass spectra. This was accompanied by both higher and lower *m*/*z* species. For example, significant oligomerization was observed by peaks at *m*/*z* 153, 163, 177, 180, 210, 215, 229, 241 and 255, but at lower intensity. Lower *m*/*z* species were observed at *m*/*z* 41, 81, 92, 93, 104, 106, 107, 118 and 121. Given that the data has been conservatively normalized using I_{measured} proportional to $1/m$, it can be seen that the species below *m*/*z* 136 are more important for polymer formation than higher *m*/*z* species. The relative intensity of the peak at *m*/*z* 136 decreased with increase in power but still this peak remained as the dominant feature of the spectra in the power range we investigated. Increasing plasma power also led to the reduction in the intensity of lower molecular weight fractions, which was expected due to the enhanced fragmentation of the monomer at higher power. It is interesting to note that oligomeric peaks corresponding to the dimer $[2M+H]^+$ also decreased with power. No peaks above *m*/*z* 400 were detected under any of the deposition conditions applied in this study.

The base peak at *m*/*z* 119 is formed by the possible elimination of a methanium ion (CH_5^+), in accordance with the preferred fragmentation at a tertiary center. A possible cleavage at quaternary center that may lead to the removal of a methyl radical ($-CH_3$) and the formation of an ion *m/z* 121 of moderate abundance, or to a ring-opening process that will not affect the molecular weight. Such a fission could occur in the following two ways (scheme I or II) since isoprene (C_5H_8) is the basic building unit of γ–terpinene [34].

Scheme I

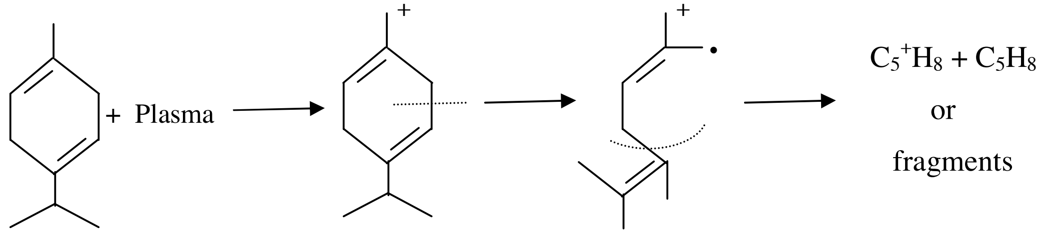

Scheme II

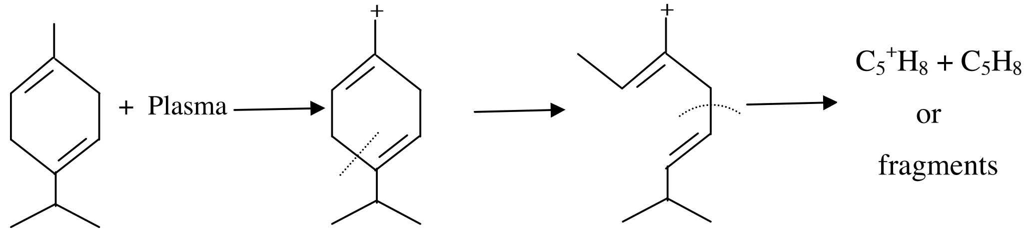

The presence of the series of abundant ion m/z = 41, 39 and 27 can be correlated with the known structure of isoprene. It is to be noted that a preferred center of fragmentation of a molecular ion occurs at a site of chain-branching [34]. Generally, the longer branch is eliminated preferentially. For γ–terpinene, scheme III is to be expected, yielding the ions m/z = 41 and 27.

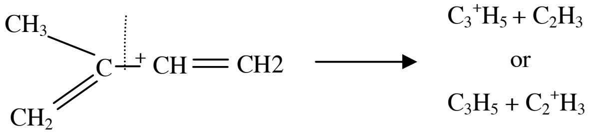

Another base peak for isomers of γ–terpinene at *m/z* = 93 may be produced due to the loss of C_3H_7 (*m/z* = 43) from the intact monomer. The moderate abundance of the ions *m/z* 27 and 29 may be derived by the hydrogen transfer (as a coexistent process) [34] since the carbon-methyl bonds are not allylic to the 1,4 double bonds in the ring.

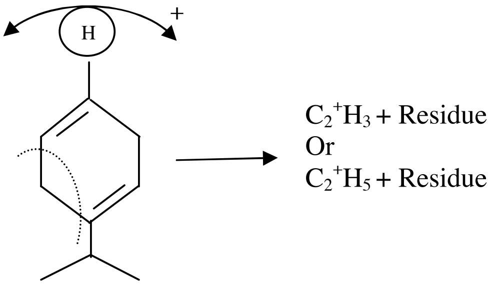

The ion $C_3H_3^+$ (m/z = 39) is considered to be of particular stability since it is found to be a prominent ion in the fragmentation patterns of many compounds [35]. This may be derived either by the loss of two hydrogen atoms, or a hydrogen molecule, from the ion m/z = 41, or by a double hydrogen rearrangement to form the ethyl radical.

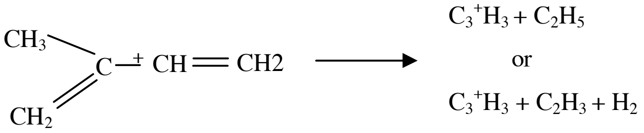

Finally, a further fragmentation at the quaternary center may lead to the elimination of seventeen mass units i.e. a methanium ion (CH_5^+) from isoprene unit and the production of an ion m/z = 51. The remaining ions are not readily explained here. It is possible that they arise from processes involving random rearrangement.

Even though we did not use O_2 as a carrier gas, some oxygen-contaminated peaks were observed such a C_3H_5O (m/z 57), CH_4O_3 (m/z 64), $CH_2(CH_2OH)_2$ (m/z 76) and $C_3H_7O_3$ (m/z 91) in the mass spectra. This may be attributed to a trace amount of oxygen, carbon and hydrogen that is contaminated in the carrier gas, gas lines and surrounding source area within the instrument. Another common contaminant of vacuum systems is the mechanical pump oil that may backstream into the vacuum chamber and causes some oxygen-contaminated peaks [36]. Cleaning parts with solvents is a common approach to remove the contaminant oil. However, organic solvents, such as acetone, are more tenacious contaminant than the oil they are designed to remove. Solvents, therefore, may produce oxygen–contaminated peaks in the mass spectra.

IV.3 CONCLUSION

In this chapter, plasma polymerization of γ–terpinene has been investigated to study the influence of the precursor chemical structure on the process of polymerization. Measurements of the ion flux and mass deposition rates at the surface of pp–GT thin films have been combined with mass spectrometry of the plasma-gas phase and analysis of the film surface by XPS. Mass spectrometry has shown that ionic species play a critical role in the overall plasma process, both in the gas-phase and at the plasma-surface interface. Ion bombardment of the surface contributes to cross linking of deposited polymeric films and can also strongly influence the surface interactions of plasma radicals. The ionic mass transported to the surface is significant (even at low RF powers), so it is likely that similar reactions are taking place at the surface of pp–GT. Active sites in the polymer surface, formed as a result of ion impact followed by grafting of neutral species (including intact monomer), would account for some of the mass deposited. No significant free radical chemistry is therefore found to take place in the gas phase [30]. However, absence of evidence for neutral species of $m/z > 136$ is not evidence of absence; it is possible that some larger species exist, but are unable to survive ionization inside the spectrometer.

On the basis of this study, a comprehensive picture of the plasma polymerization of γ–terpinene is emerging. The ion contribution to the deposit growth appears to be very important over the entire power range. Small proportion of intact monomer, γ–terpinene appears in the system as suggested by the neutral spectrum. The surface chemistry of pp–GT does not show any significant variation over the power range studied. This finding fits well with the observed gas-phase chemistry, but not with the ion energy data. This result could indicate that the increase in ion energies seen over the power range does not have a significant bearing on surface chemistry, which, in turn, would suggest that polyatomic ions with energies below 25–30 eV do not significantly fragment or cause sputtering of surface material.

Mass spectrometry has shown that the degree of cationic oligomerization in the gas phase does not change markedly across the power range studied. The data also showed that the retention of oxygen changes significantly. These findings are of great importance in order to be able to optimize the chemical selectivity of pp–GT thin films as well as their cross-linking degree. This chapter provides for the first time, the details of γ–terpinene fragmentation and oligomerization during plasma deposition, which is an important step in understanding the chemical and physical phenomena occurring during plasma polymerization.

REFERENCES

[1] J. Ahmad, K. Bazaka, L. J. Anderson, R. D. White, and M. V. Jacob, "Materials and methods for encapsulation of OPV: A review," *Renewable and Sustainable Energy Reviews,* vol. 27, pp. 104-117, 2013.

[2] L. Anderson, C. Easton, and M. Jacob, "Compatibility of plasma-deposited linalyl acetate thin films with organic electronic device fabrication techniques," *Journal of Materials Science,* vol. 48, pp. 4851-4859, 2013/07/01 2013.

[3] M. V. Jacob, N. S. Olsen, L. J. Anderson, K. Bazaka, and R. A. Shanks, "Plasma polymerised thin films for flexible electronic applications," *Thin Solid Films,* vol. 546, pp. 167-170, 2013.

[4] J. Hierso, P. Boy, K. Vallé, J. Vulliet, F. Blein, C. Laberty-Robert, and C. Sanchez, "Nanostructured ceria based thin films (≤1 μm) as cathode/electrolyte interfaces," *Journal of Solid State Chemistry,* vol. 197, pp. 113-119, 2013.

[5] M. Jacob and K. Bazaka, "Fabrication of Electronic Materials from Australian Essential Oils," Australian Government: Rural Industries Research and Development Corporation, Report20 Oct 2010 2010.

[6] H. D. Hazrati, J. D. Whittle, and K. Vasilev, "A Mechanistic Study of the Plasma Polymerization of Ethanol," *Plasma Processes and Polymers,* vol. 11, pp. 149-157, 2014.

[7] K. Bazaka, M. V. Jacob, R. J. Crawford, and E. P. Ivanova, "Plasma-assisted surface modification of organic biopolymers to prevent bacterial attachment," *Acta Biomaterialia,* vol. 7, pp. 2015-2028, 2011.

[8] L. Anderson, M. Jacob, M. Barra, F. Di Girolamo, and A. Cassinese, "Effect of a plasma polymerised linalyl acetate dielectric on the optical and morphological properties of an n-type organic semiconductor," *Applied Physics A: Materials Science & Processing,* vol. 105, pp. 95-102, 2011.

[9] J. Ahmad, K. Bazaka, and M. Jacob, "Optical and Surface Characterization of Radio Frequency Plasma Polymerized 1-Isopropyl-4-Methyl-1,4-Cyclohexadiene Thin Films," *Electronics,* vol. 3, pp. 266-281, 2014.

[10] D. H. Seo, A. E. Rider, S. Kumar, L. K. Randeniya, and K. Ostrikov, "Vertical graphene gas- and bio-sensors via catalyst-free, reactive plasma reforming of natural honey," *Carbon,* vol. 60, pp. 221-228, 2013.

[11] J. Friedrich, G. Kühn, R. Mix, and W. Unger, "Formation of plasma polymer layers with functional groups of different type and density at polymer surfaces and their interaction with Al atoms," *Plasma Processes and Polymers,* vol. 1, pp. 28-50, 2004.

[12] K. Ostrikov, E. C. Neyts, and M. Meyyappan, "Plasma nanoscience: from nano-solids in plasmas to nano-plasmas in solids," *Advances in Physics,* vol. 62, pp. 113-224, 2013/04/01 2013.

[13] P. N. Brookes, S. Fraser, R. D. Short, L. Hanley, E. Fuoco, A. Roberts, and S. Hutton, "The effect of ion energy on the chemistry of air-aged polymer films grown from the

hyperthermal polyatomic ion Si_2OMe^{5+}," *Journal of Electron Spectroscopy and Related Phenomena,* vol. 121, pp. 281-297, 2001.

[14] S. Saravanan, C. Joseph Mathai, M. R. Anantharaman, S. Venkatachalam, D. K. Avasthi, and F. Singh, "Photoluminescence studies on RF plasma-polymerized thin films," *Synthetic Metals,* vol. 155, pp. 311-315, 2005.

[15] S. M. Miladinović, V. De Vriendt, S. A. Robotham, F. Maseri, S. Lucas, and C. L. Wilkins, "Laser desorption/ionization fourier transform mass spectrometry of thin films deposited on silicon by plasma polymerization of acetylene," *Journal of the American Society for Mass Spectrometry,* vol. 21, pp. 411-420, 2010.

[16] J. D. Whittle, D. A. Steele, and R. D. Short, "Reconciling the Physical and Chemical Environments of Plasma: A Commentary on “Mechanisms of Plasma Polymerisation – Reviewed from a Chemical Point of View”," *Plasma Processes and Polymers,* vol. 9, pp. 840-843, 2012.

[17] Y. Li, B. W. Muir, C. D. Easton, L. Thomsen, D. R. Nisbet, and J. S. Forsythe, "A study of the initial film growth of PEG-like plasma polymer films via XPS and NEXAFS," *Applied Surface Science,* vol. 288, pp. 288-294, 2014.

[18] D. Barton, A. G. Shard, R. D. Short, and J. W. Bradley, "The Effect of Positive Ion Energy on Plasma Polymerization: A Comparison between Acrylic and Propionic Acids," *The Journal of Physical Chemistry B,* vol. 109, pp. 3207-3211, 2005.

[19] A. J. Beck, S. Candan, R. D. Short, A. Goodyear, and N. S. J. Braithwaite, "The Role of Ions in the Plasma Polymerization of Allylamine," *The Journal of Physical Chemistry B,* vol. 105, pp. 5730-5736, 2001.

[20] A. Michelmore, D. A. Steele, J. D. Whittle, J. W. Bradley, and R. D. Short, "Nanoscale deposition of chemically functionalised films via plasma polymerisation," *RSC Advances,* vol. 3, pp. 13540-13557, 2013.

[21] B. Chapman, *Glow Discharge Processes*. NY: John Wiley & Sons, 1980.

[22] A. Benninghoven, "Chemical Analysis of Inorganic and Organic Surfaces and Thin Films by Static Time-of-Flight Secondary Ion Mass Spectrometry (TOF-SIMS)," *Angewandte Chemie International Edition in English,* vol. 33, pp. 1023-1043, 1994.

[23] H. Yasuda, "Plasma Polymerization," *Academic Press, New York,* 1985.

[24] H. Biederman and Y. Osada, *Plasma Polymerization Processes*: Elsevier Science, 1992.

[25] K. L. Williams, I. T. Martin, and E. R. Fisher, "On the importance of ions and ion-molecule reactions to plasma-surface interface reactions," *Journal of the American Society for Mass Spectrometry,* vol. 13, pp. 518-529, 2002.

[26] S. K. S. Al-Burtamani, M. O. Fatope, R. G. Marwah, A. K. Onifade, and S. H. Al-Saidi, "Chemical composition, antibacterial and antifungal activities of the essential oil of

Haplophyllum tuberculatum from Oman," *Journal of Ethnopharmacology,* vol. 96, pp. 107-112, 2005.

[27] S.-S. Cheng, J.-Y. Liu, Y.-R. Hsui, and S.-T. Chang, "Chemical polymorphism and antifungal activity of essential oils from leaves of different provenances of indigenous cinnamon (Cinnamomum osmophloeum)," *Bioresource Technology,* vol. 97, pp. 306-312, 2006.

[28] E. Breitmaier, "Selected Syntheses of Terpenes," in *Terpenes*, ed: Wiley-VCH Verlag GmbH & Co. KGaA, 2006, pp. 119-159.

[29] S. Candan, A. J. Beck, L. O'Toole, R. D. Short, A. Goodyear, and N. St J. Braithwaite, "The role of ions in the continuous-wave plasma polymerisation of acrylic acid," *Physical Chemistry Chemical Physics,* vol. 1, pp. 3117-3121, 1999.

[30] L. O'Toole and R. D. Short, "An investigation of the mechanisms of plasma polymerisation of allyl alcohol," *Journal of the Chemical Society, Faraday Transactions,* vol. 93, pp. 1141-1145, 1997.

[31] L. Denis, D. Cossement, T. Godfroid, F. Renaux, C. Bittencourt, R. Snyders, and M. Hecq, "Synthesis of Allylamine Plasma Polymer Films: Correlation between Plasma Diagnostic and Film Characteristics," *Plasma Processes and Polymers,* vol. 6, pp. 199-208, 2009.

[32] A. Michelmore, P. Gross-Kosche, S. A. Al-Bataineh, J. D. Whittle, and R. D. Short, "On the Effect of Monomer Chemistry on Growth Mechanisms of Nonfouling PEG-like Plasma Polymers," *Langmuir,* vol. 29, pp. 2595-2601, 2013.

[33] M. R. Alexander and T. M. Duc, "The chemistry of deposits formed from acrylic acid plasmas," *Journal of Materials Chemistry,* vol. 8, pp. 937-943, 1998.

[34] R. I. Reed, "13 - Mass Spectra of Terpenes," in *Mass Spectrometry of Organic Ions*, F. W. McLafferty, Ed., ed: Academic Press, 1963, pp. 637-699.

[35] K. Komatsu and T. Kitagawa, "Cyclopropenylium cations, cyclopropenones, and heteroanaloguess - Recent advances," *Chemical Reviews,* vol. 103, pp. 1371-1427, 2003.

[36] S. R. Systems. (11-March-2015). *Vacuum Diagnosis with an RGA*.

Chapter V

OPTICAL AND SURFACE CHARACTERIZATION

As a part of an electronic device or as an encapsulation coating, the optical, mechanical and morphological properties polymer thin films influence the nature of application, performance and longevity of these materials. These properties of pp–GT thin films fabricated on a range of common substrates at varied deposition power are outlined in this chapter. Film hardness, elasticity, coating adhesion and susceptibility to wear are examined using nanoindentation analysis. Surface architecture is examined in detail using images obtained by means of AFM. The outcomes of these studies are reported in *J. Ahmad, K. Bazaka, and M. Jacob,* "*Optical and Surface Characterization of Radio Frequency Plasma Polymerized 1-isopropyl-4-Methyl-1,4-Cyclohexadiene Thin Films,*" *Electronics, vol. 3, pp. 266-281, 2014.*

OPTICAL AND SURFACE CHARACTERIZATION OF RADIO FREQUENCY PLASMA POLYMERIZED 1-ISOPROPYL-4-METHYL-1,4-CYCLOHEXADIENE THIN FILMS

The latest advances achieved in the field of organic electronics have expanded the scope of applications beyond those attainable with conventional silicon (Si) semiconducting technologies to include flexible photovoltaic (PV) and light-emitting devices, flexible displays, chemical and biological sensors, wearable and implantable electronics, to name a few [1-7]. Among these, organic thin film PV is an emerging economically-competitive PV technology that combines manufacturing adaptability, low-cost processing and a lightweight, flexible device end-product. In spite of the significant advances in OPV, commercial use of this technology remains limited, due to both low power conversion efficiency (PCE) and poor overall stability of the devices. Indeed, even though the highest PCE achieved from organic PV has risen from 2.5% to 11% for bulk heterojunction polymer: fullerene solar cells over the last ten years, it falls short of 25%–30% PCE level offered by established *Si* photovoltaic cells. The lifetime achievable by the most advanced organic solar cells is also far below the 20–25 years lifespan of commercial *Si* photovoltaic cells [8], attributed to relatively low environmental stability of organic photoactive materials.

Most of the research effort to date has concentrated around the photoactive layer, focusing on new, more efficient and stable materials with tailored energy levels and solubility, and a better understanding of the mechanism of photon–to–electron conversion [9]. However, encapsulation with high barrier performance materials has also been recognized as instrumental in significantly improving device lifetime, where device stability is extended by limiting penetration of oxygen and moisture from the environment into device layers [10]. For instance, encapsulation of solar cells based on coating of ZnO layer on top of a photoactive material and subsequent UV resin drop coating resulted in a significant increase in the stability, shelf life of the device, and the cost-effectiveness [11]. Recently synthesized silicon oxide/alumina and parylene layer had an effective water vapor transmission (WVTR) rate of $2.4 \pm 1.5 \times 10^{-5}$ g/m^2/day [12]. However, the requirements for high performance encapsulation materials include good processability, high optical transmission, high dielectric constant, low water absorptivity and permeability, high resistance to ultra-violet (UV) degradation and thermal oxidation, good adhesion, mechanical strength, and chemical inertness [13]. While inorganic barrier layers are often used for their sound durability [14], organic encapsulation materials are attracting attention for their synthetic flexibility and resulting property tunability [15].

Organic thin film materials fabricated from renewable precursors using low-cost deposition methods, such as plasma-assisted nanoassembly, have lower environmental and economic costs [16]. Low-temperature plasma deposition is a highly engineering-friendly, economical method of polymer synthesis, that delivers practically pollutant free surface chemistry, and can be easily integrated into manufacturing processes [17, 18]. The method offers a level of confidence and deposition quality comparable to and in many cases superior to other widely-used techniques, such as thermal chemical vapor deposition, wet chemistry processing, laser assisted microfabrication, *etc*. [19, 20]. Films fabricated using plasma-assisted synthesis are typically smooth, ultrathin and pinhole free, with good spatial uniformity, conformal coverage, and high adhesion to the substrate [21].

Earlier, Jacob and co-workers have successfully used plasma-assisted deposition to fabricate thin films from renewable precursors for application in electronics and biomedical fields, reporting property variability linked to both deposition conditions and the chemistry of the monomer [22-26]. This chapter reports on the plasma-assisted fabrication of new polymer thin films from γ-terpinene, with intention to use these films in OPVs, specifically as encapsulation coatings, and as insulating layers in flexible electronics. Given the proposed application for the plasma polymerized γ-terpinene (pp–GT), the material is studied in terms of optical, surface, mechanical, and adhesion properties as a function of deposition conditions.

V.1 EXPERIMENTAL

Thin film samples were deposited on high quality glass microscope slides inside a custom made, cylindrical RF polymerization chamber, 0.75 m in length with an inner diameter of 0.055 m (approximate volume of 0.018 cm^3). The slides were thoroughly cleaned using extran, an ultrasonic bath of distilled water, and rinsed with isopropanol prior to deposition. Using the procedure outlined in [22], plasma polymer films were fabricated from γ-terpinene monomer (Figure V.1) at various input RF power levels (10, 25, 50 and 75 W) and at an ambient temperature of 20°C. The monomer flow rate was estimated to be 1.57 cm^3/min by employing the procedure outlined by Gengenbach and Griesser [27].

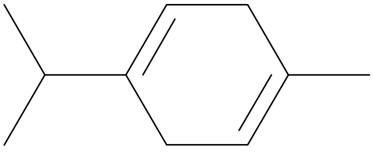

Figure V.1. Chemical structure of 1-isopropyl-4-methyl-1,4-cyclohexadiene ($C_{10}H_{16}$)

Variable angle spectroscopic ellipsometry (VASE) measurements were performed using a J.A. Woollam Co. Inc. model M-2000D variable angle spectroscopic ellipsometer to estimate sample thickness and optical properties of pp–GT thin films. The refractive index n, extinction coefficient k and thickness were derived from the experimental Δ and Ψ data via regression analysis. The relation between n and thickness for the polymer samples has also been investigated. UV-Vis spectroscopy measurements were performed using an Avantes Avaspec 2048 spectroscopy unit with an Avalight-DHc light source to measure the absorbance in the ultraviolet and visible region. From those data, values of optical band gap have been derived. Surface morphology and roughness parameters of pp–GT thin films fabricated under different RF powers were determined from atomic force microscope (AFM) images acquired on a NT-MDT NTEGRA Prima AFM operating in semi-contact mode. A Hysitron Triboscope was used to perform the nanoindentation study. During the nanoindentation study, a Berkovich indenter (70.3° equivalent semi-opening angle) was used and instrument compliance was calibrated using fused silica. Preliminary images of the samples under investigations were collected in order to evaluate the roughness of the area to be indented. Twelve indentations were made on each sample and the results presented are an average of these indentations. Typical loads used in the indentation ranged from 100 μN to 2000 μN with fixed loading time and hold time of between 2 and 5 s.

In the load-partial unload (PUL) experiment, several cycles of loading and unloading were performed in a sequence (Figure V.2). At a constant rate of loading and unloading (100 μN/s), the Berkovich indenter was first loaded and unloaded two times in succession with each of the unloadings terminated at 10% of the maximum load to assure the contact between the pp–GT thin film sample and the indenter. This was performed to examine the reversibility of the deformation and thus ensure that the unloading data used for analysis purposes were mostly elastic [28]. The load was held constant after the second unloading for a fixed period of time at 10% of the peak value while the displacement was carefully monitored to establish the rate of displacement produced by thermal expansion in the system. Following the hold period, the sample was loaded for the last time to allow any final time dependent plastic effects to diminish, with another fixed hold period inserted at peak load and then the specimen was fully unloaded.

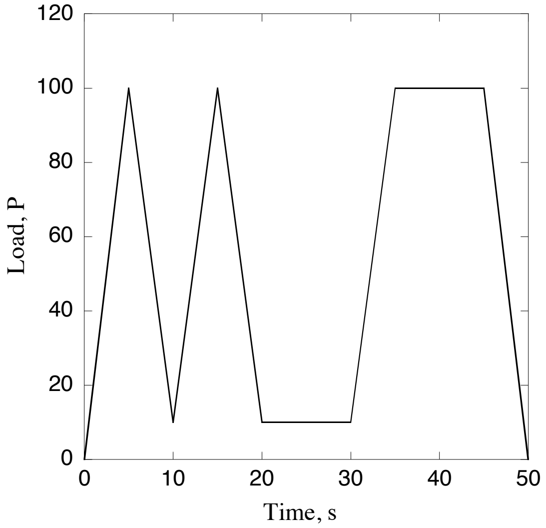

Figure V.2. Typical load–time sequence used for load–partial unloading experiments

After the indentations were performed, stiffness values and the known modulus for quartz were used to calculate the contact area for each indent. Contact parameters and mechanical properties of the pp–GT thin films are derived from the contact area and load-displacement curve as proposed by Oliver and Pharr [28]. The unloading stiffness was determined after polynomial fitting of 90% of the unloading curve.

The cross–hatch test was performed on pp–GT films fabricated at different power levels using the Elcometer 107 kit to obtain a standardized (ASTM D3359) qualitative assessment of the adhesion between the films and the glass substrate. Crosshatch patterns were made on the polymer film surfaces using the cutting tool (6 teeth, 1 mm spacing). The whole area was then brushed to remove debris and adhesive tape was applied on top of the lattice followed by smoothing out the tape with a pencil eraser across the surface. The tape was then removed by pulling at an angle of 180° and the results were analyzed by comparing the lattice of cuts with ISO standards. Three samples were fabricated for each applied RF power, with three crosshatch tests performed on each sample.

V.2 RESULTS AND DISCUSSION

V.2.1 EFFECT OF TIME ON FILM THICKNESS

The dependence of pp–GT thin film thickness on the deposition time was studied on samples fabricated for 2, 5, and 10 min at 25 W RF power along with constant monomer flow rate and pressure. A film thickness of 120 nm was obtained with deposition time of 2 min at 25 W. The sample thickness increased linearly with time, approaching 438 nm for deposition time of 10 min. Similar trend was observed for films fabricated at 10, 50, and 75 W RF power. Film thickness is also found to be linearly increasing with higher RF power. This is due to an increase in the densification of electrons with an increased crosslinking. Same phenomenon has also been observed in case of plasma polymerized terpinen-4-ol and linalyl acetate (PLA) thin films [29, 30]. Assuming constant deposition conditions (pressure, monomer flow rate, distance between electrodes, *etc*.), the desired film thickness of pp–GT thin film for a potential application can therefore be achieved by controlling the time of deposition.

V.2.2 RF POWER DEPENDENCE OF OPTICAL CONSTANTS

The effect of changing the RF power level on the optical constants of pp–GT polymer thin films has been studied using VASE and UV-Vis spectroscopy over the wavelength range of 200–1000 nm. UV-Vis absorption spectrums of samples fabricated at 10, 25, 50, and 75 W RF power level (Figure V.3) reveal that the absorption contour is replicable over the RF power range employed during fabrication. Reallocating of the peak position and/or broadening of the peak is not observed with increase in RF power, unlike other studies [31]. The maximum absorption of pp–GT films fabricated at different RF power levels is found to be at 300 nm. It is believed that the main absorption peak may be the result of pi–pi * transitions. The optical transparency of the polymer films is confirmed by these spectra as the maximum absorption peaks are outside of the visible region of the spectrums. The optical transparency of the pp-GT film can be effectively used in applications such OPV, medical imaging, optical sensor and as an encapsulating (protective) layer for the electronic circuits.

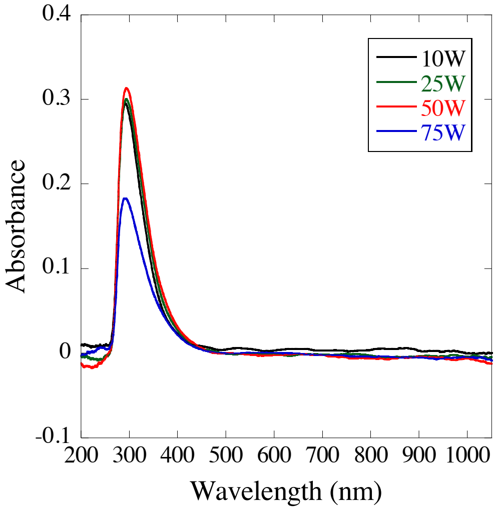

Figure V.3. UV-Vis absorption spectrum of pp–GT thin films

Figure V.4 demonstrates the *n* and *k* profiles of pp–GT thin films fabricated at various power levels. Thickness and surface roughness parameters from cauchy analysis (WVASE software) were used to obtain *n* and *k* profiles. Mean squared error (MSE) values used to assess the quality of the modeling fit were below 3. Considering the profiles, it is observed that the overall shape of the curves was similar across all the samples. At short wavelengths (below 250 nm), a sharp peak in *n* profile was detected. At wavelengths above approximately 250 nm, an increase in RF input power resulted in higher *n* values for the polymer. At 500 nm, the difference in refractive index between 10 and 75 W sample is 0.01, corresponding to a change of less than 1% that is similar to thin films fabricated from linalyl acetate [32].

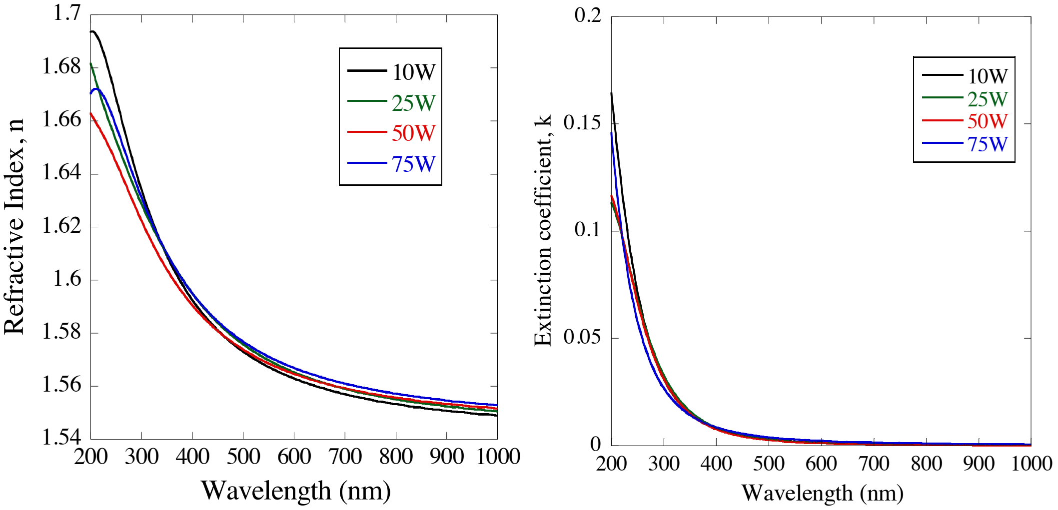

Figure V.4. Refractive indices and extinction coefficient of pp–GT thin films

Based on the refractive index values of pp–GT films, it is anticipated that it can be used as a coating on long-period fiber gratings (LPFGs) to enhance its sensitivity, similar to δ-form syndiotactic polystyrene [33]. According to [34], pp–GT can also be used in advanced optoelectronic fabrications, such as high performance substrates for advanced display devices, optical adhesives or encapsulants for OPV devices, antireflective coatings for advanced optical applications or image sensors [5, 6, 10].

The extinction coefficient (*k*) profiles for pp–GT samples fabricated at various RF power levels illustrate very similar characteristics. These results (optical similarities with glass and transparency in the visible wavelength region) confirm pp–GT thin films as a strong candidate for use as encapsulation coatings in OPV, optical devices, such as LEDs, FETs, and lenses.

Abbe number (v_D), a key parameter for the refractive index dispersion, is of great importance for optical materials used in the visible region. It is also defined as v-number or refractive efficiency or constringency of the material. The Abbe number is given by following equation [35]:

$$V_D = \frac{n_d - 1}{n_F - n'_C} \tag{V.1}$$

where n_d, n_F, and n_C are the refractive indices of the material at the wavelengths of sodium D (587.6 nm), hydrogen F (486.1 nm), and hydrogen C (656.3 nm), respectively [35]. Materials that have a higher Abbe number (v_D) have lower dispersion in the refractive index, whereas highly refractive materials have small Abbe numbers [36, 37]. A polymer having low v_D (<30), is therefore not suitable for use in optics [36].

For pp–GT films, v_D increases from 35.37 to 40.35 (Table V.1) with increase in RF power (10 W to 75 W), which confirms that films fabricated at 75 W have lower dispersion in the refractive index. These results indicate the well-balanced properties and hence the pp–GT polymer thin films are potential candidates for advanced optical applications.

Table V.1. Abbe-numbers for pp–GT thin films.

RF Power (W)	v_D
10	35.37
25	35.18
50	37.80
75	40.35

V.2.3 THICKNESS DEPENDENCE OF OPTICAL CONSTANTS

Thickness dependence study was carried out using spectroscopic ellipsometry data taken for pp–GT thin films fabricated at 25 W with different film thicknesses and the corresponding *n* and *k* profiles. With an increase of thickness over the measured wavelength region, a very small increase of *n* is observed. The shift in *n vs.* thickness is comparable to that found for polyparaxylene films [38], which were deemed to not have significant thickness dependence on *n*. The shifts found in pp–GT thin films are therefore insignificant and thus *n* is not dependent on thickness.

V.2.4 DETERMINATION OF ENERGY GAP

To determine the nature of the optical transitions, the optical absorption study was performed for pp–GT thin films. The optical absorption coefficient data were obtained from UV–Vis spectroscopy measurements. The optical absorption dependence of photon energy is expressed by the following relationship [39]:

$$\alpha h\nu = A(h\nu - E_g)^m \qquad \text{(V.2)}$$

where *A* is an energy-independent constant, E_g is the optical band gap and *m* is a constant, which is connected to the density-of-states distribution in the transport gap in the band tails and thus determines the type of transition (m = 1/2 and 3/2 for direct allowed and forbidden transitions, respectively, m = 2 and 3 for indirect allowed and forbidden transitions, respectively) [39].

The optical absorption coefficient data obtained from UV-Vis spectroscopy measurements were converted to a Tauc plot using a MATLAB program. In that curve, a value of m = 3/2 was employed for all the pp–GT thin films studied, as this value provided the most linear plot, indicating direct forbidden transitions. The indirect process is much slower than the direct transitions as it requires three entities to intersect in order to proceed: an electron, a photon, and a phonon. Materials showing direct transition are therefore much more efficient than materials that show indirect transition. Gallium arsenide (*GaAs*) and other direct band gap materials are used in optical devices, such as LEDs and lasers, whereas *Si* that is an indirect band gap material is not used. This study shows that pp–GT, having direct transition has the potential to be used in different optical devices. The optical band gap values (Table V.2) remained between 3.14 eV and 3.01 eV, falling within the insulating region of E_g. The pp–GT thin films can therefore be used as insulators for the application of flexible coating on electrical apparatus (e.g., printed circuit board, high voltage systems, circuit breakers, *etc*.).

Table V.2. Optical bandgap of pp–GT thin films for m = 3/2.

RF power (W)	E_g (eV)
10	3.14
25	3.08
50	3.07
75	3.01

V.2.5 SURFACE MORPHOLOGY

The surface profile of pp–GT thin films fabricated at various input RF power levels were studied to examine surface defects and roughness The topographical features of the investigated films deposited on glass surfaces are shown in Figure V.5.

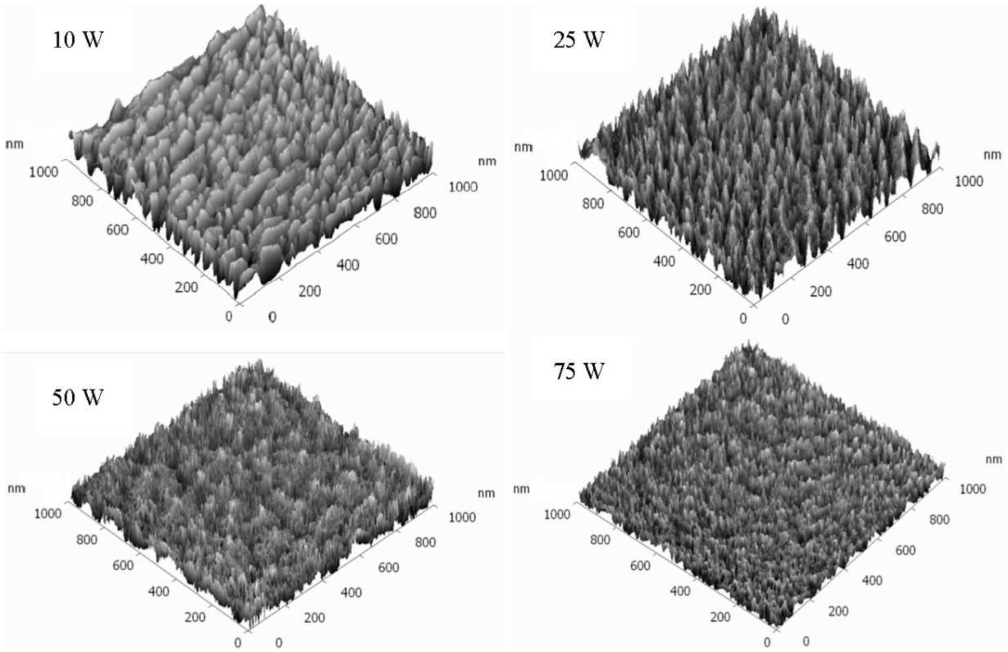

Figure V.5. AFM images of pp–GT thin films fabricated at 10, 25, 50, and 75 W input RF power levels.

From this study, pp–GT thin films are found to be smooth, uniform and defect-free, exhibiting consistent morphology across film samples. Average roughness values for all samples were approximately 0.3 nm. These roughness values were in agreement with the roughness values found by means of spectroscopic ellipsometry. Surfaces with RMS roughness values below 0.5 nm have an insignificant effect on its surface and chemical properties and performance [40]. Considering this and the determined roughness of 0.3 nm, the polymerization reactions are confirmed to take place mostly on the surface of the glass substrate rather than in the gas phase [41].

Beside the conventional roughness parameters R_a and R_q, the statistical parameters, such as R_{sk} (skewness) and R_{kur} (kurtosis), were determined for the pp–GT thin films. R_{kur} is a quantitative measure of the kurtosis, which is defined as the randomness of profile heights that determines whether the data sets are peaked or flat relative to a normal distribution. R_{kur} values can range from 0 to 8. Surfaces with distinct peaks that decline rather rapidly and have heavy tails exhibit high values; whereas rough surfaces with flat top near the mean possess lower values. The pp–GT thin film fabricated at 10 W has lower value of R_{kur} (Table V.3), whereas sharp peaks and heavier tails are found for samples fabricated at higher RF power levels (Figure V.5) that have relatively high values of R_{kur} (Table V.3). A surface skewness (R_{sk}) greater than 0 is observed for pp–GT films, i.e., the predominance of disproportionate number of peak-like surface features. Furthermore, it was observed that the 75 and 50 W samples have smaller and tapered features (narrow curves) while the 25 and 10 W samples have broad curves. Furthermore, decrease in entropy indicates the surface flatness, i.e., reduction of growth of pores at higher RF power levels [42]. Because of this behavior, R_{rms} and R_{a} values decreased with increase of RF power. However, higher deposition rate of pp–GT resulted in an increase in the surface roughness values due to the fact that the particles in the growth region were unable to relax fast enough before the next layer of the film is deposited [43]. These surface analysis results clearly indicate the difference between the peak distributions for pp–GT samples fabricated at different RF power that may affect the wettability. Uniformity of films is also confirmed from the analysis, which indicates the less prone to fracture characteristics of the pp–GT films.

Table V.3. Roughness parameters of pp–GT thin films

Roughness parameters	**10W**	**25W**	**50W**	**75W**
Maximum peak height R_{max} (nm)	4.48	2.38	2.16	2.15
Average roughness R_a (nm)	0.30	0.28	0.25	0.21
Root mean square R_q (nm)	0.39	0.34	0.32	0.30
Surface skewness R_{sk}	0.32	0.22	0.14	0.08
Coefficient of kurtosis R_{kur}	0.06	0.54	0.63	0.77
Entropy	6.12	4.5	3.9	3.56

Surface morphology can also be described in relation to the wetting behavior of the plasma films. Surface roughness generally enhances the hydrophilicity [44]. For pp–GT thin films, the decrease in roughness values with higher deposition power is therefore considered to contribute to the increased hydrophobicity of the surface. Smooth surfaces with greater hydrophobicity are vital for optical and electrical applications, and also for implementing as coating materials for surface protection or buffer layers [45].

V.2.6 NANOINDENTATION

Mechanical properties of pp–GT deposited under different RF power conditions were investigated using a single indentation method and a load-partial unload technique. A series of indentations were made in the films with depths ranging from 221.5 nm to 207.2 nm depending on the thickness of the film. Illustrative single indentation curves from 2 μm thick pp–GT film fabricated at 10 W is presented in Figure V.6.

The load-unload curve (Figure V.6) shows the typical behavior of pp–GT thin films undergoing a nanoindentation test. The initial slope of the unloading process is used to deduce the reduced elastic modulus of the material at the specific contact depth, h_c. There are a number of pop-ins in the curve initially and this phenomenon may be attributed to micro-cracking or dislocation nucleation and/or propagation during loading as have been investigated in a wide variety of materials [46].

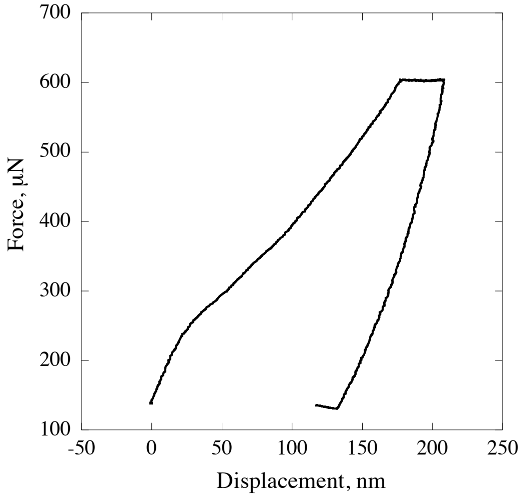

Figure V.6. Load–displacement diagram of pp–GT thin film fabricated at 10 W

The elastic moduli and hardness of different pp–GT thin film samples increased with the increasing RF power as seen from Table V.4. Elastic modulus of pp–GT thin film fabricated at 10 W is 4.22 GPa, while film fabricated at 75 W reaches an elastic modulus of 5.96 GPa. Increase in modulus is also observed with decreasing h_c. This may be due to the transition from spherical contact to conical contact behavior occurred at h_c = indenter radius/4 for the Berkovich indenter used in the study [47]. Data at lower depths should be treated with caution as the contact modulus measured varies considerably with tip radius under spherical contact conditions. Hardness of pp–GT thin films also follows the same trend as elastic modulus. The hardness of the materials increases with increase in input RF power and this can be attributed to the higher crosslinking of the polymers fabricated at higher power levels [22]. These result in an increase in resistance against deformation. Increase of elastic modulus and hardness with increasing RF power has also been reported in other materials such as linalyl acetate [26]. However, it should be noted that several sources of error may exist in these experiments, which may include the relative non-uniformity of the indent (e.g., pile-up and sink-in phenomena) observed on some samples, and difficulties in precise estimation of the indent area (e.g., possible overestimation in the case of pile-up and underestimation due to sink-in features), respective influences of material properties and sample thicknesses and creep [48]. In addition, artifacts and tip effects affecting the precision of the measurement may possibly be imaged due to the usage of same tip for the actual indentation process and imaging. In a nanoindentation test, very often the stress relaxation is observed at the maximum load during unloading process. This is due to the large strain beneath indenter and the large strain rate at this point (since the loading rate is usually finite during the experiment). Moreover, sudden withdraw of indenter causes oscillations in measurement whereas holding at maximum load may lead to uncertainties in the measured quantities [48]. In addition, the initial portion of unloading is more prone to thermal drift than the loading curve. The values presented in Table V.4 are therefore indicative of the evolution of the hardness properties of pp–GT thin films under changing fabrication conditions and may quantitatively differ from the actual material properties due to aforementioned measurement bounds.

Table V.4. Hardness parameters of pp–GT thin films

RF power (W)	Contact depth, h_c (nm)	Hardness, H ± SE (GPa)	Final depth, h_f (nm)	Elastic modulus, E (GPa)
10	221.5	0.40 ± 0.01	137.90	4.22
25	218.3	0.46 ± 0.02	102.53	4.61
50	211.7	0.51 ± 0.02	83.60	4.90
75	207.2	0.58 ± 0.03	69.76	5.96

Loading time and holding time have significant effect on the indentation behavior of pp–GT thin films. To investigate these effects, single indentations were performed on samples deposited at 75 W at constant load of 1000 μN. Figure V.7 shows typical repeat single indentation profiles under increasing indentation load of pp–GT film deposited at 75 W. Hardness value decreased from 0.57 GPa to 0.53 GPa with increasing loading and unloading time with rates (r) ranging from 0.5 to 20 nm/s. As creep deformation taking place during the holding time influences the contact depth at maximum load, the hardness values obtained using these maximum contact depth estimates will also be affected [24]. Moreover, the holding time at maximum load affects the unloading portion of the load displacement curve. In this study, an increase in the hold time showed a decrease in the positive slope value of the material. The relationship of decrease in this slope of unloading in the load-displacement curve and modulus of the pp–GT thin films can be explained by the following equation [49]:

$$S = \frac{\mathrm{dP}}{\mathrm{dh}} = \frac{2}{\sqrt{\pi}} \mathrm{E} * \sqrt{\mathrm{A}} \tag{V.3}$$

The decrease in the slope value means decrease in the *dP/dh* value that leads to a decrease in modulus value. Further increase in hold time increases the indentation depth of the indenter tip on the thin film surface, which leads to increase in contact area of the indenter with the film. The increase in the contact area decreases the hardness of the film. In the case of pp–GT thin films, increasing the hold time from 5 to 25 s at constant load of 500 μN resulted in a decrease in the calculated hardness from 0.59 to 0.53 GPa.

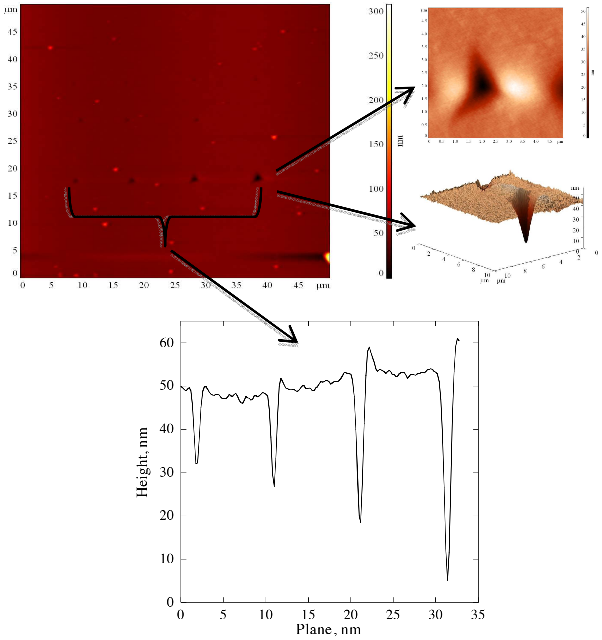

Figure V.7. Typical AFM image of plastic impressions remaining in pp–GT sample fabricated at 75 W after indentation under different load conditions

To extend the capabilities of quasistatic testing to allow depth profiling of pp–GT thin films, the partial unloading (PUL) technique was used. This investigation revealed that at depths below 190 nm (2 μm thick pp–GT film), the depth profile of the hardness follows a trend similar to that determined using the single indentation approach. The hardness of the system gradually increases above approximately 190 nm due to the stress field no longer being contained within the body of the thin film.

V.2.7 ADHESION STUDY

The adhesion behavior of pp–GT thin films deposited on glass is presented in Figure V.8. The adhesion improved with higher deposition power. Films fabricated at 10 W showed 5%–15%

delamination. However, films fabricated at 50 and 75 W showed no delamination effect with a higher cross hatch rating.

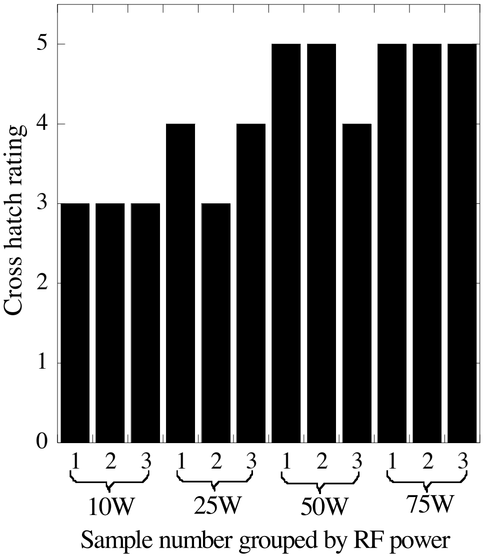

Figure V.8. Adhesion data for pp–GT thin films at 10, 25, 50, and 75 W

The optical image acquired using the microscope and CCD camera for the 10 W sample showed a significant amount of deformation occurred to the sample upon applying and consequent removal of the adhesive tape. For the thin films deposited at 25 W, the areas that were not affected by the tape test appeared uniform and with the increasing of RF power, this uniformity increased. This trend is attributed to the interfacial bonding that is improved by an increase in cross-link density associated with increasing applied RF power. These findings provide an insight into the reliability of the pp–GT films.

V.3 CONCLUSION

In this chapter, the basic optical properties and optical constants of the pp–GT thin films were investigated by means of spectroscopic ellipsometry and UV-Vis spectroscopy. The optical constants such as the refractive index (n), extinction coefficient (k), and optical band gap were determined. The films are confirmed as optically transparent and independent of RF power. The refractive index and extinction coefficient of the pp–GT thin films demonstrated very little dependence on RF power and film thickness. The optical absorption spectra showed that the absorption mechanism is a direct transition. The independence of the refractive index on the RF power level demonstrates the pp–GT thin films as an impending optically stable material for optical applications.

AFM investigation demonstrated that the pp–GT films were smooth, uniform and defect-free. The average roughness parameter decreased with increasing RF power (0.30 for 10 W and 0.21 for 75 W). In the nanoindentation study, combined effects of loading rate and holding time were investigated. For the load rates and hold time considered, pp–GT thin films were found to be a function of both the variables. The unloading portion of the load-displacement curve was found to be strongly dependent on the holding time. The hardness increased from 0.40 GPa for 10 W to 0.58 GPa for 75 W at a load of 700 μN. Elastic modulus of pp–GT thin film fabricated at 10 W was found to be 4.22 GPa, while elastic modulus of 5.96 GPa was found for 75 W film. An adhesion study established that the quality of adhesion is improved for samples fabricated at higher RF power, while the films produced at low RF power adhered poorly to the substrates. These studies demonstrate that the pp–GT polymer is a potential candidate for thin film applications in flexible electronics and OPV that entail smooth and uniform surfaces.

REFERENCES

[1] K. Jung, W.-K. Choi, K. H. Chae, J.-H. Song, S.-J. Yoon, M.-H. Lee, and J.-W. Choi, "Highly conductive and damp heat stable transparent ZnO based thin films for flexible electronics," *Journal of Alloys and Compounds,* vol. 554, pp. 240-245, 2013.

[2] D. P. Dubal and R. Holze, "All-solid-state flexible thin film supercapacitor based on Mn3O4 stacked nanosheets with gel electrolyte," *Energy,* vol. 51, pp. 407-412, March, 2013.

[3] X. Qian, T. Wang, and D. Yan, "Transparent organic thin-film transistors based on high quality polycrystalline rubrene film as active layers," *Organic Electronics,* vol. 14, pp. 1052-1056, 2013.

[4] A. J. Ferguson, J. L. Blackburn, and N. Kopidakis, "Fullerenes and carbon nanotubes as acceptor materials in organic photovoltaics," *Materials Letters,* vol. 90, pp. 115-125, 2013.

[5] F. M. Kelly, L. Meunier, C. Cochrane, and V. Koncar, "Polyaniline: application as solid state electrochromic in a flexible textile display," *Displays,* vol. 34, pp. 1-7, 2013.

[6] H. He, X.-B. Xu, and D.-F. Zhang, "An aligned macro-porous carbon nanotube/waterborne polyurethane sensor for the detection of flowing organic vapors," *Sensors and Actuators B: Chemical,* vol. 176, pp. 940-944, 2013.

[7] V. F. Curto, C. Fay, S. Coyle, R. Byrne, C. O'Toole, C. Barry, S. Hughes, N. Moyna, D. Diamond, and F. Benito-Lopez, "Real-time sweat pH monitoring based on a wearable chemical barcode micro-fluidic platform incorporating ionic liquids," *Sensors and Actuators B: Chemical,* vol. 171–172, pp. 1327-1334, 2012.

[8] F. C. Krebs, "Alternative PV: Large scale organic photovoltaics," *Refocus,* vol. 6, pp. 38-39, 2005.

[9] Y.-W. Su, S.-C. Lan, and K.-H. Wei, "Organic photovoltaics," *Materials Today,* vol. 15, pp. 554-562, 2012.

[10] J. Ahmad, K. Bazaka, L. J. Anderson, R. D. White, and M. V. Jacob, "Materials and methods for encapsulation of OPV: A review," *Renewable and Sustainable Energy Reviews,* vol. 27, pp. 104-117, 2013.

[11] H.-J. Lee, H.-P. Kim, H.-M. Kim, J.-H. Youn, D.-H. Nam, Y.-G. Lee, J.-G. Lee, A. R. b. Mohd Yusoff, and J. Jang, "Solution processed encapsulation for organic photovoltaics," *Solar Energy Materials and Solar Cells,* vol. 111, pp. 97-101, 2013.

[12] N. Kim and S. Graham, "Development of highly flexible and ultra-low permeation rate thin-film barrier structure for organic electronics," *Thin Solid Films,* 2013.

[13] E. Cuddihy, C. Coulbert, A. Gupta, and R. Liang, "Electricity from photovoltaic solar cells: Flat-Plate Solar Array Project final report. Volume VII: Module encapsulation," Jet Propulsion Laboratory, 1986.

[14] N. Kim, "Fabrication and characterization of thin-film encapsulation for organic electronics," PhD Dissertation, Mechanical Engineering, Georgia Institute of Technology, Georgia, 2009.

[15] H. Spanggaard and F. C. Krebs, "A brief history of the development of organic and polymeric photovoltaics," *Solar Energy Materials and Solar Cells,* vol. 83, pp. 125-146, 2004.

[16] S. E. Shaheen, D. S. Ginley, and G. E. Jabbour, "Organic-Based Photovoltaics: Toward Low-Cost Power Generation," *MRS Bulletin,* vol. 30, pp. 10-19, 2005.

[17] S. R. Forrest, "The path to ubiquitous and low-cost organic electronic appliances on plastic," *Nature,* vol. 428, pp. 911-918, 2004.

[18] K. Vasilev, S. S. Griesser, and H. J. Griesser, "Antibacterial Surfaces and Coatings Produced by Plasma Techniques," *Plasma Processes and Polymers,* vol. 8, pp. 1010-1023, 2011.

[19] K. Ostrikov, E. C. Neyts, and M. Meyyappan, "Plasma nanoscience: from nano-solids in plasmas to nano-plasmas in solids," *Advances in Physics,* vol. 62, pp. 113-224, 2013.

[20] A. Michelmore, C. Charles, R. W. Boswell, R. D. Short, and J. D. Whittle, "Defining Plasma Polymerization: New Insight Into What We Should Be Measuring," *ACS Applied Materials & Interfaces,* vol. 5, pp. 5387-5391, 2013.

[21] M. J. Rahman and A. H. Bhuiyan, "Structural and optical properties of plasma polymerized o-methoxyaniline thin films," *Thin Solid Films,* vol. 534, pp. 132-136, 2013.

[22] M. V. Jacob, C. D. Easton, G. S. Woods, and C. C. Berndt, "Fabrication of a novel organic polymer thin film," *Thin Solid Films,* vol. 516, pp. 3884-3887, 2008.

[23] M. V. Jacob, N. S. Olsen, L. Anderson, K. Bazaka, and R. A. Shanks, "Plasma polymerised thin films for flexible electronic applications," *Thin Solid Films,* vol. 546, pp. 167-170.

[24] K. Bazaka and M. V. Jacob, "Nanotribological and nanomechanical properties of plasma-polymerized polyterpenol thin films," *Journal of Materials Research,* vol. 26, pp. 2952-2961, 2011.

[25] K. Bazaka, M. V. Jacob, and B. F. Bowden, "Optical and chemical properties of polyterpenol thin films deposited via plasma-enhanced chemical vapor deposition," *Journal of Materials Research,* vol. 26, pp. 1018-1025, 2011.

[26] Q. F. Xu, J. N. Wang, and K. D. Sanderson, "Organic−Inorganic Composite Nanocoatings with Superhydrophobicity, Good Transparency, and Thermal Stability," *ACS Nano,* vol. 4, pp. 2201-2209, 2010.

[27] M. Berggren and A. Richter-Dahlfors, "Organic bioelectronics," *Advanced Materials,* vol. 19, pp. 3201-3213, 2007.

[28] W. C. Oliver and G. M. Pharr, "An improved technique for determining hardness and elastic modulus using load and displacement sensing indentation experiments," *Journal of Materials Research,* vol. 7, pp. 1564-1583, 1992.

[29] K. Bazaka and M. V. Jacob, "Synthesis of radio frequency plasma polymerized non-synthetic Terpinen-4-ol thin films," *Materials Letters,* vol. 63, pp. 1594-1597, 2009.

[30] L. Anderson, M. Jacob, M. Barra, F. Di Girolamo, and A. Cassinese, "Effect of a plasma polymerised linalyl acetate dielectric on the optical and morphological properties of an n-type organic semiconductor," *Applied Physics A: Materials Science & Processing,* vol. 105, pp. 95-102, 2011.

[31] M. C. Kim, S. H. Cho, J. G. Han, B. Y. Hong, Y. J. Kim, S. H. Yang, and J. H. Boo, "High-rate deposition of plasma polymerized thin films using PECVD method and characterization of their optical properties," *Surface and Coatings Technology,* vol. 169–170, pp. 595-599, 2003.

[32] L. J. Anderson and M. V. Jacob, "Effect of RF power on the optical and morphological properties of RF plasma polymerised linalyl acetate thin films," *Applied Surface Science,* vol. 256, pp. 3293-3298, 2010.

[33] P. Pilla, A. Iadicicco, L. Contessa, S. Campopiano, A. Cutolo, M. Giordano, G. Guerra, and A. Cusano, "Optical chemo-sensor based on long period gratings coated with δ form syndiotactic polystyrene," *Photonics Technology Letters, IEEE,* vol. 17, pp. 1713-1715, 2005.

[34] J.-g. Liu and M. Ueda, "High refractive index polymers: fundamental research and practical applications," *Journal of Materials Chemistry,* vol. 19, pp. 8907-8919, 2009.

[35] J. O. Enlow, H. Jiang, J. T. Grant, K. Eyink, W. Su, and T. J. Bunning, "Plasma polymerized ferrocene films," *Polymer,* vol. 49, pp. 4042-4045, 2008.

[36] T. Okubo†, S. Kohmoto, and M. Yamamoto, "Optical polymer having a high refractive index and high abbe number prepared by radical polymerization using 2,5-BiS(2-Thia-3-Butenyl)-1,4-Dithiane," *Journal of Macromolecular Science, Part A,* vol. 35, pp. 1819-1834, 1998/11/01 1998.

[37] H. Dislich, "Plastics as optical materials," *Angewandte Chemie International Edition in English,* vol. 18, pp. 49-59, 1979.

[38] J. F. Gaynor and S. B. Desu, "Optical properties of polymeric thin films grown by chemical vapor deposition," *Journal of Materials Research,* vol. 11, pp. 236-242, 1996.

[39] Z. Z. You and G. J. Hua, "Refractive index, optical bandgap and oscillator parameters of organic films deposited by vacuum evaporation technique," *Vacuum,* vol. 83, pp. 984-988, 2009.

[40] S. E. Fritz, T. W. Kelley, and C. D. Frisbie, "Effect of dielectric roughness on performance of pentacene TFTs and restoration of performance with a polymeric smoothing layer," *The Journal of Physical Chemistry B,* vol. 109, pp. 10574-10577, 2005.

[41] X. Hu, X. Zhao, A. Uddin, and C. B. Lee, "Preparation, characterization and electronic and optical properties of plasma-polymerized nitriles," *Thin Solid Films,* vol. 477, pp. 81-87, 2005.

[42] C.-L. Tien, Y.-R. Lyu, and S.-S. Jyu, "Surface flatness of optical thin films evaluated by gray level co-occurrence matrix and entropy," *Applied Surface Science,* vol. 254, pp. 4762-4767, 2008.

[43] E. E. Johnston and B. D. Ratner, "Surface characterization of plasma deposited organic thin films," *Journal of Electron Spectroscopy and Related Phenomena,* vol. 81, pp. 303-317, 1996.

[44] R. N. Wenzel, "Resistance of solid surfaces to wetting by water " *Industrial & Engineering Chemistry,* vol. 28, pp. 988-994, 1936.

[45] F. F. Shi, "Recent advances in polymer thin films prepared by plasma polymerization Synthesis, structural characterization, properties and applications," *Surface and Coatings Technology,* vol. 82, pp. 1-15, 1996.

[46] S. J. Bull, "Nanoindentation of coatings," *Journal of Physics D: Applied Physics,* vol. 38, p. R393, 2005.

[47] A. M. Korsunsky and A. Constantinescu, "The influence of indenter bluntness on the apparent contact stiffness of thin coatings," *Thin Solid Films,* vol. 517, pp. 4835-4844, 2009.

[48] M. Zhao, Y. Xiang, J. Xu, N. Ogasawara, N. Chiba, and X. Chen, "Determining mechanical properties of thin films from the loading curve of nanoindentation testing," *Thin Solid Films,* vol. 516, pp. 7571-7580, 2008.

[49] R. Tarefder and H. Faisal, "Effects of dwell time and loading rate on the nanoindentation behavior of asphaltic materials," *Journal of Nanomechanics and Micromechanics,* vol. 3, pp. 17-23, 2013.

CHAPTER VI

WETTING, SOLUBILITY AND CHEMICAL CHARACTERIZATION

The goal of this chapter is to undertake a detailed study of the surface energy, wettability and solubility characteristics of pp–GT thin films when in contact with common processing solvents. In this chapter we examine, by means of a sessile drop CA measurement, the wettability of a wide range of practically relevant solvents on pp–GT thin films fabricated at a range of RF deposition powers. From these data, surface energies and solubility behaviors are extracted. The wettability is correlated with the elemental composition of the film's surface determined using FTIR and XPS analysis. The outcomes of these studies are reported in *J. Ahmad, K. Bazaka, M. Oelgemöller, and M. V. Jacob, "Wetting, solubility and chemical characteristics of plasma polymerized 1-isopropyl-4-methyl-1,4-cyclohexadiene thin films," Coatings, vol. 4, pp. 527-552, 2014.*

WETTING, SOLUBILITY AND CHEMICAL CHARACTERISTICS OF PLASMA–POLYMERIZED 1-ISOPROPYL-4-METHYL-1, 4-CYCLOHEXADIENE THIN FILMS

Organic thin film materials have many potential and implemented applications, from biocompatible and antifouling coatings in medical devices to protective coatings, waveguides and component materials in optoelectronic devices, such as flexible organic electroluminescent devices (OLED), OPV and organic thin film transistors (OTFT) [1-6]. The motivation for using organic materials stems from their chemical versatility, low cost, low temperature fabrication and ability for reel-to-reel printing, as well as mechanical flexibility [1]. The attractive synthetic and processing flexibility of organic materials allows for fine tuning of their properties to achieve a desired combination of optoelectronic, physicochemical, mechanical and biological characteristics, and controlling the manner in which these materials interact with relevant liquids [7]. The latter is an important aspect for optoelectronics and biomedical applications alike. Solution processing of electronic circuits demands dielectric interlayer stability in organic solvents and strong interfacial adhesion, while the susceptibility of the coating to the uptake of moisture is critical for OPV encapsulation applications. Surface wetting by physiological fluids is a key determinant of biocompatibility and degradation under *in vitro* and *in vivo* conditions [1, 8]. The surface-solvent kinetics and ensuing degradation of organic materials under aqueous conditions is an important consideration for biodegradable and compostable electronics, where it would affect both operational performance and the physical transience of the device [9].

One of the key predictors of surface-solvent interactions, the wetting behavior at polymer surfaces and interfaces, is dependent on the nature of the variable length of polymer chains, density fluctuations and the relatively slow motion of the long chain molecules [10]. CA analysis is typically used to obtain primary data from which the degree of wettability for a specific solid-liquid combination can be inferred [7, 11], with lower CAs indicating better wetting compared to larger CAs. This analysis also provides indirect information about the structure of the film matrix, where observed changes to θ at the liquid/solid interface are attributed to specific solid-liquid interaction mechanisms, such as absorption, spreading and swelling [12]. Fundamentally, wettability is affected by the chemical composition, topography, rigidity and homogeneity of the surfaces. The chemical composition of the surface determines its surface energy: whereas surfaces rich in non-polar groups (e.g., $–CH_x$, with $x = 1–3$) have low surface energies and, thus, are hydrophobic, surfaces with a high density of polar groups (e.g., –OH or –C=O) exhibit high surface energies and are hydrophilic [13]. With regard to surface topography, an increase in the surface roughness enhances the surface hydrophilicity of hydrophilic materials and hydrophobicity in the case of hydrophobic surfaces [14]. The micro- and nano-scale variations in the slope on the surface are believed to create physical barriers that directly affect the motion of the contact line, thus affecting CAs observed at the macro scale. In a similar way, distinct domains of chemically heterogeneous surfaces, e.g., those with higher hydrophobicity, are thought to interfere with the motion of the contact angle by hindering the advancement or contraction of the water front and, thus, increasing or decreasing the observed CA. Several models propose a relationship between the measured CAs of a given non-ideal surface and its flat, homogenous counterpart of the same composition, among them Wenzel and Cassie–Baxter models [15, 16]. In the Wenzel model, the liquid is assumed to be in contact with all of the parts of the irregular surface and is typically applied to chemically homogenous surfaces, whereas the Cassie-Baxter model places the drop on the surface protrusions without wetting the entire surface and is believed to be more appropriate for chemically heterogeneous surfaces.

Recently, growing interest in environmentally-friendly technologies has led to the exploration of a number of alternative organic source materials, e.g., unprocessed raw agricultural, food and waste substances [17], and energy-efficient green fabrication methodologies, e.g., plasma-assisted nanofabrication [18, 19]. The key driver of this research therefore rests in the need to support robust and sustainable economic and societal development, which, in practical terms, means the development of materials and technologies that are cheaper, more efficient and can address the objectives of modern societies in an environmentally sustainable fashion. Most of the existing chemical synthesis processes used for the fabrication of electronics device components are energy-inefficient and require multi-step processing and the use of hazardous auxiliary substances, such as organic solvents and catalysts [20]. These synthesis routes often rely on expensive and/or toxic, high purity, non-renewable materials [1]. In addition to using hazardous materials, modern electronic devices also use valuable and scarce materials, the availability of some of which (e.g., gallium, indium, *etc*.) is reducing at a high rate [1]. At the same time, only a limited portion of high-tech waste is recycled, with the bulk of the waste being deposited into landfills, where it slowly degrades, leaching out potentially harmful by-products. By using minimally processed, renewable natural resources, such as non-petrochemical oils, e.g., essential oils, and highly reactive non-equilibrium dry plasma-based chemistry, it is possible to lower the environmental footprint and the economic costs of organic electronics and other such technologies throughout their lifecycle, from their fabrication to their use and disposal [21].

Essential oils are volatile aromatic compounds that are widely used in pharmacological, perfumery and culinary preparations for their aromatic and medicinal properties. Their availability in commercial quantities, relative low-cost, renewable nature and minimal toxicity makes them a suitable precursor for “green” functional materials [22]. As a volatile material, essential oil is well suited to chemical vapour deposition (CVD), as no carrier gas is required to deliver the monomer into the polymerization chamber. Using plasma as a catalyst, the oils can be converted into functional polymer thin films in a one-step process at room temperature, without the need for pre- or post-processing, e.g., annealing, or catalysts. Unlike most plasma deposited films, plasma polymers of essential oils are optically transparent and smooth. Over the last few years, thin films from lavender and tea tree essential oils have been developed and identified as promising candidates for applications in electronics, as dielectric and encapsulation layers [23-27]. Plasma polymers of terpinen-4-ol also display a valuable and rare electron blocking hole-transporting property that is very attractive for OLEDs [27]. Versatile biological activity, including antibacterial activity against drug-resistant strains of *Staphylococcus*, *Streptococcus* and *Candida* species, also makes essential oils an attractive candidate for the fabrication of antibacterial and biocompatible implantable systems, including implantable electronics [28].

This chapter focuses on the wetting, solubility and chemical characteristics of these films and the compatibility of the material with solvents typically utilized in the manufacturing of organic electronic devices, with the intention to use these films in OPVs, especially as encapsulation coatings and insulating layers in flexible electronics.

VI.1 EXPERIMENTAL

VI.1.1 PREPARATION OF THIN FILMS

Thin film samples were deposited on high quality glass microscope slides using a custom-made RF polymerization chamber, 0.75 m in length with an inner diameter of 0.055 m (volume of 0.0035 m^3). RF power is delivered to the system via an ENI RF generator at 13.56 MHz through a matching network and capacitively coupled copper electrodes. The copper electrodes were placed 0.11 m from the monomer inlet and 0.1 m apart, with the active electrode closest to the monomer inlet. The electrode configuration used was based on the uniformity of the RF discharge it produced and the corresponding uniformity of resulting thin films for the particular reaction chamber utilized throughout this work.

Prior to deposition, the substrates were thoroughly washed in extran, cleaned ultrasonically in water, rinsed in isopropanol and distilled water, air dried and placed in the reaction chamber. For each deposition, 5 mL of γ-terpinene (GT) monomer was used. The chamber was evacuated to a pressure of ~100 mTorr, at which stage the monomer inlet was opened to allow the monomer to evaporate. Argon gas was then used to flush the chamber for 1 min at a pressure of 1000 mTorr to remove residual background gas and ensure an oxygen-free surface. The chamber was then evacuated to 100 mTorr, at which stage the monomer inlet was closed, and RF glow (10, 25, 50 and 75 W) was initiated. The monomer-free plasma state was maintained for 2 min to stabilize the pressure, as well as to etch potential residual contaminants from the surface of the substrate. Once the pressure had reached 150 mTorr, the monomer inlet was opened, beginning the deposition. The flow rate was controlled via a vacuum stopcock and was estimated to be 1.57 cm^3/min by employing the procedure outlined by Gengenbach and Griesser [29].

Following the aforementioned experimental procedure, plasma polymer thin films were fabricated from γ-terpinene (GT) monomer (Figure VI.1) at various RF power levels (10, 25, 50 and 75 W) and an ambient temperature of 20 °C. pp–GT thin-films were examined over the wavelength range 190–1000 nm using a variable angle spectroscopic ellipsometer (model M-2000, J.A. Woollam Co., Inc., Lincoln, NE, USA). Ellipsometric parameters Ψ and Δ were obtained at three different angles of incidence, φ = 55°, 60° and 65°. In addition, the transmission data were also collected. Ψ and Δ were used to derive the optical constants based on a multilayer model consisting of a previously modelled substrate and Cauchy layer built in the J.A. Woollam Inc. analysis software (WVASE32) [30] via regression analysis. The quality of the fit was measured quantitatively by determining the mean-squared error and through the use of the correlation matrix. Gaussian oscillators were employed within the model to provide an optimal fit of the data, with a lower mean square error and lower average correlation between fitting terms. A more detailed review of the procedure has been reported elsewhere [31]. Samples for Fourier transform infrared (FTIR) and CA measurements were deposited for 30 min to obtain films of ~700 nm thickness. Depositions were performed for 45 min to obtain films of ~1 μm for atomic force microscope (AFM) measurements.

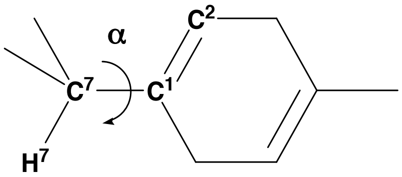

Figure VI.1. Conformers of 1-isopropyl-4-methyl-1,4-cyclohexadiene resulting from the rotation about the C^7–C^1 bond, adapted from [32]

VI.1.2 CHEMICAL CHARACTERIZATION

The surface chemistry of the deposited samples was analysed by XPS on a SPECS SAGE XPS system equipped with a Phoibos 150 hemispherical analyser and an MCD-9 detector. The background pressure was held at 2×10^{-6} Pa during experiments. For wide scan spectra and high resolution scans of the C 1s peak, an Mg Ka X-ray source was used (hν = 1,253.6 eV), operated at 10 kV and 20 mA (200 W). Measurements were performed with pass energy of 100 eV, and 0.5 eV energy steps were used for wide scan spectra, while 20 eV pass energy and 0.1 eV energy steps were used for high resolution scans. Spectra were analysed using CasaXPS (Case Software Ltd, Teignmouth, UK). Synthetic peaks were fitted to the C 1s envelops following the methodology of Beamson and Briggs [33] with the spectra correction for charging effects during analysis using a reference value of 285 eV, the binding energy of the C–C component from neutral hydrocarbon [34]. The analysis area was circular with a diameter Of 5mm, and spectra were acquired at a take-off angle of 90°. The full width at half maximum (FWHM) of the C 1s synthetic peaks remained constant at 1.5 eV.

FTIR spectroscopy was also carried out for the chemical characterization of the γ-terpinene monomer and the pp–GT thin films using a Perkin Elmer Spectrum 100 FTIR spectrometer. Spectra were obtained in transmission mode in the region of 4000–500 cm^{-1}, where 32 scans were acquired for each sample at a resolution of 1 cm^{-1}. Contributions from CO_2 and H_2O were eliminated from the spectra by a background subtraction procedure, where the background was pre-recorded under the same atmospheric conditions.

VI.1.3 CONTACT ANGLE (CA) MEASUREMENTS

Static and dynamic CAs (using water, diiodomethane (DIM) and ethylene glycol (EG) as probing liquids) of pp–GT thin films are measured. Static CAs are commonly used in calculations of surface tension parameters. However, they may not provide a reliable description of a non-ideal surface, *i.e.*, that is chemically and/or morphologically heterogeneous. Plasma-modified and plasma-polymerized surfaces are often characterized by both chemical and morphological heterogeneity [35]. Non-ideal surfaces typically display hysteresis, which can be estimated by measuring advancing and receding CAs.

CA measurements were performed using a KSV 101 system and a micrometre syringe with a narrow diameter stainless steel needle. The static CA was measured by the sessile drop method, whereby a drop of probing liquid was gently placed onto the thin film surface. The apex of each drop was confirmed using a CCD camera prior to each measurement to ensure consistency in drop volume (8 μL). The evolution of the CA (θ, the angle between the baseline of the drop and the tangent at the drop boundary), the droplet volume (V, μL), the droplet surface area (A, mm^2), the droplet height (h, mm) and the droplet basal diameter ($2r$, mm) were monitored using a software-assisted image-processing procedure. The reported values are an average of a minimum of seven measurements taken for each examined surface.

Advancing and receding CAs were measured using the dynamic sessile drop technique. First, a sessile drop of probe liquid of known volume was placed on the surface of the sample, ensuring that the needle remained in the drop during the measurement to avoid undesired vibration. The drop was then modified by slowly adding volume, with the advancing angle estimated as the largest contact angle possible without increasing its solid/liquid interfacial area. The receding angle was estimated as the minimum possible angle that can be achieved by slowly removing the probe liquid from the drop without decreasing the drop's contact area. Both the advancing and receding angle were estimated as the average of the angles on both sides of the drop profile. CA hysteresis (CAH) was estimated as the difference between the advancing and receding angle.

The presence of the needle is known to distort the contour line of the drop, due to the interactions between the surface of the needle and the liquid with the drop. The distortion of the drop shape is more prominent in the case of receding angles, where the needle's receding angle tends to pull the drop up around the needle. This distortion may result in significant errors [36].

VI.1.4 SURFACE FREE ENERGY ANALYSIS

There are several widely applied approaches for the determination of the solid surface free energy and its components from CA measurements [37]. Most theories of solid surface energy have a basis in Young's equation that employs the equilibrium CA, where the solid is considered close to ideal. The ideal surface is one that is chemically and morphologically homogenous, and thus, CAH is assumed to be absent or negligible.

For the non-ideal surfaces that are chemically and morphologically inhomogeneous, with a measurable, substantial CAH, the apparent surface free energy γ_{SV} and other interfacial interaction parameters, adhesive film tension Π, work of adhesion W_A and work of spreading W_S, can be derived from the CAH approach developed by Chibowski [40] with only three measurable quantities: the surface tension of the probe liquid γ_{LV} and its advancing θ_A and receding θ_R CA hysteresis ($CAH = \theta_A - \theta_R$). The solid surface free energy γ_{SF} can be expressed by the following relation [38]:

$$\gamma_{SF} = \gamma_{SV} + \Pi \tag{VI.1}$$

$$\Pi = \gamma_{LV}(\cos\theta_R - \cos\theta_A) \tag{VI.2}$$

The apparent, total surface free energy of a solid γ_{SV} ($\approx \gamma_{SF}$) can be expressed as [38]:

$$\gamma_{SV} = \frac{\Pi(1+\cos\theta_A)^2}{(1+\cos\theta_R)^2-(1+\cos\theta_A)^2} \tag{VI.3}$$

CAH can be related to the work of spreading W_S of liquid on the polymer surface. W_S is a thermodynamic quantity that relates the wettability to the mechanical strength of adhesion. It enables one to characterize the competition between solid-liquid adhesions with different liquids [37]. W_S can be easily calculated from the work of adhesion W_A and the work of cohesion W_C:

$$W_S = W_A - W_C \tag{VI.4}$$

where $W_A = \gamma_{LV}\,(1 + \cos\theta_A)$ and $W_C = 2\gamma_{LV}$ [39].

For surfaces that are chemically heterogeneous, but very smooth, the experimentally observed advancing CA, θ_A might be expected to be a good approximation of Young's CA, θ_Y, whereas the experimental receding angle, θ_R, is expected to have less reproducibility, due to liquid sorption or solid swelling [36]. With the assumption of $\theta_A = \theta_Y = \theta$, the surface free energy can be calculated by means of the van Oss' adaptation of Young's theory [39, 40]. The quantitative determination of all of the surface thermodynamic properties of the polymer coatings was performed using the Young-Dupré equation [40]:

$$(1 + \cos\theta_a)\gamma_L = 2\left(\sqrt{\gamma_S^{LW}\gamma_L^{LW}} + \sqrt{\gamma_S^{+}\gamma_L^{-}} + \sqrt{\gamma_S^{-}\gamma_L^{+}}\right) \tag{VI.5}$$

where θ_a is the advancing CA (°), γ_L is the surface tension (SFT) of the liquid in contact with the solid surface (mJ/m^2), γ_L^{LW} is the apolar component (Lifshitz–van der Waals [LW]) of the SFT of the liquid (mJ/m^2), γ_L^{+} is the electron-acceptor parameter of the polar component (acid–base [AB]) of the liquid (mJ/m^2), γ_L^{-} is the electron-donor parameter of the polar component (AB) of the liquid (mJ/m^2), γ_S^{LW} is the apolar component (LW) of the surface energy of the solid (mJ/m^2), γ_S^{+} is the electron-acceptor parameter of the polar component (AB) of the solid (mJ/m^2) and γ_S^{-} is the electron-donor parameter of the polar component (AB) of the solid (mJ/m^2).

The interface interaction of the polymer and the solvent is determined from their interfacial tension γ_{12} using the following equation [40]:

$$\Delta G_{121} = -2\gamma_{12} \quad \text{(VI.6)}$$

where ΔG_{121} is the free energy change. In the case of two completely miscible substances, where the interfacial tension cannot be measured directly, γ_{12} can be calculated using the following equation:

$$\gamma_{12} = (\sqrt{\gamma_1^{LW}} - \sqrt{\gamma_2^{LW}})^2 + 2(\sqrt{\gamma_1^{+}\gamma_1^{-}} + \sqrt{\gamma_2^{+}\gamma_2^{-}} - \sqrt{\gamma_1^{+}\gamma_2^{-}} - \sqrt{\gamma_1^{-}\gamma_2^{+}}) \quad \text{(VI.7)}$$

In case of two completely immiscible substances (or any given solid-liquid system), the interfacial tension can be derived directly from the measured contact angle θ:

$$\gamma_{SL} = \gamma_S - \gamma_L \cos\theta \quad \text{(VI.8)}$$

There are several other methods for obtaining surface tension values; however, the appropriateness of these methods for the probing of particular polymer/solvent combinations remains a subject of debate [41-43]. Fowkes [44] and Neumann's [41, 45] approaches were chosen in this study to provide a basis for comparison.

Fowkes method is commonly used for the determination of the surface free energy of polymeric materials [46]. Two-phase systems are investigated that contain a substance (solid or liquid) in which only the dispersion interactions appear. Considering such systems, Fowkes determined the surface free energy corresponding to the solid-liquid interface using the following equation [46]:

$$\gamma_{SL} = \gamma_S + \gamma_L - 2(\gamma_S^{LW}\gamma_L^{LW})^{0.5} \quad \text{(VI.9)}$$

According to Fowkes [47, 48], the combination of Eq. VI.8 and VI.9 yields the formula that enables one to calculate the surface free energy of a solid for which $\gamma_S = \gamma_S^{LW}$ is valid [46]:

$$\gamma_S = \gamma_S^{LW} = \gamma_L^2(1 + \cos\theta)^2/4\gamma_L^{LW} \quad \text{(VI.10)}$$

If the measuring liquid is a dispersive one ($\gamma_L = \gamma_L^{LW}$), Eq. VI.10 simplifies to:

$$\gamma_S = \gamma_S^{LW} = 0.25\gamma_L(1 + \cos\theta)^2 \quad \text{(VI.11)}$$

To determine γ_S of any solid, the CA for the solid is measured using the dispersion liquid. Then, γ_S^{LW} is calculated from Eq. VI.11. Next, the CA (θ_p) is measured using a liquid for which $\gamma_L = \gamma_L^{LW} + \gamma_L^{AB}$. The γ_S^{AB} can be estimated using [46]:

$$\gamma_S^{AB} = [0.5\gamma_L(1+\cos\theta_p) - (\gamma_S^{LW}\gamma_L^{LW})^{0.5}]^2/\gamma_L^{AB} \tag{VI.12}$$

Fowkes method is based on the independence and additivity of the dispersion and polar interactions [46]. On the other hand, Neumann's approach derives the SFT from a purely thermodynamic point of view and, therefore, neglects the molecular origins of SFT [7]. However, this is the only theory that allows the calculations to be done by using just one probing liquid. The following equation provides a method for calculating the surface energy of a solid from a single CA value [41, 45]:

$$\cos\theta = -1 + 2\sqrt{\frac{\gamma_S}{\gamma_L}}e^{-\beta(\gamma_L-\gamma_S)^2} \tag{VI.13}$$

where β is an experimentally-derived constant ($\beta \approx 0.0001247$) [45].

VI.1.5 DETERMINATION OF ROUGHNESS AND WETTING BEHAVIOR OF SURFACES

To analyse the effect of surface roughness on the wetting properties of the pp–GT thin films, the polymer was deposited on glass, silicon (Si), silicon dioxide (SiO_2) and indium tin oxide (ITO) substrates using RF plasma polymerization at 75 W RF power. The surface morphology and roughness parameters of the films were determined from AFM images acquired on a NT-MDT NTEGRA Prima AFM operating in semi-contact (tapping) mode, using (NSC05, NT-MDT) cantilevers with a spring constant of 11 N/m, a tip radius of curvature of 10 nm, an aspect ratio of 10:1 and a resonance frequency of 150 KHz. 3D interactive visualization and statistical approximation was used to analyse the topographic profiles of the surfaces. Scanning was performed perpendicular to the axis of the cantilever at a rate of typically 1 Hz, with scan areas of 1 μm × 1 μm, 10 μm × 10 μm and 50 μm × 50 μm.

VI.2 RESULTS AND DISCUSSION

VI.2.1 XPS ANALYSIS OF pp–GT FILMS

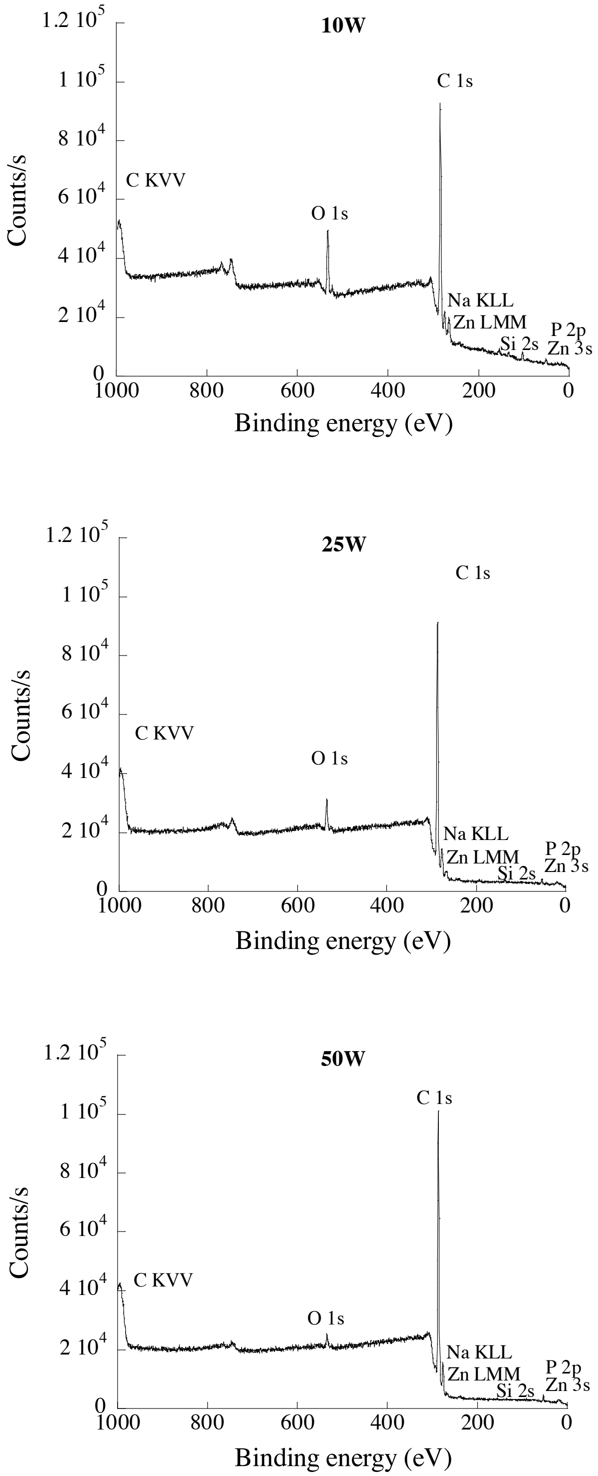

Figure VI.2. Wide scan of XPS spectrum collected for pp–GT thin films fabricated at 10, 25 and 50W

Post deposition, pp–GT thin films were analyzed by XPS to relate the results obtained from the mass spectroscopy of the plasma phase to the properties of the deposits. This elemental analysis confirmed that carbon and oxygen dominated the surface of the films with Si, Zn, P and Na present in trace amounts (Figure VI.2). Experimental core binding energies are presented in Table VI.1. Table VI.2 present the ratio of C–C and C–O in films deposited using different RF powers. The results indicate that the oxygen content significantly decreases from 11.8 to 2.1% while the carbon fraction increases from 88.2 to 97.8% when RF deposition power is increased from 10 to 50 W. Previous investigations also showed the similar trend, with films becoming more hydrophobic and thus less wettable [49]. Mass spectroscopy data reveals that some oxygen-contaminated peaks such a C_3H_5O (*m/z* 57), CH_4O_3 (*m/z* 64), $CH_2(CH_2OH)_2$ (*m/z* 76) etc. in the mass spectra decrease with increase of RF power. XPS spectra thus confirmed the hydrocarbon-rich nature of pp–GT film surfaces that is dissimilar to the original γ-terpinene monomer observed from Fourier transform infrared spectroscopy (FTIR) data [49].

This is in agreement with the mass spectroscopy observations that show decreased intensity of oxygen related peaks with increasing RF power. The low oxygen content of pp–GT might be attributed to the process used to minimize post-plasma reactions with the atmosphere. The γ-terpinene vapor was allowed to continue flowing through the plasma reactor for some time after the plasma had been extinguished. The rationale behind this procedure was that it would allow many of the active sites in the plasma polymer to decay or to react with the γ-terpinene before the polymer was exposed to the atmosphere. Alternatively, the low acceleration of the ions (Figure IV.2), particularly at high RF power, might account for the low level of oxygen uptake observed.

Table VI.1. Comparison of elemental composition of γ-terpinene monomer (thin film under 10W RF power)

Element	Level	BE (eV) (experimental)
C	KVV	995.93
O	KLL	768.93
O	KLL	747.93
O	1s	532.93
C	1s	284.43
Zn	LMM	261.82
Si	2s	157.43
Zn	3s	138.43
Si	2p	105.43

Table VI.2. Results of C 1s level fitting for pp–GT at different RF powers

RF Power, W	[C]%	[O]%	O/C	[C–C]%	[C–O]%
10	88.2	11.8	0.13	91.1	8.9
25	94.7	5.3	0.06	93	7
50	97.8	2.1	0.02	95.74	4.3

Contaminations originating from the Si substrate and ambient air were determined to be the most likely contributors of Si, Zn, P and Na. LMM auger peak at 261.82 eV with 3s peak at 138.43 eV and 3p peak at 88.51 confirms the presence of Zn in trace amount on the pp–GT surface. This Zn 3s peak is mixed up with the Phosphorous (P) 2p peak at 136 eV (2p). P 2s peak at 189.06 is also observed on the pp–GT XPS spectra. Na KLL auger peak is found at 278.62 eV with 2s and 2p peaks present at 63.01 eV and 31.42 eV respectively. The high-resolution XPS C1s spectrum appears to be comprised of contributions from carbon atoms in at least two bonding environments (Figure VI.3) with the most prominent peaks attributable to C–C species (BE) 285.0 eV. The peak at binding energy 286.5 was assigned to functional group with increasing bonding to oxygen, namely, C–O species.

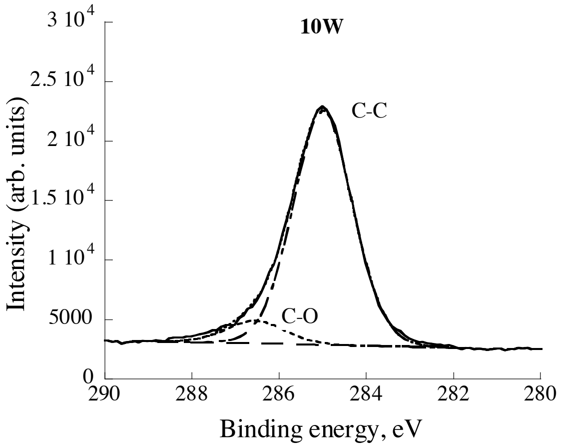

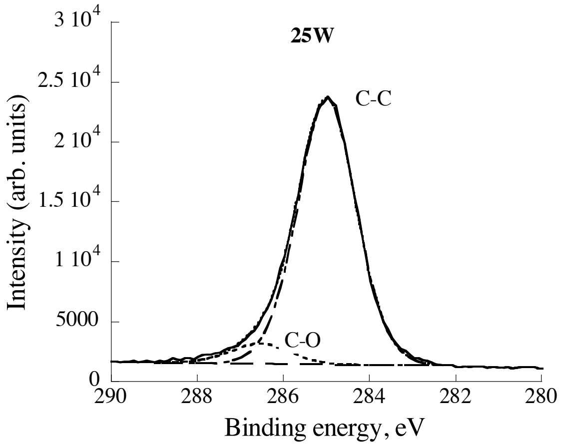

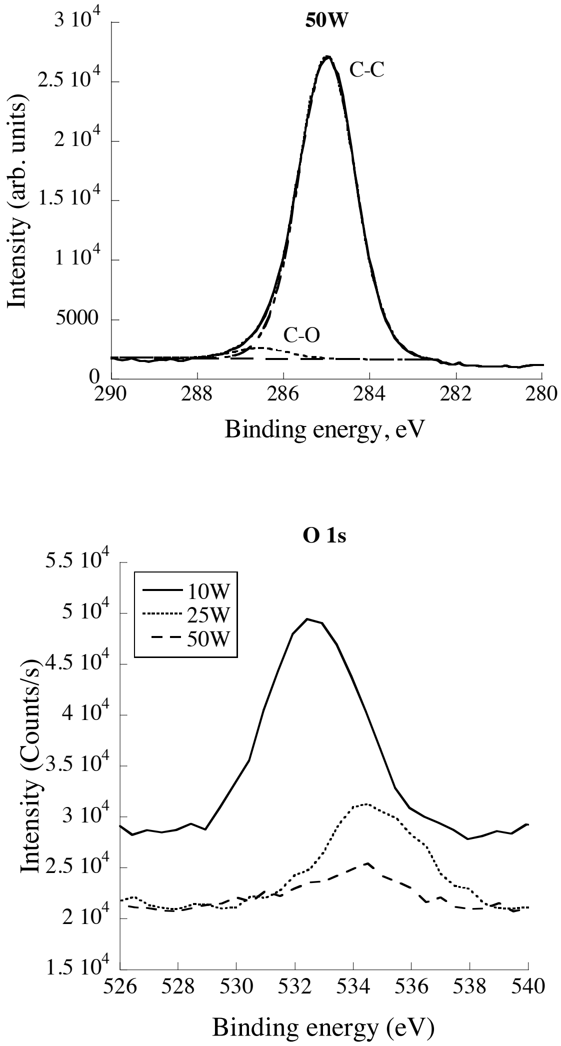

Figure VI.3. XPS C 1s spectrum and O 1s spectrum for films fabricated at 10W, 25W and 50W

The evolution of O 1s spectrum upon increasing RF deposition power is shown in Figure VI.3. pp–GT polymer O 1s signal is positioned at ~532.5 eV: upon increasing RF deposition power, the O 1s signal seems to be broadened and gradually shifts to higher binding energy. This is similar to the O 1s spectrum evolution of the π-conjugated polymer phenylacetylene *para*-nitro phenylacetylene (P(PA-*p*NO_2PA)) where the broad O 1s signals was resolved into two peaks [50]. The asymmetry and width of the O 1s spectrum for pp–GT (full width at half maximum (FWHM) is ~1.6eV) suggest that it is also made up of contributions from more than one chemical state of the element (Figure VI.3) [51]. However, the spectrum appears as a single peak, with no obvious fine structure to assist fitting. Almost all of the contributions are likely to come from the various functional groups containing oxygen bonded to carbon [52], but there is a great deal of overlap in the O 1s binding energies reported for these species. The Si 2p spectrum contains contributions from a single Si species at binding energy 105.43 eV, which is within the range observed for Si atoms bonded to O.

VI.2.2 FTIR ANALYSIS OF pp–GT FILMS

The monomer, 1-isopropyl-4-methyl-1,4-cyclohexadiene ($C_{10}H_{16}$), belongs to the group of monocyclic terpinenes commonly designated as monoterpenes. It contains two double bonds in its ring-structure, which are not conjugated (1,4-diene group).

Due to the highly unsaturated nature of cyclohexa-1,4-diene with its 4 sp^2 carbon atoms, γ-terpinene is considered almost planar. The molecular structure is characterized by one conformationally relevant internal rotation axis (C^1–C^7), which allows for the formation of various conformations (Figure VI.1). Density functional theory (DFT) calculations conducted by Marzec and co-workers led to the identification of three minima on the molecule's potential energy surface [32]. According to the orientation of the C^2–C^1–C^7–H^7 dihedral angle (α), the conformers were named trans, gauche+ and gauche−. The gauche+ ($\alpha = 47.5°$) and gauche− ($\alpha = -47.5°$) conformers (C_1) are mirror images, while the trans-like ($\alpha = 180.0°$) conformer has C_s symmetry. Since different conformations characterize the amount and type of contact between adjacent atoms or groups, these data are important for defining the macroscopic properties of the material.

The IR spectra of the monomer, 1-isopropyl-4-methyl-1,4-cyclohexadiene, and the various pp–GT thin films are shown in Figure VI.4. Characteristic IR vibrations are summarized in Table VI.3. For the monomer, multiple C–H stretching vibrations were found as a strong signal between 2818 and 2960 cm^{-1}, whereas the corresponding C–H bending vibrations appeared as broad signals and with weak to medium intensities in the range of 1300 to 1466 cm^{-1}, confirming the population of various conformers [32]. The stretching vibrations of the C–C bonds were observed in the fingerprint region below 1200 cm^{-1}. In contrast, no clear stretching vibrations of the C=C bonds could be observed. The data collected was in agreement with some previous publications reporting the interpretation of vibrational spectra of 1-isopropyl-4-methyl-1,4-cyclohexadiene [53, 54]. Comparing the IR spectra for the pp–GT thin films with that of the monomer, it is evident that the number of absorption frequencies in the spectra has reduced significantly upon polymerization, particularly in the fingerprint region of the spectrum (1500 cm^{-1} and below). Peaks also broadened for the pp–GT thin films, indicating very high degrees of polymerization. This is further supported by the disappearance of the =C–H vibration at 3088 cm^{-1}.

Electron-generated dissociation of GT monomer (rather than thermally excited or by direct chemical reaction) forces the input RF power to strongly affect the nature of the chemically-reactive species that engage in polymerization and film formation. Considering the bond strengths for 1-isopropyl-4-methyl-1,4-cyclohexadiene, the C–C single bonds are likely to dissociate first to form reactive fragments. Dissociation of higher energy bonds will occur when RF power is increased, and hence, the resultant fragmentation of the precursor molecule and subsequent crosslinking will increase. The double bonds in 1-isopropyl-4-methyl-1,4-cyclohexadiene are likely to undergo saturation through a reaction with these reactive fragments. Furthermore, the temperature of the substrate will also increase as a result of the exposure of the substrate to a large amount of energy. This will result in a reduction in the retention of the original precursor moieties [55].

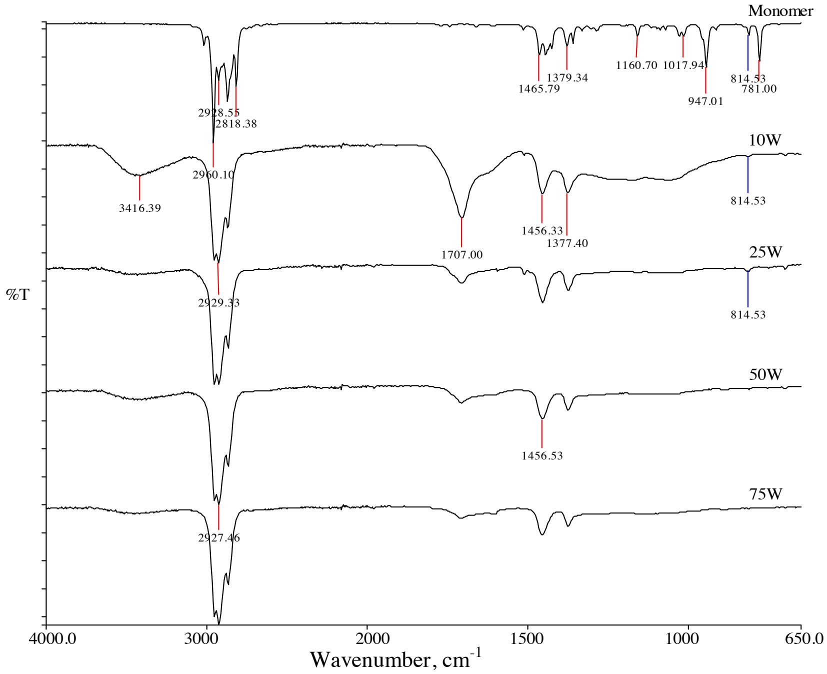

Figure VI.4. FTIR spectra (% transmittance *vs*. wavenumber, cm^{-1}) for γ-terpinene monomer and pp–GT thin films

Table VI.3. FTIR assignments for γ-terpinene monomer and plasma polymerized γ-terpinene (pp–GT) films, adapted from [56]

Assignment	**Group Frequency, cm^{-1}**	
	Monomer	**pp–GT Films**
v (OH) of water	absent	3416 (medium to weak)
v (=C–H)	3088 (weak)	absent
v (C–H)	2818–2960 (medium to strong)	2872–2960 (strong)

v (C=O)	absent	1707 (medium to weak, broad)
δ (C–H)	1300–1466 (medium to weak)	1377, 1456 (medium, broad)
v (C–C)	947–1161 (strong to weak)	unresolved or absent
ω (C–H)	781 (strong), 815 (medium)	815 (medium to absent)

Vibrational modes: v = stretching, δ = bending, ω = out of plane bending.

A broad absorbance band emerged at 3416 cm^{-1} (Figure VI.4) in the pp–GT spectrum that is considered to be the O–H stretching vibration of residual water. This is further supported by the absence of a C–O vibration. The infrared band associated with C–H stretching vibrations observed for the monomer also remained for the polymeric films; their intensity broadened, thus suggesting high degrees of cross-linking. Absorptions corresponding to C–H bending vibrations (between 1300 and 1466 cm^{-1}) decreased in magnitude and broadened with higher input RF power. Likewise, skeletal C–C vibrations between 947 and 1161 cm^{-1} vanished completely. A peak emerged at 1707 cm^{-1}, indicating the presence of carbonyl groups (C=O stretch), which were presumably formed from the reactions of radical intermediates with residual molecular oxygen and subsequent decompositions. The peak, however, decreased and eventually almost disappeared with higher RF power, possibly due to increased fragmentations and combinations of the carbon skeleton under these extreme conditions. The presence of C=O bonds in the polymer films obtained at lower powers aligns with the differences in the properties of these materials. In general, polymer materials containing C=O (and –OH) groups are characterized by a high-dielectric constant, because of their high polarizability [56] and lower hydrophobicity. In addition, these polymers are likely to be more unstable (chemically and mechanically) compared to hydrocarbon polymers, as C=O (and –OH) bonds allow increased interactions with polar solvents. The CA investigations in this study revealed that pp–GT films deposited at lower RF power were indeed less stable when in contact with common processing solvents, such as acetone or alcohol. The reduction or complete disappearance of the C=O moiety renders pp–GT more stable.

The FTIR findings are consistent with the results of elemental analysis (X-ray photoelectron spectroscopy (XPS)) of pp–GT thin films deposited at various RF power levels. The oxygen content significantly decreased, while the carbon fraction increased with RF deposition power increasing from 10 to 50 W (Table VI.2). This result showed a substantial reduction in magnitude of the H-bonded O–H stretch-related band for pp–GT fabricated under higher RF power conditions.

VI.2.3 CONTACT ANGLE (CA) AND WETTABILITY

A CAH approach provides several parameters listed in Table VI.4, useful in quantitative evaluations of water/solid surface interactions. An increase in deposition power resulted in a greater values for the advancing CA and W_A and smaller values for the receding CA, CAH, γ_{SV} and W_S. The relatively low receding CA reflects higher liquid sorption and/or solid swelling observed in the films fabricated at lower RF power [36]. The relatively low CAH for films fabricated at high RF power may be the result of the lower content of unsaturated double bonds in the pp–GT films and the film being more chemically homogenous [57]. At high RF power, intense fragmentation takes place and a very little amount of the original monomer/oligomeric units get integrated into the film structure. At this condition, the plasma-polymerized film is also highly cross-linked, which prevents the rotational motion of the surface moieties away from the surface towards the bulk of the film. The low CAH for 75-W film is also consistent with the low surface roughness, which, in earlier investigations, was found to decrease with deposition power [26]. CAH increases, as the RF power is decreased, which might be attributed to the higher content of unsaturated double bonds in the pp–GT films and loose cross-linking [57]. Incorporation of many monomer and oligomer units also takes place during this process at low RF power. These may lead to a decrease in the homogenous surface chemical composition and an increase in surface roughness with the decrease in RF power.

Table VI.4. Wettability parameters of pp–GT thin films deposited at various RF power derived from contact angle hysteresis (CAH)

RF Power, W	θ_A, °	θ_R, °	*CAH*, °	γ_{SV} (mJ·m^{-2})	W_A (mJ·m^{-2})	W_S (mJ·m^{-2})
10	63.14	8.28	54.86	44.60	105.69	−39.91
25	69.25	17.43	51.82	40.27	98.59	−47.01
50	72.98	29.15	43.83	38.39	94.11	−51.49
75	73.53	36	37.53	38.91	93.44	−52.16

Dynamic CAs determined using other probing liquids, e.g., DIM and EG, showed similar trends.

The surface hydrophobicity/hydrophilicity of the pp–GT films of different RF power levels for different solvents based on the static CA measurements are summarized in Table VI.5. Independent of thickness, the application of the pp–GT coating affected the static CA values for all three probing liquid ($p < 0.05$): water, EG and DIM. According to Olivares-Navarrete *et al.* [58] a similar phenomenon is observed for Niobium coatings. Significant differences in static

CAs were observed in the case of water for pp–GT films fabricated at different RF power. In all other cases, CA values were found in the same range.

Table VI.5. Static CAs for pp–GT thin film surfaces. DIM, diiodomethane

Sample, W	CA ± SD, °		
	Water	**Ethylene Glycol**	**DIM**
10	61.03 ± 1.79	36.29 ± 2.56	36.56 ± 1.29
25	68.93 ± 0.88	37.44 ± 2.03	36.47 ± 2.24
50	72.72 ±1.47	41.97 ± 3.60	36.58 ± 2.01
75	80.72 ± 1.94	49.33 ± 1.25	38.70 ± 3.45

The static CA data presents important information regarding interactions between the surface and the liquid system. A relatively high rate of change in the water CA signifies the reorientation of functionalities at the solid-solvent interface [59]. From the raw data for EG (Figure VI.5), an initial rapid drop in CA was attributed to the absorption of the solvent into the pp–GT thin film. Subsequently, the CA remained relatively stable for the duration of recording. While this rate of change was considered insignificant, the positive ramp suggested the occurrence of the reorientation of functionalities at the interface. For the DIM data, all of the films were stable with time, and the highest CA was found for films fabricated at 75 W. These results indicate that pp–GT is more stable as the RF power is increased, due to an increase in the degree of cross-link density associated with these deposition conditions [7].

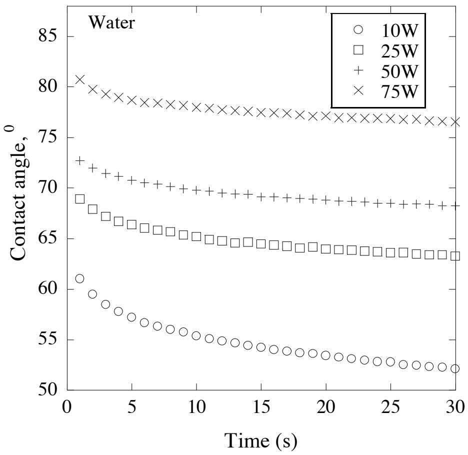

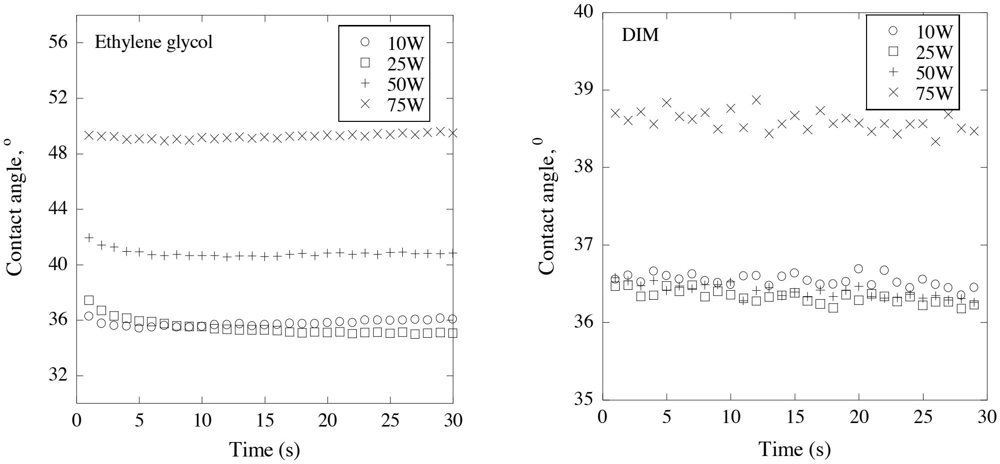

Figure VI.5. Representative static CA curves for pp–GT thin films for water, EG and DIM

The initial water CAs, θ_0 suggested that pp–GT thin films deposited at higher RF power were more hydrophobic compared to the films fabricated at lower RF power, with CAs of 61.0° (10 W) and 80.7° (75 W). This was attributed to the reduction of hydrophilic moieties at the top surface of the polymer and the decrease in the oxygen content associated with the higher deposition power.

Investigating the evolution of the droplet profile may also be appropriate and meaningful to determine the wetting behavior of thin films, especially if supported by considerations accounting for the phenomena involved at the solid/liquid interface [12]. The relationship between CA and the relevant surface phenomena can be simplified by the following general expression:

$$\theta(t) = \sum_{i=1}^{n} f_i(t) \tag{VI.14}$$

where each $f_i(t)$ is related to one of the n independent phenomena involved (e.g., absorption, spreading, swelling and evaporation of the water drop). The derivative of $\theta(t)$ can be used to compute the θ evolution rate and predict the time required to reach the steady-state condition, $(\Delta\theta/\Delta t) \approx 0$.

$$\frac{\Delta\theta}{\Delta t} = \sum_{i=1}^{n} \frac{\Delta f_i(t)}{\Delta t} \tag{VI.15}$$

The phenomena involved at the water droplet-polymer interface can also be profitably investigated by using a suitable image analysis procedure [12]. A reliable description of droplet evolution that depends on two major effects, namely, absorption and spreading, can be determined from a combined trigonometric (detection of θ) and geometric (changes in the droplet shape) approach. The absorption effect can be described as the sinking of the water droplet beneath the contact surface, with decreases in its volume (*V*) and contact area, but the volume is not affected in case of spreading effect, although it widens the contact area [12]. In this work, the detection of θ and the shape parameters (droplet height h, basal radius r, contact area and droplet volume *V*) determined by image analysis were used to describe absorption and spreading quantitatively, as well as their correlation with the surface topography of the films.

The evaporation of a sessile droplet can go through four consecutive stages: (i) spreading until the value of static advancing CA is reached; (ii) evaporation proceeds with a constant contact area and decreasing CA, until it reaches the receding value; (iii) evaporation with a constant receding CA and decreasing radius of the contact line; and (iv) evaporation with a decrease of both the radius of the contact line and CA until the droplet disappears. During Stage (i), the evaporation can be neglected [60]. In the present work, the contribution of evaporation to the total water droplet kinetics was examined directly by measuring the CA on pp–GT thin films. For films fabricated at 50 and 75 W, spreading phenomena was found to be in effect until static CA of 69.9° and 78.0° was reached. No significant difference between the water droplet volume values (Table VI.6) was found throughout the analysis. The effect of evaporation is therefore considered to be negligible for pp–GT thin films fabricated at 50- and 75-W RF power. The same trend was observed in case of poly(ethylene terephthalate) (PET) [12].

Given the negligible evaporation effects, the CA evolution was considered to be related to changes in the droplet volume and the solid/liquid surface contact area for all pp–GT thin films tested in this work. This would indicate that, at least at the early stages, two different physicochemical phenomena are occurring at the solid/liquid interface: absorption and spreading. At first glance, rather large differences in θ were observed within the first 30 s for the 10- and 25-W polymer thin films, which were confirmed by the data reported in Table VI.6 and by Figure VI.6.

The water droplet profile began to change once the droplet was in contact with the 10-W polymer thin film. Figure VI.7 shows that over the period of 0–10 s, the perceptible increase in the solid/liquid contact area on the pp–GT film fabricated at 10 W was accompanied by a decrease in volume, possibly because of the spontaneous diffusion of water inside the thin film via absorption. The drop surface area data suggests that, after this early phase, spreading began to take place and contributed to the overall kinetics of the evolution of the droplet profile. Both the absorption and spreading phenomena then continued to contribute, until the end of the 30-s period of analysis. The 25-W pp–GT thin film showed the same phenomena over the 0–10-s period. There was an early interaction of the surface and water that is evident from the increased drop surface area (Figure VI.6). After this early phase, the solid/liquid contact area remained stable for the remainder of the period of analysis. However, a decrease in volume suggests the evaporation phenomenon for that period of analysis.

Table VI.6. Main parameters derived from static water CA measurement of pp–GT thin films

RF Power, W	**$\Delta\theta_{t30\text{-}t0}$, ° [a]**	**$\Delta V_{t30\text{-}t0}$, µL [b]**	**$\Delta A_{t30\text{-}t0}$, mm² [c]**	**Phenomenon**
10	−8.91 ± 0.72	−0.08 ± 0.07	0.51 ± 0.79	Absorption + spreading
25	−5.67 ± 1.09	−0.08 ± 0.05	0.15 ± 0.27	Absorption + evaporation
50	−4.47 ± 0.44	−0.07 ± 0.05	0.05 ± 0.11	Evaporation
75	−4.16 ± 0.03	−0.06 ± 0.01	−0.04 ± 0.02	Evaporation

[a] The CA variation during the time of analysis (30 s); [b] water droplet volume variation; [c] drop surface area variation.

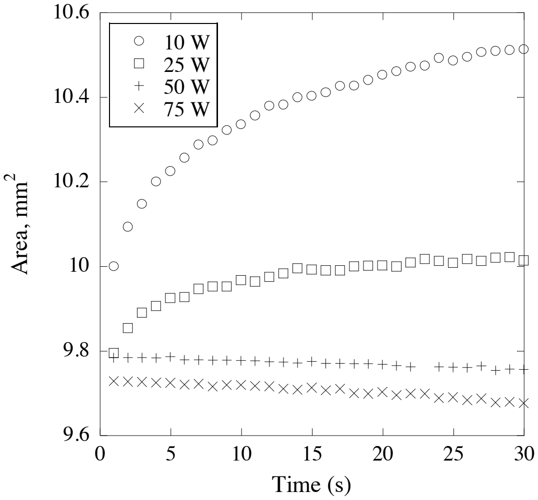

Figure VI.6. Solid/liquid contact area (mm²) evolution over time (30 s) for pp–GT thin films

Figure VI.7 illustrates that curves for the pp–GT thin films fabricated at 10 W and 25 W could not attain a zero-order-rate state at the end of the 30-s analysis. Both absorption and spreading were therefore still occurring at the end of the analysis period at the solid/liquid interface.

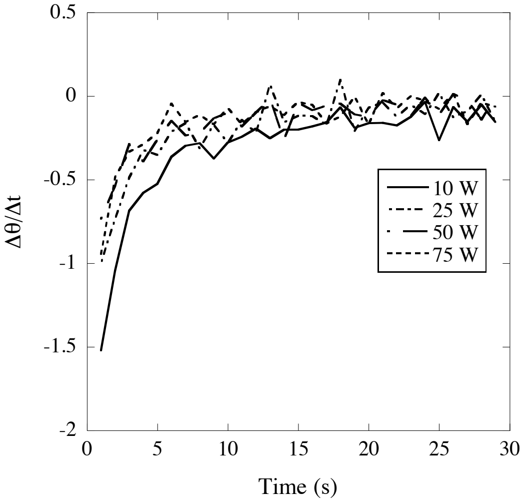

Figure VI.7. The first derivative of the curves of static water CA evolution during the 30-s period of analysis

The water droplet profile of 50 and 75W polymer thin films did not change substantially during the 30-s analysis, although the difference between θ_0 and θ_{30} was statistically significant ($p < 0.05$) (Table VI.6). According to the literature, these observations may be due to two factors: (i) the inclination of the water droplet to minimize its surface area when interacting with the polymer surface, which is capable of changing its free energy through the reorientation of certain polymer chains exposed at the solid/air interface [61]; and (ii) molecular conformation changes. The preferred orientation of functional groups could justify the θ values, as well as the decrease in the drop surface area (Figure VI.6).

VI.2.3.1 CONTACT ANGLE/IMAGE ANALYSIS COMBINED APPROACH

To gain information on the main driving forces governing drop evolution on pp–GT thin film surfaces, such as absorption, spreading, swelling and evaporation, and to determine their individual contributions to the overall wetting phenomenon, a combined CA/image analysis approach was adopted that enabled the spherical condition of the dome formed by the droplet at the solid/liquid interface to be assessed.

The shape of the water droplets changed with time, and pp–GT thin film fabricated at 10 W showed the most profound change observed from the CCD camera images. Physicochemical features of 10 W films and the inherent structural flexibility can explain this phenomenon. These two factors are recognized as crucial factors in aggregation on the molecular level [62]. The 10-W pp–GT thin films also showed the largest variations for both spreading and absorption. However, smaller effects were observed for 75-W films, where the evaporation

]

phenomenon was detected, but was almost negligible ($\Delta A = -0.01$ mm^2). An indication of this is also provided in Figure VI.8, where the experimental heights of the water droplet are displayed.

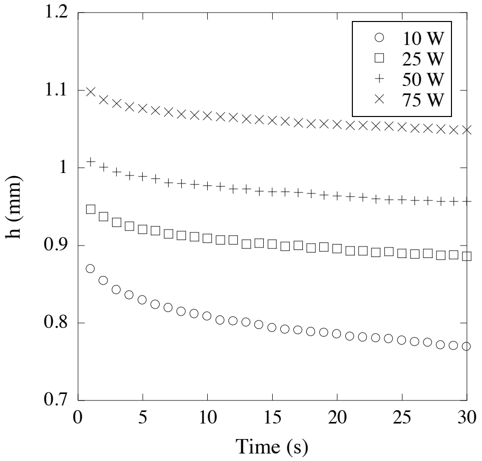

Figure VI.8. Experimental heights of the droplet on pp–GT thin films

As noticeable from Figure VI.8, the height of the water droplet on pp–GT thin film fabricated at 10 W dropped further and at a faster rate compared to the respective heights of droplets on films fabricated at other RF powers. This may be due to the wider and deeper undulations present in the 10 W film (Figure VI.9) compared to the films fabricated at 25, 50 and 75 W.

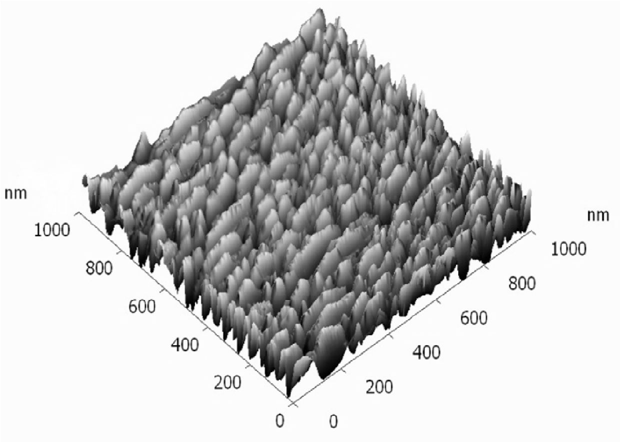

Figure VI.9. AFM image (1×1 μm^2) of the pp–GT film fabricated at 10 W

VI.2.3.2 EFFECT OF SURFACE ROUGHNESS ON WETTABILITY

Wetting of a surface by a liquid is influenced by the roughness of that surface [15]. Thin films of pp–GT were deposited at 75-W RF power on topographically-distinct surfaces of glass, Si, SiO_2 and ITO substrates to attain chemically similar, but morphologically different, pp–GT surfaces and, thus, to investigate the influence of roughness on the wetting properties of the material. Surface roughness was characterized by AFM, with the corresponding roughness values shown in Table VI.7. After the surface roughness characterization, wetting studies by CA measurements were carried out using the sessile drop technique, as described in the Experimental Section. A CA correlation with surface roughness, as determined by AFM, is evident from these results.

Table VI.7. RMS roughness and CA values of pp–GT thin films deposited on different substrates

Substrate	RMS Roughness ± SD, nm	CA ± SD, °
Glass	0.30 ± 1.51	80.72 ± 1.94
SiO_2	5.06 ± 1.03	81.95 ± 0.98
Si	7.14 ± 1.58	82.08 ± 1.54
ITO	13.94 ± 1.27	83.80 ± 1.47

The measurement of the water CAs on the pp–GT films deposited on glass and SiO_2 substrates show a virtually constant or a very small increase in the static CA values (Table VI.7), while films deposited on Si and ITO present an increase by 2°– 4°. This tendency, even if very small, confirms that the water CAs increase with the surface roughness. As expected from this limited variation in roughness, the variation range in the water CAs reported for pp–GT thin films was very small. The results from this work also show that surface roughness influences the wetting of the pp–GT, even at extremely low R_q values. Busscher *et al.* [63] and Hitchcock *et al.* [64] reported similar effects of roughness on the wettability of several polymers. The effect of surface roughness on the wettability of pp–GT is therefore needed to be considered for potential applications.

VI.2.3.3 SURFACE TENSION (SFT) PARAMETERS

SFT parameters for pp–GT thin films fabricated at different RF power levels were derived using the Van Oss-Chaudhury-Good (VCG), Fowkes and Neumann approach and are summarized in Table VI.8. The CA data obtained for the solvents, together with the widely used SFT parameters for water, DIM and EG [65] were employed in this study.

Table VI.8. The surface tension (SFT) components obtained via VCG, Fowkes and Neumann's approach for pp–GT thin films

Approach	**SFT Components, mJ/m^2**	**Solvent**	**10 W**	**25 W**	**50 W**	**75 W**
VCG	γ^{LW}	–	41.3	41.3	41.3	40.3
	γ^{AB}	–	3.4	3.7	2.7	1.6
	γ+	–	0.2	0.3	0.2	0.1
	γ-	–	19.1	10.9	8.7	4.5
	γ_s	–	44.7	45	44	41.8
Fowkes	γ_s		52.6	48.8	47.1	43.4
Neumann	γ_s	Water	40.1	33.6	30.6	24.5
		DIM	39.1	38.6	36.5	32.7
		EG	41.3	41.3	41.3	40.3

Most monopolar materials are water soluble [65] and their values of γ^- are relatively large. For all pp–GT thin films, γ^- was significantly higher than γ^+, indicating a monopolar nature. It is possible to use these values of γ^- to determine an upper limit above which solubility will occur. Van Oss *et al.* [65] demonstrated that for a given Solute 1 (monopolar surface 1)-solvent 2 (bipolar) combination, the following equation can provide that limit:

$$\gamma_{12}^{TOT} = (\sqrt{\gamma_1^{LW}} - \sqrt{\gamma_2^{LW}})^2 + 2(\sqrt{\gamma_1^{+}\gamma_2^{-}} - \sqrt{\gamma_1^{-}\gamma_2^{+}}) \qquad \text{(VI.16)}$$

Employing $\gamma_2^{LW} \approx 40\ \mathrm{mJ/m^2}$, it was found that Eq. VI.5 becomes negative. Interfacial tension therefore becomes negative for $\gamma_1^- > 28.31$ mJ/m^2. A negative interfacial tension between the material and water indicates the possibility of the penetration of water into the material, leading to repulsion between the molecules or particles and promoting solubilisation [66]. The pp–GT thin films have $\gamma^- < 28.31$ mJ/m^2 (Table VI.8). The films are therefore not water–soluble. The 75-W film gave the lowest γ^- value, indicating that the hydrophobicity of the polymer increased with RF power.

The results obtained using Fowkes approach roughly compare with those obtained via VCG and Neumann's approaches. However, the VCG and Fowkes approaches are expected to be more accurate, as they require more than one CA measurements to determine SFT values. There was some variance in the values obtained using Neumann's approach between different solvents for each polymer film (Table VI.8). These values are smaller than those found with VCG approach, with the exception of the values for DIM. The total SFT (γ_s) was found between 41 and 45 mJ·m^{-2} for all samples investigated using the VCG approach. Values between 43 and 52 mJ·m^{-2}

were found using the Fowkes approach. This is similar to the value of ≈44 mJ·m^{-2} for PET obtained by Wu *et al*. [67], as well as 42 mJ·m^{-2} for PMMA. The values are also consistent with those reported for plasma thin films deposited from other secondary plant metabolites, where total SFTs of 45–48, 36–40 and 31–37 mJ·m^{-2} were found for thin films derived from linalyl acetate [68], *Lavandula angustifolia* essential oil [7] and terpinen-4-ol [69], respectively.

VI.2.3.4 WETTING BEHAVIOR

The wettability of each solution on the pp–GT surface can be quantified by computing the spreading parameter $\Delta W = \gamma_L(\cos\theta - 1)$ [70]. It shows the extent to which the liquid will adhere to the surface relative to itself and, hence, indicates the ability of a liquid drop to stick to the solid surface during solution processing [71].

Table VI.9. Spreading parameter (ΔW, mN/m) of pp–GT thin films

Solvent	10 W	25 W	50 W	75 W
Water	−37.54	−46.63	−51.18	−61.10
EG	−9.31	−9.89	−12.31	−16.72
DIM	−9.99	−9.95	−10.00	−11.15

The pp–GT thin films fabricated at low RF power were characterized by increased wettability (Table VI.9). It is also observed that EG and DIM wets the pp–GT surface better than water. At $\theta = 0°$ and $\Delta W = 0$, the liquid can adhere well to the surface of the solid, and hence, complete wetting is observed. It is to be noted that the value of the work of spreading, W_S determined from the advancing and receding CAs are almost similar to the values of ΔW (calculated in this section), which gives the validation of the investigation.

Another important illustration of the wetting behavior of liquids on the pp–GT thin film surface can be performed from their wetting envelopes. These are the lines of constant equilibrium CA on a plot of the polar fraction (γ_L^{AB}) *versus* the dispersive fraction (γ_L^{LW}) of the liquid determined from the following equation [68]:

$$(1 + \cos\theta_a)\gamma_L = 2\left(\sqrt{\gamma_s^{LW}\gamma_L^{LW}} + \sqrt{\gamma_s^{AB}\gamma_L^{AB}}\right) \qquad \text{(VI.17)}$$

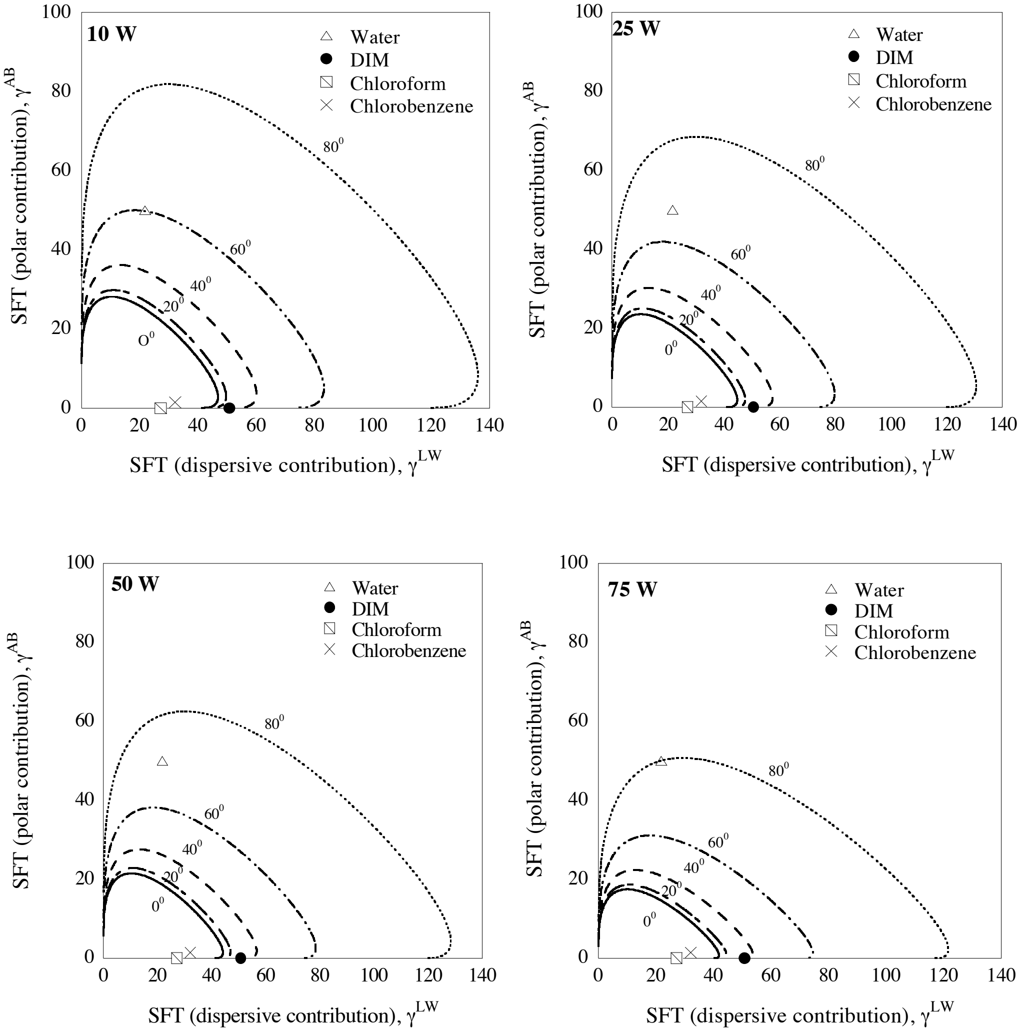

Figure VI.10. Wetting envelopes at 0°, 20°, 40°, 60° and 80° using surface tension components for pp–GT samples fabricated at 10 W, 25 W, 50 W and 75 W

Figure VI.10 demonstrates the degree to which various liquids wet the pp–GT film surfaces fabricated at different RF power if γ_L^{AB} and γ_L^{LW} are known. It also illustrates the surface properties of ideal liquids for solution processing on the pp–GT thin films. By placing a boundary on the curve at a CA of 0°, complete wetting behavior can be determined. Liquids with surface energy components that lie above the line of $\theta = 40°$ will not wet the surfaces of pp–GT films sufficiently to enable suitable film formation from solution processing [71]. The points for water are lying on or between the 60° and 80° contour of the pp–GT wetting envelope, which means that it will not wet a pp–GT film surface, but rather, show a CA between 60° and 80°. This behavior may be desirable if these films are considered as mechanically flexible encapsulating coatings for organic electronics. The behavior of chloroform and chlorobenzene was also examined, as these solvents are commonly used in the deposition of organic semiconducting layers from solution [72]. Both of them are found to lie within the 0° contour, indicating that each solvent will wet the pp–GT surface completely. If complete wetting of the surface by solution processing is needed for a specific application, both of these solvents would be appropriate in conjunction with the pp–GT thin film surface.

VI.2.3.5 THE INTERFACIAL TENSION AND SOLUBILITY

The SFT parameters obtained using the VCG, Fowkes and Neumann's approach were used to calculate the interfacial tension between the solid and liquid given by Eq. VI.7 and VI.8. The solubility of the solid (ΔG_{121}) in that liquid was then determined by incorporating interfacial tension values into Eq. VI.6. Results using Eq. (VI.6)–(VI.8) are presented in Table VI.10.

For $\Delta G_{121} >> 0$, the polymer is solvophilic for the solvent; for $\Delta G_{121} << 0$, the polymer is solvophobic for the solvent; for $\Delta G_{121} \approx 0$, the polymer is partially dissolved in the solvent. The values obtained (Table VI.10) indicate that the pp–GT polymer is solvophobic, and the strongest solvophobic response was found to be assigned to water, which is expected, as the CA values for water are found to be the most stable. The absence of negative γ_{SL} and γ_{12} values for the solvents investigated (Table VI.10) indicates that pp–GT is insoluble in the three liquids. ΔG_{121} values increased in magnitude with increasing RF power for all of the probe liquids, except DIM. This shows a less soluble behavior for water and EG. However, measurements using DIM indicate swelling or partial dissolution of pp–GT thin films.

Table VI.10. ΔG_{121} values obtained using Eq. (VI.5)–(VI.7) from the derived surface tension data

Solvent	RF Power (W)	γ_s Data	SFT Parameters, mJ/m^2		Solubility, mJ/m^2	
			γ_{SL} (eq. VI.8)	γ_{12} (eq. VI.7)	$\Delta G_{121} = -2\gamma_{SL}$	$\Delta G_{121} = -2\gamma_{12}$
Water	10 W	VCG	9.43	9.41	−18.86	−18.82
		Fowkes	17.34		−34.68	
		Neumann	4.84		−9.68	
	25 W	VCG	18.85	18.82	−37.7	−37.64
		Fowkes	22.6		−45.2	
		Neumann	7.47		−14.94	
	50 W	VCG	22.37	22.39	−44.74	−44.78
		Fowkes	25.47		−50.94	
		Neumann	9		−18	

	75 W	VCG	30.11	30.11	−60.22	−60.22
		Fowkes	31.67		−63.34	
		Neumann	12.80		−25.6	
EG	10 W	VCG	6.01	6.03	−12.02	−12.06
		Fowkes	13.92		−27.84	
		Neumann	0.45		−0.9	
	25 W	VCG	6.92	6.99	−13.84	−13.98
		Fowkes	10.67		−21.34	
		Neumann	0.51		−1.02	
	50 W	VCG	8.31	8.32	−16.62	−16.64
		Fowkes	11.41		−22.82	
		Neumann	0.79		−1.58	
	75 W	VCG	10.57	10.67	−21.14	−21.34
		Fowkes	12.13		24.26	
		Neumann	1.45		−2.90	
DIM	10 W	VCG	3.89	3.87	−7.78	−7.74
		Fowkes	11.8		−23.6	
		Neumann	0.5		−1	
	25 W	VCG	4.17	4.17	−8.34	−8.34
		Fowkes	7.92		−15.84	
		Neumann	0.49		−0.98	
	50 W	VCG	3.2	3.19	−6.40	−6.38
		Fowkes	6.30		−12.60	
		Neumann	0.5		−1	
	75 W	VCG	2.20	2.21	−4.40	−4.42
		Fowkes	3.76		7.52	
		Neumann	0.61		−1.22	

According to the wetting envelopes for pp–GT thin films, the CAs for several important organic solvents typically used in organic electronics, e.g., chloroform and chlorobenzene, will be too low to be determined experimentally. Therefore, the parameter θ_S is assumed to be 0° for the purpose of calculating the solubility values for these solvents. These values were found to be strongly negative, indicating that the pp–GT films are insoluble for solvents employed in the processing of organic electronics.

VI.3 CONCLUSION

In this chapter, the pp–GT films were successfully prepared and characterized. An FTIR analysis confirmed that exposure to an RF plasma field can effectively initiate the polymerization of the monomer. Some functional groups observed in the monomer were retained during the polymerization process, but the C=O stretching vibration (observed in pp–GT spectra) was not present in the monomer spectrum. An increase in RF power resulted in a reduction of the magnitude of the remaining groups, which was attributed to increased fragmentation and, consequently, polymerization of the monomer. RF power can therefore be an effective tool for the fabrication of polymer thin films with tuned properties.

The pp–GT films exhibited different wetting properties, as indicated by the investigation of CA analysis and wetting envelopes. The trends observed were directed by two main phenomena at the solid/liquid interface, namely absorption and spreading, which affect the overall wetting behavior. This interpretation of the data was based on the assessment of the geometry of the water droplet placed on the film surfaces. The greatest absorption was detected for 10-W pp–GT films while using water as the solvent. Improved stability was observed for films fabricated at higher RF power with the increased hydrophobicity of the polymer surface, from 61.0° (10 W) to 80.7° (75 W). The polymer demonstrated a strong electron donor component and a negligible electron acceptor component and was therefore monopolar in nature. Wetting curves showed that the samples became more hydrophobic as the deposition energy was increased. Chloroform and chlorobenzene were both found to fall within the 0° boundary, indicating that they would completely wet the surface. Solubility results confirmed that the polymer would resist solubilisation from the solvents investigated.

The wettability and compatibility of pp–GT thin films with solvents utilized in the manufacturing of organic electronic devices has been investigated in this chapter. From the wettability studies, it is concluded that pp–GT layers are suitable for encapsulation purpose and also for use in a variety of organic electronic devices requiring solution-processed layers.

REFERENCES

[1] J. Ahmad, K. Bazaka, L. J. Anderson, R. D. White, and M. V. Jacob, "Materials and methods for encapsulation of OPV: A review," *Renewable and Sustainable Energy Reviews,* vol. 27, pp. 104-117, 2013.

[2] R. S. Koti, S. R. Sanjaykumar, S.-J. Hong, C. E. Song, I.-N. Kang, S. K. Lee, W. S. Shin, S.-J. Moon, and J.-C. Lee, "3,8-Dialkoxynaphthodithiophene based copolymers

for efficient polymer solar cells," *Solar Energy Materials and Solar Cells,* vol. 108, pp. 213-222, 2013.

[3] S. Prakash, T. Chakrabarty, A. K. Singh, and V. K. Shahi, "Polymer thin films embedded with metal nanoparticles for electrochemical biosensors applications," *Biosensors and Bioelectronics,* vol. 41, pp. 43-53, 2013.

[4] J. Hierso, P. Boy, K. Vallé, J. Vulliet, F. Blein, C. Laberty-Robert, and C. Sanchez, "Nanostructured ceria based thin films (≤1 μm) as cathode/electrolyte interfaces," *Journal of Solid State Chemistry,* vol. 197, pp. 113-119, 2013.

[5] K. Sownthari and S. A. Suthanthiraraj, "Synthesis and characterization of an electrolyte system based on a biodegradable polymer," *eXPRESS Polymer Letters,* vol. 7, pp. 495-504, 2013.

[6] H. D. Hazrati, J. D. Whittle, and K. Vasilev, "A Mechanistic Study of the Plasma Polymerization of Ethanol," *Plasma Processes and Polymers,* vol. 11, pp. 149-157, 2014.

[7] C. D. Easton and M. V. Jacob, "Solubility and adhesion characteristics of plasma polymerized thin films derived from Lavandula angustifolia essential oil," *Journal of Applied Polymer Science,* vol. 115, pp. 404-415, 2010.

[8] K. Bazaka, M. Jacob, V. K. Truong, R. J. Crawford, and E. P. Ivanova, "The Effect of Polyterpenol Thin Film Surfaces on Bacterial Viability and Adhesion," *Polymers,* vol. 3, pp. 388-404, 2011.

[9] M. Graham and N. Cady, "Nano and Microscale Topographies for the Prevention of Bacterial Surface Fouling," *Coatings,* vol. 4, pp. 37-59, 2014.

[10] M. Geoghegan and G. Krausch, "Wetting at polymer surfaces and interfaces," *Progress in Polymer Science,* vol. 28, pp. 261-302, 2003.

[11] R. Bollström, M. Tuominen, A. Määttänen, J. Peltonen, and M. Toivakka, "Top layer coatability on barrier coatings," *Progress in Organic Coatings,* vol. 73, pp. 26-32, 2012.

[12] S. Farris, L. Introzzi, P. Biagioni, T. Holz, A. Schiraldi, and L. Piergiovanni, "Wetting of biopolymer coatings: contact angle kinetics and image analysis investigation," *Langmuir,* vol. 27, pp. 7563-7574, 2011.

[13] O. Kylián, O. Polonskyi, J. Kratochvíl, A. Artemenko, A. Choukourov, M. Drábik, P. Solař, D. Slavínská, and H. Biederman, "Control of Wettability of Plasma Polymers by Application of Ti Nano-Clusters," *Plasma Processes and Polymers,* vol. 9, pp. 180-187, 2012.

[14] W. Xie, J. Wang, and C. C. Berndt, "Spreading Behavior and Morphology of Ethylene Methacrylic Acid (EMAA) Deposits via the Flame Spray Process," *Coatings,* vol. 2, pp. 76-93, 2012.

[15] R. N. Wenzel, "Resistance of solid surfaces to wetting by water " *Industrial & Engineering Chemistry,* vol. 28, pp. 988-994, 1936.

[16] A. B. D. Cassie and S. Baxter, "Wettability of porous surfaces," *Transactions of the Faraday Society,* vol. 40, pp. 546-551, 1944.

[17] P. Gallezot, "Conversion of biomass to selected chemical products," *Chemical Society Reviews,* vol. 41, pp. 1538-1558, 2012.

[18] K. Ostrikov, E. C. Neyts, and M. Meyyappan, "Plasma nanoscience: from nano-solids in plasmas to nano-plasmas in solids," *Advances in Physics,* vol. 62, pp. 113-224, 2013.

[19] A. Michelmore, P. Gross-Kosche, S. A. Al-Bataineh, J. D. Whittle, and R. D. Short, "On the Effect of Monomer Chemistry on Growth Mechanisms of Nonfouling PEG-like Plasma Polymers," *Langmuir,* vol. 29, pp. 2595-2601, 2013.

[20] M. Irimia-Vladu, ""Green" electronics: biodegradable and biocompatible materials and devices for sustainable future," *Chemical Society Reviews,* vol. 43, pp. 588-610, 2014.

[21] A. A. Bazmi and G. Zahedi, "Sustainable energy systems: Role of optimization modeling techniques in power generation and supply – A review," *Renewable and Sustainable Energy Reviews,* vol. 15, pp. 3480-3500, 2011.

[22] U. Pongprayoon, P. Soontornsaratune, S. Jarikasem, T. Sematong, S. Wasuwat, and P. Claeson, "Topical antiinflammatory activity of the major lipophilic constituents of the rhizome of Zingiber cassumunar. Part I: The essential oil," *Phytomedicine,* vol. 3, pp. 319-322, 1997.

[23] M. V. Jacob, K. Bazaka, M. Weis, D. Taguchi, T. Manaka, and M. Iwamoto, "Fabrication and characterization of polyterpenol as an insulating layer and incorporated organic field effect transistor," *Thin Solid Films,* vol. 518, pp. 6123-6129, 2010.

[24] D. Taguchi, T. Manaka, M. Iwamoto, K. Bazaka, and M. V. Jacob, "Analyzing hysteresis behavior of capacitance–voltage characteristics of IZO/C60/pentacene/Au diodes with a hole-transport electron-blocking polyterpenol layer by electric-field-induced optical second-harmonic generation measurement," *Chemical Physics Letters,* vol. 572, pp. 150-153, 2013.

[25] L. J. Anderson and M. V. Jacob, "Effect of RF power on the optical and morphological properties of RF plasma polymerised linalyl acetate thin films," *Applied Surface Science,* vol. 256, pp. 3293-3298, 2010.

[26] J. Ahmad, K. Bazaka, and M. Jacob, "Optical and Surface Characterization of Radio Frequency Plasma Polymerized 1-Isopropyl-4-Methyl-1,4-Cyclohexadiene Thin Films," *Electronics,* vol. 3, pp. 266-281, 2014.

[27] K. Bazaka, M. V. Jacob, D. Taguchi, T. Manaka, and M. Iwamoto, "Investigation of interfacial charging and discharging in double-layer pentacene-based metal-insulator-metal device with polyterpenol blocking layer using electric field induced second harmonic generation," *Chemical Physics Letters,* vol. 503, pp. 105-111, 2011.

[28] K. Bazaka, M. V. Jacob, V. K. Truong, F. Wang, W. A. A. Pushpamali, J. Y. Wang, A. V. Ellis, C. C. Berndt, R. J. Crawford, and E. P. Ivanova, "Plasma-Enhanced Synthesis of Bioactive Polymeric Coatings from Monoterpene Alcohols: A Combined Experimental and Theoretical Study," *Biomacromolecules,* vol. 11, pp. 2016-2026, 2010.

[29] T. R. Gengenbach and H. J. Griesser, "Deposition conditions influence the postdeposition oxidation of methyl methacrylate plasma polymer films," *Journal of Polymer Science Part A: Polymer Chemistry,* vol. 36, pp. 985-1000, 1998.

[30] J. A. W. Co. Guide to Using WVASE32.

[31] C. D. Easton and M. V. Jacob, "Optical characterisation of radio frequency plasma polymerised Lavandula angustifolia essential oil thin films," *Thin Solid Films,* vol. 517, pp. 4402-4407, 2009.

[32] K. M. Marzec, I. Reva, R. Fausto, and L. M. Proniewicz, "Comparative Matrix Isolation Infrared Spectroscopy Study of 1,3- and 1,4-Diene Monoterpenes (α-Phellandrene and γ-Terpinene)," *The Journal of Physical Chemistry A,* vol. 115, pp. 4342-4353, 2011.

[33] L. O'Toole, A. J. Beck, A. P. Ameen, F. R. Jones, and R. D. Short, "Radiofrequency-induced plasma polymerisation of propenoic acid and propanoic acid," *Journal of the Chemical Society, Faraday Transactions,* vol. 91, pp. 3907-3912, 1995.

[34] J. F. Watts, "High resolution XPS of organic polymers: The Scienta ESCA 300 database. G. Beamson and D. Briggs. 280pp., £65. John Wiley & Sons, Chichester, ISBN 0471 935921, (1992)," *Surface and Interface Analysis,* vol. 20, pp. 267-267, 1993.

[35] M. Strobel and C. S. Lyons, "An Essay on Contact Angle Measurements," *Plasma Processes and Polymers,* vol. 8, pp. 8-13, 2011.

[36] Y. Yuan and T. R. Lee, "Contact Angle and Wetting Properties," in *Surface Science Techniques*. vol. 51, G. Bracco and B. Holst, Eds., ed: Springer Berlin Heidelberg, 2013, pp. 3-34.

[37] S. J. Pogorzelski, P. Rochowski, and J. Szurkowski, "Pinus sylvestris L. needle surface wettability parameters as indicators of atmospheric environment pollution impacts: Novel contact angle hysteresis methodology," *Applied Surface Science,* vol. 292, pp. 857-866, 2014.

[38] E. Chibowski, "Surface free energy of a solid from contact angle hysteresis," *Advances in Colloid and Interface Science,* vol. 103, pp. 149-172, 2003.

[39] R. J. Good, "Estimation of Surface Energies from Contact Angles," *Nature,* vol. 212, pp. 276-277, 1966.

[40] C. J. Van Oss, "Long-range and short-range mechanisms of hydrophobic attraction and hydrophilic repulsion in specific and aspecific interactions," *Journal of Molecular Recognition,* vol. 16, pp. 177-190, 2003.

[41] D. Y. Kwok and A. W. Neumann, "Contact angle measurement and contact angle interpretation," *Advances in Colloid and Interface Science,* vol. 81, pp. 167-249, 1999.

[42] S. Shalel-Levanon and A. Marmur, "Validity and accuracy in evaluating surface tension of solids by additive approaches," *Journal of Colloid and Interface Science,* vol. 262, pp. 489-499, 2003.

[43] R. R. Deshmukh and A. R. Shetty, "Comparison of surface energies using various approaches and their suitability," *Journal of Applied Polymer Science,* vol. 107, pp. 3707-3717, 2008.

[44] F. M. Fowkes, "Additivity of intermolecular forces at interfaces. I. Determination of the contribution to surface and interfacial tensions of dispersion forces in various liquids," *The Journal of Physical Chemistry,* vol. 67, pp. 2538-2541, 1963.

[45] H. Tavana and A. W. Neumann, "Recent progress in the determination of solid surface tensions from contact angles," *Advances in Colloid and Interface Science,* vol. 132, pp. 1-32, 2007.

[46] M. Zenkiewicz, "Methods for the calculation of surface free energy of solids," *Journal of Achievements in Materials and Manufacturing Engineering,* vol. 24, pp. 137-145, 2007.

[47] F. M. Fowkes, "Donor-Acceptor Interactions at Interfaces," *The Journal of Adhesion,* vol. 4, pp. 155-159, 1972.

[48] F. M. Fowkes, "Attractive forces at interfaces," *Industrial & Engineering Chemistry,* vol. 56, pp. 40-52, 1964.

[49] J. Ahmad, K. Bazaka, M. Oelgemöller, and M. V. Jacob, "Wetting, solubility and chemical characteristics of plasma polymerized 1-isopropyl-4-methyl-1,4-cyclohexadiene thin films," *Coatings,* vol. 4, pp. 527-552, 2014

[50] G. Iucci, G. Polzonetti, P. Altamura, G. Paolucci, A. Goldoni, R. D'Amato, and M. V. Russo, "Reactivity of the nitro-group of a π-conjugated polymer upon the interface formation with chromium: a photoelectron spectroscopy investigation," *Applied Surface Science,* vol. 153, pp. 10-18, 1999.

[51] Q. Cheng, S. Xu, and K. Ostrikov, "Single-step, rapid low-temperature synthesis of Si quantum dots embedded in an amorphous SiC matrix in high-density reactive plasmas," *Acta Materialia,* vol. 58, pp. 560-569, 2010.

[52] G. Beamson and D. Briggs, "High Resolution XPS of Organic Polymers: The Scienta ESCA300 Database," *Journal of Chemical Education,* vol. 70, p. A25, 1993.

[53] D. J. Daferera, P. A. Tarantilis, and M. G. Polissiou, "Characterization of Essential Oils from Lamiaceae Species by Fourier Transform Raman Spectroscopy," *Journal of Agricultural and Food Chemistry,* vol. 50, pp. 5503-5507, 2002.

[54] H. Schulz, G. Özkan, M. Baranska, H. Krüger, and M. Özcan, "Characterisation of essential oil plants from Turkey by IR and Raman spectroscopy," *Vibrational Spectroscopy,* vol. 39, pp. 249-256, 2005.

[55] G. P. Lopez and B. D. Ratner, "Substrate temperature effects on film chemistry in plasma deposition of organics. I. Nonpolymerizable precursors," *Langmuir,* vol. 7, pp. 766-773, 1991.

[56] J. Coates, "Interpretation of Infrared Spectra, A Practical Approach," in *Encyclopedia of Analytical Chemistry*, ed: John Wiley & Sons, Ltd, 2006.

[57] L. Shi, "The investigation of polymer surface dynamics modified by plasma using dynamic contact angle method," *European Polymer Journal,* vol. 36, pp. 987-992, 2000.

[58] R. Olivares-Navarrete, J. J. Olaya, C. Ramírez, and S. E. Rodil, "Biocompatibility of Niobium Coatings," *Coatings,* vol. 1, pp. 72-87, 2011.

[59] M. R. Alexander and T. M. Duc, "A study of the interaction of acrylic acid/1,7-octadiene plasma deposits with water and other solvents," *Polymer,* vol. 40, pp. 5479-5488, 1999.

[60] S. Semenov, V. M. Starov, R. G. Rubio, H. Agogo, and M. G. Velarde, "Evaporation of sessile water droplets: Universal behaviour in presence of contact angle hysteresis," *Colloids and Surfaces A: Physicochemical and Engineering Aspects,* vol. 391, pp. 135-144, 2011.

[61] F. J. Holly and M. F. Refojo, "Wettability of hydrogels. I. Poly (2-hydroxyethyl methacrylate)," *J Biomed Mater Res,* vol. 9, pp. 315-26, 1975.

[62] A. Podestà, M. Indrieri, D. Brogioli, G. Manning, P. Milani, R. Guerra, L. Finzi, and D. Dunlap, "Positively charged surfaces increase the flexibility of DNA," *Biophysics Journal,* vol. 89, pp. 2558-2563, 2005.

[63] H. J. Busscher, A. W. J. van Pelt, P. de Boer, H. P. de Jong, and J. Arends, "The effect of surface roughening of polymers on measured contact angles of liquids," *Colloids and Surfaces,* vol. 9, pp. 319-331, 1984.

[64] S. J. Hitchcock, N. T. Carroll, and M. G. Nicholas, "Some effects of substrate roughness on wettability," *Journal of Materials Science,* vol. 16, pp. 714-732, 1981.

[65] S. Wu and R. A. Shanks, "Solubility study of polyacrylamide in polar solvents," *Journal of Applied Polymer Science,* vol. 93, pp. 1493-1499, 2004.

[66] C. J. Van Oss, M. K. Chaudhury, and R. J. Good, "Monopolar surfaces," *Advances in Colloid and Interface Science,* vol. 28, pp. 35-64, 1987.

[67] W. Wu, R. F. Giese, Jr., and C. J. van Oss, "Evaluation of the Lifshitz-van der Waals/Acid-Base Approach To Determine Surface Tension Components," *Langmuir,* vol. 11, pp. 379-382, 1995.

[68] L. Anderson, C. Easton, and M. Jacob, "Compatibility of plasma-deposited linalyl acetate thin films with organic electronic device fabrication techniques," *Journal of Materials Science,* vol. 48, pp. 4851-4859, 2013.

[69] K. Bazaka and M. V. Jacob, "Solubility and Surface Interactions of RF Plasma Polymerized Polyterpenol Thin Films," *Materials Express,* vol. 2, pp. 285-293, 2012.

[70] P. G. de Gennes, "Wetting: statics and dynamics," *Reviews of Modern Physics,* vol. 57, pp. 827-863, 1985.

[71] P. H. Wobkenberg, J. Ball, F. B. Kooistra, J. C. Hummelen, D. M. de Leeuw, D. D. C. Bradley, and T. D. Anthopoulos, "Low-voltage organic transistors based on solution processed semiconductors and self-assembled monolayer gate dielectrics," *Applied Physics Letters,* vol. 93, pp. 013303-3, 2008.

[72] X. Cheng, M. Caironi, Y.-Y. Noh, C. Newman, J. Wang, M. J. Lee, K. Banger, R. Di Pietro, A. Facchetti, and H. Sirringhaus, "Downscaling of n-channel organic field-effect transistors with inkjet-printed electrodes," *Organic Electronics,* vol. 13, pp. 320-328, 2012.

CHAPTER VII

ELECTRICAL CHARACTERIZATION

This chapter presents an overview of the electrical characterization of the pp–GT polymer thin films fabricated at different RF deposition powers conditions. With potential application as an encapsulating and interlayer dielectrics (ILD) material, this chapter investigates the dielectric constant, conductivity and breakdown field of pp–GT thin films. These properties were investigated as a function of deposition conditions, input RF energy used for fabrication, and frequency and temperature dependence on the the structural and chemical properties of pp–GT material. The results of this chapter are reported in the journal article *Ahmad, Jakaria, Bazaka, Kateryna, and Jacob, Mohan V. (2014) Electrical conduction in plasma polymerized thin films of γ-terpinene* that is accepted for publication in the *Journal of Applied Polymer Science*.

ELECTRICAL CONDUCTION IN PLASMA POLYMERIZED THIN FILMS OF γ - TERPINENE

Plasma polymerization or plasma–enhanced chemical vapor deposition (PECVD) [1] is a promising modern technique for direct polymer thin films deposition of varying thickness on various substrates from almost any organic vapor [2, 3]. The properties of the polymers obtained by this method are of high quality, different and in contradistinction to the conventional polymerization methods [4, 5]. By employing this technique it is possible to deposit polymer films that are generally homogeneous, adherent, pinhole free, chemically inert, adhesive and thermally stable [4, 6, 7]. The properties of the thin films can also be altered by varying the deposition parameters like deposition power, pressure, monomer flow rate and deposition time [2]. These films have therefore been extensively investigated in the recent past due to their potential applications in electronics and optoelectronics [8-12]. They can be used as insulating, dielectric and functional layers for electronic functional elements in thin film transistors, diodes, switching elements, PV devices, capacitors etc [11, 13, 14]. However, plasma polymerization usually yields polymer of highly cross–linked, highly branched and highly insulating materials and applications of these polymers are therefore mostly suited for the field of dielectric films [15, 16].

In organic thin film transistors (OTFTs) a gate insulating material is generally used. As an example polymethyl-methacrylate-co-glyciclyl-methacrylate (PMMA-GMA) is employed as the gate insulator with dielectric constant (k) of ~3.9 [17]. Another polymeric material has been developed from pyrrole by radio frequency (RF) PECVD with k □ 3.8 [16]. However, there are several drawbacks in the devices with these high–*k* material including high leakage current and hysteresis [17]. It is also important to decrease the thickness of the gate dielectric. In conventional metal−oxide−semiconductor (MOS), for 2.0 μm to 0.25 μm nodes, tetraethyl orthosilicate (TEOS) with a dielectric constant *k* of < 4 is typically used as the interlayer dielectrics (ILD) material [8]. Fluorinated silicon oxide (FSO) offers a lower dielectric constant of < 3.5, due to lower polarizability of Si−F bonds compared to Si−O bonds. The lowest dielectric constant values achievable by FSO are in the range 3.2 to 3.7, which are not sufficiently low for complementary MOS technologies of 0.13-microns and below [9]. A number of reliability concerns also accompany the use of FSO as an ILD [18]. Even lower values of *k* have been achieved by introducing organic groups, such as CH_3, and Si−H terminals into the silica network yielding organosilica glasses (OSG) with k ~2.7−3.0. However, to ensure process compatibility and high device reliability, materials need to meet some electrical requirements as well as suitable dielectric behavior [19].

Another important application for organic thin films is OPV. This technology is economically competitive and it virtues collective advantages such as manufacturing adaptability, low-cost processing and a lightweight, flexible device end–product, reel-to-reel processing on low cost substrates, with numerous printing techniques, namely screen, inkjet, offset or flexo printing, already available [20, 21]. However, the OPV technology is yet to reach a desirable level of performance, which would render it suitable for wide commercial use [11]. Present power conversion efficiency (PCE) and operational stability of OPV are considerably lower than those offered by *Si* technology. Significant research efforts have been devoted to development of materials, designs and structures to improve PCE of OPV, with a recent report of 12% for an organic cell. Although this value falls short of ~25% PCE level offered by *Si* PV cells, it may well be sufficient for a feasible commercial proposition when substantially less expensive production budget for OPV is considered. Long-term operation stability of OPV, however, is far below what would be considered acceptable for a commercial product, with the replacement costs negating the cost savings from inexpensive manufacturing. Currently, the acceptable lifetime of an inorganic solar cell is 20–25 years [22] well beyond the lifetime achievable by the most advanced organic solar cells available. Such profound discrepancy in device life expectancy between inorganic and organic PV cells stems from relatively high susceptibility of organic materials to water vapor and oxygen, which lead to reduced reliability and lifetime of organic devices under normal environmental conditions [11, 23]. Encapsulation with high barrier performance materials and structures is one of the key ways to address these issues and improve device lifetime [24-27].

Thin film encapsulation is a critical technology required for the application and commercialization of OPVs [11]. For effective encapsulation, the materials have to meet the requirements of good processability, high optical transmission, high dielectric constant, low water absorptivity and permeability, high resistance to ultra-violet (UV) degradation and thermal oxidation, good adhesion, mechanical strength, and chemical inertness [11]. However, the materials currently available cannot yet satisfy these aforementioned requirements. Adhesion strength of ethylene vinyl acetate (EVA), for example, is affected by the processing conditions, damp heat and exposure time [28]. The deposition of the SiO_x and SiN_x encapsulation structure causes plasma damage on the devices owing to the high sensitivity of the organic films to radiation, charging and heating [29, 30]. Al_2O_3 has a slow deposition rate compared to PECVD-based methods that makes it more difficult to use in low-cost mass manufacturing processes [11]. New materials are needed which will satisfy the encapsulation requirements and achieve the reliability and lifetime required.

1-isopropyl-4-methyl-1,4-cyclohexadiene has been used in this study to synthesize an organic polymer by RF PECVD. The precursor, also known as γ-terpinene, is a natural, minimally processed plant-derived source, and is considered as an environmentally friendly alternative to highly purified monomers typically used for fabrication of electronic materials. The fabricated polymer (pp–GT) thin films are transparent to the optical wavelengths, with an energy gap of 3.1 eV indicative of an insulating material [2]. In terms of surface morphology, the films are smooth (average roughness around 0.3 nm), uniform, defect free and show high adhesion to a variety of substrates [2]. The pp–GT are stable when in contact with many types of common solvents. Moderately hydrophobic, the films are completely wetted by chloroform and chlorobenzene, the solvent commonly used in deposition of organic semiconducting layers [31]. Since the performance of an organic device relies on the charge carrier injection and transport in the active material, adequate understanding of the nature of the carrier transport within the polymer thin films is significant for microelectronic and optoelectronic applications. As such, with potential application as an encapsulating and ILD material, the present work investigates the electrical properties of pp–GT films, specifically the dielectric constant, conductivity and breakdown field. These properties were investigated as a function of deposition conditions, input RF energy used for fabrication, and frequency and temperature dependence on the structural and chemical properties of pp–GT material.

VII.1 EXPERIMENTAL

VII.1.1 SAMPLE PREPARATION

Thin film samples were deposited on high quality glass microscope slides inside a custom made, cylindrical RF polymerization chamber, 0.75 m in length with an inner diameter of 0.055 m (approximate volume of 0.018 cm^3). Extran and ultrasonic bath of distilled water was used to thoroughly clean the substrates. These were also rinsed with isopropanol and air dried prior to deposition. Using the procedure outlined in [32], plasma polymer films of approximately ~800 nm thickness were fabricated from γ-terpinene monomer at various RF deposition power levels (10, 25, 50 and 75W). Time of deposition was varied to obtain films of desired thickness.

For J–V measurements, three-layered sandwich MIM structures (Al/pp–GT thin film/Al) were deposited onto thoroughly cleaned glass substrates. Using a custom made shadow mask, devices were prepared by first depositing bottom Al electrode using thermal evaporation at a pressure of 10^{-6} Torr. The pp–GT thin films were then fabricated using RF plasma polymerization. Finally, top electrodes were deposited using thermal evaporation technique and the electrical contact was made by the conductive silver epoxy (CW2400). The bottom and top Al electrodes were rectangular in shape with an effective area of ~3×10^{-5} m^2.

VII.1.2 MEASUREMENTS

The thickness measurements of the pp–GT thin films were performed by M-2000, J. A. Woollam Co., Inc. variable angle spectroscopic ellipsometer (VASE). Hioki 3552-50 LCR meter was used to analyze the dielectric function between frequencies of 10 Hz–100 kHz. The impedance z, capacitance C, phase angle θ and dielectric loss $tan\delta$ were measured with no applied DC bias. From these values together with the device geometry, real and imaginary parts of the dielectric constant ε_r and $\varepsilon_{r'}$ of the thin films were determined from the following relations:

$$\varepsilon_r = \frac{dC}{A\varepsilon_o} \tag{VII.1}$$

$$\varepsilon_{r'} = \varepsilon_r \tan\delta \tag{VII.2}$$

where d is the thickness of the film, A is the cross section area and ε_o is the permittivity of free space.

Temperature measurements were performed using the same measurement device by placing the samples on a temperature-controlled hotplate (323 K, 333 K, 343 K and 348 K). The sample was left on the hotplate for 10 min at each temperature to ensure uniform heating, and the temperature of the sample was confirmed via a digital thermocouple prior to measurement of the dielectric function.

Dielectric breakdown measurements were performed on the MIM structures using a Keithley 2636A source meter. A staircase function swept the voltage and current was measured until a sudden increase in current occurred. The point at which the meter indicated current limiting was set at 100 μA for all devices so that the short circuit current could be clearly ascertained from the current–density voltage (*J*–*V*) plot.

VII.2 RESULTS AND DISCUSSION

VII.2.1 DIELECTRIC PROPERTIES

Dielectric polarization and relaxation effects govern the behavior of dielectric properties of polymeric materials as a function of frequency. The dielectric relaxation mechanisms can be grouped into three classes, viz. α, β and γ relaxations in order of decreasing temperature [33, 34]. α relaxation is a high temperature process that may involve crystalline regions and is usually related to the main chain motions. Its intensity increases with the degree of crystallinity [35]. The β relaxation process is related to the movement of the side group chains or branches of the polymer and it related to the amorphous regions. The γ-process is related to the local intermolecular relaxation at a temperature below *Tg* [35]. Since the measurement temperature in this section of the study is maintained constant, the identification of the different relaxation mechanisms (α, β, γ) becomes difficult without studies involving temperature.

Table VII.1. Dielectric properties of pp–GT thin films determined from capacitive measurements

Sample	ε_r			
	100Hz	1KHz	10KHz	100KHz
10W	3.98	3.89	3.81	3.69
25W	3.84	3.76	3.66	3.57
50W	3.72	3.63	2.55	3.44
75W	3.41	3.38	3.32	3.24

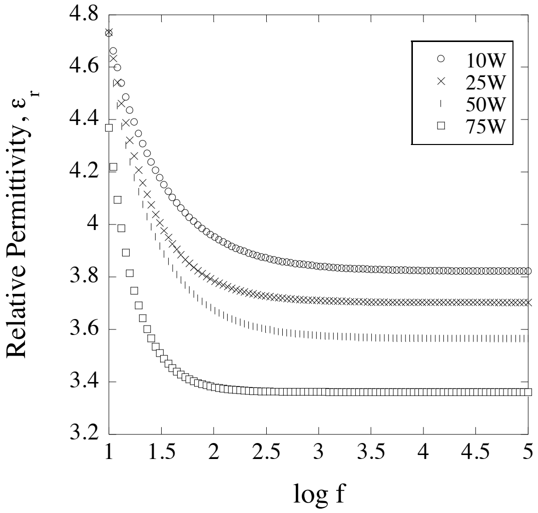

Figure VII.1. Frequency dependence of the dielectric function of pp–GT thin films

Results of the dielectric constants of the pp–GT thin films are summarized in Table VII.1. Representative curves of the dielectric function of pp–GT thin films at various power levels are also depicted in Figure VII.1. The experimental results indicate that the dielectric constant value decreases with increasing the RF deposition power. This is attributed to increase of carbon and decrease of oxygen content in pp–GT films with RF deposition power [31]. The initial decrease in dielectric constant at low frequencies can be traced to orientational polarizations of trapped free radicals, unpaired electron sites, oligomeric structures, and polar groups under an applied external electrical field [36]. Higher dielectric constant has also been previously reported in the low frequency region for other plasma deposited thin films, and was generally attributed to interfacial phenomena (e.g. formation of depletion regions and interfacial polarizations) at the metal/insulator junction due to inefficiency of charge transport through the interface under applied electric field [16]. Interfacial phenomena is less dominant at higher frequencies with the measured capacitance approaching the bulk, or insulator capacitance. Steadily decreasing dielectric constant is observed for all pp–GT thin films in higher frequency region. The dielectric constant is generally composed of contributions from electronic, ionic and orientational polarizations [37].

The pure electronic contribution to the dielectric constant was calculated from the refractive index (*n*) obtained in the UV/Vis region. Since the extinction coefficient (*k*) is normally negligible in this region, the relative dielectric constant can be simply expressed as [38]:

$$\varepsilon_{\text{electronic}} = n^2 \tag{VII.3}$$

For validating the dielectric constants of pp–GT polymer thin films, data from ellipsometric study were used. If the refractive index, *n*, of a sample at optical frequencies (~600 nm) is considered, the value of $\varepsilon_{electronic}$ is estimated to be 2.44. Hence, contribution from electronic phenomena is approximately 61.3–75.3% of the dielectric constant at frequencies greater than 10 Hz. Ionic and orientational phenomena contribute the rest in the bulk of the plasma deposited thin films. Large amount of cross–linking induced by the plasma deposition process is the reason for these low contributions, as cross–linking reduces molecular mobility and ionic polarization of molecular structures present in the bulk of the material [39]. The frequency dependence of ε_r is indicative of electronic polarization [35] due to oligomers/fragments, polar side groups, and residual free radicals effects on interfacial polarization and microscopic field distortion.

VII.2.2 DIELECTRIC LOSS

The dielectric dissipation factor (also known as power factor or electrical loss tangent) $\tan\delta$ is one of the key electrical properties of the polymer. It is defined as the ratio of an insulating material's resistance to its capacitive reactance at a specified frequency. It is always greater than 0, but usually much smaller than the dielectric constant. Loss tangent measurements are an excellent means of quality control that can yield indication of degradation or moisture pick-up. It is important in many applications such as in the insulation of cables, encapsulates for OPV and electric components, ILD, and printed wiring board materials.

The variations of the dielectric loss tangent, *tan δ*, with respect to frequency in pp–GT thin films at different input power levels are shown in Figure VII.2. It is observed that all samples show similar behavior, reaching a minimum value at approximately 100 Hz before beginning to increase again. Both the magnitude and characteristics of the dielectric loss values as a function of frequency are similar to other plasma deposited films [37].

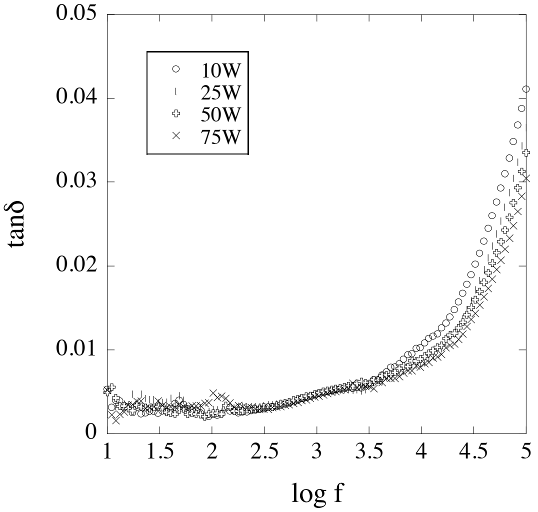

Figure VII.2. Dielectric loss tangent, *tan δ,* as a function of frequency of the pp–GT thin films at different input RF power

In the present study, the capacitor system is assumed to comprise a frequency-independent capacitive element $C^{/}$ in parallel with a resistive element *R*, whereas both are in series with a constant low value resistance *r*. The measured equivalent series capacitance C_s, of the circuit is governed by:

$$C_s = C^{/} + \frac{1}{\omega^2 R^2 C^{/}} \tag{VII.4}$$

This equation reveals that the measured capacitance C_s should decrease with increasing frequency. The loss tangent is given by:

$$\tan\delta = \frac{(1+\frac{r}{R})}{\omega R C^{/}} + \omega r C^{/} \tag{VII.5}$$

where *ω* is the angular frequency. This equation reveals that *tan δ* is proportional to the frequency and is not dependent on charge carrier concentrations within the material. Thus, the

Eq. VII.4 predicts a decrease in *tan δ* at low frequency followed by a loss minimum at [40]:

$$\omega_{\min} \approx \left(\frac{1}{rRC^{/2}}\right)^{1/2} \qquad \text{(VII.6)}$$

and an increase in *tan δ* at high frequency. Figure VII.2 demonstrates that in all the pp–GT thin films, initial drop is followed by an increase in *tan δ* values with increasing frequency. This increase is dominated by resistive losses since the mobile charges contained in the film cannot follow higher frequency electric fields. This loss of energy is associated with the degree of orientation of molecules in addition to the degree of internal friction of the polymer [19]. Since pp–GT films are strongly cross–linked, the polymer backbones have limited molecular mobility and this loss of rigidity of the polymer network facilitates the translational motion of charged impurities. The increase in *tan δ* with frequency can therefore be attributed to the introduction of polar impurities in the pp–GT polymers [41].

Lower *tan δ* values at low frequencies in pp–GT thin films can be due to a lower electrical conductivity in them. The motion of charge carriers that contributes to the conductivity at high frequencies occurs predominantly along polymer chains [42]. Defects and inter-chain charge transport can create a barrier to the charge transport in polymers that can in turn cause a reduction in electrical conductivity. The presence of a number of polymer chain entanglements in pp–GT thin films are the probable reasons for the motion of charges in the system that caused a reduction in the electrical conductivity (hence lower *tan δ* values). For any electrical insulation system, a low *tan δ* value is always desired in the dielectric material whereas the desired permittivity of the material can be high or low depending on the end application [43]. Lower *tan δ* values of pp–GT thin films can therefore be suitable for use in electrical insulation systems.

VII.2.3 TEMPERATURE DEPENDENCE OF THE DIELECTRIC CONSTANT

The capacitance of pp–GT thin films as a function of frequency is measured at different temperatures as shown in Figure VII.3. It is observed that the capacitance is frequency dependent at all frequencies. Similar results have been obtained and were adequately interpreted in terms of an equivalent circuit model [44]. According to this model the measured capacitance C_s is given by Eq. VII.4. This equation reveals the decrease of C_s with increasing frequency and that for any given frequency, C_s will increase with increasing temperature. pp–GT thin films show the same behavior.

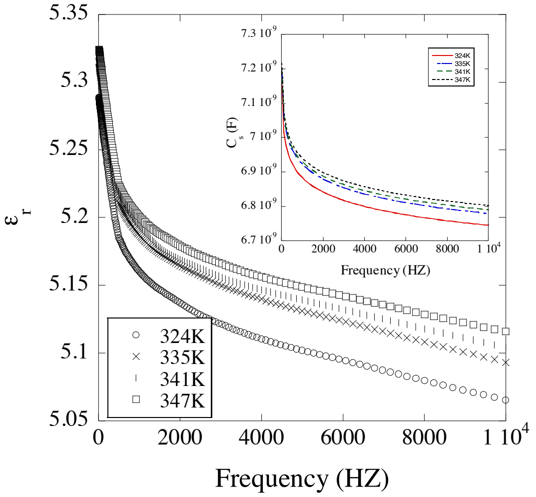

Figure VII.3. Real part of the dielectric function and frequency dependence of capacitance (inset) for pp–GT thin films (50W) at different temperatures

The dielectric constants, ε_r (Eq. VII.1) at different temperatures for pp–GT thin films has also been observed to decrease with increasing frequency (Figure VII.3). This decrease can be attributed to the fact that at low frequencies, ε_r for a polar material is due to the contribution of multi-components of polarizability, deformational and relaxation polarization.

Figure VII.3 also revealed that ε_r increases with increasing temperature. This increase can be attributed to the fact that the orientational polarization is connected with the thermal motion of molecules. Dipoles cannot therefore orient themselves at low temperatures [45]. When the temperature is increased the orientation of dipoles is facilitated and this increases the value of orientational polarization, which increases ε_r [45].

VII.2.4 TEMPERATURE DEPENDENCE OF THE DIELECTRIC LOSS

The variation of tan δ with frequency at various temperatures is represented in Figure VII.4. The expression of tan δ (Eq. VII.5) predicts a decrease in tan δ with increasing frequency [44] and an increase with frequency above $\omega_{\min}=1/[C^{/}(rR)^{1/2}]$, where the term in ω is dominant. As shown in Figure VII.4, the decrease of tan δ with frequency is evident as predicted for low frequency and a loss minimum is observed at ~300 Hz. After this point, tan δ started to increase with frequency.

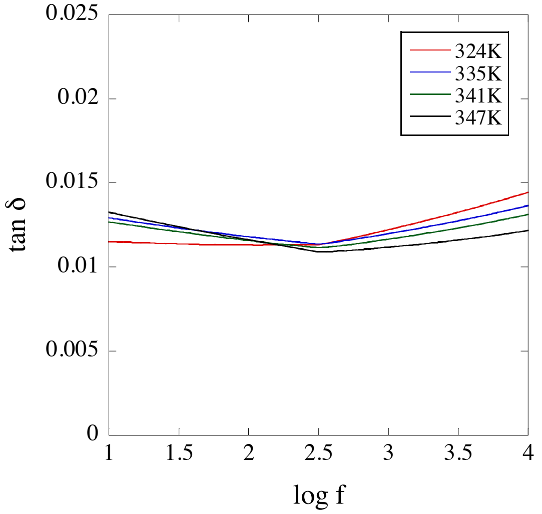

Figure VII.4. Frequency dependence of loss tan δ for pp–GT thin films (50W) at different temperatures

VII.2.5 RELAXATION TIME DISTRIBUTIONS

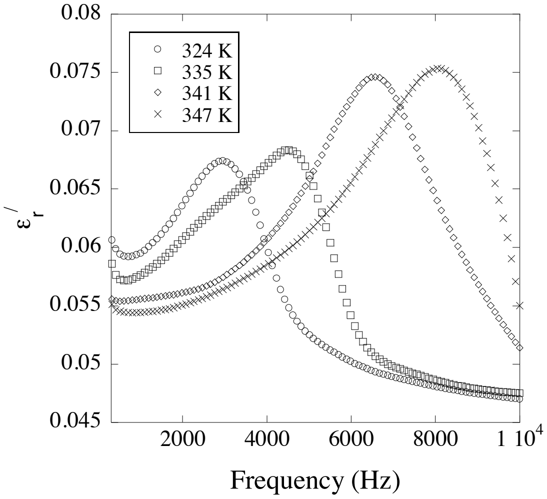

Figure VII.5. Imaginary part of the dielectric function measured at 324, 335, 341 and 347 K for pp–GT thin films (50W)

The imaginary part of the measured dielectric function (Figure VII.5) reveals distinct relaxation features in the measured data at all temperatures, shifting from lower to higher frequencies as temperature increases. The width of these peaks is quite large, indicating contributions from multiple relaxation times.

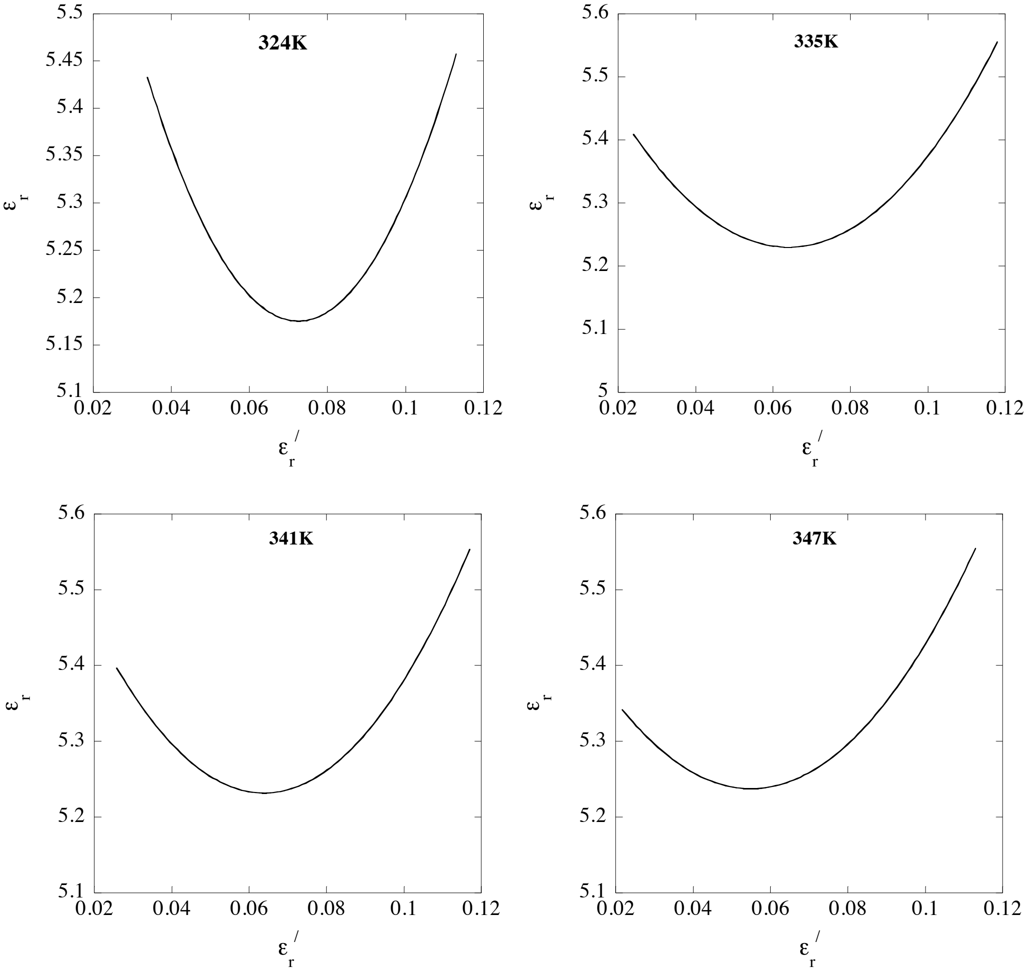

Figure VII.6. The variation of the real dielectric constant ε_r on its imaginary part $\boldsymbol{\varepsilon_{r'}}$ of pp–GT films (50W) at different temperatures for different frequencies

The Cole–Cole plots of the real part dielectric constant (ε_r) on its imaginary part dielectric loss ($\varepsilon_{r'}$) of pp–GT films at different temperatures are also shown in Figure VII.6 and the centers in the figures lie above the abscissa axes. This confirms that there exists a distribution of relaxation times in pp–GT films [45]. It is clear from Figure VII.5 also that $\varepsilon_{r'}$ increases with increasing temperature. At low temperatures conduction losses (one of the three parts of relaxation phenomena) have minimum value. As the temperature increases the conductivity increases and so the conduction losses increases. This increases the value of $\varepsilon_{r'}$ with increasing temperature [45].

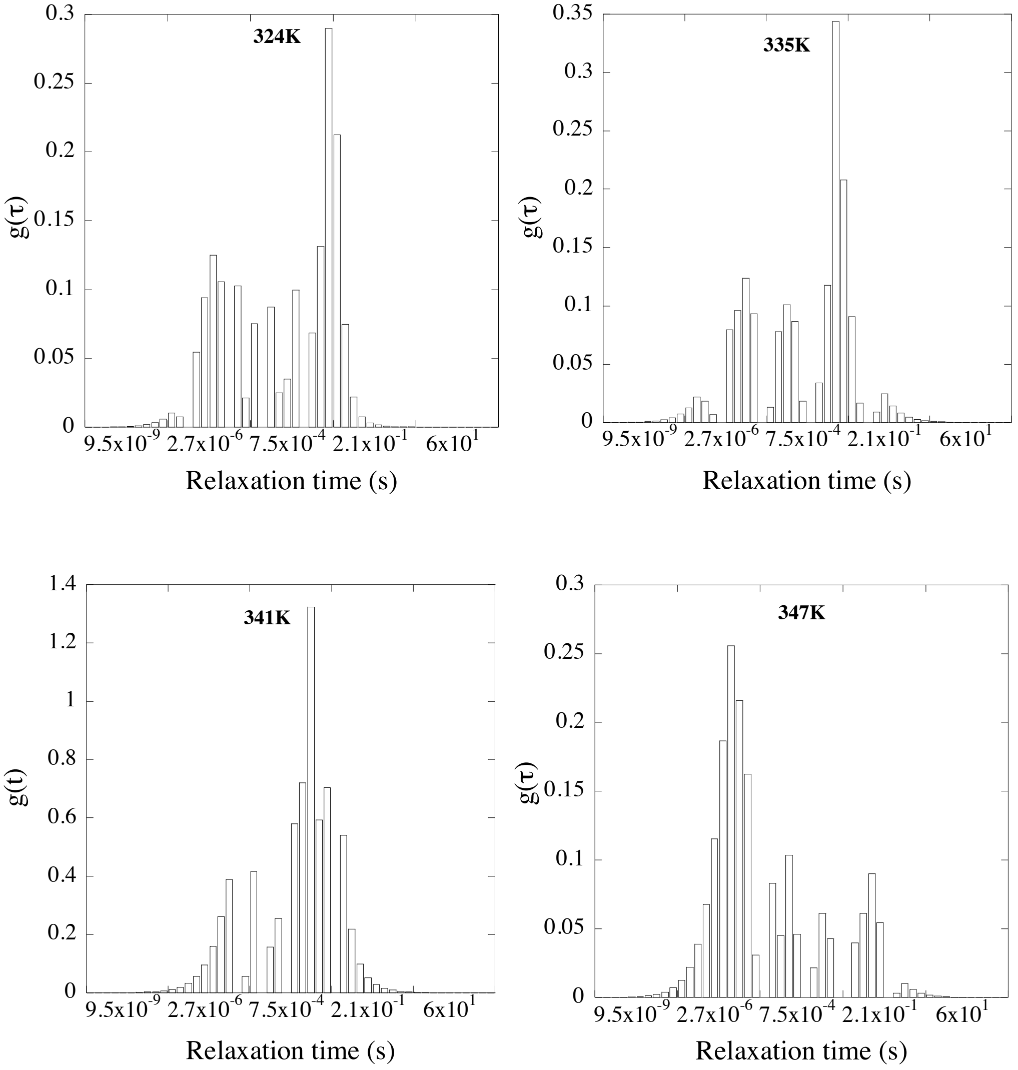

Figure VII.7. Distribution of relaxation times evaluated from dielectric spectra at 323 K, 333 K, 343 K and 348 K for pp–GT thin films (50W)

Figure VII.7 shows the approximate discrete relaxation time distributions derived from dielectric measurements at 323 K, 333 K, 343 K and 348 K as histograms showing the relative contribution of each relaxation time to the overall dielectric function. Each of the distributions show a dominant feature of higher magnitude than any others that moved to smaller relaxation times as the temperature increased. This feature corresponded to the peak measured in the imaginary permittivity data and approximately four additional peaks contributed to the overall dielectric function. The presence of these additional peaks in the relaxation time distribution reveals information not immediately evident from the dielectric spectroscopy measurements, which indicated the possibility of presence of a single relaxation process. At 348 K, a large portion of the relaxation peak was outside the measurable frequency range of the meter. The behavior at relaxation times below the principle group characteristic to measurements at 323 K, 333 K and 343 K was therefore not present in the sample measured at 348 K. These features demonstrate the highly fragmented, cross–linked nature of the pp–GT films.

VII.2.6 J–V STUDY

Various mechanisms have been suggested for the carrier transport in polymer thin films based on the dependence of current density on voltage, temperature and thickness. To ascertain the prevalence of a particular mechanism it is necessary to investigate the dependence of current density on the above-mentioned parameters. In this study, conduction mechanisms were investigated for pp–GT thin films by measuring standard *I–V* characteristics in the voltage range 0 – 200 V. For all examined devices, the measured *I–V* dependence showed low current over a wide range of applied voltage. Figure VII.8 shows the observed current density, *J*, of devices at room temperature with an applied voltage between 0 V and 200 V. Independent of pp–GT thin film deposition conditions, the *J*–*V* curves have approximately the same shape, having two sections of different slope in the low and high voltage regions that implies two different conduction processes.

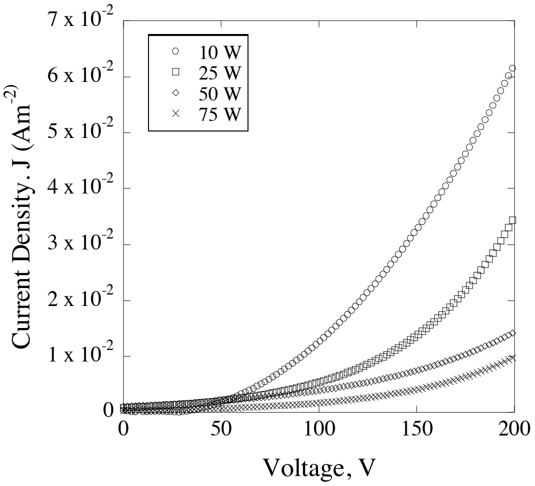

Figure VII.8. Current density (*J*) –Voltage (*V*) relationship for pp–GT films

In the low field region, the *J*–*V* characteristic can be described by a power law relation, where $J \propto V^m$, *m* being the power law index [46]. In this region, the value of *m* for all pp–GT thin films lies within the range of $0.5 < m < 0.7$ and the current density *J* can be considered to exhibit an approximately ohmic dependence with the applied voltage, *V* [46]. Ohmic conduction describes injection of carriers through the bulk of the material, limited only by the device geometry and number of carriers available for transport and the material mobility. In this region electrode and potential barrier effects have not yet begun to dominate charge transport through the device. In the high field region (>100V), the slope of the graph m is found to lie in 1.12–1.39, indicating a nonohmic conducting mechanism.

In the high field region several possible transport phenomena in plasma polymer thin films have been reported that can be used to model the observed data [38]. The three most likely mechanisms are space-charge-limited conduction (SCLC), resistive switching (RS) conduction and Poole–Frenkel (PF) conduction. SCLC is a mechanism where the current conducted through the material is limited by a distribution of traps in the bulk material [46]. In the MIM configuration, the injection of electrons at an ohmic contact causes this space-charge-limited current [47]. RS conduction is reported in many plasma polymers, i.e. polyaniline [48], polyfurfural [49] and the plasma polymers of some natural extracts like lemon grass oil, eucalyptus oil, and lynalyl acetate [46]. It is a conduction mechanism where the electrons obtain enough energy to overcome the energy barrier at the metal-dielectric interface to go to the dielectric [47]. PF conduction mechanism is very similar to RS wherein the trap barrier of the material is lowered by the application of a sufficiently high electric field across the dielectric film and electrons may emit from traps into the conduction band [46, 47]. The following equation is applicable to both PF and RS process [50]:

$$J = J_o \exp\left(\frac{\beta F^{1/2} - \phi}{kT}\right) \tag{VII.7}$$

where J_o is the low field current density, F is the applied electric field, β is the coefficient of the static electric field, k is Boltzmann's constant in eV/K, T is the absolute temperature and ϕ is the ionization energy of localized centers and coulomb barrier height of the electrode polymer interface in the case of PF and RS mechanisms, respectively. The parameter β is the field lowering coefficient and is given by β_{PF} and β_{RS} for PF and RS conduction, respectively [50]:

$$2\beta_{RS} = \beta_{PF} = \left(\frac{q^3}{\pi \varepsilon_o \varepsilon_r}\right)^{1/2} \tag{VII.8}$$

where q is the charge of an electron, ε_o the permittivity of free space, ε_r the dielectric constant of the bulk material and the units of β given in eV $m^{1/2}$ $V^{-1/2}$.

In order to explain the means of conduction in insulators, each of the three aforementioned mechanisms can be used and it is important to determine which effect most adequately accounts for the charge transport. This can be achieved by analyzing the shape of the $J-V$ curves under different conditions. In the case of SCLC, double log plot of the form ln $J-$ln V should provide a linear characteristic, while for PF and RS conduction, plotting ln J vs. $V^{0.5}$ will provide a linear characteristic. Furthermore, differentiation between the types of the electronic conduction can be done by investigating the dependence of J on film thickness, d ($J \propto d^{-l}$) for the samples of different thickness at a constant voltage, where l is the parameter dependent on the trap distribution within the material. A slope $l < 3$ is indicative of PF or RS conduction, while $l \geq 3$ indicates the possibility of SCLC.

For pp–GT thin films, plotting ln J vs. ln V produced less linear plots than ln J vs. $V^{0.5}$ suggesting the possibility that PF or RS conduction may dominate in this region (Figure VII.9). Additionally, no film thickness dependence of current density was observed discounting SCLC as the dominating charge transport effect in pp–GT films. The J–V characteristics in the high field region (V >1.5 V) were therefore demonstrated from the viewpoint of PF and RS conduction, using Eq. VII.8.

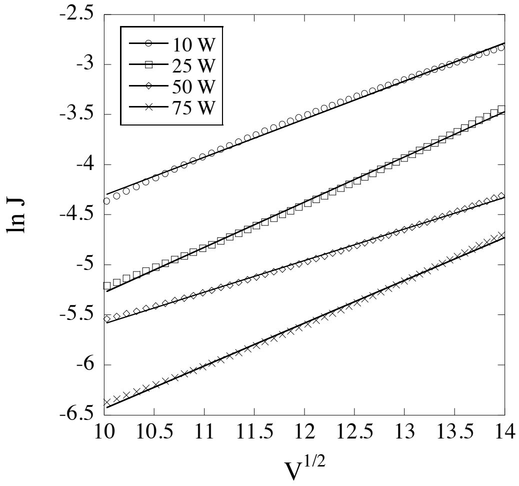

Figure VII.9. Variation of ln J with square root of applied voltage V for pp–GT thin films

In order to differentiate between PF and RS mechanisms, β_{PF} and β_{RS} values can be compared to experimentally determined β coefficient (β_{exp}) [46]. The following equation can be used to determine β_{exp}:

$$\beta_{\mathrm{exp}} = \mathrm{skTd}^{1/2} \qquad \text{(VII.9)}$$

where s is the coefficient of the linear fit of on ln J–$V^{0.5}$ characteristic. Table VII.2 summarizes the experimental and theoretical values of β calculated from Eq. VII.8 and VII.9 for pp–GT thin films.

Table VII.2. Experimental β_{exp} and theoretical β_{PF} and β_{RS} values of pp–GT thin films

RF power	β_{exp}	β_{PF}	β_{RS}
10W	1.80×10^{-5}	4.61×10^{-5}	2.30×10^{-5}
25W	1.82×10^{-5}	4.73×10^{-5}	2.36×10^{-5}
50W	1.87×10^{-5}	4.79×10^{-5}	2.38×10^{-5}
75W	1.89×10^{-5}	5.21×10^{-5}	2.60×10^{-5}

From Table VII.2, β_{exp} is in best agreement with β_{RS} and hence, in the higher field region Schottky mechanism is likely to dominate charge transport. Furthermore, the value of β_{exp} does not change significantly indicating that ε_r remains constant with variations in deposition power.

VII.2.7 ELECTRICAL RESISTIVITY MEASUREMENTS

The resistivity of the pp–GT thin films was determined from the relation:

$$\rho = \frac{\left(\frac{V}{I}\right)A}{d} \tag{VII.10}$$

where ρ is the resistivity of the material, A is the MIM structure's surface area and d is the thin film thickness. The resistivity for all pp–GT samples are in the order of 10^{10} – 10^{11} Ωm (calculated at 200 V) that confirms the insulating characteristic of pp–GT thin films. An increase in resistivity of the samples with increasing RF deposition power is attributed to the increase in degree of cross-linking in pp–GT thin films fabricated under higher powers. Furthermore, the conductivity (σ) values for films fabricated at different RF deposition powers are presented in Table VII.3. This conductivity value is very low compared with other amorphous, plasma deposited insulators such as plasma polymerized thiophenes that are on the order of 10^{-6} – 10^{-10} [49]. The lowest reported conductivity for thiophenes was also found for sample fabricated at higher RF deposition powers, and this decrease attributed to the more amorphous nature of the film.

Table VII.3. Conductivity values (at 6V) and breakdown strength (F_b) of pp–GT thin films

RF power	σ, S/cm	F_b, MV/cm
10W	1.39×10^{-12}	1.48
25W	2.91×10^{-13}	1.72
50W	1.92×10^{-13}	1.94

75W	1.02×10^{-13}	2.05

VII.2.8 DIELECTRIC BREAKDOWN

Insulating properties of pp–GT thin films are determined by measuring the leakage current density with different applied fields. As the plasma power increased from 10 to 75 W, the leakage current densities decreased and the field (F_b) at which breakdown occurred, is ~2 MV/cm (Table VII.3). This indicates that the films have a compact structure with a high density and are pinhole-free. These phenomena are well known to have a lower leakage current density and higher breakdown field. This value of 2 MV/cm is comparable to plasma deposited thiophene and octafluorocylcobutane, which have a reported value of 2 MV/cm [39]. The dielectric breakdown study was performed on pp–GT samples fabricated at 75W, at different thicknesses (250nm, 500nm and 800nm) to determine whether the property showed any thickness dependence. For all the films, the breakdown field was found be ~2 MV/cm and the property of the films were therefore independent of thickness.

The dielectric strength of polymer thin films is usually dependent on various structural characteristics associated with the packing density of the materials, including the polarity, dimension, and steric structure of the molecules and/or molecular building blocks [39]. The breakdown strength (2 MV/cm) at 75W for pp–GT film reveals that a suitable reaction environment for the γ-terpinene molecules create a relatively high concentration of small molecular activated species with mostly aliphatic C–H moieties [31], promoting the formation of a highly cross–linked structure. The lower dielectric strengths observed for films fabricated at lower RF deposition power are attributed to the less-densely cross–linked structures.

VII.3 CONCLUSION

Electrical properties of the plasma polymerized γ-terpinene thin films fabricated using the plasma–enhanced chemical vapor deposition is studied using the MIM structure. The real part of permittivity decreases linearly below 10 Hz for all the samples fabricated with RF powers 10, 25, 50 and 75 W. The bulk of the contribution is electronic. The initial drop in dielectric constant at low frequencies can primarily be attributed to some orientational polarization caused by the presence of trapped free radicals or the formation of polar/oxygenated groups. At a frequency of 100 KHz, the dielectric constant of samples fabricated using 10 W RF power is around 12% higher than samples fabricated using 75 W RF deposition power. The conduction mechanism responsible for the charge transport through the material was recognized as ohmic in the low voltage region, while Schottky conduction was found to be the dominating mechanism for charge transport through the films at the higher voltage region. Variations in RF deposition power did not influence the conduction mechanism, while conductivity values was found to decrease with increasing RF deposition power.

The pp–GT film cross–link density is found to play a key role in determining the breakdown strength. The continuity of the path provided to charge carriers is disrupted by increased cross–link density (as RF deposition power increases) that in turn results in higher breakdown strength. The breakdown field for the samples were in the range of 1.5 MV/cm to 2 MV/cm. No relaxation peaks were observed in the measured frequency range at room temperatures, indicative of very long relaxation times, which provide further evidence of the minimal contribution of orientation polarization to the measured relative permittivity. The dielectric function has been measured as a function of temperature, and a single relaxation peak was found to dominate the dielectric function. Determination of the distribution of relaxation times from the data using regularization methods revealed the presence of several underlying relaxation processes in addition to the dominant peak.

In summary, permittivity values of pp–GT thin films combined with high resistivity confirms the material's potential as an insulating layer for fabrication of organic electronic devices. These properties, in addition to the other desirable properties of the films such as optical transparency and high adhesion to a variety of substrates, also make pp–GT thin films a suitable candidate for other dielectric applications in electronics.

REFERENCES

[1] D. Z. Pai, K. Ostrikov, S. Kumar, D. A. Lacoste, I. Levchenko, and C. O. Laux, "Energy efficiency in nanoscale synthesis using nanosecond plasmas," *Sci. Rep.,* vol. 3, 2013.

[2] J. Ahmad, K. Bazaka, and M. Jacob, "Optical and Surface Characterization of Radio Frequency Plasma Polymerized 1-Isopropyl-4-Methyl-1,4-Cyclohexadiene Thin Films," *Electronics,* vol. 3, pp. 266-281, 2014.

[3] K. Bazaka, M. Jacob, V. Truong, F. Wang, W. Pushpamali, J. Wang, A. Ellis, C. Berndt, R. Crawford, and E. Ivanova, "Effect of plasma-enhanced chemical vapour deposition on the retention of antibacterial activity of terpinen-4-ol," *Biomacromolecules,* vol. 11, p. 2016, 2010.

[4] H. Yasuda, "Plasma Polymerization," *Academic Press, New York,* 1985.

[5] L. J. Anderson and M. V. Jacob, "Effect of RF power on the optical and morphological properties of RF plasma polymerised linalyl acetate thin films," *Applied Surface Science,* vol. 256, pp. 3293-3298, 2010.

[6] K. Bazaka and M. V. Jacob, "Post-deposition ageing reactions of plasma derived polyterpenol thin films," *Polymer Degradation and Stability,* vol. 95, pp. 1123-1128, 2010.

[7] M. V. Jacob, K. Bazaka, M. Weis, D. Taguchi, T. Manaka, and M. Iwamoto, "Fabrication and characterization of polyterpenol as an insulating layer and incorporated organic field effect transistor," *Thin Solid Films,* vol. 518, pp. 6123-6129, 2010.

[8] L. Trabzon and O. O. Awadelkarim, "Changes in material properties of low-k interlayer dielectric polymers induced by exposure to plasmas," *Microelectronic Engineering,* vol. 65, pp. 463-477, 2003.

[9] Y. Taur, Y. J. Mii, D. J. Frank, H. S. Wong, D. A. Buchanan, S. J. Wind, S. A. Rishton, G. A. Sai-Halasz, and E. J. Nowak, "CMOS scaling into the 21st century: 0.1 μm and beyond," *IBM Journal of Research and Development,* vol. 39, pp. 245-260, 1995.

[10] Y. C. Quan, J. Joo, and D. Jung, "Polymer-like organic thin films deposited by plasma enhanced chemical vapor deposition using the para-xylene precursor as low dielectric constant interlayer dielectrics for multilevel metallization," *Japanese Journal of Applied Physics, Part 1: Regular Papers and Short Notes and Review Papers,* vol. 38, pp. 1356-1358, 1999.

[11] J. Ahmad, K. Bazaka, L. J. Anderson, R. D. White, and M. V. Jacob, "Materials and methods for encapsulation of OPV: A review," *Renewable and Sustainable Energy Reviews,* vol. 27, pp. 104-117, 2013.

[12] C. D. Easton and M. V. Jacob, "Optical characterisation of radio frequency plasma polymerised Lavandula angustifolia essential oil thin films," *Thin Solid Films,* vol. 517, pp. 4402-4407, 2009.

[13] X. Jiang, W. F. Burgoyne Jr, and L. M. Robeson, "Sequestration of electroactive materials in a high Tg, insulating polymer matrix for optoelectronic applications. Part 2. Photovoltaic devices," *Polymer,* vol. 47, pp. 4124-4131, 2006.

[14] W.-J. Yoon, D. Bhattacharyya, R. B. Timmons, and P. R. Berger, "Plasma-polymerized multistacked bipolar gate dielectric for organic thin-film transistors," *Organic Electronics,* vol. 11, pp. 1767-1771, 2010.

[15] H. Biederman and D. Slavinska, "Plasma polymer films and their future prospects," *Surface and Coatings Technology,* vol. 125, pp. 371-376, 2000.

[16] D. Sakthi Kumar and Y. Yoshida, "Dielectric properties of plasma polymerized pyrrole thin film capacitors," *Surface and Coatings Technology,* vol. 169–170, pp. 600-603, 2003.

[17] L. Xueqiang, B. Weihong, and Z. Tong, "Low voltage copper phthalocyanine organic thin film transistors with a polymer layer as the gate insulator," *Journal of Semiconductors,* vol. 31, p. 124007, 2010.

[18] L. Trabzon, O. O. Awadelkarim, and J. Werking, "The effects of interlayer dielectric deposition and processing on the reliability of N-channel transistors," *Solid-State Electronics,* vol. 42, pp. 2031-2037, 1998.

[19] C. Biloiu, L. A. Biloiu, Y. Sakai, H. Sugawara, and A. Ohta, "Amorphous fluorocarbon polymer (a-C:F) films obtained by plasma enhanced chemical vapor deposition from perfluoro-octane (C 8F 18) vapor. II. Dielectric and insulating properties," *Journal of Vacuum Science and Technology A: Vacuum, Surfaces and Films,* vol. 22, pp. 1158-1165, 2004.

[20] H. Spanggaard and F. C. Krebs, "A brief history of the development of organic and polymeric photovoltaics," *Solar Energy Materials and Solar Cells,* vol. 83, pp. 125-146, 2004.

[21] C.-K. Tai, C.-A. Hsieh, K.-L. Hsiao, B.-C. Wang, and Y. Wei, "Novel dipolar 5,5,10,10-tetraphenyl-5,10-dihydroindeno[2,1-a]-indene derivatives for SM-OPV: A combined theoretical and experimental study," *Organic Electronics,* vol. 16, pp. 54-70, 2015.

[22] F. C. Krebs, "Alternative PV: Large scale organic photovoltaics," *Refocus,* vol. 6, pp. 38-39, 2005.

[23] H. C. Weerasinghe, S. E. Watkins, N. Duffy, D. J. Jones, and A. D. Scully, "Influence of moisture out-gassing from encapsulant materials on the lifetime of organic solar cells," *Solar Energy Materials and Solar Cells,* vol. 132, pp. 485-491, 2015.

[24] D.-w. Choi, S.-J. Kim, J. H. Lee, K.-B. Chung, and J.-S. Park, "A study of thin film encapsulation on polymer substrate using low temperature hybrid ZnO/Al_2O_3 layers atomic layer deposition," *Current Applied Physics,* vol. 12, Supplement 2, pp. S19-S23, 2012.

[25] S.-W. Seo, E. Jung, H. Chae, and S. M. Cho, "Optimization of Al_2O_3/ZrO_2 nanolaminate structure for thin-film encapsulation of OLEDs," *Organic Electronics,* vol. 13, pp. 2436-2441, 2012.

[26] N. Kim, W. J. Potscavage Jr, A. Sundaramoothi, C. Henderson, B. Kippelen, and S. Graham, "A correlation study between barrier film performance and shelf lifetime of encapsulated organic solar cells," *Solar Energy Materials and Solar Cells,* vol. 101, pp. 140-146, 2012.

[27] M. D. Clark, M. L. Jespersen, R. J. Patel, and B. J. Leever, "Ultra-thin alumina layer encapsulation of bulk heterojunction organic photovoltaics for enhanced device lifetime," *Organic Electronics,* vol. 15, pp. 1-8, 2014.

[28] J. Jin, S. Chen, and J. Zhang, "Investigation of UV aging influences on the crystallization of ethylene-vinyl acetate copolymer via successive self-nucleation and annealing treatment," *Journal of Polymer Research,* vol. 17, pp. 827-836, 2010.

[29] W. Ma, C. Yang, X. Gong, K. Lee, and A. J. Heeger, "Thermally Stable, Efficient Polymer Solar Cells with Nanoscale Control of the Interpenetrating Network Morphology," *Advanced Functional Materials,* vol. 15, pp. 1617-1622, 2005.

[30] H.-K. Kim, D. G. Kim, K. S. Lee, M. S. Huh, S. H. Jeong, K. I. Kim, and T.-Y. Seong, "Plasma damage-free sputtering of indium tin oxide cathode layers for top-emitting organic light-emitting diodes," *Applied Physics Letters,* vol. 86, pp. 183503-3, 2005.

[31] J. Ahmad, K. Bazaka, M. Oelgemöller, and M. V. Jacob, "Wetting, solubility and chemical characteristics of plasma polymerized 1-isopropyl-4-methyl-1,4-cyclohexadiene thin films," *Coatings,* vol. 4, pp. 527-552, 2014

[32] M. V. Jacob, C. D. Easton, G. S. Woods, and C. C. Berndt, "Fabrication of a novel organic polymer thin film," *Thin Solid Films,* vol. 516, pp. 3884-3887, 2008.

[33] L. Zong, S. Zhou, R. Sun, L. C. Kempel, and M. C. Hawley, "Dielectric analysis of a crosslinking epoxy resin at a high microwave frequency," *Journal of Polymer Science Part B: Polymer Physics,* vol. 42, pp. 2871-2877, 2004.

[34] R. Casalini, D. Fioretto, A. Livi, M. Lucchesi, and P. A. Rolla, "Influence of the glass transition on the secondary relaxation of an epoxy resin," *Physical Review B,* vol. 56, pp. 3016-3021, 1997.

[35] T. Corrales, M. M. Villavieja, C. Peinado, and P. Bosch, "β- and γ-relaxations of low density polyethylene: Study by fluorescent probes," *Journal of Photochemistry and Photobiology A: Chemistry,* vol. 182, pp. 52-59, 2006.

[36] K. Endo, K. Shinoda, and T. Tatsumi, "Plasma deposition of low-dielectric-constant fluorinated amorphous carbon," *Journal of Applied Physics,* vol. 86, pp. 2739-2745, 1999.

[37] L. J. Anderson and M. V. Jacob, "Temperature dependent electrical impedance spectroscopy measurements of plasma enhanced chemical vapour deposited linalyl acetate thin films," *Thin Solid Films,* vol. 5347, pp. 452-458, 2013.

[38] A. A. Dakhel, "Mechanisms of dc-current transfer in tris(acetylacetonato)iron(III) films," *Journal of Non-Crystalline Solids,* vol. 353, pp. 1529-1533, 2007.

[39] H. Jiang, L. Hong, N. Venkatasubramanian, J. T. Grant, K. Eyink, K. Wiacek, S. Fries-Carr, J. Enlow, and T. J. Bunning, "The relationship between chemical structure and

dielectric properties of plasma-enhanced chemical vapor deposited polymer thin films," *Thin Solid Films,* vol. 515, pp. 3513-3520, 2007.

[40] A. Goswami and A. P. Goswami, "Dielectric and optical properties of ZnS films," *Thin Solid Films,* vol. 16, pp. 175-185, 1973.

[41] S. D. Phadke, "Dielectric properties of plasma-polymerized ferrocene films," *Thin Solid Films,* vol. 48, pp. 319-324, 1978.

[42] P. Prins, F. C. Grozema, J. M. Schins, and L. D. A. Siebbeles, "Frequency dependent mobility of charge carriers along polymer chains with finite length," *physica status solidi (b),* vol. 243, pp. 382-386, 2006.

[43] S. Singha and J. M. Thomas, "Permittivity and Tan Delta Characteristics of Epoxy Nanocomposites in the Frequency Range of 1 MHz–1 GHz," *IEEE Transactions on Dielectrics and Electrical Insulation,* vol. 15, pp. 2-11, 2008.

[44] M. El-Shabasy and A. S. Riad, "Dielectric behaviour of polycarbonate," *Physica B: Condensed Matter,* vol. 222, pp. 153-159, 1996.

[45] M. A. M. Seyam, "Dielectric relaxation in polycrystalline thin films of In_2Te_3," *Applied Surface Science,* vol. 181, pp. 128-138, 2001.

[46] L. J. Anderson and M. V. Jacob, "Electrical characterisations of plasma polyermised linalyl acetate," *Materials Science and Engineering: B,* vol. 177, pp. 311-315, 2012.

[47] F.-C. Chiu, "A Review on Conduction Mechanisms in Dielectric Films," *Advances in Materials Science and Engineering,* vol. 2014, p. 18, 2014.

[48] C. J. Mathai, S. Saravanan, S. Jayalekshmi, S. Venkitachalam, and M. R. Anantharaman, "Conduction mechanism in plasma polymerized aniline thin films," *Materials Letters,* vol. 57, pp. 2253-2257, 2003.

[49] M. S. Silverstein and I. Visoly-Fisher, "Plasma polymerized thiophene: molecular structure and electrical properties," *Polymer,* vol. 43, pp. 11-20, 2002.

[50] S. Majumder and A. H. Bhuiyan, "DC conduction mechanism in plasma polymerized vinylene carbonate thin films prepared by glow discharge technique," *Polymer Science Series A,* vol. 53, pp. 85-91, 2011/01/01 2011.

CHAPTER VIII

AGING AND STABILITY STUDY

In this chapter, the effect of ambient aging, heat treatment and UV exposure on the material properties of pp–GT thin films is investigated. pp–GT thin film encapsulation performance was also examined on a PCPDTBT:$PC_{70}BM$ solar cell. A manuscript outlining the finding of this study are communicated as *Ahmad, J., Oelgemöller, M., Bazaka, K., Uddin, A. and Jacob, M. V. (2014) Aging, thermal degradation, and photostability of plasma polymerized γ-terpinene thin films* (submitted to *Polymer Degradation and Stability* for publication)**.**

AGING, THERMAL DEGRADATION, AND PHOTOSTABILITY OF PLASMA POLYMERIZED γ –TERPINENE THIN FILMS

Organic polymeric thin films have many promising applications, primarily in organic light emitting diodes (OLEDs), thin film transistors, and OPVs because of many advantages such as mechanical flexibility, low-temperature processing capability at low cost, and applicability to plastic substrates [1-7]. Typically, these devices have layered structures in a form of thin films of different functional materials [3]. Organic polymeric thin films can be obtained by spin coating, physical vapor deposition (PVD), printing, doctor blading etc. However, the practicality of these materials depends on whether the stability, *i.e.*, their properties are retained throughout the lifetime of the device under ambient environment or when subjected to extreme conditions, such as annealing or ultraviolet (UV) irradiation [8].

The stability of OPVs and flexible electronic devices over time can be divided into two levels, the inherent stability of the cells and the overall stability of the devices. The overall device stability can be tackled by ensuring a proper encapsulation coating. An efficiency of 14.1% was found with V_{OC} = 590 mV at 360 °C for solar cells with SiN_x encapsulation deposited by low frequency plasma polymerization. The oxygen transmission rate (OTR) and water vapor transmission rate (WVTR) for SiN_x films are $0.01\ \text{cm}^3\ \text{m}^{-2}\ \text{day}^{-1}$ and $0.01\ \text{g m}^{-2}\ \text{day}^{-1}$, respectively [9]. However, *Si* is very permeable to gas and water vapor and damp heat can cause reduction in transmission [10]. Ethylene vinyl acetate (EVA) is another encapsulating material that offers weather resistance and long-term reliability under long periods of exposure to different elements [11]. However, weatherability testing of EVA under UV irradiation and evaluation by FTIR measurements shows apparent absorption growth at about $1715\ \text{cm}^{-1}$ and $1175\ \text{cm}^{-1}$, both representing carbonyl C=O stretching vibration in the rapidly forming ketone structure [9]. Such ketone structures are unstable and lead to molecular decomposition in EVA. Furthermore, adhesion strength can be affected by the processing conditions, in particular damp heat and exposure time. New materials for encapsulation of OPVs and other devices are therefore essential.

Over the last few years, thin films from essential oils have been developed and identified as promising candidates for applications in electronics, as dielectric and encapsulation layers [4, 12-15], and as bio-interface coatings for implantable electronics [16]. This chapter reports the fabrication of polymer thin films from 1-isopropyl-4-methyl-1,4-cyclohexadiene, also known as γ-terpinene, using radio frequency (RF) plasma polymerization. γ-terpinene belongs to the group of monocyclic terpinenes that is an isomeric hydrocarbon isolated directly from *Melaleuca alternifolia* essential oil. Recent studies revealed that the optical properties of the fabricated plasma polymerized γ-terpinene (pp–GT) thin films are promising, with transparency to the optical wavelengths and refractive index of 1.57–1.58 (at 500 nm) [4]. It is reported that these polymers possess an optical band gap (E_g) of ~3 eV that falls into the insulating E_g region. Independent of deposition conditions, the surfaces are smooth and defect-free, with uniformly distributed morphological features and average roughness well below 0.30 nm [4]. The optical and surface characteristics suggest that the pp–GT thin films have the potential to be implemented in optoelectronic and insulating applications. With the intention to use these films in OPVs, especially as encapsulation coatings and insulating layers in flexible electronics, this chapter primarily aims at investigating the stability of pp–GT thin films under ambient environment and extreme conditions, *i.e.*, annealing or UV irradiation. Samples fabricated at 10, 25, 50 and 75W RF power levels are compared to investigate the effect of deposition power on the stability of the polymer films.

VIII.1 EXPERIMENTAL

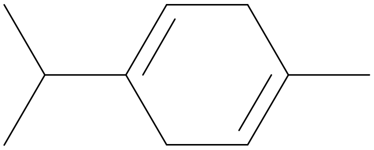

Figure VIII.1. Chemical structure of 1-isopropyl-4-methyl-1,4-cyclohexadiene ($C_{10}H_{16}$)

VIII.1.1 PREPARATION OF pp–GT THIN FILMS

pp–GT Thin films were deposited on high quality glass microscope slides inside a custom made, cylindrical RF polymerization chamber, 0.75 m in length with an inner diameter of 0.055 m (approximate volume of 0.018 cm^3). The substrates were thoroughly cleaned using extran, an ultrasonic bath of distilled water, and rinsed with isopropanol prior to deposition. Using this procedure outlined in [7] plasma polymer films were fabricated from γ-terpinene monomer (figure 1) at various RF power levels (10, 25, 50 and 75 W). Samples were also produced at a constant RF power level (25 W) and varying deposition times to investigate thickness dependency of material degradation.

VIII.1.2 OPTICAL STUDY

pp–GT thin films were stored in ambient conditions (23 °C) and their optical properties are observed for a period of 1400h. Psi and delta data are collected using variable angle spectroscopic ellipsometer (model M-2000, J. A. Woollam Co. Inc.) over the spectral range from 200 to 1000 nm at three angles of incidence, φ = 55°, 60°, and 65°, (near the Brewster angle) to minimize noise and systematic errors in the measured data [17]. The procedures and methods of measurement are described elsewhere [18, 19]. The refractive index was calculated using the Cauchy theory (Eq. VII.1) at the sodium (Na) D wavelength (λ = 589.3 nm) [18] at room temperature for pp–GT thin films, where the parameters A, B, and C are constants obtained from the ellipsometry measurements:

$$n(\lambda) = A + \frac{B}{\lambda^2} + \frac{C}{\lambda^4} \tag{VII.1}$$

VIII.1.3 SURFACE STUDY

The surface morphology and roughness parameters of the films were determined from AFM images acquired on a NT-MDT NTEGRA Prima AFM operating in semi-contact (tapping) mode, using (NSC05, NT-MDT) cantilevers with a spring constant of 11 N/m, a tip radius of curvature of 10 nm, an aspect ratio of 10:1 and a resonance frequency of 150 KHz. 3D interactive visualization and statistical approximation was used to analyze the topographic profiles of the surfaces. Scanning was performed perpendicular to the axis of the cantilever at a rate of typically 1 Hz, with scan areas of 1 μm × 1 μm, 10 μm × 10 μm and 50 μm × 50 μm.

VIII.1.4 WETTING AND CHEMICAL STUDY

Wettability of pp–GT thin films was evaluated by contact angle (CA) measurements with water using a video-based optical CA measuring system (KSV 101). Advancing and receding CAs were measured using the dynamic sessile drop technique. First, a sessile drop of probe liquid of known volume was placed on the surface of the pp–GT sample, ensuring that the needle remained in the drop during the measurement to avoid undesired vibration. The drop was then modified by slowly adding volume, with the advancing angle estimated as the largest contact angle possible without increasing its solid/liquid interfacial area. The receding angle was estimated as the minimum possible angle that can be achieved by slowly removing the probe liquid from the drop without decreasing the drop's contact area. Both the advancing and receding angle were estimated as the average of the angles on both sides of the drop profile. CA hysteresis (CAH) was estimated as the difference between the advancing and receding angle.

FTIR spectroscopy was carried out for the chemical characterization of the pp–GT thin films using a Perkin Elmer Spectrum 100 FTIR spectrometer. Spectra were obtained in transmission mode in the region of 4000–500 cm^{-1}, where 32 scans were acquired for each sample at a resolution of 1 cm^{-1}. Contributions from CO_2 and H_2O were eliminated from the spectra by a background subtraction procedure, where the background was pre-recorded under the same atmospheric conditions.

VIII.1.5 THERMAL DEGRADATION STUDY

The thermal degradation studies of pp–GT thin films are accomplished using the temperature stage attachment of the spectroscopic ellipsometer. The temperature of the stage is increased in steps of 5 °C every 5 min up to 405 °C to ensure thermal equilibrium between the stage and sample. Dynamic ellipsometric measurements were performed using the CompleteEASE software, which measures dynamic Ψ and Δ parameters at fixed $\varphi = 70°$. The data was then imported into the WVASE32 software package for analysis. Experimentally obtained Ψ and Δ were used to derive the optical constants based on a model of the sample built in the analysis software (WVASE32) via regression analysis. FTIR spectrometry was also employed to analyze the alteration in the chemical conformation of the films.

VIII.1.6 PHOTOSTABILITY STUDY

A top irradiation chamber photoreactor (Luzchem LZC-1) was used in this study. The reactor was equipped with fluorescent tubes (8 × 8 W) of different wavelengths ($\lambda = 254$, 300 ± 25 and 350 ± 25 nm). The internal irradiation chamber had internal dimensions of approximately 30.48 cm wide, 30.48 cm deep and 21.59 cm high, respectively. A build-in fan and exhaust stabilized the temperature to about 3–4 °C above room temperature. For UV–A (350 ± 25 nm) and UV–B (300 ± 25 nm) irradiations, 8W fluorescent tubes from Southern New England Ultraviolet Company (model RPR-3000Å and RPR-3500Å, respectively) were used. Philips UVC (germicidal) lamps (model TUV 8W FAM) were used for UV–C (254 nm) irradiations. After the irradiation, pp–GT samples were examined by ellipsometer, ATR-FTIR, AFM and CA measuring system (KSV 101).

VIII.1.7 ORGANIC SOLAR CELL STUDY (WITH pp–GT ENCAPSULATION)

This work investigates the effects of the pp–GT encapsulation on solution-processed OPV, *i.e.*, organic solar cells based on a thin film blend of poly[2,1,3-benzothiadiazole-4,7-diyl[4,4-bis(2-ethyl- hexyl)-4H-cyclopenta[2,1-b:3,4-b$'$]dithiophene-2,6-diyl]] (PCPDTBT) and [6,6]-phenyl C70 butyric acid methyl ester ($PC_{70}BM$). The device area used was 0.13 cm^2. OPV device efficiency measurements were performed using a QEX10 spectral response system from PV measurements, Inc. The current density–voltage (*J–V*) measurements were performed using an

IV5 solar cell *I–V* testing system from PV measurement, Inc. (using a Keithley 2400 source meter) under illumination power of 100 mW cm^{-2} by an AM 1.5G solar simulator (Oriel model 94023A; 100 mW cm^{-2}). OPV device efficiency and *J–V* properties of as-fabricated and pp–GT-encapsulated devices were measured for a period of 80 days.

VIII.2 RESULTS AND DISCUSSION

VIII.2.1 AGING OF POLYMER

pp–GT thin films fabricated at 10, 25, 50 and 75W were stored for up to 1400 h and subsequently investigated by spectroscopic ellipsometry. The percentage (%) changes in refractive index for the duration of the aging period are detailed in Table VIII.1. The change in refractive index at 600 nm for the polymers is also presented in Figure VIII.2.

Table VIII.1. Post-deposition change in refractive index (%) (at different wavelengths) after approximately 1400 h

Power (W)	Refractive index change, %		
	300 nm	600 nm	900 nm
10	0.08	0.11	0.14
25	0.38	0.27	0.09
50	0.51	0.32	0.11
75	0.59	0.36	0.17

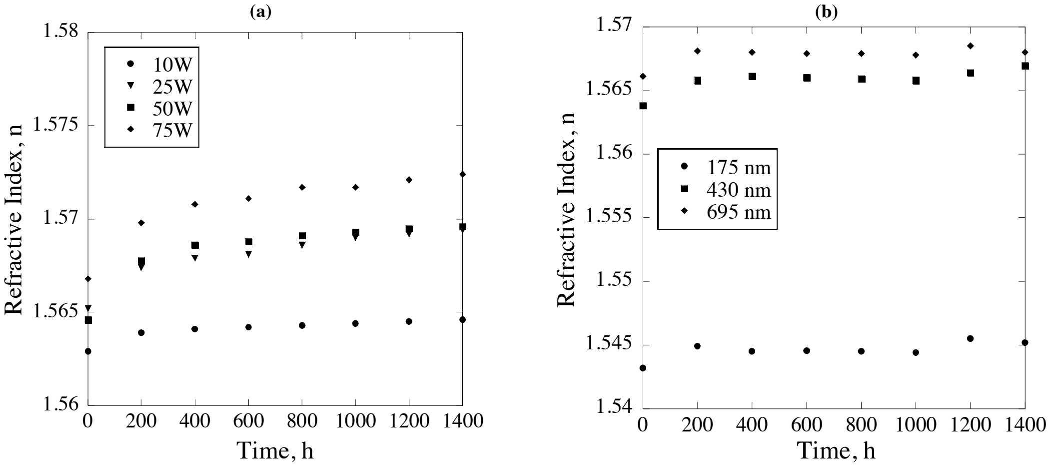

Figure VIII.2. Refractive index (at a wavelength of 600 nm) for pp–GT films at (a) various RF powers and (b) thicknesses

The refractive index increased for approximately 150 h after deposition for all the samples independent of deposition power, followed by a slowdown in the rate of change. The refractive index remained stable for the remainder of the measurement. Thin films having large oxygen content show very low values of refractive index [20]. Oxygenated pp–GT film fabricated at 10W (oxygen content of 11.8% [7]) therefore showed much lower refractive index value compared to 25W, 50W and 75W.

The effect of thickness on the aging for pp–GT films fabricated at 25 W RF power was also investigated. Samples of thicknesses 175, 430 and 695 nm were monitored for approximately 1400 h. The changes in refractive index at 600 nm are presented in Figure VIII.2. These results reveal that the aging rate is independent of the film thickness, as a small increase in refractive index exists for an increase in thickness.

UV-Vis absorption spectra of pp–GT films fabricated at 10W, 25W, 50W and 75W RF power levels were collected as-deposited and after 12 months of exposure to ambient environmental conditions using UV–Vis spectroscope to determine if films retained their optical transparency over the visible part of the light spectrum. Exposing the films to ambient environmental conditions had no significant effect on the absorbance spectrum. The films possessed similar absorption spectra with absorption ranging to around 400 nm (not shown).

The surface physical states for the pp–GT films immediately after deposition and subsequently after 1400 h of storage in an ambient environment were measured. The topographical features of the investigated pp–GT thin films deposited on glass surfaces are shown in Figure VIII.3.

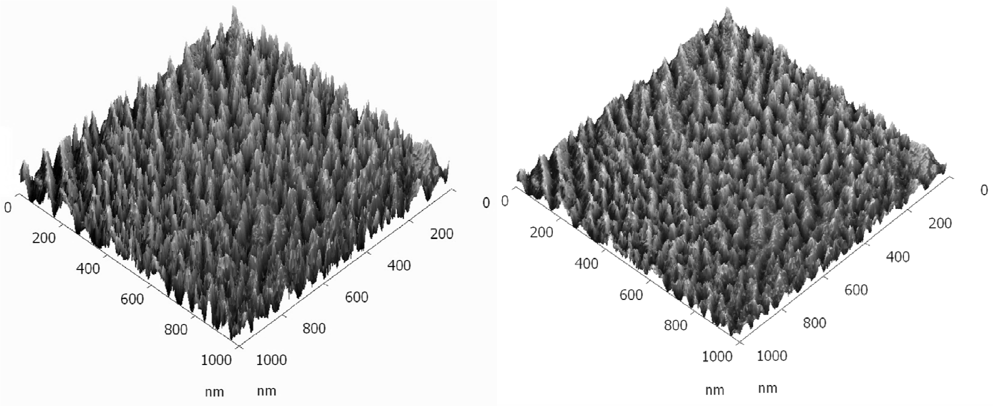

Figure VIII.3. AFM image of pp–GT films fabricated at 25 W as deposited and after 1400 h

pp–GT thin films (as deposited) are smooth, uniform and defect-free, exhibiting consistent morphology across the same film sample. These films do not have prominent features (maximum peak height of 14.8 nm) present on the surface of unmodified substrate. Average roughness (R_a) values for all samples are approximately 0.3 nm. Previous investigations show that surfaces with RMS roughness values below 0.5 nm have an insignificant effect on the fundamental properties of the films [21, 22]. Considering this and the determined roughness of 0.3 nm, the polymerization reactions are considered to take place mostly on the surface of the glass substrate rather than in the gas phase [23]. All polymer surfaces displayed the surface skewness (R_{sk}) > 0 and coefficient of kurtosis (R_{kur}) < 3. Such values for R_{sk} and R_{kur} indicate a disproportionate number of peaks pertinent to the film surfaces and a well spread out height distribution, respectively.

The variation of the chemical structure of the pp–GT films as deposited and after 1400 h of exposure to ambient conditions was used to understand the nature of the degradation process taking place. FTIR spectra of pp–GT films fabricated at 10 W and 75 W are presented in Figure VIII.4.

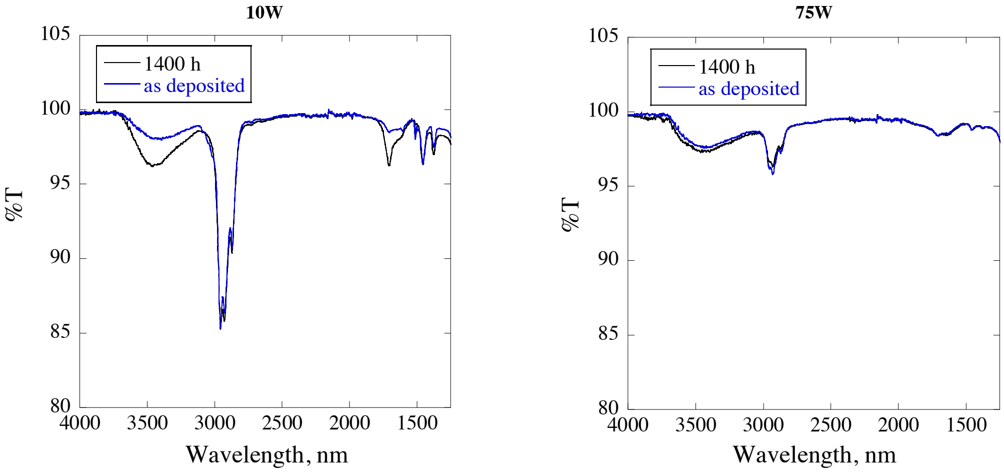

Figure VIII.4. FTIR spectra for 10W and 75W pp–GT thin films as deposited and after 1400 h

Due to the hydrocarbon-based nature of the polymeric films, all FTIR spectra displayed strong C-H stretching vibrations in the range 3000–2800 cm^{-1}. Additional bending vibrations were found around 1500 cm^{-1} [24], although with much lower intensity. The film deposited at higher power showed a drop in intensities, broadening of peaks and loss of fine-structure, indicating a higher degree of cross-linkage and subsequently a reduced homogeneity of bonding. The broad band at approximately 3425 cm^{-1} in all spectra was attributed to water that condensed on the films prior to measurements. Minor oxidation after 1400 h was observed for the film generated at 10W, as evident from the occurrence of a characteristic carbonyl (C=O) stretching vibration at approx. 1700 cm^{-1}. For all other samples, the absence of any clear C-O or C=O vibrations suggests that autooxidation does not occur for the pp-GT films prepared, possibly due to a higher degree of polymerization. In contrast, the film generated at 10W may contain a substantial number of reactive sites for autooxidation [25]. Autooxidation of plasma polymers and thus incorporation of oxygen-containing functional groups (such as hydroxyl, C-OH, carbonyl, C=O, and carboxyl groups, CO_2H) has been reported for poly(α-methylstyrene) [26].

For samples deposited at 25, 50 and 75W, the dominant ν(C-H) peaks remained stable in intensity and location in both as deposited and post-1400 h spectra, confirming stability in the chemical structure (Figure VIII.4). The respective change in refractive indices is therefore attributable to material relaxation [26]. Poly(α-methylstyrene) samples deposited at higher power show higher levels of oxygen incorporation due to the presence of higher concentration of radical sites and increased radical stability, whereas pp–GT films remain largely intact.

VIII.2.2 ESTIMATION OF VOLUMETRIC AGING RATE

From the above analysis, the change in refractive index is found be related to the change in density of the pp–GT films. Refractive index change is therefore used in this chapter to predict the volumetric aging rate. The isothermal volumetric aging rate, *r,* is defined as follows [27]:

$$\mathrm{r} = -\frac{1}{\mathrm{V}}\left(\frac{\partial \mathrm{V}}{\partial \ln \mathrm{t}}\right)_{\mathrm{P,T}} = \left(\frac{\partial \ln \rho}{\partial \ln \mathrm{t}}\right)_{\mathrm{P,T}} \tag{VIII.2}$$

where V is the material specific volume and P and T refer to the pressure and temperature during aging, ρ is the density of the polymer and t is the aging time. Lorentz – Lorentz equation [28] can be used to find this isothermal volumetric aging rate, r.

$$\frac{\mathrm{n}^2-1}{\mathrm{n}^2+2} = \frac{\rho \mathrm{N}_{\mathrm{av}}\alpha}{3\mathrm{M}_0\epsilon_0} \tag{VIII.3}$$

where N_{av} is Avogadro's number, M_0 is the molecular weight of the polymer repeat unit, ε_0 is the permittivity of free space constant and α is the average polarizability of the polymer repeat unit. Eq. VII.3 can be formatted as follows

$$\mathrm{L} = \frac{\mathrm{n}^2-1}{\mathrm{n}^2+2} = \rho \mathrm{C} \tag{VIII.4}$$

where L is defined as the Lorentz-Lorenz parameter and $C = N_{av}\ \alpha\ /\ 3M_0\varepsilon_0$.

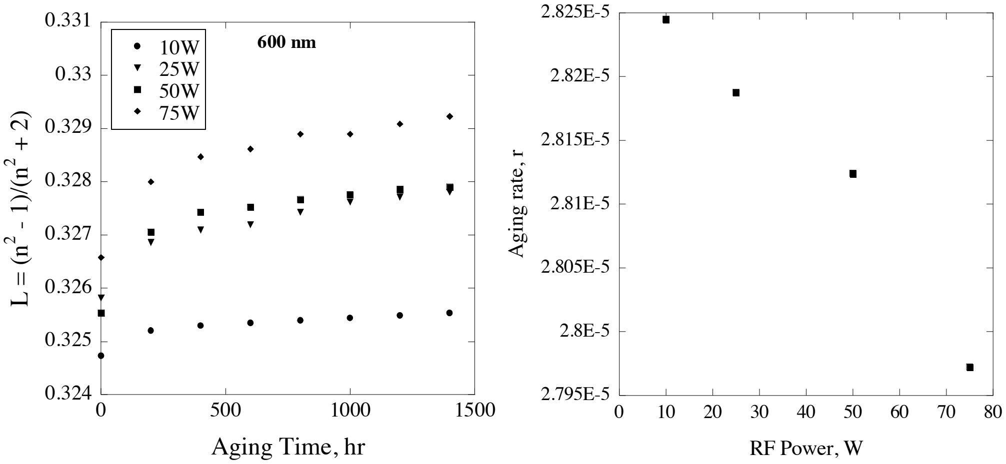

Figure VIII.5. Refractive index change (at a wavelength of 600 nm) in the form of the Lorentz-Lorenz parameter, *L* and volumetric aging rate, *r,* determined from the Lorentz-Lorenz equation *vs*. RF power for pp–GT films thin films

The refractive index data at the wavelength of 600 nm is plotted in the form of the Lorentz-Lorenz parameter for pp–GT polymer thin films in Figure VIII.5. Since the change in refractive index is quite small and *C* may be assumed to be constant during aging, *L* is a linear function of log *t* as observed for the refractive index and also a linear function of density. Indeed, the volumetric aging rate can be calculated from the change of the Lorentz-Lorenz parameter as follows:

$$r = \left(\frac{\partial \ln \rho}{\partial \ln t}\right)_{P,T} = \left(\frac{\partial \ln L}{\partial \ln t}\right)_{P,T} = \left(\frac{\partial \log L}{\partial \log t}\right)_{P,T} \qquad \text{(VIII.5)}$$

Linear relationships were also observed for all pp–GT film samples in the double-logarithmic plot of log *L vs*. log *t,* whose slopes are the volumetric aging rates as shown by Eq. VIII.5. Figure VIII.5 illustrates the aging rates *vs*. RF power for the films fabricated at 10, 25, 50 and 75W. Clearly, the aging rate decreases as the RF power increases for all these polymers. This is consistent with the results obtained from FTIR, CA and optical measurements and surface analysis of pp–GT thin films.

VIII.2.3 EFFECT OF AGING–RELATED CHEMICAL CHANGES ON WETTABILITY

One of the key predictors of surface-solvent interactions, the wetting behavior at polymer surfaces and interfaces, is dependent on the nature and the variable length of polymer chains, density fluctuations and the relatively slow motion of the long chain molecules [29]. CA analysis is typically used to obtain primary data from which the degree of wettability for a specific solid-liquid combination can be inferred [7], with lower CAs indicating better wetting compared to larger CAs. This analysis also provides indirect information about the structure of the film matrix, where observed changes to CAs at the liquid/solid interface are attributed to specific solid-liquid interaction mechanisms, such as absorption, spreading and swelling [30]. Chemical changes caused by aging and specifically oxidation can also alter the CA. Furthermore, interfacial forces may cause surface rearrangement motions and the surface layers (outermost few nm) of polymeric materials may therefore possess a composition that differs from that of the bulk material. This surface restructuring can lead to reduction of the hydrophilic nature of the modified surface. Figure 6 presents the dependence of the hydrophilicity of the pp–GT film surfaces on aging time. With the exemption of the polymer film deposited at 10W, all films showed stable behavior with CAs dropping only slowly after deposition and they stabilized after about 350 h.

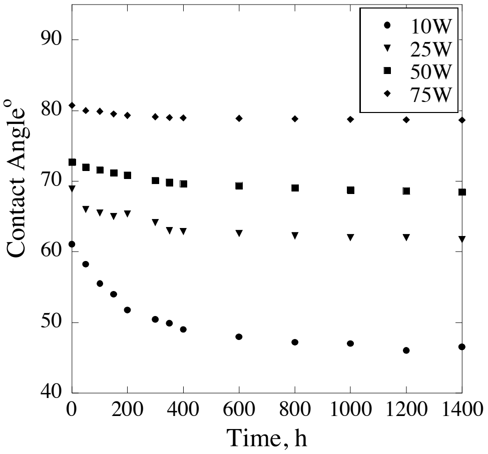

Figure VIII.6. Evolution of the water CAs of pp–GT film surfaces as a function of time

The surfaces of the pp–GT films are thus fairly stable, especially if compared to other surfaces such as polydimethylsiloxane (PDMS). The advancing CA of PDMS decreases from 114° to 108° and the receding CA from 81° to 64° within 5 min of contact between water drop and solid surface [31], respectively. The small CA changes of pp–GT film surfaces with time are consistent with the FTIR data (Figure VIII.4) showing a high degree of chemical stability. The film deposited at 10W showed the largest drop in CA, which is caused by its reduced stability towards autooxidation (as evident from FTIR spectral changes in Figure VIII.4).

VIII.2.4 THERMAL DEGRADATION

The thermal stability of pp–GT films fabricated at 10, 25, 50 and 75 W was investigated by annealing samples to 405 °C (Figure VIII.7). All samples showed a stable behavior up to ~250 °C with no significant change in the refractive index of the material. An increase in RF power resulted in an increase in thermal stability, *i.e.*, higher degradation onset temperature. Greater thermal stability can be attributed to larger degree of cross-linking in polymers fabricated at higher RF powers, as also evident in the FTIR spectra (Figure VIII.4).

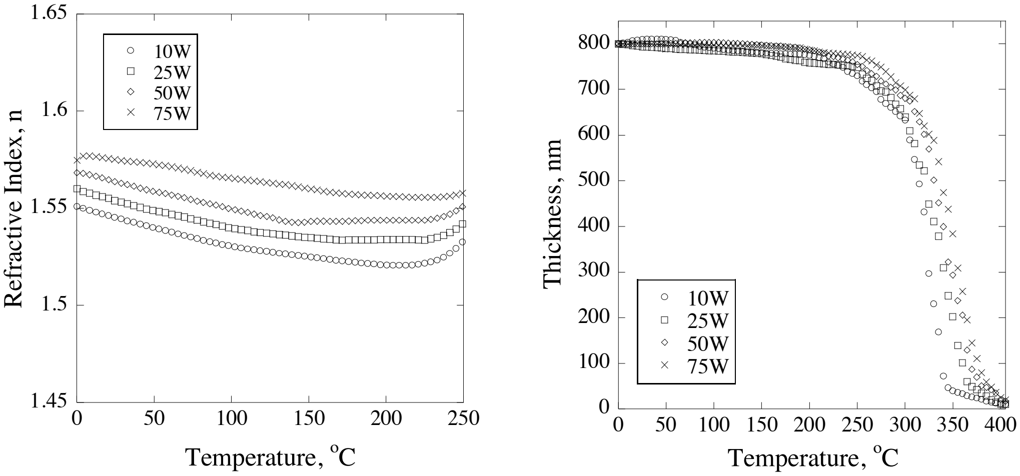

Figure VIII.7. Refractive index (up to 250 °C) and film thicknesses (to 405 °C) of pp-GT as a function of temperature

In general, the mobility of the cross-linked polymer chains increases while annealing up to a specific temperature [32]. This is often used to improve the stability of the plasma polymer. However, it also commonly results in a notable weight loss [32]. Figure VIII.7 shows the variation of refractive index and the film thickness when the sample is heated using the heat cell. The film thickness started decreasing slowly above 200 °C and rapidly above 300 °C. The refractive index also decreased slowly up to 200 °C and beyond that an increase in refractive index is noticed. This increase may be attributed to a phase change and the deposited molecule obtains larger kinetic energy at higher temperature [33] and low-molecular weight polymers are evaporated from the film.

A similar nature of material degradation has been observed for hydrogen-terminated and 2,2-diphenyl hexyl group-terminated poly(methyl methacrylate) (PMMA) [34]. Overall pp-GT can be applied in devices or applications without significant variation in properties up to 200 °C.

FTIR spectra for pp–GT films as deposited at 25W and post-annealing were compared to understand the degradation mechanisms occurring during heat treatment. Identical spectra (Figure VIII.8) obtained confirmed the stable behavior of pp–GT thin films upon annealing up to ~250 °C. As noted above, between approximately 250 °C and 350 °C, all pp–GT films underwent a phase change and the optical parameters of the films experience a large degree of variation. The FTIR spectra of the films after heating to 400 °C (Figure VIII.8) also confirmed this observation. For the hydrocarbon-based pp-GT films produced, thermal oxidation is believed to be the only possible process, subsequently transforming them into less hydrocarbon dense structures [24]. In contrast, functionalized polymers can undergo a variety of thermal degradation processes that can significantly alter their structure. For example, polyvinylalcohol (PVA) based films thermally degrade by dehydration above 220 °C [35].

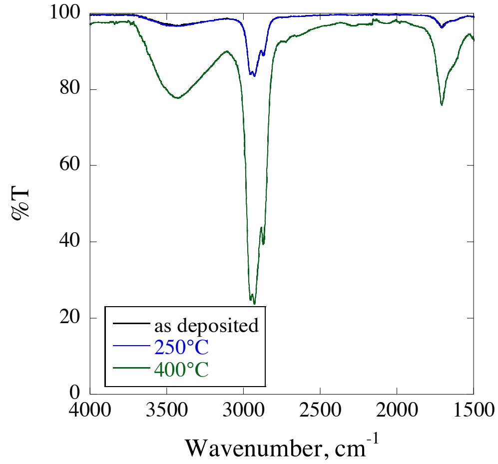

Figure VIII.8. FTIR spectra of as deposited pp–GT film and at 250° and 400°C

The FTIR spectrum of the film treated at 400 °C solely revealed an increase in peak intensity with little changes in peak composition and shape. This intensity change is in line with the change of film density at elevated temperature. The peaks found at 3416 cm^{-1} and 1707 cm^{-1} suggest the presence of oxygen-containing functional groups, specifically hydroxyl (-OH) and carbonyl (C=O) [23], and thus further oxidation of the polymeric film upon heat treatment. However, since these signals were found in similar relative intensity in the initially deposited film, subsequent thermal autooxidation is considered a minor degradation pathway.

VIII.2.5 PHOTO–STABILITY STUDY

Photostability of polymer thin films is a crucial parameter, especially for exterior surfaces or applications as OPV devices that are exposed to radiation. Typically these films are exposed to UV light via sunlight. Solar radiation reaching the surface of the earth is characterized by wavelengths from approximately 295 up to 2500 nm. The solar radiation classified as UV–B (280–315 nm) has an energy of 426–380 kJ mol^{-1} and can thus cause bond cleavages [36]. However, the higher energetic part of UV–B (280–295 nm) is filtered by the stratosphere and does not reach the earth's surface. UV–A light (315–400 nm) has energy between 389 and 300 kJ mol^{-1} and is thus less harmful for organic materials than UV-B [36]. Likewise, visible (400–760 nm) and infrared (760–2500 nm) radiation do not possess sufficient energy amounts to cause chemical changes. UV radiation below 295 nm (UV–C) causes significant degradation that does not occur under normal conditions [37]. However, a high dose of UV radiation (UV–A or UV–B) can have detrimental effects on the properties of these polymers, as cross-linking bonds (linking of polymer chains) are most vulnerable to degradation due to UV exposure. This degradation generally occurs due to C–C bond scission [38] resulting not only in chain scission but also photolysis and/or dissociation of side groups. Other complexities may arise due to the potential reversibility of the degradation. In the presence of oxygen, photooxidation processes with triplet oxygen ($^3O_2$) can furthermore occur, resulting in oxygenation of the polymer and generation of oxygen-containing functional groups. Likewise, photosensitized oxygenations involving singlet oxygen ($^1O_2$) may operate [39, 40], especially in the presence of suitable sensitizing agents. While undesired for polymers, these reactions are useful in organic synthesis with sunlight [41, 42]. Photostable polymers are often used as solid supports for photooxygenation reactions [43].

It has been demonstrated using absorption spectroscopy that pp–GT thin films possessed similar absorption spectra over time and photodegradation followed the dame trend due to UV exposure [4]. Any changes in optical absorbance of pp–GT after UV exposure may be attributed to the formation of photodegradation products [38, 44]. Easton and Jacob, for example, observed similar changes in optical properties in case of oxygen uptake, which was typically extremely rapid during the first few days after deposition associated with a high radical density, followed by a decline and eventual termination [45]. The decrease in decomposition may alternatively be caused by light-absorption and thus filtering by certain photodegradants.

pp–GT thin films have been exposed to UV–A (λ = 350±25 nm), UV–B (λ = 300±25 nm) and UV–C (λ = 254 nm) for 24, 48 and 672 hours. Although not naturally occurring, UV–C is commonly used for sterilization purposes and was thus chosen as an extreme wavelength range. After irradiation, the films were investigated by FTIR, AFM and CA measurements. The overlaid FTIR absorption spectra shown in Figure VIII.9 are recorded at 24, 48 and 672 hours for pp–GT thin films fabricated at 50W RF power. To test the effect on available oxygen, selected experiments were repeated using a quartz cover plate ('oxygen-poor' conditions).

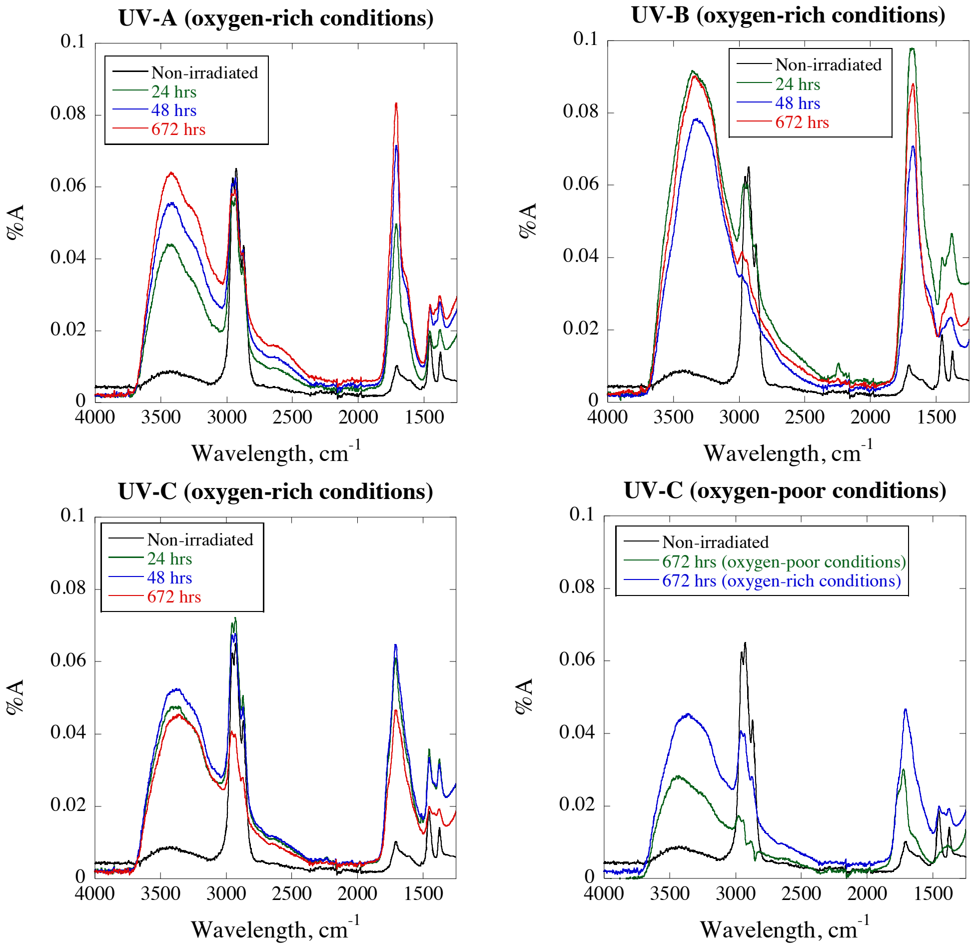

Figure VIII.9. FTIR spectrum of non-irradiated and UV–A, UV–B and UV–C irradiated pp–GT thin films (50W) in oxygen–rich and UV–C irradiated films in oxygen–poor conditions

The wavelength and oxygen content had significant effects on the photostability of the pp–GT thin films. The UV-spectra of the films reached to approx. 400 nm (not shown). Consequently, light absorption was achieved under all irradiation conditions. Upon irradiation with UV–A light in an oxygen-rich environment, strong and broad bands rapidly emerged at approx. 3400 cm^{-1} and 1700 cm^{-1}, respectively. The changes in intensities decreased during the course of the irradiation, suggesting 'inner-filter' effects by the photodegradants. The newly formed peaks were assigned to oxygen-containing functional groups, in particular O-H (hydroxyl- and carboxyl-groups) and C=O stretching vibrations (carbonyl- and carboxyl-groups). Peak broadening furthermore occurred in the region below 1500 cm^{-1}, possibly due to the emergence of C-O stretching vibrations. The observed changes thus clearly confirm rapid photooxidation of the pp–GT thin films upon light exposure. Similar observations have been reported for ethylene-propylene [46] and styrenic polymers [47]. When exposed to UV–B light, the same changes were in principle observed in the IR-spectra, although more rapidly. In contrast to UV–A exposure, the intensity of the C-H stretching vibrations around 2900 cm^{-1} dropped significantly, thus suggesting a higher degree of oxidation. This behavior can be explained by the stronger absorption of the polymeric film in the UV–B range. In addition, the initial photooxidants formed, i.e. carbonyl-containing compounds, absorb in the same region, thus enabling further oxidation to carboxylic acid [48]. Rapid degradation was again observed upon exposure to UV-C light. The generation of oxygen-containing functional groups was somewhat retarded, likely due to alternative degradation processes such as rearrangements, chain scissions and crosslinking reactions [36, 49], respectively.

Selected pp–GT thin films have also been irradiated under oxygen-poor conditions by covering the films with a suitable quartz plate (transmission approx. >200 nm). UV-A and UV-C light were chosen to represent the two extreme light conditions. No changes were observed in the FTIR spectra of UV–A irradiated pp-GT thin films compared to the non-irradiated films (not shown). This observation suggests that photooxidation is initiated by other processes and that the radical intermediates formed are subsequently trapped by molecular oxygen. The photostability observed suggests that the power of the UV-A light was insufficient to induce the formation of any reactive species. In contrast, when the pp-GT thin film was photolyzed with highly energetic UV-C light, degradation was again observed, although the process was significantly slower than in an oxygen-rich environment. The FTIR-spectrum taken after 675 hours of exposure revealed the presence of oxygen-containing functional groups. Thus, the radicals formed rapidly reacted with any oxygen present in the polymeric film.

(a)

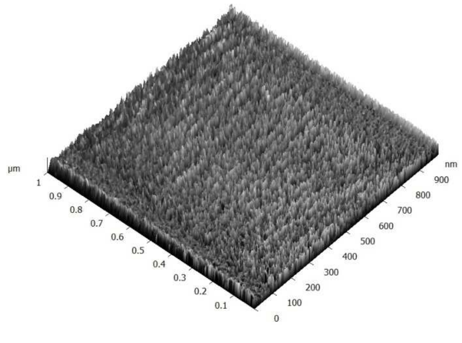

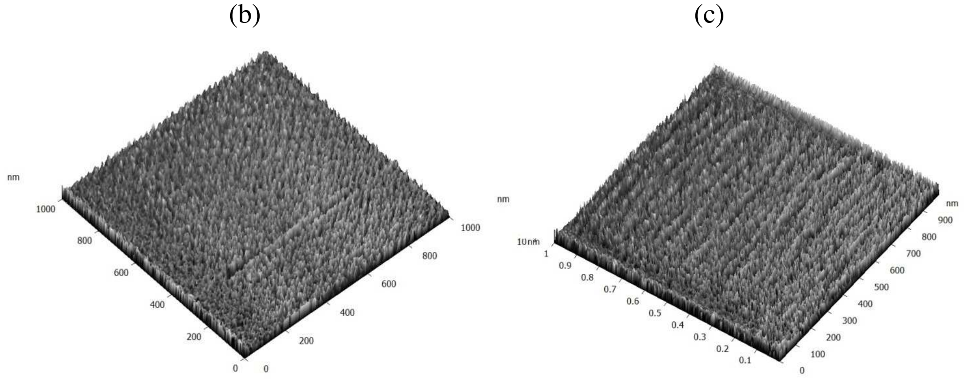

Figure VIII.10. AFM images of pp–GT thin films (50W) after (a) UV–A, (b) UV–B and (C) UV–C irradiation for 24 hours

Figure VIII.10 shows a series of AFM images taken for the pp–GT samples fabricated at 50W RF power that have been illuminated with UV–A, UV–B and UV–C light for 24 hours in oxygen–rich conditions. The pp–GT thin films were generally smooth, uniform and defect-free, exhibiting consistent morphology across the film samples. Average roughness values for non-irradiated samples were approximately 0.25 nm [4]. However, the UV-illuminated samples showed an increase in roughness with prolonged exposure time. An increase of the intensity of UV irradiation also increased the roughness (Table VIII.2). This observation confirms that chemical changes due to photochemical transformations occurred at the polymer surface but required initiation by high-energy light.

Table VIII.2. Roughness of Non–irradiated and UV–A, UV–B and UV–C irradiated pp–GT thin films (50W)

Irradiation time (Hours)	Non–irradiated (nm)	UV–A (nm)	UV–B (nm)	UV–C (nm)
24	0.25	2.24	2.57	2.81
48		2.84	2.98	3.18
672		3.85	3.91	4.41

The mechanical properties of pp–GT thin films deposited at 50W RF power were also investigated using a load–partial unload technique. A series of indentations were made and the hardness of pp–GT thin film samples was found to decrease with increasing both the UV–illumination time and the energy of UV irradiation (Table VIII.3).

Table VIII.3. Hardness of Non–irradiated and UV–A, UV–B and UV–C irradiated pp–GT thin films (50W)

Irradiation time (Hours)	Non–irradiated (GPa)	UV–A (GPa)	UV–B (GPa)	UV–C (GPa)
24	0.51	0.51	0.47	0.42
48		0.47	0.44	0.36
672		0.48	0.41	0.31

A CAH approach [7] was adopted to investigate the wetting behavior of UV–A, UV–B and UV–C irradiated pp–GT films fabricated at 50W (oxygen-rich conditions). The results (advancing CA θ_A, receding CA θ_R, and work of spreading W_S) are listed in Table VIII.4. In line with previous characterizations, an increase in irradiation time and energy of the UV light resulted in lower values of advancing and receding CAs, thus indicating higher liquid sorption and/or solid swelling behavior. The relatively low CA hysteresis (CAH) for 24-hour UV–irradiated films is considered a result of its higher chemical homogeneity, i.e. a lower degree of photodecomposition. CAH subsequently increased as the irradiation time increased (Table VIII.4), which is attributed to the higher degree of chemical changes in combination with a reduction of cross-linkages in the pp–GT films [50]. These subsequently lead to a decrease in the homogeneity of the surface's chemical composition and an increase in surface roughness as supported by the AFM study.

Table VIII.4. Wettability parameters of UV–A, UV–B and UV–C irradiated pp–GT thin films (50W)

UV irradiation	θ_A, °	θ_R, °	CAH, °	W_S (mJ·m−2)
UV-A (24 hrs)	72.84	28.15	44.69	-50.74
UV-B (24 hrs)	63.69	25.98	37.71	-40.07
UV-C (24 hrs)	49.78	19.48	30.30	-25.5
UV-A (672 hrs)	69.03	23.98	45.05	-46.21
UV-B (672 hrs)	58.75	19.09	39.66	-34.63
UV-C (672 hrs)	42.32	10.80	31.52	-18.76

The wettability of each solution on the pp–GT surface can also be quantified by computing the work of spreading W_S [51]. It shows the extent to which the liquid will adhere to the surface relative to itself and, hence, indicates the ability of a liquid drop to stick to the solid surface during solution processing [52]. The pp–GT thin films were characterized by increased wettability with increased irradiation time and intensity of UV light (Table VIII.4). This confirms the continuous formation of polar functional groups through photooxidation during the course of the irradiation [36].

VIII.2.6 STABILITY OF ENCAPSULATED SOLAR CELL

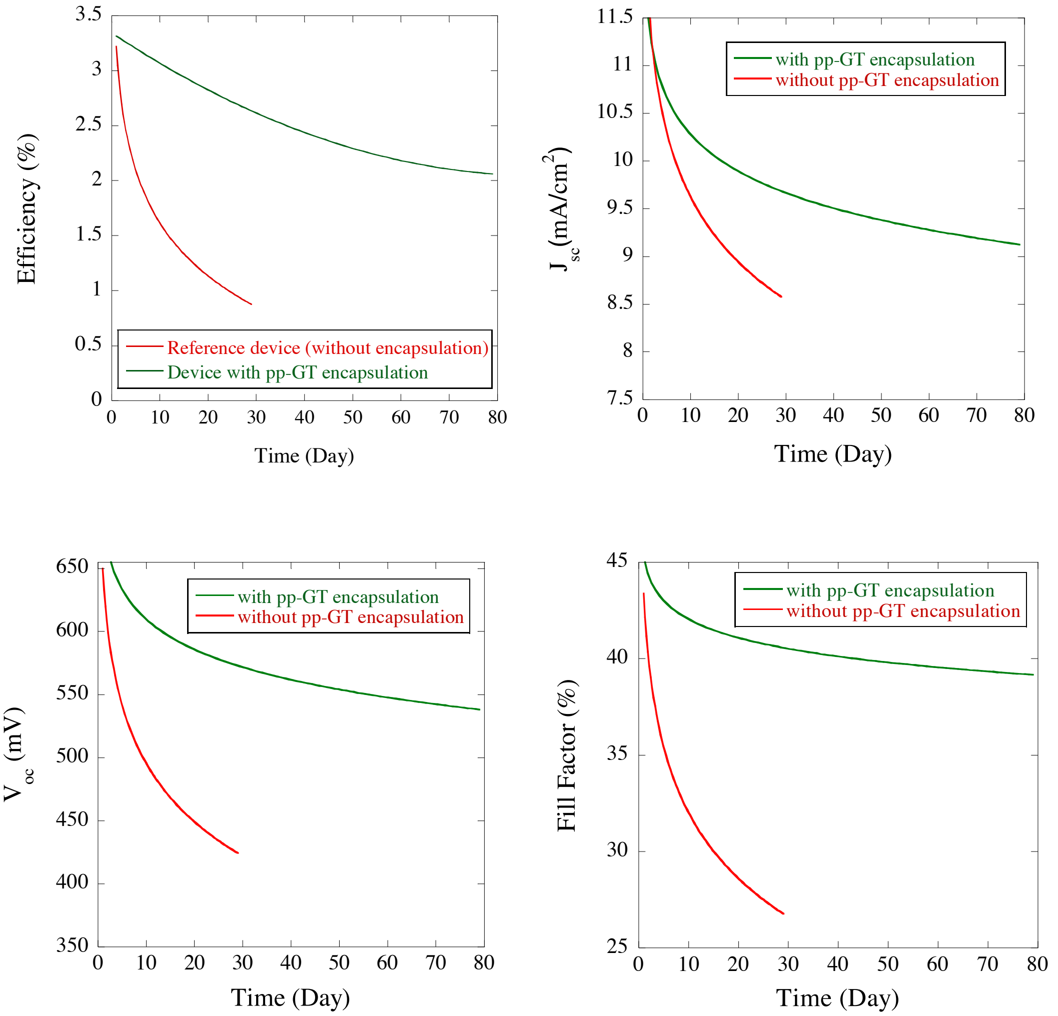

Figure VIII.11. OPV device efficiency spectra, current density, open circuit voltage and fill factor *vs*. time curves of the reference device and the device with pp–GT thin film encapsulation

Figure VIII.11 displays the device efficiency spectra of inverted structure solar cells fabricated with and without pp–GT encapsulation. The device with pp–GT thin film encapsulation showed a significantly improved performance, when compared to the reference device. It has a maximum device efficiency value of 3.34% just after fabrication and a value of 2.03% after 80 days. In comparison, the reference device (without encapsulation) exhibits a device efficiency value of 1.07% just after 29 days. These efficiency enhancements may be related to increased charge carrier mobility and charge carrier lifetime due to pp–GT thin film encapsulation that reduces the decay rate of photogenerated excitons and improves the efficiency of exciton dissociation [53].

Figure VIII.11 also displays the current density *vs*. time profiles of PCPDTBT:$PC_{70}BM$ solar cell fabricated with and without pp–GT thin film encapsulation. The measured short circuit current density follows a similar trend to the device efficiency profiles. The maximum value of 11.52 mA cm^{-2} was achieved using pp-GT encapsulation. A value of 8.80 mA cm^{-2} was measured after 80 days, whereas a short circuit current density value of 7.96 mA cm^{-2} was measured after 29 days for the reference device (without encapsulation). Fill factor (FF) and open circuit voltage (V_{oc}) of the encapsulated device was also improved. A FF value of 31.89% was measured after 80 days, whereas a value of 28.78% was measured just after 29 days for the reference device (without encapsulation). Dennnler *et.al*. encapsulated MDMO-PPV:PCBM solar cells with poly(ethylene naphthalate) (PEN)-based barrier material fabricated by PECVD [54]. After 80 days, maximum encapsulated device efficiency was ~60%, which is similar to pp–GT thin film encapsulation architecture. However, encapsulated MDMO-PPV:PCBM solar cell had a short circuit current density of ~70% of its initial value after 80 days, whereas pp–GT thin film encapsulation provided ~76% of its initial value.

VIII.3 PLAUSIBLE DEGRADATION PATHWAYS

In general, polymers can degrade by a variety of different mechanisms [55]. Of these, oxidation, i.e. the reaction with molecular oxygen, in the absence or presence of light, occurs naturally and can significantly reduce the lifespan of polymer films [25, 36, 56]. Commonly, materials subjected to oxygen are degraded much faster in the presence of radiation than in its absence and vice versa. Due to the low diffusion coefficient of oxygen in most polymers (such as polyolefins, polyamides, and polycarbonate) oxidation typically occurs gradually from the surface to the bulk [56].

For pp-GT films produced at low power (10W), minor autooxidation was observed after 1400 h, as evident by characteristic C=O vibrations in its FTIR spectra. For hydrocarbon-based polymers, autooxidation is likely to occur preferentially in activated positions [25]. Consequently, the film produced at 10W still contains reactive allylic positions, which were prone to autooxidation. The intermediary formed allylic hydroperoxides (scheme 1) (Figure VIII.12) subsequently undergo rapid decomposition to the corresponding allyl alcohols (scheme 2) (Figure VIII.12) [25, 56]. Alternatively, the intermediary alkoxy-radical converted to the corresponding carbonyl compound and subsequently to the carboxylic acid through further oxidation (scheme 3) (Figure VIII.12) [25, 36, 48]. The films produced at higher power levels remained stable over 1400 h, thus suggesting a high degree of saturation through cross-linkage.

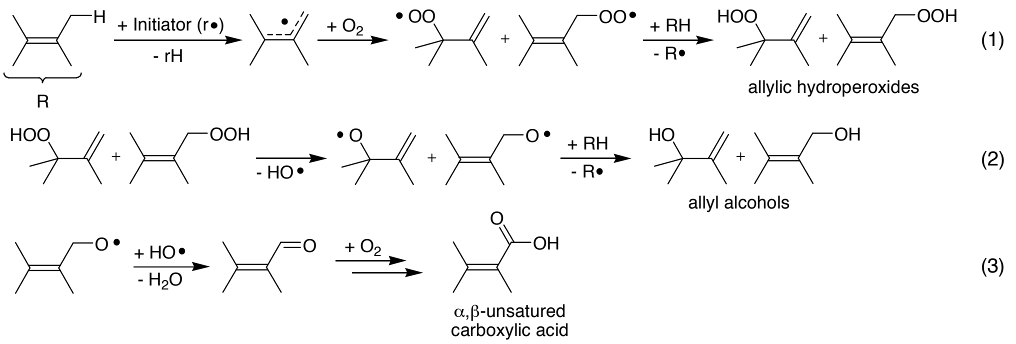

Figure VIII.12. General mechanism of allylic thermal oxidation of pp–GT films

Due to their hydrocarbon nature, pp-GT films remained stable upon heating to 250-300°C. Thermal oxidation, i.e. homolytic bond cleavages and subsequent trapping by molecular oxygen only occurred at elevated temperatures. For the film deposited at 25W and heated to 400°C, FTIR analysis showed an increase in intesities for characteristic oxygen-containing groups (Figure VIII.9), thus indicating further oxidative thermal degradation [25]. The film prepared with 75W power showed the highest thermal stability of up to about 300°C (Figure VIII.8). Its high cross-linkage offers some improved thermal stability towards bond cleavages and subsequent oxidation. At elevated temperature, degradation occurred via polycondensation process [57], where pp–GT degrades to lower molecular weight fragments.

When pp–GT films were subjected to UV irradiation under oxygen–rich conditions, rapid photooxidation was observed. In contrast to other polymers, e.g. polystryrene [36], no visible changes such as yellowing or gradual embrittlement could be observed. The presence of oxygen-containing functional groups was unambiguously demonstrated by FTIR analysis (Figure VIII.9) [24, 48]. In contrast to thermal oxidations, photooxidation is not limited to activated positions. Instead, the degradation pathways for pp–GT films depended on the energy of the light [58, 59]. Consequently, additional degradation pathways to that described in figure VIII.12 are possible. As an example, the excess excitation energy from UV-irradiation initiated the cleavage of a C-H bond in the isopropyl-sidechains of the polymer (scheme 4) (Figure VIII.13). Instant oxygen trapping, followed by β-scission furnished the corresponding ketone-containing degradants (scheme 5) (Figure VIII.13) [4, 9, 10, 11]. Subsequent Norrish-I cleavage followed by reaction of the acyl radical with molecular oxygen and successive follow-up reactions produced the carboxylic acid functions detected by FTIR (scheme 6) (Figure VIII.13).

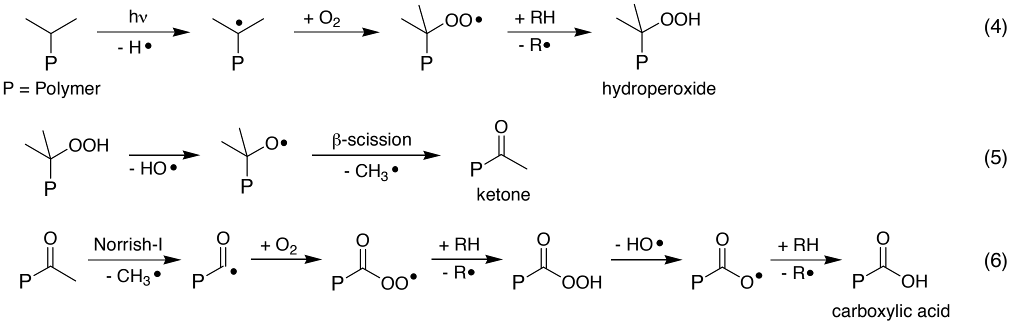

Figure VIII.13. General mechanism of photooxidation of pp–GT films

UV irradiation has a significant impact on the photodegradation of pp–GT films. Upon irradiation with UV-A light, the initially formed hydroperoxides [scheme 1 (Figure VIII.12) and scheme 4 (Figure VIII.13)] readily decomposed to produce carbonyl groups (Figures VIII.12 and VIII.13) [36, 61]. Photolysis with even more energy-rich UV-B light showed faster oxidation and a significant drop in the intensity of the C-H FTIR-vibration peak (Figure VIII.9). UV-B light is able to activate the intermediary formed carbonyl compounds that are the main products of photodegradation [59], thus opening Norrish-type cleavage pathways [scheme 6 (Figure VIII.13)] [44]. Rapid photooxidation was also observed upon irradiation using UV-C light. This light is capable of cleaving a variety of chemical bonds including residual C=C bonds. The intermediates formed were subsequently trapped by oxygen to yield oxygen-containing functional groups. In oxygen-poor conditions, the pp-GT films remained stable when exposed to UV-A light. However, photooxidative decomposition was still observed with UV-C light, thus highlighting the importance of homogeneous bond cleavages for this energy-rich light.

VIII.4 CONCLUSION

The aging behavior of plasma polymer thin films deposited from γ-terpinene was investigated and monitored by spectroscopic ellipsometry, UV-Vis absorption spectroscopy, AFM, FTIR spectroscopy and CA measurements. Under ambient conditions, the bulk of aging occurred within first 150 h after deposition and was ascribed to volumetric easing. Variations of refractive index and thickness (under 0.59 and 0.37% respectively) were insignificant, thus confirming the stability of pp–GT thin films in an ambient environment. Thermal stability increased for the films manufactured at higher RF powers. The volumetric aging rate was calculated by using the Lorentz-Lorenz equation and was RF power dependent; films fabricated at lower RF power aged faster than films fabricated at higher RF power. FTIR spectra of the films demonstrated little differences in the molecular structure of the deposited and annealed films. Spectral changes after the thermal treatment of films deposited at lower RF powers corresponded to their less cross-linked structure compared to the films fabricated at higher RF power. The change in intensity of the absorption bands compared to those of as-deposited films was attributed to the structural rearrangement due to heat treatment. Minor thermal oxidation was indicative from FTIR analysis. The optical, chemical and structural properties of pp–GT thin films did not change significantly upon heat treatment up to 200°C. Photostability studies were conducted with UV-light and showed significant aging due to photooxidation. These could be suppressed in an oxygen-poor environment as demonstrated for UV-A irradiations. With high-energy UV-C light, photochemical degradation and oxidation operated even under oxygen-poor conditions, but to a lower extend. While the overall photostability remains a concern, it may be further improved in future studies by the addition of common UV-stabilizers [36, 62].

The pp–GT thin film encapsulation on PCPDTBT:$PC_{70}BM$ solar cell without any additional UV-curable epoxy resin protection enhanced the performance of the device. A combination of photodegradation study of the pp-GT thin films and the performance study of PCPDTBT:$PC_{70}BM$ solar cell encapsulated with pp-GT thin films has given a new insight on the potential to use them as encapsulants for OPVs.

REFERENCES

[1] F. M. Kelly, L. Meunier, C. Cochrane, and V. Koncar, "Polyaniline: application as solid state electrochromic in a flexible textile display," *Displays,* vol. 34, pp. 1-7, 2013.

[2] S. Chen, L. Deng, J. Xie, L. Peng, L. Xie, Q. Fan, and W. Huang, "Recent developments in top-emitting organic light-emitting diodes," *Advanced Materials,* vol. 22, pp. 5227-5239, 2010.

[3] S. Prakash, T. Chakrabarty, A. K. Singh, and V. K. Shahi, "Polymer thin films embedded with metal nanoparticles for electrochemical biosensors applications," *Biosensors and Bioelectronics,* vol. 41, pp. 43-53, 2013.

[4] J. Ahmad, K. Bazaka, and M. Jacob, "Optical and Surface Characterization of Radio Frequency Plasma Polymerized 1-Isopropyl-4-Methyl-1,4-Cyclohexadiene Thin Films," *Electronics,* vol. 3, pp. 266-281, 2014.

[5] K. Bazaka and M. V. Jacob, "Nanotribological and nanomechanical properties of plasma-polymerized polyterpenol thin films," *Journal of Materials Research,* vol. 26, pp. 2952-2961, 2011.

[6] L. Anderson, C. Easton, and M. Jacob, "Compatibility of plasma-deposited linalyl acetate thin films with organic electronic device fabrication techniques," *Journal of Materials Science,* vol. 48, pp. 4851-4859, 2013.

[7] J. Ahmad, K. Bazaka, M. Oelgemöller, and M. V. Jacob, "Wetting, solubility and chemical characteristics of plasma polymerized 1-isopropyl-4-methyl-1,4-cyclohexadiene thin films," *Coatings,* vol. 4, pp. 527-552, 2014

[8] T. R. Gengenbach and H. J. Griesser, "Post-deposition ageing reactions differ markedly between plasma polymers deposited from siloxane and silazane monomers," *Polymer,* vol. 40, pp. 5079-5094, 1999.

[9] J. Ahmad, K. Bazaka, L. J. Anderson, R. D. White, and M. V. Jacob, "Materials and methods for encapsulation of OPV: A review," *Renewable and Sustainable Energy Reviews,* vol. 27, pp. 104-117, 2013.

[10] K. R. McIntosh, N. E. Powell, A. W. Norris, J. N. Cotsell, and B. M. Ketola, "The effect of damp-heat and UV aging tests on the optical properties of silicone and EVA encapsulants," *Progress in Photovoltaics: Research and Applications,* vol. 19, pp. 294-300, 2011.

[11] J. Jin, S. Chen, and J. Zhang, "Investigation of UV aging influences on the crystallization of ethylene-vinyl acetate copolymer via successive self-nucleation and annealing treatment," *Journal of Polymer Research,* vol. 17, pp. 827-836, 2010.

[12] M. V. Jacob, K. Bazaka, D. Taguchi, T. Manaka, and M. Iwamoto, "Electron-blocking hole-transport polyterpenol thin films," *Chemical Physics Letters,* vol. 528, pp. 26-28, 2012.

[13] D. Taguchi, T. Manaka, M. Iwamoto, K. Bazaka, and M. V. Jacob, "Analyzing hysteresis behavior of capacitance–voltage characteristics of IZO/C_{60}/pentacene/Au diodes with a hole-transport electron-blocking polyterpenol layer by electric-field-induced optical second-harmonic generation measurement," *Chemical Physics Letters,* vol. 572, pp. 150-153, 2013.

[14] L. Anderson and M. Jacob, "Microwave characterization of a novel, environmentally friendly, plasma polymerized organic thin film," *Physics Procedia,* vol. 14, pp. 87-90, 2011.

[15] K. Bazaka, M. V. Jacob, D. Taguchi, T. Manaka, and M. Iwamoto, "Investigation of interfacial charging and discharging in double-layer pentacene-based metal-insulator-metal device with polyterpenol blocking layer using electric field induced second harmonic generation," *Chemical Physics Letters,* vol. 503, pp. 105-111, 2011.

[16] K. Bazaka, M. V. Jacob, R. J. Crawford, and E. P. Ivanova, "Plasma assisted surface modification of organic biopolymers," *Acta Biomaterialia,* vol. 7, pp. 2015-2028, 2011.

[17] H. A. Al-Attar and A. D. Telfah, "Optical constants of polyaniline/poly (methylmethacrylate) blend," *Optics Communications,* vol. 229, pp. 263-270, 2004.

[18] Y. Huang and D. R. Paul, "Physical aging of thin glassy polymer films monitored by gas permeability," *Polymer,* vol. 45, pp. 8377-8393, 2004.

[19] Y. Huang and D. R. Paul, "Experimental methods for tracking physical aging of thin glassy polymer films by gas permeation," *Journal of Membrane Science,* vol. 244, pp. 167-178, 2004.

[20] E. Knox-Davies, J. Shannon, and S. Silva, "The properties and deposition process of GaN films grown by reactive sputtering at low temperatures," *Journal of Applied Physics,* vol. 99, 2006.

[21] S. Steudel, S. De Vusser, S. De Jonge, D. Janssen, S. Verlaak, J. Genoe, and P. Heremans, "Influence of the dielectric roughness on the performance of pentacene transistors," *Applied Physics Letters,* vol. 85, pp. 4400-4402, 2004.

[22] S. E. Fritz, T. W. Kelley, and C. D. Frisbie, "Effect of dielectric roughness on performance of pentacene TFTs and restoration of performance with a polymeric smoothing layer," *The Journal of Physical Chemistry B,* vol. 109, pp. 10574-10577, 2005.

[23] X. Hu, X. Zhao, A. Uddin, and C. B. Lee, "Preparation, characterization and electronic and optical properties of plasma-polymerized nitriles," *Thin Solid Films,* vol. 477, pp. 81-87, 2005.

[24] J. Coates, "Interpretation of Infrared Spectra, A Practical Approach," in *Encyclopedia of Analytical Chemistry*, ed: John Wiley & Sons, Ltd, 2006.

[25] G. Gryn'ova, J. L. Hodgson, and M. L. Coote, "Revising the mechanism of polymer autooxidation," *Organic & Biomolecular Chemistry,* vol. 9, pp. 480-490, 2011.

[26] J. R. White, "Polymer ageing: physics, chemistry or engineering? Time to reflect," *Comptes Rendus Chimie,* vol. 9, pp. 1396-1408, 2006.

[27] A. J. Kovacs, "Transition vitreuse dans les polymères amorphes. Etude phénoménologique," in *Fortschritte Der Hochpolymeren-Forschung*. vol. 3/3, ed: Springer Berlin Heidelberg, 1964, pp. 394-507.

[28] Y. Huang and D. R. Paul, "Physical Aging of Thin Glassy Polymer Films Monitored by Optical Properties," *Macromolecules,* vol. 39, pp. 1554-1559, 2006.

[29] M. Geoghegan and G. Krausch, "Wetting at polymer surfaces and interfaces," *Progress in Polymer Science,* vol. 28, pp. 261-302, 2003.

[30] S. Farris, L. Introzzi, P. Biagioni, T. Holz, A. Schiraldi, and L. Piergiovanni, "Wetting of biopolymer coatings: contact angle kinetics and image analysis investigation," *Langmuir,* vol. 27, pp. 7563-7574, 2011.

[31] M. Morra, E. Occhiello, R. Marola, F. Garbassi, P. Humphrey, and D. Johnson, "On the aging of oxygen plasma-treated polydimethylsiloxane surfaces," *Journal of Colloid and Interface Science,* vol. 137, pp. 11-24, 1990.

[32] K. Bazaka and M. V. Jacob, "Post-deposition ageing reactions of plasma derived polyterpenol thin films," *Polymer Degradation and Stability,* vol. 95, pp. 1123-1128, 2010.

[33] H. B. Bohidar, *Fundamentals of Polymer Physics and Molecular Biophysics*: Cambridge University Press, 2014.

[34] B. J. Holland and J. N. Hay, "The kinetics and mechanisms of the thermal degradation of poly(methyl methacrylate) studied by thermal analysis-Fourier transform infrared spectroscopy," *Polymer,* vol. 42, pp. 4825-4835, 2001.

[35] A. Hollander and J. Thome, "H. Biederman (Ed.), Plasma polymer films: degradation and stability of plasma polymers," *Imperial Collage Press, London,* p. 252, 2004.

[36] E. Yousif and R. Haddad, "Photodegradation and photostabilization of polymers, especially polystyrene: review," *SpringerPlus,* vol. 2, p. 398, 2013.

[37] G. Wypych and T. Faulkner, "Basic Parameters in Weathering Studies," in *Weathering of Plastics*, G. Wypych, Ed., ed Norwich, NY: William Andrew Publishing, 1999, pp. 1-13.

[38] N. J. H. Al-Mashhadan and S. Mohamad, "Study of Degradation Effect on Physical Properties of Methyl Orange Doped PMMA," *Engineering & Technology Journal* vol. 29, pp. 20-32, 2011.

[39] J. F. Larché, P. O. Bussière, S. Thérias, and J. L. Gardette, "Photooxidation of polymers: Relating material properties to chemical changes," *Polymer Degradation and Stability,* vol. 97, pp. 25-34, 2012.

[40] S. I. Kuzina and A. I. Mikhailov, "Chain and photochain mechanisms of photooxidation of polymers," *High Energy Chemistry,* vol. 44, pp. 37-51, 2010.

[41] M. Oelgemöller, C. Jung, and J. Mattay, "Green photochemistry: Production of fine chemicals with sunlight," in *Pure and Applied Chemistry* vol. 79, ed, 2007, p. 1939.

[42] M. Oelgemoller, C. Jung, J. Ortner, J. Mattay, and E. Zimmermann, "Green photochemistry: solar photooxygenations with medium concentrated sunlight," *Green Chemistry,* vol. 7, pp. 35-38, 2005.

[43] F. Ronzani, P. Saint-Cricq, E. Arzoumanian, T. Pigot, S. Blanc, M. Oelgemöller, E. Oliveros, C. Richard, and S. Lacombe, "Immobilized Organic Photosensitizers with Versatile Reactivity for Various Visible-Light Applications," *Photochemistry and Photobiology,* vol. 90, pp. 358-368, 2014.

[44] J. M. Taguenang, A. Kassu, P. B. Ruffin, C. Brantley, E. Edwards, and A. Sharma, "Reversible UV degradation of PMMA plastic optical fibers," *Optics Communications,* vol. 281, pp. 2089-2092, 2008.

[45] C. D. Easton and M. V. Jacob, "Ageing and thermal degradation of plasma polymerised thin films derived from Lavandula angustifolia essential oil," *Polymer Degradation and Stability,* vol. 94, pp. 597-603, 2009.

[46] P. Delprat, X. Duteurtre, and J.-L. Gardette, "Photooxidation of unstabilized and HALS-stabilized polyphasic ethylene-propylene polymers," *Polymer Degradation and Stability,* vol. 50, pp. 1-12, 1995.

[47] J.-L. Gardette, B. Mailhot, and J. Lemaire, "Photooxidation mechanisms of styrenic polymers," *Polymer Degradation and Stability,* vol. 48, pp. 457-470, 1995.

[48] C. Wilhelm and J.-L. Gardette, "Infrared identification of carboxylic acids formed in polymer photooxidation," *Journal of Applied Polymer Science,* vol. 51, pp. 1411-1420, 1994.

[49] A. Rivaton, A. Tournebize, J. Gaume, P.-O. Bussière, J.-L. Gardette, and S. Therias, "Photostability of organic materials used in polymer solar cells," *Polymer International,* vol. 63, pp. 1335-1345, 2014.

[50] L. Shi, "The investigation of polymer surface dynamics modified by plasma using dynamic contact angle method," *European Polymer Journal,* vol. 36, pp. 987-992, 2000.

[51] P. G. de Gennes, "Wetting: statics and dynamics," *Reviews of Modern Physics,* vol. 57, pp. 827-863, 1985.

[52] P. H. Wobkenberg, J. Ball, F. B. Kooistra, J. C. Hummelen, D. M. de Leeuw, D. D. C. Bradley, and T. D. Anthopoulos, "Low-voltage organic transistors based on solution processed semiconductors and self-assembled monolayer gate dielectrics," *Applied Physics Letters,* vol. 93, pp. 013303-3, 2008.

[53] R. Lin, M. Wright, and A. Uddin, "Effects of solvent additive on inverted structure PCPDTBT:$PC_{71}BM$ bulk heterojunction organic solar cells," *physica status solidi (a),* vol. 210, pp. 1785-1790, 2013.

[54] G. Dennler, C. Lungenschmied, H. Neugebauer, N. S. Sariciftci, M. Latrèche, G. Czeremuszkin, and M. R. Wertheimer, "A new encapsulation solution for flexible organic solar cells," *Thin Solid Films,* vol. 511-512, pp. 349-353, 2006.

[55] D. Cheneler and J. Bowen, "Degradation of polymer films," *Soft Matter,* vol. 9, pp. 344-358, 2013.

[56] D. Feldman, "Polymer Weathering: Photo-Oxidation," *Journal of Polymers and the Environment,* vol. 10, pp. 163-173, 2002.

[57] B. Singh and N. Sharma, "Mechanistic implications of plastic degradation," *Polymer Degradation and Stability,* vol. 93, pp. 561-584, 2008.

[58] S. I. Kuzina and A. I. Mikhailov, "The photo-oxidation of polymers – 1. Initiation of polystyrene photo-oxidation," *European Polymer Journal,* vol. 29, pp. 1589-1594, 1993.

[59] H. Cui, R. Hanus, and M. R. Kessler, "Degradation of ROMP-based bio-renewable polymers by UV radiation," *Polymer Degradation and Stability,* vol. 98, pp. 2357-2365, 2013.

[60] E. Andrzejewska, "Photopolymerization kinetics of multifunctional monomers," *Progress in Polymer Science,* vol. 26, pp. 605-665, 2001.

[61] G. Scott, "Developments in the photo-oxidation and photo-stabilisation of polymers," *Polymer Degradation and Stability,* vol. 10, pp. 97-125, 1985.

[62] D. Noukakis and P. Suppan, "Mechanism of protection of polymers by photostabilizers," *Journal of Photochemistry and Photobiology A: Chemistry,* vol. 58, pp. 393-396, 1991.

CHAPTER IX

CONCLUSION AND FUTURE WORKS

Thin-film encapsulation is a critical technology for the commercialization of flexible organic electronics, and OPVs in particular. The key for achieving the reliability and desired lifetime required for a desired application is the effective encapsulation to prevent the permeation of water vapour and oxygen and other degradation mechanism. However, the materials applied for this purpose cannot yet satisfy the encapsulation requirements discussed in chapter II. Hence, new materials are needed which will satisfy the encapsulation requirements and achieve the reliability and lifetime required. In this thesis, an environmentally friendly, low cost and transparent thin film material suitable for applications in OPVs, especially as encapsulation coatings was developed. This material was derived from the monomer γ-terpinene, which is a non-synthetic isomeric hydrocarbon derived from *Melaleuca alternifolia* essential oil, and fabricated using PECVD. The fundamental properties of the material were investigated, in addition to the photo–stability of the pp–GT thin films and stability of pp–GT encapsulated solar cell. The following are important findings of, and insights obtained in, this dissertation, summarized by chapter. Furthermore, based on current results of this dissertation, future work to address outstanding research issues is suggested.

pp–GT thin films were successfully fabricated using PECVD under a range of processing parameters to achieve materials with distinct material (physical, chemical, optical, electrical), and degradation characteristics. These properties were defined based upon the attributes most commonly reported in literature for new materials. Deposition time was found to significantly affect film thickness, with minimal influence over material properties of pp–GT. Input RF power, on the other hand, was demonstrated to be a significant determinant of material properties of pp–GT thin films. Therefore, properties of pp–GT films deposited at various RF powers were investigated using the characterization facilities available at James Cook University and collaborating national institutions.

Structural characterization of pp–GT thin films deposited on silicon substrate by plasma polymerization of γ-terpinene at different discharge powers (5W–50W) were analyzed by plasma mass spectrometry. High-resolution mass spectra positive ion mass spectrometry data of the plasma phase demonstrated the presence of oligomeric species of the type $[M+H]^+$ and $[2M+H]^+$, where M represents a unit of the starting material. At the same time, there were abundant fragmented species, with most dominant being $[M^{\bullet+}]$ (136 m/z), $C_{10}H_{13}^+$ (133 m/z), $C_9H_{11}^+$ (119 m/z) and $C_7H_9^+$ (93 m/z). When plasma is ignited the relative intensity of intact monomer peak (e.g. 136 m/z) and fragment peaks (e.g. 119, 93 m/z) decreased. Higher mass peaks with very low intensity did appear at higher RF powers, which are attributed to ablation of polymeric material within the spectrometer. In positive ion mode, the dominant feature for all plasmas was the peak at *m/z* 136, which corresponds to the $M^{\bullet+}$ ($C_{10}H_{16}^{\bullet+}$) ion. A dimer $[2M+H]^+$ was also observed at *m/z* 273, whereas protonated molecule $[M+H]^+$ at *m/z* 137 was also found in the mass spectra. Based on these observations, a possible fragmentation pattern during the plasma polymerization of the precursor, γ-terpinene, was proposed.

To investigate pp–GT thin film optical properties, spectroscopic ellipsometry (VASE) and UV-Vis spectroscopy measurements were undertaken. VASE measurements confirmed the effect of deposition RF power on optical properties of the films was limited, with all films being optically transparent, with refractive indices in a range of 1.57–1.58 at 500 nm. Independent of deposition power, the extinction coefficient approximated zero at wavelengths above 500 nm. UV-Vis spectroscopy measurements also showed the films to be optically transparent, with only one absorbance peak at approximately 300 nm. From these absorbance measurements, the optical band gap of the films was determined to be ~3 eV, categorizing the films as insulating materials.

The topographical properties of the material were investigated using AFM to measure the surface topography and nanoindentation was used to measure its hardness. Independent of deposition conditions, the surfaces were smooth and defect-free, with uniformly distributed morphological features. From analysis of the topography, the roughness was determined to have an average value between 0.30 nm (at 10 W) and 0.21 nm (at 75 W). Deposition power did not have an effect on surface skewness or coefficient of kurtosis, with all pp–GT thin films characterized by a disproportionate number of peak and a well spread out height distribution pertaining to the pp–GT surfaces. Films fabricated at higher deposition power displayed enhanced resistance to delamination and wear, and improved hardness, from 0.40 GPa for 10 W to 0.58 GPa for 75 W at a load of 700 μN.

Investigations on the wetting, solubility and chemical composition of pp–GT thin films provided an insight into the feasibility of implementing the material in OPVs, particularly where wet solution processing is involved. FTIR showed the polymers to be structurally dissimilar to the original monomer and highly cross-linked, where the loss of original functional groups and the degree of cross-linking increased with deposition power. The polymer surfaces were hydrocarbon-rich, with oxygen present in the form of O–H and C=O functional groups. The oxygen content decreased with deposition power, with films becoming more hydrophobic and, thus, less wettable. XPS characterization of chemical composition and structure of pp–GT surfaces provided additional confirmation of the chemical properties of the material, through analysis of high-resolution C1s spectra showing predominately hydrocarbon bonding environments in addition to some oxygen-containing moieties. This analysis revealed an inverse relationship between power and the presence of oxygen functionality in pp–GT. Reduction of oxygen content in the deposit correlated with greater fragmentation in the plasma phase at higher plasma power. The thin film which featured the highest degree of incorporation of oxygen (11.8%) was obtained from plasma operated at 10 W, but was deposited at the lowest rate (12.83 $\mu gm^{-2}s^{-1}$).

Surface tension and solubility parameters of pp–GT thin films as a function of the deposition RF power were also examined using three different solvents (water, EG and DIM). Improved stability was observed for films fabricated at higher RF powers due to the increased degree of cross linking and the decrease in the oxygen content associated with the higher deposition power. The advancing and receding CAs were investigated, and the water advancing contact angle was found to increase from 63.14° to 73.53° for thin films prepared with an RF deposition power of 10 W to 75 W. The effect of roughness on the wetting behavior of the films was insignificant. The polymers were determined to resist solubilization in solvents commonly used in the deposition of organic semiconducting layers, including chloroform and chlorobenzene, with higher stability observed in films fabricated at higher RF power.

The electrical properties of pp–GT thin films were investigated in the frequency range of 0 Hz – 100 kHz. From the *IV* characterization it was determined that RS conduction was the predominate mechanism of charge transport in the pp–GT thin films. The resistivity of the pp–GT thin films was found to decrease from $1.77 \times 10^{12}\ \Omega$ cm (10W) to $5.24 \times 10^{11}\ \Omega$ cm (75W), attributed to the change in the chemical composition and structure of the polymer. IS measurements determined that at a frequency of 100 kHz, the dielectric constant varied with input RF power, from 3.69 (10 W) to 3.24 (75 W). These measurements were also performed under heating in order to excite relaxation phenomena to frequencies within the experimental measurement range to allow better modeling of the material's dielectric function. The distribution of relaxation times was found to possess multiple peaks, one of which clearly dominated and was responsible for the main peak in the measured loss spectrum.

A comparative analysis on the changes of optical, morphological and structural properties of as deposited, aged (1400 h) and heat treated pp–GT thin films revealed that the bulk of the aging under ambient conditions occurred within the first 150 h after fabrication. Changes in refractive index and thickness were insignificant confirming the pp–GT films were stable when in contact with ambient environment and therefore can potentially be used as an encapsulating layer in

OPVs. The volumetric aging rate of pp–GT thin films was found to be dependent on the polymer structure and the RF power. The chemical characterization indicated that the aging of pp–GT thin film deposited at lower RF power occurred via oxidation, as observed by a slight increase in the −OH stretch (3424 cm^{-1}).

The thermal degradation studies of pp–GT thin films indicated an increase in thermal stability for films fabricated at higher RF power. Between approximately 260 °C and 350 °C, all pp–GT films underwent a phase change and the optical parameters of the films experience a large rate of change. Annealing up to 250°C had minimal effect on chemical composition and refractive index of the material, whereas thickness reduced due to desorption of low molecular weight species. The FTIR spectra of the films after heating to 400 °C confirmed hydrogen abstraction that is likely to be the process to transmute the original film into a less hydrocarbon dense structure.

Solar stability study was performed using solar simulator that showed photo–oxidation to be the degradation mechanism for pp–GT thin films under UV irradiation in oxygen–rich conditions. pp–GT thin film was also applied as encapsulation coating over a PCPDTBT:$PC_{70}BM$ solar cell. EQE measurements performed using a QEX10 spectral response system revealed a maximum EQE value of 3.34% just after fabrication and a value of 1.86% after 60 days. However, the reference device (without encapsulation) had EQE value of 1.46% after 60 days. The measured short circuit current density followed a similar trend to the EQE profiles. Fill factor (FF) and open circuit voltage (V_{oc}) of the encapsulated device was also improved compared to the reference device (without encapsulation).

Table IX.1 shows the summary of pp–GT material properties. Given the outcomes of the fundamental characterization and stability studies, potential application for pp–GT has also been identified in this thesis. The flexible nature of the pp–GT films confirms the material's potential as an encapsulating layer in flexible electronics. Optical transparency and variable optical band gap indicate pp–GT can be suitable for encapsulation of OPVs. Good adhesion, chemical and physical stability, and low temperature of fabrication further substantiates the material's potential as an encapsulation coating of OPVs. Electrical measurements showed the material to demonstrate highly insulating behavior that is needed for encapsulation purpose. Encapsulating an organic solar cell and comparing device performance parameters before and after encapsulation also verified the effectiveness of this developed encapsulation structure.

Table IX.1. Summary of material properties of pp–GT fabricated at different RF powers

Property	**Input RF power**			
	10 W	**25W**	**50W**	**75W**
Refractive index (λ=600 nm)	1.57 ± 0.004	1.57 ± 0.004	1.57 ± 0.003	1.58 ± 0.004
Extinction coefficient (λ=600 nm)	0.006 ± 0.003	0.004 ± 0.003	0.003 ± 0.004	0.001± 0.004
Optical band gap (eV)	3.14	3.08	3.07	3.01
Abbe number	35.37	35.18	37.80	40.35
Average surface roughness (nm)	0.30 ± 0.1	0.28 ± 0.02	0.25 ± 0.03	0.21 ± 0.02
Hardness (GPa)	0.40 ± 0.01	0.46 ± 0.02	0.51 ± 0.02	0.58 ±0.03
Elastic modulus, E (GPa)	4.22 ± 0.03	4.61 ± 0.02	4.90 ± 0.02	5.96 ± 0.03
Static Water contact angle (°)	61.03 ±1.79	68.93 ± 0.88	72.72 ± 1.47	80.72 ± 1.94
Advancing contact angle (°)	63.14 ± 1.04	69.25 ± 1.74	72.98 ± 0.91	73.53 ± 1.27
Receding contact angle (°)	8.28 ± 0.89	17.43 ± 1.16	29.15 ± 1.39	36 ± 1.07
Surface free energy (mJ m^{-2})	44.60	40.27	38.39	38.91
Water spreading parameter (mN/m)	–37.54	–46.63	–51.18	–61.10
Wetting behavior	Absorption + spreading	Absorption + evaporation	Evaporation	Evaporation
Conductivity (S/cm)	1.39×10^{-12}	2.91×10^{-13}	1.92×10^{-13}	1.02×10^{-13}
Dielectric constant (100 kHz)	3.69	3.57	3.44	3.24
Dielectric breakdown (MV/cm)	1.48	1.72	1.94	2.05

The main research contributions of this dissertation were providing a systematical study exploring the parameters that impact the pp–GT encapsulation films and their integration with OPVs. Through the efforts of this work, the overall encapsulation film barrier performance was determined with intention to use these films in OPVs, specifically as encapsulation coatings. This new film effectively provides barrier with a simplified architecture by treating the degradation mechanisms that commonly exist in currently available materials. Fundamental characterizations of pp–GT thin films provided the basic understanding of the properties of the films and the critical guidelines for designing efficient barrier layers. Additional studies of the degradation behavior and solar stability of thin films provided an insight to enable the use of these films as encapsulation coatings.

This thesis provided the conclusion that pp–GT is a promising candidate for encapsulation of OPVs. However, further extensive investigations are required into fundamental studies behind pp–GT encapsulating layers. These studies may include water vapor diffusion, which shows non-ideal gas behavior through the films. Interaction with water vapor resulting in changing properties of pp–GT films, and its impact on the performance of organic devices should also be further investigated. pp-GT thin film performance while irradiating UV light for a long time, requires further investigation to assess the polymer’s degradation mechanism. Performance of pp–GT−incorporated electronic devices also necessitates detailed exploration to demonstrate improvement. pp–GT has been applied as encapsulation coating over only one specific type of organic solar cell and analyzed. Future research could involve investigations into different device architectures and modification of deposition parameters and procedures to accommodate these.

The thermal degradation and solubility of pp–GT thin films have been studied in this thesis. However, the influence of these processes on specific properties should further be investigated. In this thesis, dielectric function and conductivity was determined before exposure to UV and/or various solvents. These can also be investigated to ensure that the properties remain unaffected after the exposure.

Appendix A

Appendix A.1

Materials and methods for encapsulation of OPV: A review

As published in: Ahmad, Jakaria, Bazaka, Kateryna, Anderson, Liam J., White, Ronald D., and Jacob, Mohan V. (2013) *Materials and methods for encapsulation of OPV: a review*. Renewable and Sustainable Energy Reviews, 27. pp. 104-117.

Renewable and Sustainable Energy Reviews 27 (2013) 104–117

Contents lists available at SciVerse ScienceDirect

Renewable and Sustainable Energy Reviews

journal homepage: www.elsevier.com/locate/rser

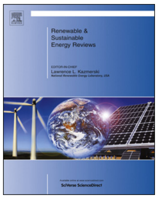

Materials and methods for encapsulation of OPV: A review

Jakaria Ahmad, Kateryna Bazaka, Liam J. Anderson, Ronald D. White, Mohan V. Jacob*

Electronic Materials Research Laboratory, School of Engineering and Physical Sciences, James Cook University, Townsville 4811, Australia

ARTICLE INFO

Article history:
Received 2 January 2013
Received in revised form
19 June 2013
Accepted 24 June 2013

Keywords:
Organic photovoltaic
Encapsulation
Organic solar cells
Efficiency

ABSTRACT

Amongst alternative energy sources, photovoltaics hold a considerable promise for it is a plentiful, easily accessible and renewable source of power. Yet, the overall cost of generating electricity using the most advanced silicon based solar cells remains high compared to both traditional and other renewable power generation approaches. Organic thin film photovoltaics are an emerging economically competitive photovoltaic technology that combines manufacturing adaptability, low-cost processing and a light-weight, flexible device end-product. At present, however, commercial use of organic photovoltaics is hindered by low conversion efficiency and poor overall stability of the devices. Encapsulation with high barrier performance materials and structures is one of the key ways to address these issues and improve device lifetime. This paper will briefly outline the current understanding of the major degradation mechanisms, their interrelation and the internal and external factors that initiate these processes. Then, the paper will provide an overview of currently available encapsulant materials, their utility in limiting chemical (water vapor and oxygen penetration) and mechanical degradation within individual layers and device as a whole, and potential drawbacks to their application in organic photovoltaic devices.

Appendix A.2

Optical and Surface Characterization of Radio Frequency Plasma Polymerized 1-Isopropyl-4-Methyl-1,4-Cyclohexadiene Thin Films

As published in: Ahmad, Jakaria, Bazaka, Kateryna, and Jacob, Mohan V. (2014) *Optical and surface characterization of radio frequency plasma polymerized 1-isopropyl-4-methyl-1,4-cyclohexadiene thin films*. Electronics, 3 (2). pp. 266-281.

Electronics **2014**, *3*, 266-281; doi:10.3390/electronics3020266

OPEN ACCESS

electronics

ISSN 2079-9292

www.mdpi.com/journal/electronics

Article

Optical and Surface Characterization of Radio Frequency Plasma Polymerized 1-Isopropyl-4-Methyl-1,4-Cyclohexadiene Thin Films

Jakaria Ahmad, Kateryna Bazaka and Mohan V. Jacob *

Electronic Materials Research Laboratory, School of Engineering and Physical Sciences,
James Cook University, Townsville 4811, Australia; E-Mails: Jakaria.Ahmad@my.jcu.edu.au (J.A.);
Katia.Bazaka@jcu.edu.au (K.B.)

* Author to whom correspondence should be addressed; E-Mail: mohan.jacob@jcu.edu.au;
Tel.: +61-7-478-14379.

Received: 21 February 2014 / Accepted: 14 April 2014 / Published: 23 April 2014

Abstract: Low pressure radio frequency plasma-assisted deposition of 1-isopropyl-4-methyl-1,4-cyclohexadiene thin films was investigated for different polymerization conditions. Transparent, environmentally stable and flexible, these organic films are promising candidates for organic photovoltaics (OPV) and flexible electronics applications, where they can be used as encapsulating coatings and insulating interlayers. The effect of deposition RF power on optical properties of the films was limited, with all films being optically transparent, with refractive indices in a range of 1.57–1.58 at 500 nm. The optical band gap (E_g) of ~3 eV fell into the insulating E_g region, decreasing for films fabricated at higher RF power. Independent of deposition conditions, the surfaces were smooth and defect-free, with uniformly distributed morphological features and average roughness between 0.30 nm (at 10 W) and 0.21 nm (at 75 W). Films fabricated at higher deposition power displayed enhanced resistance to delamination and wear, and improved hardness, from 0.40 GPa for 10 W to 0.58 GPa for 75 W at a load of 700 μN. From an application perspective, it is therefore possible to tune the mechanical and morphological properties of these films without compromising their optical transparency or insulating property.

Keywords: plasma polymerization; thin film; 1-isopropyl-4-methyl-1,4-cyclohexadiene; γ-terpenine; optical properties; AFM

---

1. Introduction

The latest advances achieved in the field of organic electronics have expanded the scope of applications beyond those attainable with conventional silicon (Si) semiconducting technologies to include flexible photovoltaic (PV) and light-emitting devices, flexible displays, chemical and biological sensors, wearable and implantable electronics, to name a few [1–7]. Among these, organic thin film photovoltaics (OPV) is an emerging economically-competitive PV technology that combines manufacturing adaptability, low-cost processing and a lightweight, flexible device end-product. In spite of the significant advances in OPV, commercial use of this technology remains limited, due to both low power conversion efficiency (PCE) and poor overall stability of the devices. Indeed, even though the highest PCE achieved from organic PV has risen from 2.5% to 11% for bulk heterojunction polymer: fullerene solar cells over the last ten years, it falls short of 25%–30% PCE level offered by established *Si* photovoltaic cells. The lifetime achievable by the most advanced organic solar cells is also far below the 20–25 years lifespan of commercial *Si* photovoltaic cells [8], attributed to relatively low environmental stability of organic photoactive materials.

Most of the research effort to date has concentrated around the photoactive layer, focusing on new, more efficient and stable materials with tailored energy levels and solubility, and a better understanding of the mechanism of photon–to–electron conversion [9]. However, encapsulation with high barrier performance materials has also been recognized as instrumental in significantly improving device lifetime, where device stability is extended by limiting penetration of oxygen and moisture from the environment into device layers [10]. For instance, encapsulation of solar cells based on coating of ZnO layer on top of a photoactive material and subsequent UV resin drop coating resulted in a significant increase in the stability, shelf life of the device, and the cost-effectiveness [11]. Recently synthesized silicon oxide/alumina and parylene layer had an effective water vapor transmission (WVTR) rate of $2.4 \pm 1.5 \times 10^{-5}$ g/m^2/day [12]. However, the requirements for high performance encapsulation materials include good processability, high optical transmission, high dielectric constant, low water absorptivity and permeability, high resistance to ultra-violet (UV) degradation and thermal oxidation, good adhesion, mechanical strength, and chemical inertness [13]. While inorganic barrier layers are often used for their sound durability [14], organic encapsulation materials are attracting attention for their synthetic flexibility and resulting property tunability [15].

Organic thin film materials fabricated from renewable precursors using low-cost deposition methods, such as plasma-assisted nanoassembly, have lower environmental and economic costs [16]. Low-temperature plasma deposition is a highly engineering-friendly, economical method of polymer synthesis, that delivers practically pollutant free surface chemistry, and can be easily integrated into manufacturing processes [17,18]. The method offers a level of confidence and deposition quality comparable to and in many cases superior to other widely-used techniques, such as thermal chemical vapor deposition, wet chemistry processing, laser assisted microfabrication, *etc*. [19,20]. Films fabricated using plasma-assisted synthesis are typically smooth, ultrathin and pinhole free, with good spatial uniformity, conformal coverage, and high adhesion to the substrate [21].

1-isopropyl-4-methyl-1,4-cyclohexadiene, also known as γ-terpinene, is a non-synthetic isomeric hydrocarbon derived from *Melaleuca alternifolia* essential oil. Earlier, Jacob and co-workers have successfully used plasma-assisted deposition to fabricate thin films from other renewable precursors for application in electronics and biomedical fields, reporting property variability linked to both deposition conditions and the chemistry of the monomer [22–26]. This paper reports on the plasma-assisted fabrication of new polymer thin films from γ-terpinene, with intention to use these films in OPVs, specifically as encapsulation coatings, and as insulating layers in flexible electronics. Given the proposed application for the plasma polymerized γ-terpinene (pp–GT), the material is studied in terms of optical, surface, mechanical, and adhesion properties as a function of deposition conditions.

2. Experimental Section

Thin film samples were deposited on high quality glass microscope slides inside a custom made, cylindrical RF polymerization chamber, 0.75 m in length with an inner diameter of 0.055 m (approximate volume of 0.018 cm^3). The slides were thoroughly cleaned using extran, an ultrasonic bath of distilled water, and rinsed with isopropanol prior to deposition. Using the procedure outlined in [22], plasma polymer films were fabricated from γ-terpinene monomer (Figure 1) at various input RF power levels (10, 25, 50 and 75 W) and at an ambient temperature of 20 °C. The monomer flow rate was estimated to be 1.57 cm^3/min by employing the procedure outlined by Gengenbach and Griesser [27].

Figure 1. Chemical structure of 1-Isopropyl-4-methyl-1,4-cyclohexadiene ($C_{10}H_{16}$).

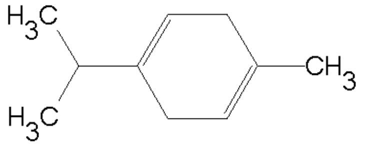

Variable angle spectroscopic ellipsometry (VASE) measurements were performed using a J.A. Woollam Co. Inc. model M-2000D variable angle spectroscopic ellipsometer to estimate sample thickness and optical properties of pp–GT thin films [28]. The refractive index *n*, extinction coefficient *k* and thickness were derived from the experimental Δ and Ψ data via regression analysis. The relation between *n* and thickness for the polymer samples has also been investigated. UV-Vis spectroscopy measurements were performed using an Avantes Avaspec-2048 spectroscopy unit with an Avalight-DHc light source to measure the absorbance in the ultraviolet and visible region. From those data, values of optical band gap have been derived. Surface morphology and roughness parameters of pp–GT thin films fabricated under different RF powers were determined from atomic force microscope (AFM) images acquired on a NT-MDT NTEGRA Prima AFM operating in semi-contact mode. A Hysitron Triboscope was used to perform the nanoindentation study. During the nanoindentation study, a Berkovich indenter (70.3° equivalent semi-opening angle) was used and instrument compliance was calibrated using fused silica. Preliminary images of the samples under investigations were collected in order to evaluate the roughness of the area to be indented. Twelve indentations were made on each sample and the results presented are an average of these indentations. Typical loads used in the indentation ranged from 100 μN to 2000 μN with fixed loading time and hold time of between 2 and 5 s.

In the load-partial unload (PUL) experiment, several cycles of loading and unloading were performed in a sequence (Figure 2). At a constant rate of loading and unloading (100 μN/s), the Berkovich indenter was first loaded and unloaded two times in succession with each of the unloadings terminated at 10% of the maximum load to assure the contact between the pp–GT thin film sample and the indenter. This was performed to examine the reversibility of the deformation and thus ensure that the unloading data used for analysis purposes were mostly elastic [29]. The load was held constant after the second unloading for a fixed period of time at 10% of the peak value while the displacement was carefully monitored to establish the rate of displacement produced by thermal expansion in the system. Following the hold period, the sample was loaded for the last time to allow any final time dependent plastic effects to diminish, with another fixed hold period inserted at peak load and then the specimen was fully unloaded.

Figure 2. Typical load–time sequence used for load–partial unloading experiments.

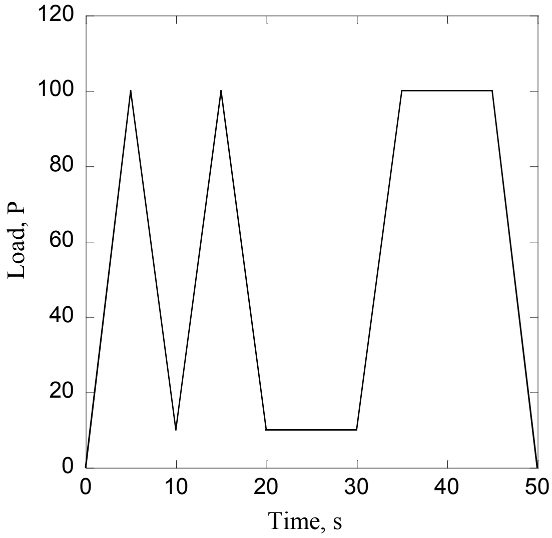

After the indentations were performed, stiffness values and the known modulus for quartz were used to calculate the contact area for each indent. Contact parameters and mechanical properties of the pp–GT thin films are derived from the contact area and load-displacement curve as proposed by Oliver and Pharr [29]. The unloading stiffness was determined after polynomial fitting of 90% of the unloading curve.

The cross-hatch test was performed on pp–GT films fabricated at different power levels using the Elcometer 107 kit to obtain a standardized (ASTM D3359) qualitative assessment of the adhesion between the films and the glass substrate. Crosshatch patterns were made on the polymer film surfaces using the cutting tool (6 teeth, 1 mm spacing). The whole area was then brushed to remove debris and adhesive tape was applied on top of the lattice followed by smoothing out the tape with a pencil eraser across the surface. The tape was then removed by pulling at an angle of 180° and the results were analyzed by comparing the lattice of cuts with ISO standards. Three samples were fabricated for each applied RF power, with three crosshatch tests performed on each sample.

3. Results and Discussion

3.1. Effect of Time on Film Thickness

The dependence of pp–GT thin film thickness on the deposition time was studied on samples fabricated for 2, 5, and 10 min at 25 W RF power along with constant monomer flow rate and pressure.

A film thickness of 120 nm was obtained with deposition time of 2 min at 25 W. The sample thickness increased linearly with time, approaching 438 nm for deposition time of 10 min. Similar trend was observed for films fabricated at 10, 50, and 75 W RF power. Film thickness is also found to be linearly increasing with higher RF power. This is due to an increase in the densification of electrons with an increased crosslinking. Same phenomenon has also been observed in case of plasma polymerized terpinen-4-ol and linalyl acetate (PLA) thin films [26,30]. Assuming constant deposition conditions (pressure, monomer flow rate, distance between electrodes, *etc*.), the desired film thickness of pp–GT thin film for a potential application can therefore be achieved by controlling the time of deposition.

3.2. RF Power Dependence of Optical Constants

The effect of changing the RF power level on the optical constants of pp–GT polymer thin films has been studied using VASE and UV-Vis spectroscopy over the wavelength range of 200–1000 nm. UV-Vis absorption spectrums of samples fabricated at 10, 25, 50, and 75 W RF power level (Figure 3) reveal that the absorption contour is replicable over the RF power range employed during fabrication. Reallocating of the peak position and/or broadening of the peak are not observed with increase in RF power, unlike other studies [31]. The maximum absorption of pp–GT films fabricated at different RF power levels is found to be at 300 nm. It is believed that the main absorption peak may be the result of pi–pi * transitions. The optical transparency of the polymer films is confirmed by these spectra as the maximum absorption peaks are outside of the visible region of the spectrums. The optical transparency of the pp-GT film can be effectively used in applications such OPV, medical imaging, optical sensor and as an encapsulating (protective) layer for the electronic circuits.

Figure 3. UV-Vis absorption spectrum of pp–GT thin films.

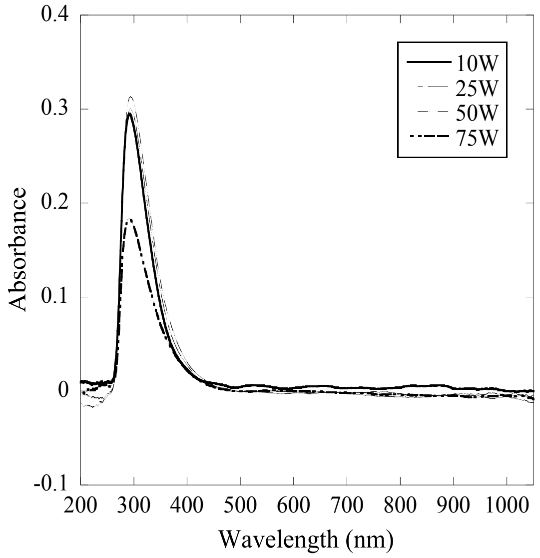

Figure 4 demonstrates the *n* and *k* profiles of pp–GT thin films fabricated at various power levels. Thickness and surface roughness parameters from Cauchy analysis (WVASE software) were used to obtain *n* and *k* profiles. Mean squared error (MSE) values used to assess the quality of the modeling fit were below 3. Considering the profiles, it is observed that the overall shape of the curves was similar across all the samples. At short wavelengths (below 250 nm), a sharp peak in *n* profile was detected.

At wavelengths above approximately 250 nm, an increase in RF input power resulted in higher *n* values for the polymer. At 500 nm, the difference in refractive index between 10 and 75 W sample is 0.01, corresponding to a change of less than 1% that is similar to thin films fabricated from linalyl acetate [32].

Figure 4. Refractive indices and extinction coefficient of pp–GT thin films.

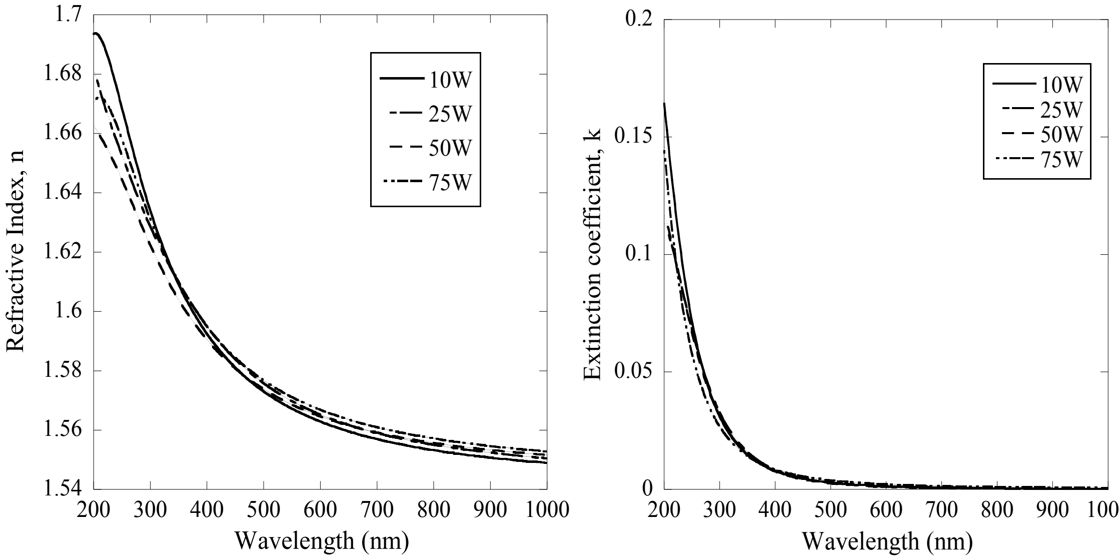

Based on the refractive index values of pp–GT films, it is anticipated that it can be used as a coating on long-period fiber gratings (LPFGs) to enhance its sensitivity, similar to δ-form syndiotactic polystyrene [33]. According to [34], pp–GT can also be used in advanced optoelectronic fabrications, such as high performance substrates for advanced display devices, optical adhesives or encapsulants for OPV devices, antireflective coatings for advanced optical applications or image sensors [4,5,10].

The extinction coefficient (*k*) profiles for pp–GT samples fabricated at various RF power levels illustrate very similar characteristics. These results (optical similarities with glass and transparency in the visible wavelength region) confirm pp–GT thin films as a strong candidate for use as encapsulation coatings in OPV, optical devices, such as LEDs, FETs, and lenses.

Abbe number (v_D), a key parameter for the refractive index dispersion, is of great importance for optical materials used in the visible region. It is also defined as *v*-number or refractive efficiency or constringency of the material. The Abbe number is given by following equation [35]:

$$v_D = \frac{n_{d-1}}{n_F - n'_c} \tag{1}$$

where n_d, n_F, and n_C are the refractive indices of the material at the wavelengths of sodium D (587.6 nm), hydrogen F (486.1 nm), and hydrogen C (656.3 nm), respectively [35]. Materials that have a higher Abbe number (v_D) have lower dispersion in the refractive index, whereas highly refractive materials have small Abbe numbers [36,37]. A polymer having low v_D (<30), is therefore not suitable for use in optics [36].

For pp–GT films, v_D increases from 35.37 to 40.35 (Table 1) with increase in RF power (10 W to 75 W), which confirms that films fabricated at 75 W have lower dispersion in the refractive index.

These results indicate the well-balanced properties and hence the pp–GT polymer thin films are potential candidates for advanced optical applications.

Table 1. Abbe-numbers for pp–GT thin films.

RF Power (W)	v_D
10	35.37
25	35.18
50	37.80
75	40.35

3.3. Thickness Dependence of Optical Constants

Thickness dependence study was carried out using spectroscopic ellipsometry data taken for pp–GT thin films fabricated at 25 W with different film thicknesses and the corresponding n and k profiles. With an increase of thickness over the measured wavelength region, a very small increase of n is observed. The shift in n *vs*. thickness is comparable to that found for polyparaxylene films [38], which were deemed to not have significant thickness dependence on n. The shifts found in pp–GT thin films are therefore insignificant and thus n is not dependent on thickness.

3.4. Determination of the Energy Gap

To determine the nature of the optical transitions, the optical absorption study was performed for pp–GT thin films. The optical absorption coefficient data were obtained from UV–Vis spectroscopy measurements. The optical absorption dependence of photon energy is expressed by the following relationship [39]:

$$\alpha h v = A(hv - E_g)^m \tag{2}$$

where A is an energy-independent constant, E_g is the optical band gap and m is a constant which is connected to the density-of-states distribution in the transport gap in the band tails and thus determines the type of transition (m = 1/2 and 3/2 for direct allowed and forbidden transitions, respectively, m = 2 and 3 for indirect allowed and forbidden transitions, respectively) [39].

The optical absorption coefficient data obtained from UV-Vis spectroscopy measurements were converted to a Tauc plot using a MATLAB program. In that curve, a value of m = 3/2 was employed for all the pp–GT thin films studied, as this value provided the most linear plot, indicating direct forbidden transitions. The indirect process is much slower than the direct transitions as it requires three entities to intersect in order to proceed: an electron, a photon, and a phonon. Materials showing direct transition are therefore much more efficient than materials that show indirect transition. Gallium arsenide (*GaAs*) and other direct band gap materials are used in optical devices, such as LEDs and lasers, whereas *Si* that is an indirect band gap material is not used. This study shows that pp–GT, having direct transition has the potential to be used in different optical devices. The optical band gap values (Table 2) remained between 3.14 eV and 3.01 eV, falling within the insulating region of E_g. The pp–GT thin films can therefore be used as insulators for the application of flexible coating on electrical apparatus (e.g., printed circuit board, high voltage systems, circuit breakers, *etc*.).

Table 2. Optical bandgap of pp–GT thin films for $m = 3/2$.

RF power (W)	E_g (eV)
10	3.14
25	3.08
50	3.07
75	3.01

3.5. Surface Morphology

The surface profile of pp–GT thin films fabricated at various input RF power levels were studied to examine surface defects and roughness The topographical features of the investigated films deposited on glass surfaces are shown in Figure 5.

Figure 5. AFM images of pp–GT thin films fabricated at 10, 25, 50, and 75 W input RF power levels.

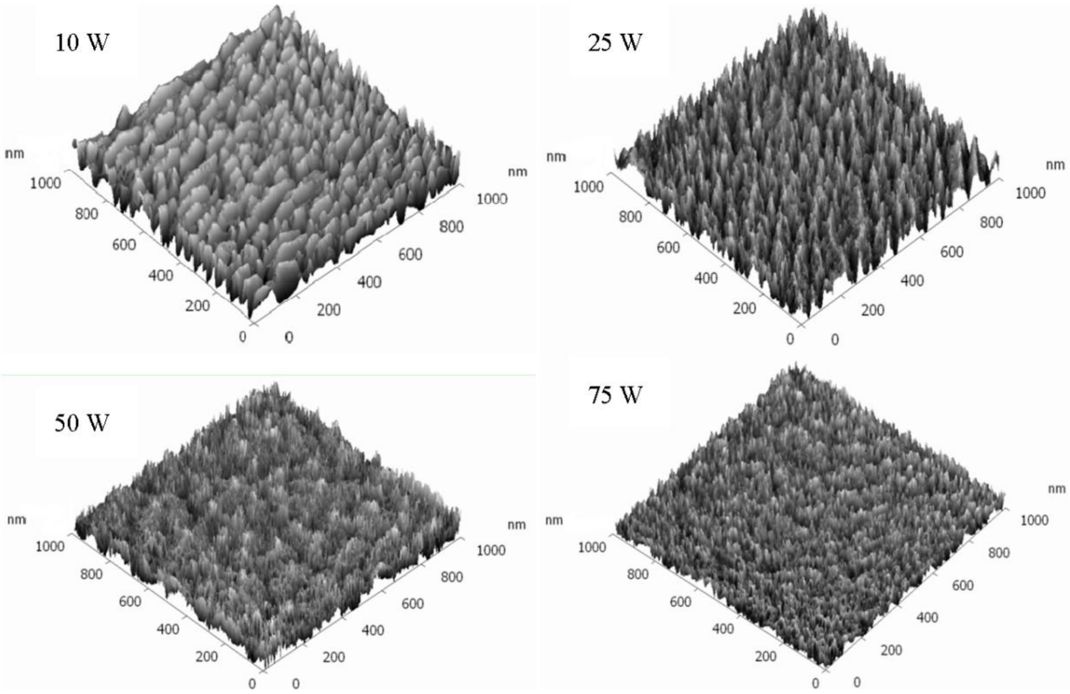

From this study, pp–GT thin films are found to be smooth, uniform and defect-free, exhibiting consistent morphology across film samples. Average roughness values for all samples were approximately 0.3 nm. These roughness values were in agreement with the roughness values found by means of spectroscopic ellipsometry. I Surfaces with RMS roughness values below 0.5 nm have an insignificant effect on its surface and chemical properties and performance [40]. Considering this and the determined roughness of 0.3 nm, the polymerization reactions are confirmed to take place mostly on the surface of the glass substrate rather than in the gas phase [41].

Beside the conventional roughness parameters R_a and R_q, the statistical parameters, such as R_{sk} (skewness) and R_{kur} (kurtosis), were determined for the pp–GT thin films. R_{kur} is a quantitative measure of the kurtosis, which is defined as the randomness of profile heights that determines whether the data sets are peaked or flat relative to a normal distribution. R_{kur} values can range from 0 to 8. Surfaces with distinct peaks that decline rather rapidly and have heavy tails exhibit high values;

whereas rough surfaces with flat top near the mean possess lower values. The pp–GT thin film fabricated at 10 W has lower value of R_{kur} (Table 3), whereas sharp peaks and heavier tails are found for samples fabricated at higher RF power levels (Figure 5) that have relatively high values of R_{kur} (Table 3). A surface skewness (R_{sk}) greater than 0 is observed for pp–GT films, *i.e*., the predominance of disproportionate number of peak-like surface features. Furthermore, it was observed that the 75 and 50 W samples have smaller and tapered features (narrow curves) while the 25 and 10 W samples have broad curves. Furthermore, decrease in entropy indicates the surface flatness, *i.e*., reduction of growth of pores at higher RF power levels [42]. Because of this behavior, R_{rms} and R_{a} values decreased with increase of RF power. However, higher deposition rate of pp–GT resulted in an increase in the surface roughness values due to the fact that the particles in the growth region were unable to relax fast enough before the next layer of the film is deposited [43]. These surface analysis results clearly indicate the difference between the peak distributions for pp–GT samples fabricated at different RF power that may affect the wettability. Uniformity of films is also confirmed from the analysis, which indicates the less prone to fracture characteristics of the pp–GT films.

Table 3. Roughness parameters of pp–GT thin films.

Roughness parameters	**10 W**	**25 W**	**50 W**	**75 W**
Maximum peak height R_{max} (nm)	4.48	2.38	2.16	2.15
Average roughness R_a (nm)	0.30	0.28	0.25	0.21
Root mean square R_q (nm)	0.39	0.34	0.32	0.30
Surface skewness R_{sk}	0.32	0.22	0.14	0.08
Coefficient of kurtosis R_{kur}	0.06	0.54	0.63	0.77
Entropy	6.12	4.5	3.9	3.56

Surface morphology can also be described in relation to the wetting behavior of the plasma films. Surface roughness generally enhances the hydrophilicity [44]. For pp–GT thin films, the decrease in roughness values with higher deposition power is therefore considered to contribute to the increased hydrophobicity of the surface. Smooth surfaces with greater hydrophobicity are vital for optical and electrical applications, and also for implementing as coating materials for surface protection or buffer layers [45].

3.6. Nanoindentation

Mechanical properties of pp–GT deposited under different RF power conditions were investigated using a single indentation method and a load-partial unload technique. A series of indentations were made in the films with depths ranging from 221.5 nm to 207.2 nm depending on the thickness of the film. Illustrative single indentation curves from 2 μm thick pp–GT film fabricated at 10 W is presented in Figure 6.

The load-unload curve (Figure 6) shows the typical behavior of pp–GT thin films undergoing a nanoindentation test. The initial slope of the unloading process is used to deduce the reduced elastic modulus of the material at the specific contact depth, h_c. There are a number of pop-ins in the curve initially and this phenomenon may be attributed to micro-cracking or dislocation nucleation and/or propagation during loading as have been investigated in a wide variety of materials [46].

Figure 6. Load–displacement diagram of pp–GT thin film fabricated at 10 W.

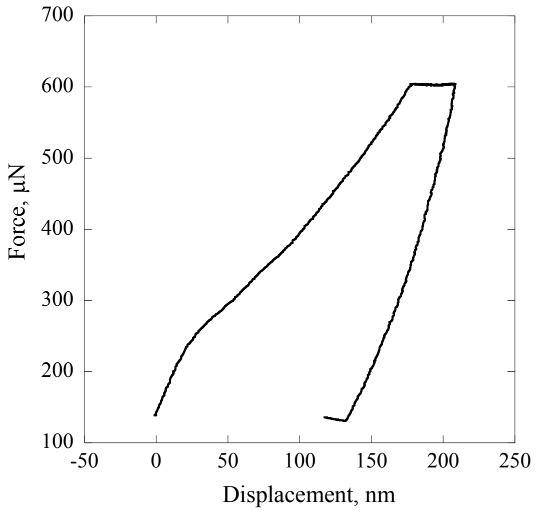

The elastic moduli and hardness of different pp–GT thin film samples increased with the increasing RF power as seen from Table 4. Elastic modulus of pp–GT thin film fabricated at 10 W is 4.22 GPa, while film fabricated at 75 W reaches an elastic modulus of 5.96 GPa. Increase in modulus is also observed with decreasing h_c. This may be due to the transition from spherical contact to conical contact behavior occurred at h_c = indenter radius/4 for the Berkovich indenter used in the study [47]. Data at lower depths should be treated with caution as the contact modulus measured varies considerably with tip radius under spherical contact conditions. Hardness of pp–GT thin films also follows the same trend as elastic modulus. The hardness of the materials increases with increase in input RF power and this can be attributed to the higher crosslinking of the polymers fabricated at higher power levels [22]. This results in an increase in resistance against sample deformation. Increase of elastic modulus and hardness with increasing RF power has also been reported in other materials such as linalyl acetate [26]. However, it should be noted that several sources of error may exist in these experiments, which may include the relative non-uniformity of the indent (e.g., pile-up and sink-in phenomena) observed on some samples, and difficulties in precise estimation of the indent area (e.g., possible overestimation in the case of pile-up and underestimation due to sink-in features), respective influences of material properties and sample thicknesses and creep [48]. In addition, artifacts and tip effects affecting the precision of the measurement may possibly be imaged due to the usage of same tip for the actual indentation process and imaging. In a nanoindentation test, very often the stress relaxation is observed at the maximum load during unloading process. This is due to the large strain beneath indenter and the large strain rate at this point (since the loading rate is usually finite during the experiment). Moreover, sudden withdraw of indenter causes oscillations in measurement whereas holding at maximum load may lead to uncertainties in the measured quantities [48]. In addition, the initial portion of unloading is more prone to thermal drift than the loading curve. The values presented in Table 4 are therefore indicative of the evolution of the hardness properties of pp–GT thin films under changing fabrication conditions and may quantitatively differ from the actual material properties due to aforementioned measurement bounds.

Table 4. Hardness parameters of pp–GT thin films.

RF power (W)	**Contact depth, h_c (nm)**	**Hardness, H ± SE (GPa)**	**Final depth, h_f (nm)**	**Elastic modulus, E (GPa)**
10	221.5	0.40 ± 0.01	137.90	4.22
25	218.3	0.46 ± 0.02	102.53	4.61
50	211.7	0.51 ± 0.02	83.60	4.90
75	207.2	0.58 ± 0.03	69.76	5.96

Loading time and holding time have significant effect on the indentation behavior of pp–GT thin films. To investigate these effects, single indentations were performed on samples deposited at 75 W at constant load of 1000 μN. Figure 7 shows typical repeat single indentation profiles under increasing indentation load of pp–GT film deposited at 75 W. Hardness value decreased from 0.57 GPa to 0.53 GPa with increasing loading and unloading time with rates (r) ranging from 0.5 to 20 nm/s. As creep deformation taking place during the holding time influences the contact depth at maximum load, the hardness values obtained using these maximum contact depth estimates will also be affected [24]. Moreover, the holding time at maximum load affects the unloading portion of the load displacement curve. In this study, an increase in the hold time showed a decrease in the positive slope value of the material. The relationship of decrease in this slope of unloading in the load-displacement curve and modulus of the pp–GT thin films can be explained by the following equation [49]:

$$S = \frac{dP}{dh} = \frac{2}{\sqrt{\pi}} E^{*} \sqrt{A} \tag{3}$$

The decrease in the slope value means decrease in the dP/dh value that leads to a decrease in modulus value. Further increase in hold time increases the indentation depth of the indenter tip on the thin film surface, which leads to increase in contact area of the indenter with the film. The increase in the contact area decreases the hardness of the film. In the case of pp–GT thin films, increasing the hold time from 5 to 25 s at constant load of 500 μN resulted in a decrease in the calculated hardness from 0.59 to 0.53 GPa.

To extend the capabilities of quasistatic testing to allow depth profiling of pp–GT thin films, the partial unloading (PUL) technique was used. This investigation revealed that at depths below 190 nm (2 μm thick pp–GT film), the depth profile of the hardness follows a trend similar to that determined using the single indentation approach. The hardness of the system gradually increases above approximately 190 nm due to the stress field no longer being contained within the body of the thin film.

Figure 7. Typical AFM image of plastic impressions remaining in pp–GT sample fabricated at 75 W after indentation under different load conditions.

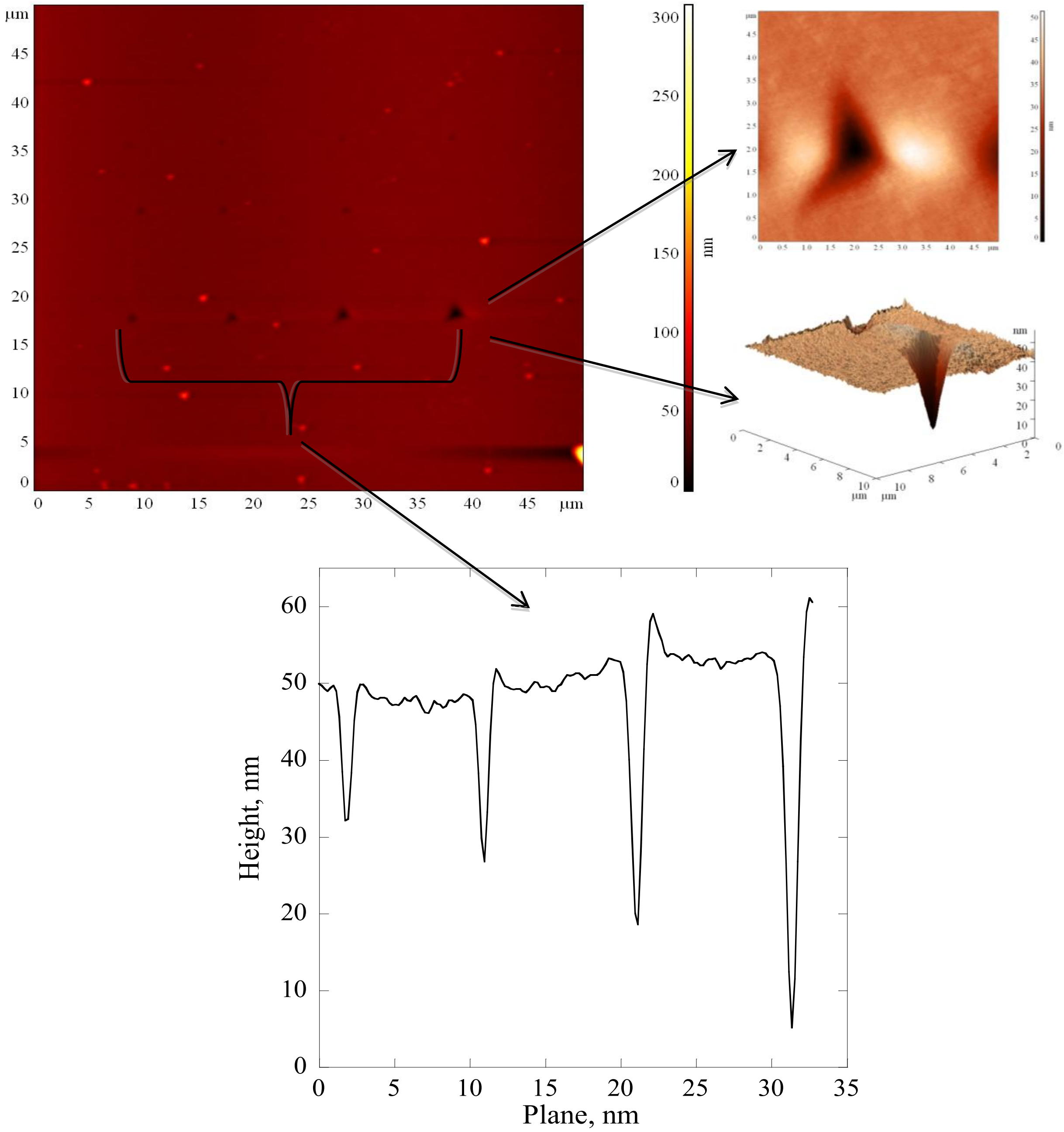

3.7. Adhesion Study

The adhesion behavior of pp–GT thin films deposited on glass is presented in Figure 8. The adhesion improved with higher deposition power. Films fabricated at 10 W showed 5%–15% delamination. However, films fabricated at 50 and 75 W showed no delamination effect with a higher cross hatch rating.

Figure 8. Adhesion data for pp–GT thin films at 10, 25, 50, and 75 W.

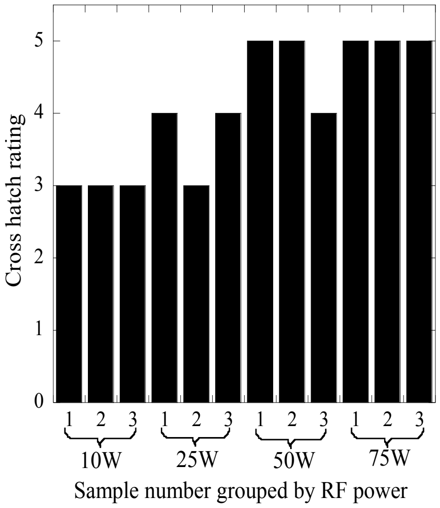

The optical image acquired using the microscope and CCD camera for the 10 W sample showed a significant amount of deformation occurred to the sample upon applying and consequent removal of the adhesive tape. For the thin films deposited at 25 W, the areas that were not affected by the tape test appeared uniform and with the increasing of RF power, this uniformity increased. This trend is attributed to the interfacial bonding that is improved by an increase in cross-link density associated with increasing applied RF power. These findings provide an insight into the reliability of the pp–GT films.

4. Conclusions

The basic optical properties and optical constants of the pp–GT thin films were investigated by means of spectroscopic ellipsometry and UV-Vis spectroscopy. The optical constants such as the refractive index (n), extinction coefficient (k), and optical band gap were determined. The films are confirmed as optically transparent and independent of RF power. The refractive index and extinction coefficient of the pp–GT thin films demonstrated very little dependence on RF power and film thickness. The optical absorption spectra showed that the absorption mechanism is a direct transition. The independence of the refractive index on the RF power level demonstrates the pp–GT thin films as an impending optically stable material for optical applications.

AFM investigation demonstrated that the pp–GT films were smooth, uniform and defect-free. The average roughness parameter decreased with increasing RF power (0.30 for 10 W and 0.21 for 75 W). In the nanoindentation study, combined effects of loading rate and holding time were investigated. For the load rates and hold time considered, pp–GT thin films were found to be a function of both the variables. The unloading portion of the load-displacement curve was found to be strongly dependent on the holding time. The hardness increased from 0.40 GPa for 10 W to 0.58 GPa for 75 W at a load of 700 μN. Elastic modulus of pp–GT thin film fabricated at 10 W was found to be 4.22 GPa, while elastic modulus of 5.96 GPa was found for 75 W film. An adhesion study established that the quality of adhesion is improved for samples fabricated at higher RF power, while the films produced at low RF power adhered poorly to the substrates. These studies demonstrate that the pp–GT polymer is a potential candidate for thin film applications in flexible electronics and OPV that entail smooth and uniform surfaces.

Acknowledgments

JA is grateful to the financial support provided by the JCUPRS scholarship. KB acknowledges funding from JCU and ARC (DE130101550).

Conflicts of Interest

The authors declare no conflict of interest.

References

1. Jung, K.; Choi, W.-K.; Chae, K.H.; Song, J.-H.; Yoon, S.-J.; Lee, M.-H.; Choi, J.-W. Highly conductive and damp heat stable transparent ZnO based thin films for flexible electronics. *J. Alloys Compd*. **2013**, *554*, 240–245.
2. Dubal, D.P.; Holze, R. All-solid-state flexible thin film supercapacitor based on Mn3O4 stacked nanosheets with gel electrolyte. *Energy* **2013**, *51*, 407–412.
3. Qian, X.; Wang, T.; Yan, D. Transparent organic thin-film transistors based on high quality polycrystalline rubrene film as active layers. *Org. Electron*. **2013**, *14*, 1052–1056.
4. Ferguson, A.J.; Blackburn, J.L.; Kopidakis, N. Fullerenes and carbon nanotubes as acceptor materials in organic photovoltaics. *Mater. Lett*. **2013**, *90*, 115–125.
5. Kelly, F.M.; Meunier, L.; Cochrane, C.; Koncar, V. Polyaniline: Application as solid state electrochromic in a flexible textile display. *Displays* **2013**, *34*, 1–7.
6. He, H.; Xu, X.-B.; Zhang, D.-F. An aligned macro-porous carbon nanotube/waterborne polyurethane sensor for the detection of flowing organic vapors. *Sens. Actuators B: Chem*. **2013**, *176*, 940–944.
7. Curto, V.F.; Fay, C.; Coyle, S.; Byrne, R.; O'Toole, C.; Barry, C.; Hughes, S.; Moyna, N.; Diamond, D. Real-time sweat pH monitoring based on a wearable chemical barcode micro-fluidic platform incorporating ionic liquids. *Sens. Actuators B: Chem*. **2012**, *171–172*, 1327–1334.
8. Krebs, F.C. Alternative PV: Large scale organic photovoltaics. *Refocus* **2005**, *6*, 38–39.
9. Su, Y.-W.; Lan, S.-C.; Wei, K.-H. Organic photovoltaics—Review article. *Mater. Today* **2012**, *15*, 554–562.
10. Ahmad, J.; Bazaka, K.; Anderson, L.J.; White, R.D.; Jacob, M.V. Materials and methods for encapsulation of OPV: A review. *Renew. Sustain. Energy Rev*. **2013**, *27*, 104–117.
11. Lee, H.-J.; Kim, H.-P.; Kim, H.-M.; Youn, J.-H.; Nam, D.-H.; Lee, Y.-G.; Leeb, J.-G.; Yusoffa, A.R.M.; Jang, J. Solution processed encapsulation for organic photovoltaics. *Sol. Energy Mater. Sol. Cells* **2013**, *111*, 97–101.
12. Kim, N.; Graham, S. Development of highly flexible and ultra-low permeation rate thin-film barrier structure for organic electronics. *Thin Solid Films* **2013**, *547*, 57–62.
13. Cuddihy, E.; Coulbert, C.; Gupta, A.; Liang, R. Electricity from Photovoltaic Solar Cells: Flat-Plate Solar Array Project Final Report. Volume VII: Module Encapsulation; Jet Propulsion Laboratory: 1986. Available online: http://resolver.caltech.edu/JPLpub86-31-volumeVII (accessed on 17 April 2014).

14. Kim, N. Fabrication and Characterization of Thin-Film Encapsulation for Organic Electronics. Ph.D. Thesis, Mechanical Engineering, Georgia Institute of Technology, Atlanta, GA, USA, 2009.
15. Spanggaard, H.; Krebs, F.C. A brief history of the development of organic and polymeric photovoltaics. *Sol. Energy Mater. Sol. Cells* **2004**, *83*, 125–146.
16. Shaheen, S.E.; Ginley, D.S.; Jabbour, G.E. Organic-Based Photovoltaics: Toward Low-Cost Power Generation. *MRS Bull.* **2005**, *30*, 10–19.
17. Forrest, S.R. The path to ubiquitous and low-cost organic electronic appliances on plastic. *Nature* **2004**, *428*, 911–918.
18. Vasilev, K.; Griesser, S.S.; Griesser, H.J. Antibacterial Surfaces and Coatings Produced by Plasma Techniques. *Plasma Process. Polym.* **2011**, *8*, 1010–1023.
19. Ostrikov, K.; Neyts, E.C.; Meyyappan, M. Plasma nanoscience: From nano-solids in plasmas to nano-plasmas in solids. *Adv. Phys.* **2013**, *62*, 113–224.
20. Michelmore, A.; Charles, C.; Boswell, R.W.; Short, R.D.; Whittle, J.D. Defining Plasma Polymerization: New Insight Into What We Should Be Measuring. *ACS Appl. Mater. Interfaces* **2013**, *5*, 5387–5391.
21. Rahman, M.J.; Bhuiyan, A.H. Structural and optical properties of plasma polymerized o-methoxyaniline thin films. *Thin Solid Films* **2013**, *534*, 132–136.
22. Jacob, M.V.; Easton, C.D.; Woods, G.S.; Berndt, C.C. Fabrication of a novel organic polymer thin film. *Thin Solid Films* **2008**, *516*, 3884–3887.
23. Jacob, M.V.; Olsen, N.S.; Anderson, L.; Bazaka, K.; Shanks, R.A. Plasma polymerised thin films for flexible electronic applications. *Thin Solid Films* **2013**, *546*, 167–170.
24. Bazaka, K.; Jacob, M.V. Nanotribological and nanomechanical properties of plasma-polymerized polyterpenol thin films. *J. Mater. Res.* **2011**, *26*, 2952–2961.
25. Bazaka, K.; Jacob, M.V.; Bowden, B.F. Optical and chemical properties of polyterpenol thin films deposited via plasma-enhanced chemical vapor deposition. *J. Mater. Res.* **2011**, *26*, 1018–1025.
26. Xu, Q.F.; Wang, J.N.; Sanderson, K.D. Organic−Inorganic Composite Nanocoatings with Superhydrophobicity, Good Transparency, and Thermal Stability. *ACS Nano* **2010**, *4*, 2201–2209.
27. Berggren, M.; Richter-Dahlfors, A. Organic bioelectronics. *Adv. Mater.* **2007**, *19*, 3201–3213.
28. Li, Y.X.; Yan, L.; Shrestha, R.P.; Yang, D.; Ounaies, Z.; Irene, E.A. A study of the optical and electronic properties of poly (vinylidene fluoride–trifluoroethylene) copolymer thin films. *Thin Solid Films* **2006**, *513*, 283–288.
29. Oliver, W.C.; Pharr, G.M. An improved technique for determining hardness and elastic modulus using load and displacement sensing indentation experiments. *J. Mater. Res.* **1992**, *7*, 1564–1583.
30. Bazaka, K.; Jacob, M.V. Synthesis of radio frequency plasma polymerized non-synthetic Terpinen-4-ol thin films. *Mater. Lett.* **2009**, *63*, 1594–1597.
31. Kim, M.C.; Cho, S.H.; Han, J.G.; Hong, B.Y.; Kim, Y.J.; Yang, S.H.; Boo, J.-H. High-rate deposition of plasma polymerized thin films using PECVD method and characterization of their optical properties. *Surf. Coat. Technol.* **2003**, *169–170*, 595–599.
32. Anderson, L.J.; Jacob, M.V. Effect of RF power on the optical and morphological properties of RF plasma polymerised linalyl acetate thin films. *Appl. Surf. Sci.* **2010**, *256*, 3293–3298.

33. Pilla, P.; Iadicicco, A.; Contessa, L.; Campopiano, S.; Cutolo, A.; Giordano, M.; Guerra, G.; Cusano, A. Optical chemo-sensor based on long period gratings coated with δ form syndiotactic polystyrene. *IEEE Photonics Technol. Lett.* **2005**, *17*, 1713–1715.
34. Liu, J.-G.; Ueda, M. High refractive index polymers: Fundamental research and practical applications. *J. Mater. Chem.* **2009**, *19*, 8907–8919.
35. Enlow, J.O.; Jiang, H.; Grant, J.T.; Eyink, K.; Su, W.; Bunning, T.J. Plasma polymerized ferrocene films. *Polymer* **2008**, *49*, 4042–4045.
36. Okubo, T.; Kohmoto, S.; Yamamoto, M. Optical polymer having a high refractive index and high abbe number prepared by radical polymerization using 2,5-BiS(2-Thia-3-Butenyl)-1,4-Dithiane. *J. Macromol. Sci. Part A* **1998**, *35*, 1819–1834.
37. Dislich, H. Plastics as optical materials. *Angew. Chem. Int. Ed. Engl.* **1979**, *18*, 49–59.
38. Gaynor, J.F.; Desu, S.B. Optical properties of polymeric thin films grown by chemical vapor deposition. *J. Mater. Res.* **1996**, *11*, 236–242.
39. You, Z.Z.; Hua, G.J. Refractive index, optical bandgap and oscillator parameters of organic films deposited by vacuum evaporation technique. *Vacuum* **2009**, *83*, 984–988.
40. Fritz, S.E.; Kelley, T.W.; Frisbie, C.D. Effect of dielectric roughness on performance of pentacene TFTs and restoration of performance with a polymeric smoothing layer. *J. Phys. Chem. B* **2005**, *109*, 10574–10577.
41. Hu, X.; Zhao, X.; Uddin, A.; Lee, C.B. Preparation, characterization and electronic and optical properties of plasma-polymerized nitriles. *Thin Solid Films* **2005**, *477*, 81–87.
42. Tien, C.-L.; Lyu, Y.-R.; Jyu, S.-S. Surface flatness of optical thin films evaluated by gray level co-occurrence matrix and entropy. *Appl. Surf. Sci.* **2008**, *254*, 4762–4767.
43. Johnston, E.E.; Ratner, B.D. Surface characterization of plasma deposited organic thin films. *J. Electron Spectrosc. Relat. Phenom.* **1996**, *81*, 303–317.
44. Wenzel, R.N. Resistance of solid surfaces to wetting by water. *Ind. Eng. Chem.* **1936**, *28*, 988–994.
45. Shi, F.F. Recent advances in polymer thin films prepared by plasma polymerization Synthesis, structural characterization, properties and applications. *Surf. Coat. Technol.* **1996**, *82*, 1–15.
46. Bull, S.J. Nanoindentation of coatings. *J. Phys. D* **2005**, *38*, R393.
47. Korsunsky, A.M.; Constantinescu, A. The influence of indenter bluntness on the apparent contact stiffness of thin coatings. *Thin Solid Films* **2009**, *517*, 4835–4844.
48. Zhao, M.; Xiang, Y.; Xu, J.; Ogasawara, N.; Chiba, N.; Chen, X. Determining mechanical properties of thin films from the loading curve of nanoindentation testing. *Thin Solid Films* **2008**, *516*, 7571–7580.
49. Tarefder, R.; Faisal, H. Effects of dwell time and loading rate on the nanoindentation behavior of asphaltic materials. *J. Nanomech. Micromech.* **2013**, *3*, 17–23.

Appendix A.3

Wetting, Solubility and Chemical Characteristics of Plasma-Polymerized 1-Isopropyl-4-Methyl-1,4-Cyclohexadiene Thin Films

As published in: Ahmad, Jakaria, Bazaka, Katia, Oelgemöller, Michael, and Jacob, Mohan V. (2014) *Wetting, solubility and chemical characteristics of plasma-polymerized 1-isopropyl-4-methyl-1,4-cyclohexadiene thin films*. Coatings, 4 (3). pp. 527-552.

Coatings **2014**, *4*, 527-552; doi:10.3390/coatings4030527

OPEN ACCESS

coatings

ISSN 2079-6412

www.mdpi.com/journal/coatings

Article

Wetting, Solubility and Chemical Characteristics of Plasma-Polymerized 1-Isopropyl-4-Methyl-1,4-Cyclohexadiene Thin Films

Jakaria Ahmad [1], Kateryna Bazaka [1], Michael Oelgemöller [2] and Mohan V. Jacob [1,*]

[1] Electronic Materials Research Lab, College of Science, Technology and Engineering, James Cook University, Townsville 4811, Australia; E-Mails: jakaria.ahmad@my.jcu.edu.au (J.A.); katia.bazaka@jcu.edu.au (K.B.)

[2] Applied and Green Photochemistry Group, College of Science, Technology and Engineering, James Cook University, Townsville 4811, Australia; E-Mail: michael.oelgemoeller@jcu.edu.au

* Author to whom correspondence should be addressed; E-Mail: mohan.jacob@jcu.edu.au; Tel.: +61-7-4781-4379.

Received: 8 April 2014; in revised form: 11 July 2014 / Accepted: 22 July 2014 / Published: 31 July 2014

Abstract: Investigations on the wetting, solubility and chemical composition of plasma polymer thin films provide an insight into the feasibility of implementing these polymeric materials in organic electronics, particularly where wet solution processing is involved. In this study, thin films were prepared from 1-isopropyl-4-methyl-1,4-cyclohexadiene (γ-Terpinene) using radio frequency (RF) plasma polymerization. FTIR showed the polymers to be structurally dissimilar to the original monomer and highly cross-linked, where the loss of original functional groups and the degree of cross-linking increased with deposition power. The polymer surfaces were hydrocarbon-rich, with oxygen present in the form of O–H and C=O functional groups. The oxygen content decreased with deposition power, with films becoming more hydrophobic and, thus, less wettable. The advancing and receding contact angles were investigated, and the water advancing contact angle was found to increase from 63.14° to 73.53° for thin films prepared with an RF power of 10 W to 75 W. The wetting envelopes for the surfaces were constructed to enable the prediction of the surfaces' wettability for other solvents. The effect of roughness on the wetting behaviour of the films was insignificant. The polymers were determined to resist solubilization in solvents commonly used in the deposition of organic semiconducting layers, including chloroform and chlorobenzene, with higher stability observed in films fabricated at higher RF power.

Keywords: coatings; wetting; plasma polymerization; FTIR; contact angle

---

1. Introduction

Organic thin film materials have many potential and implemented applications, from biocompatible and antifouling coatings in medical devices to protective coatings, waveguides and component materials in optoelectronic devices, such as flexible organic electroluminescent devices (OLED), organic photovoltaics (OPV) and organic thin film transistors (OTFT) [1–6]. The motivation for using organic materials stems from their chemical versatility, low cost, low temperature fabrication and ability for reel-to-reel printing, as well as mechanical flexibility [1]. The attractive synthetic and processing flexibility of organic materials allows for fine tuning of their properties to achieve a desired combination of optoelectronic, physicochemical, mechanical and biological characteristics, and controlling the manner in which these materials interact with relevant liquids [7]. The latter is an important aspect for optoelectronics and biomedical applications alike. Solution processing of electronic circuits demands dielectric interlayer stability in organic solvents and strong interfacial adhesion, while the susceptibility of the coating to the uptake of moisture is critical for OPV encapsulation applications. Surface wetting by physiological fluids is a key determinant of biocompatibility and degradation under *in vitro* and *in vivo* conditions [1,8]. The surface-solvent kinetics and ensuing degradation of organic materials under aqueous conditions is an important consideration for biodegradable and compostable electronics, where it would affect both operational performance and the physical transience of the device [9].

One of the key predictors of surface-solvent interactions, the wetting behaviour at polymer surfaces and interfaces, is dependent on the nature of the variable length of polymer chains, density fluctuations and the relatively slow motion of the long chain molecules [10]. Contact angle (CA) analysis is typically used to obtain primary data from which the degree of wettability for a specific solid-liquid combination can be inferred [7,11], with lower CAs indicating better wetting compared to larger CAs. This analysis also provides indirect information about the structure of the film matrix, where observed changes to θ at the liquid/solid interface are attributed to specific solid-liquid interaction mechanisms, such as absorption, spreading and swelling [12]. Fundamentally, wettability is affected by the chemical composition, topography, rigidity and homogeneity of the surfaces. The chemical composition of the surface determines its surface energy: whereas surfaces rich in non-polar groups (e.g., $–CH_x$, with $x = 1–3$) have low surface energies and, thus, are hydrophobic, surfaces with a high density of polar groups (e.g., –OH or –C=O) exhibit high surface energies and are hydrophilic [13]. With regard to surface topography, an increase in the surface roughness enhances the surface hydrophilicity of hydrophilic materials and hydrophobicity in the case of hydrophobic surfaces [14]. The micro- and nano-scale variations in the slope on the surface are believed to create physical barriers that directly affect the motion of the contact line, thus affecting CAs observed at the macro scale. In a similar way, distinct domains of chemically heterogeneous surfaces, e.g., those with higher hydrophobicity, are thought to interfere with the motion of the contact angle by hindering the advancement or contraction of the water front and, thus, increasing or decreasing the observed CA. Several models propose a relationship between the measured CAs of a given non-ideal surface and its flat, homogenous counterpart of the same composition, among them Wenzel and Cassie–Baxter models [15,16]. In the Wenzel model, the liquid is assumed to be in contact with all of the parts of the irregular surface and is typically applied to chemically homogenous surfaces, whereas the Cassie-Baxter model places the drop on the surface protrusions without wetting the entire surface and is believed to be more appropriate for chemically heterogeneous surfaces.

Recently, growing interest in environmentally-friendly technologies has led to the exploration of a number of alternative organic source materials, e.g., unprocessed raw agricultural, food and waste substances [17], and energy-efficient green fabrication methodologies, e.g., plasma-assisted nanofabrication [18,19]. The key driver of this research therefore rests in the need to support robust and sustainable economic and societal development, which, in practical terms, means the development of materials and technologies that are cheaper, more efficient and can address the objectives of modern societies in an environmentally-sustainable fashion. Most of the existing chemical synthesis processes used for the fabrication of electronics device components are energy-inefficient and require multi-step processing and the use of hazardous auxiliary substances, such as organic solvents and catalysts [20]. These synthesis routes often rely on expensive and/or toxic, high purity, non-renewable materials [1]. In addition to using hazardous materials, modern electronic devices also use valuable and scarce materials, the availability of some of which (e.g., gallium, indium, *etc.*) is reducing at a high rate [1]. At the same time, only a limited portion of high-tech waste is recycled, with the bulk of the waste being deposited into landfills, where it slowly degrades, leaching out potentially harmful by-products. By using minimally processed, renewable natural resources, such as non-petrochemical oils, e.g., essential oils, and highly reactive non-equilibrium dry plasma-based chemistry, it is possible to lower the environmental footprint and the economic costs of organic electronics and other such technologies throughout their lifecycle, from their fabrication to their use and disposal [21].

Essential oils are volatile aromatic compounds that are widely used in pharmacological, perfumery and culinary preparations for their aromatic and medicinal properties. Their availability in commercial quantities, relative low-cost, renewable nature and minimal toxicity makes them a suitable precursor for "green" functional materials [22]. As a volatile material, essential oil is well suited to chemical vapour deposition (CVD), as no carrier gas is required to deliver the monomer into the polymerization chamber. Using plasma as a catalyst, the oils can be converted into functional polymer thin films in a one-step process at room temperature, without the need for pre- or post-processing, e.g., annealing, or catalysts. Unlike most plasma deposited films, plasma polymers of essential oils are optically transparent and smooth. Over the last few years, thin films from lavender and tea tree essential oils have been developed and identified as promising candidates for applications in electronics, as dielectric and encapsulation layers [23–27]. Plasma polymers of terpinen-4-ol also display a valuable and rare electron blocking hole-transporting property that is very attractive for OLEDs [27]. Versatile biological activity, including antibacterial activity against drug-resistant strains of *Staphylococcus*, *Streptococcus* and *Candida* species, also makes essential oils an attractive candidate for the fabrication of antibacterial and biocompatible implantable systems, including implantable electronics [28].

This paper reports the fabrication of polymer thin films from 1-isopropyl-4-methyl-1,4-cyclohexadiene, also known as γ-Terpinene, using RF plasma polymerization. γ-Terpinene is an isomeric hydrocarbon distilled directly from *Melaleuca alternifolia* essential oil and used extensively in cosmetics and cleaning products for its aromatic and medicinal properties. While γ-Terpinene has been determined as a component in plants using many quantitative analysis methods [29,30], it had not been studied extensively as the main topic compound [31]. However, recent investigations of γ-Terpinene revealed that the optical properties of the fabricated plasma-polymerized γ-Terpinene (pp–GT) thin films are promising, with transparency to the optical wavelengths and refractive index of 1.57–1.58 (at 500 nm) [26]. It is reported that these polymers possess an optical band gap (E_g) of ~3 eV that falls into the insulating E_g region. Independent of deposition conditions, the surfaces are smooth and defect-free, with uniformly distributed morphological features and average roughness well below 0.30 nm [26]. The optical and surface characteristics suggest that the pp–GT thin films have the potential to be implemented in optoelectronic and insulating applications. This paper focuses on the wetting, solubility and chemical characteristics of these films and the compatibility of the material with solvents typically utilized in the manufacturing of organic electronic devices, with the intention to use these films in OPVs, especially as encapsulation coatings and insulating layers in flexible electronics.

2. Experimental Section

2.1. Preparation of Thin Films

Thin film samples were deposited on high quality glass microscope slides using a custom-made RF polymerization chamber, 0.75 m in length with an inner diameter of 0.055 m (volume of 0.0035 m^3). RF power is delivered to the system via an ENI RF generator at 13.56 MHz through a matching network and capacitively coupled copper electrodes. The copper electrodes were placed 0.11 m from the monomer inlet and 0.1 m apart, with the active electrode closest to the monomer inlet. The electrode configuration used was based on the uniformity of the RF discharge it produced and the corresponding uniformity of resulting thin films for the particular reaction chamber utilized throughout this work.

Prior to deposition, the substrates were thoroughly washed in extran, cleaned ultrasonically in water, rinsed in isopropanol and distilled water, air dried and placed in the reaction chamber. For each deposition, 5 mL of γ-Terpinene (GT) monomer was used. The chamber was evacuated to a pressure of ~100 mTorr, at which stage the monomer inlet was opened to allow the monomer to evaporate. Argon gas was then used to flush the chamber for 1 min at a pressure of 1000 mTorr to remove residual background gas and ensure an oxygen-free surface. The chamber was then evacuated to 100 mTorr, at which stage the monomer inlet was closed, and RF glow (10, 25, 50 and 75 W) was initiated. The monomer-free plasma state was maintained for 2 min to stabilize the pressure, as well as to etch potential residual contaminants from the surface of the substrate. Once the pressure had reached 150 mTorr, the monomer inlet was opened, beginning the deposition. The flow rate was controlled via a vacuum stopcock and was estimated to be 1.57 cm^3/min by employing the procedure outlined by Gengenbach and Griesser [32].

Following the aforementioned experimental procedure, plasma polymer thin films were fabricated from γ-Terpinene (GT) monomer (Figure 1) at various RF power levels (10, 25, 50 and 75 W) and an ambient temperature of 20 °C. pp–GT thin-films were examined over the wavelength range 190–1000 nm using a variable angle spectroscopic ellipsometer (model M-2000, J.A. Woollam Co., Inc., Lincoln, NE, USA). Ellipsometric parameters Ψ and Δ were obtained at three different angles of incidence, $\varphi = 55°$, 60° and 65°. In addition, the transmission data were also collected. Ψ and Δ were used to derive the optical constants based on a multilayer model consisting of a previously modelled substrate and Cauchy layer built in the J.A. Woollam Inc. analysis software (WVASE32) [33] via regression analysis. The quality of the fit was measured quantitatively by determining the mean-squared error and through the use of the correlation matrix. Gaussian oscillators were employed within the model to provide an optimal fit of the data, with a lower mean square error and lower average correlation between fitting terms. A more detailed review of the procedure has been reported elsewhere [34]. Samples for Fourier transform infrared (FTIR) and CA measurements were deposited for 30 min to obtain films of ~700 nm thickness. Depositions were performed for 45 min to obtain films of ~1 µm for atomic force microscope (AFM) measurements.

Figure 1. Conformers of 1-isopropyl-4-methyl-1,4-cyclohexadiene resulting from the rotation about the C^7–C^1 bond, adapted from [35].

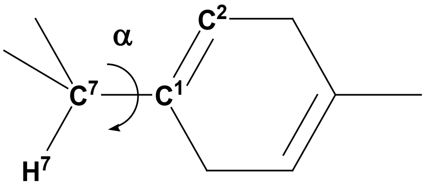

2.2. Chemical Characterization

FTIR spectroscopy was carried out for the chemical characterization of the γ-Terpinene monomer and the pp–GT thin films using a Perkin Elmer Spectrum 100 FTIR spectrometer. Spectra were obtained in transmission mode in the region of 4000–500 cm^{-1}, where 32 scans were acquired for each sample at a resolution of 1 cm^{-1}. Contributions from CO_2 and H_2O were eliminated from the spectra by a background subtraction procedure, where the background was pre-recorded under the same atmospheric conditions.

The surface chemistry of the deposited samples was further analysed by XPS on a SPECS SAGE XPS system equipped with a Phoibos 150 hemispherical analyser and an MCD-9 detector. The background pressure was held at 2×10^{-6} Pa during experiments. For wide scan spectra and high resolution scans of the C 1s peak, an Mg Ka X-ray source was used ($h\nu = 1253.6$ eV), operated at 10 kV and 20 mA (200 W). Measurements were performed with a pass energy of 100 eV, and 0.5 eV energy steps were used for wide scan spectra, while 20 eV pass energy and 0.1 eV energy steps were used for high resolution scans. Spectra were analysed using CasaXPS (Case Software Ltd, Teignmouth, UK). Synthetic peaks were fitted to the C 1s envelops following the methodology of Beamson and Briggs [36] with the spectra correction for charging effects during analysis using a reference value of 285 eV, the binding energy of the C–C component from neutral hydrocarbon [37]. The analysis area was circular with a diameter of 5mm, and spectra were acquired at a take-off angle of 90°.The full width at half maximum (FWHM) of the C 1s synthetic peaks remained constant at 1.5 eV.

2.3. Contact Angle (CA) Measurements

Static and dynamic CAs (using water, diiodomethane (DIM) and ethylene glycol (EG) as probing liquids) of pp–GT thin films are measured. Static CAs are commonly used in calculations of surface tension parameters. However, they may not provide a reliable description of a non-ideal surface, *i.e.*, that is chemically and/or morphologically heterogeneous. Plasma-modified and plasma-polymerized surfaces are often characterized by both chemical and morphological heterogeneity [38]. Non-ideal surfaces typically display hysteresis, which can be estimated by measuring advancing and receding CAs.

CA measurements were performed using a KSV 101 system and a micrometre syringe with a narrow diameter stainless steel needle. The static CA was measured by the sessile drop method, whereby a drop of probing liquid was gently placed onto the thin film surface. The apex of each drop was confirmed using a CCD camera prior to each measurement to ensure consistency in drop volume (8 μL). The evolution of the CA (θ, the angle between the baseline of the drop and the tangent at the drop boundary), the droplet volume (V, μL), the droplet surface area (A, mm^2), the droplet height (h, mm) and the droplet basal diameter ($2r$, mm) were monitored using a software-assisted image-processing procedure. The reported values are an average of a minimum of seven measurements taken for each examined surface.

Advancing and receding contact angles were measured using the dynamic sessile drop technique. First, a sessile drop of probe liquid of known volume was placed on the surface of the sample, ensuring that the needle remained in the drop during the measurement to avoid undesired vibration. The drop was then modified by slowly adding volume, with the advancing angle estimated as the largest contact angle possible without increasing its solid/liquid interfacial area. The receding angle was estimated as the minimum possible angle that can be achieved by slowly removing the probe liquid from the drop without decreasing the drop's contact area. Both the advancing and receding angle were estimated as the average of the angles on both sides of the drop profile. Contact angle hysteresis (CAH) was estimated as the difference between the advancing and receding angle.

The presence of the needle is known to distort the contour line of the drop, due to the interactions between the surface of the needle and the liquid with the drop. The distortion of the drop shape is more prominent in the case of receding angles, where the needle's receding angle tends to pull the drop up around the needle. This distortion may result in significant errors [39].

2.4. Surface Free Energy Analysis

There are several widely applied approaches for the determination of the solid surface free energy and its components from CA measurements [40]. Most theories of solid surface energy have a basis in Young's equation that employs the equilibrium CA, where the solid is considered close to ideal. The ideal surface is one that is chemically and morphologically homogenous, and thus, CAH is assumed to be absent or negligible.

For the non-ideal surfaces that are chemically and morphologically inhomogeneous, with a measurable, substantial CAH, the apparent surface free energy γ_{SV} and other interfacial interaction parameters, adhesive film tension Π, work of adhesion W_A and work of spreading W_S, can be derived from the CAH approach developed by Chibowski [41] with only three measurable quantities: the surface tension of the probe liquid γ_{LV} and its advancing θ_A and receding θ_R CA hysteresis ($CAH = \theta_A - \theta_R$). The solid surface free energy γ_{SF} can be expressed by the following relation [41]:

$$\gamma_{SF} = \gamma_{SV} + \Pi \tag{1}$$

$$\Pi = \gamma_{LV}(\cos\theta_R - \cos\theta_A) \tag{2}$$

The apparent, total surface free energy of a solid γ_{SV} ($\approx \gamma_{SF}$) can be expressed as [41]:

$$\gamma_{SV} = \frac{\Pi(1+\cos\theta_A)^2}{(1+\cos\theta_R)^2 - (1+\cos\theta_A)^2} \tag{3}$$

CAH can be related to the work of spreading W_S of liquid on the polymer surface. W_S is a thermodynamic quantity that relates the wettability to the mechanical strength of adhesion. It enables one to characterize the competition between solid-liquid adhesions with different liquids [40]. W_S can be easily calculated from the work of adhesion W_A and the work of cohesion W_C:

$$W_S = W_A - W_C \tag{4}$$

where $W_A = \gamma_{LV}(1 + \cos\theta_A)$ and $W_C = 2\gamma_{LV}$ [40].

For surfaces that are chemically heterogeneous, but very smooth, the experimentally observed advancing CA θ_A might be expected to be a good approximation of Young's CA θ_Y, whereas the experimental receding angle, θ_R, is expected to have less reproducibility, due to liquid sorption or solid swelling [39]. With the assumption of $\theta_A = \theta_Y = \theta$, the surface free energy can be calculated by means of the van Oss' adaptation of Young's theory [42,43]. The quantitative determination of all of the surface thermodynamic properties of the polymer coatings was performed using the Young-Dupré equation [43]:

$$(1+\cos\theta_a)\gamma_L = 2\left(\sqrt{\gamma_S^{LW}\gamma_L^{LW}} + \sqrt{\gamma_S^{+}\gamma_L^{-}} + \sqrt{\gamma_S^{-}\gamma_L^{+}}\right) \tag{5}$$

where θ_a is the advancing CA (°), γ_L is the surface tension (SFT) of the liquid in contact with the solid surface (mJ/m^2), γ_L^{LW} is the apolar component (Lifshitz–van der Waals [LW]) of the SFT of the liquid (mJ/m^2), γ_L^{+} is the electron-acceptor parameter of the polar component (acid–base [AB]) of the liquid (mJ/m^2), γ_L^{-} is the electron-donor parameter of the polar component (AB) of the liquid (mJ/m^2), γ_S^{LW} is the apolar component (LW) of the surface energy of the solid (mJ/m^2), γ_S^{+} is the electron-acceptor parameter of the polar component (AB) of the solid (mJ/m^2) and γ_S^{-} is the electron-donor parameter of the polar component (AB) of the solid (mJ/m^2).

The interface interaction of the polymer and the solvent is determined from their interfacial tension γ_{12} using the following equation [43]:

$$\Delta G_{121} = -2\gamma_{12} \tag{6}$$

where ΔG_{121} is the free energy change. In the case of two completely miscible substances, where the interfacial tension cannot be measured directly, γ_{12} can be calculated using the following equation:

$$\gamma_{12} = \left(\sqrt{\gamma_1^{LW}} - \sqrt{\gamma_2^{LW}}\right)^2 + 2\left(\sqrt{\gamma_1^{+}\gamma_1^{-}} + \sqrt{\gamma_2^{+}\gamma_2^{-}} - \sqrt{\gamma_1^{+}\gamma_2^{-}} - \sqrt{\gamma_1^{-}\gamma_2^{+}}\right) \tag{7}$$

In case of two completely immiscible substances (or any given solid-liquid system), the interfacial tension can be derived directly from the measured contact angle θ:

$$\gamma_{SL} = \gamma_S - \gamma_L\cos\theta \tag{8}$$

There are several other methods for obtaining surface tension values; however, the appropriateness of these methods for the probing of particular polymer/solvent combinations remains a subject of debate [44–46]. Fowkes [47] and Neumann's [44,48] approaches were chosen in this study to provide a basis for comparison.

Fowkes method is commonly used for the determination of the surface free energy of polymeric materials [49]. Two-phase systems are investigated that contain a substance (solid or liquid) in which only the dispersion interactions appear. Considering such systems, Fowkes determined the surface free energy corresponding to the solid-liquid interface using the following equation [49]:

$$\gamma_{SL} = \gamma_S + \gamma_L - 2(\gamma_S^{LW}\gamma_L^{LW})^{0.5} \tag{9}$$

According to Fowkes [50,51], the combination of Equations (8) and (9) yields the formula that enables one to calculate the surface free energy of a solid for which $\gamma_S = \gamma_S^{LW}$ is valid [49]:

$$\gamma_S = \gamma_S^{LW} = \gamma_L^2(1 + \cos\theta)^2/4\gamma_L^{LW} \tag{10}$$

If the measuring liquid is a dispersive one ($\gamma_L = \gamma_L^{LW}$), Equation (10) simplifies to:

$$\gamma_S = \gamma_S^{LW} = 0.25\gamma_L(1 + \cos\theta)^2 \tag{11}$$

To determine γ_S of any solid, the CA for the solid is measured using the dispersion liquid. Then, γ_S^{LW} is calculated from Equation (11). Next, the CA (θ_p) is measured using a liquid for which $\gamma_L = \gamma_L^{LW} + \gamma_L^{AB}$. The γ_S^{AB} can be estimated using [49]:

$$\gamma_S^{AB} = [0.5\gamma_L\left(1 + \cos\theta_p\right) - \left(\gamma_S^{LW}\gamma_L^{LW}\right)^{0.5}]^2/\gamma_L^{AB} \tag{12}$$

Fowkes method is based on the independence and additivity of the dispersion and polar interactions [49]. On the other hand, Neumann's approach derives the SFT from a purely thermodynamic point of view and, therefore, neglects the molecular origins of SFT [7]. However, this is the only theory that allows the calculations to be done by using just one probing liquid. The following equation provides a method for calculating the surface energy of a solid from a single CA value [44,48]:

$$\cos\theta = -1 + 2\sqrt{\frac{\gamma_S}{\gamma_L}}e^{-\beta(\gamma_L-\gamma_S)^2} \tag{13}$$

where β is an experimentally-derived constant ($\beta \approx 0.0001247$) [49].

2.5. Determination of Roughness and Wetting Behaviour of Surfaces

To analyse the effect of surface roughness on the wetting properties of the pp–GT thin films, the polymer was deposited on glass, silicon (Si), silicon dioxide (SiO_2) and indium tin oxide (ITO) substrates using RF plasma polymerization at 75 W RF power. The surface morphology and roughness parameters of the films were determined from AFM images acquired on a NT-MDT NTEGRA Prima AFM operating in semi-contact (tapping) mode, using (NSC05, NT-MDT) cantilevers with a spring constant of 11 N/m, a tip radius of curvature of 10 nm, an aspect ratio of 10:1 and a resonance frequency of 150 KHz. 3D interactive visualization and statistical approximation was used to analyse the topographic profiles of the surfaces. Scanning was performed perpendicular to the axis of the cantilever at a rate of typically 1 Hz, with scan areas of 1 μm × 1 μm, 10 μm × 10 μm and 50 μm × 50 μm.

3. Results and Discussion

3.1. Chemical Analysis of pp–GT Films

The monomer, 1-isopropyl-4-methyl-1,4-cyclohexadiene ($C_{10}H_{16}$), belongs to the group of monocyclic Terpinenes commonly designated as monoterpenes. It contains two double bonds in its ring-structure, which are not conjugated (1,4-diene group).

Due to the highly unsaturated nature of cyclohexa-1,4-diene with its 4 sp^2 carbon atoms, γ-Terpinene is considered almost planar. The molecular structure is characterized by one conformationally relevant internal rotation axis (C^1–C^7), which allows for the formation of various conformations (Figure 1). Density functional theory (DFT) calculations conducted by Marzec and co-workers led to the identification of three minima on the molecule's potential energy surface [35]. According to the orientation of the C^2–C^1–C^7–H^7 dihedral angle (α), the conformers were named trans, gauche+ and gauche−. The gauche+ ($\alpha = 47.5°$) and gauche− ($\alpha = -47.5°$) conformers (C_1) are mirror images, while the trans-like ($\alpha = 180.0°$) conformer has C_s symmetry. Since different conformations characterize the amount and type of contact between adjacent atoms or groups, these data are important for defining the macroscopic properties of the material.

The IR spectra of the monomer, 1-isopropyl-4-methyl-1,4-cyclohexadiene, and the various pp–GT thin films are shown in Figure 2. Characteristic IR vibrations are summarized in Table 1. For the monomer, multiple C–H stretching vibrations were found as a strong signal between 2818 and 2960 cm^{-1}, whereas the corresponding C–H bending vibrations appeared as broad signals and with weak to medium intensities in the range of 1300 to 1466 cm^{-1}, confirming the population of various conformers [35]. The stretching vibrations of the C–C bonds were observed in the fingerprint region below 1200 cm^{-1}. In contrast, no clear stretching vibrations of the C=C bonds could be observed. The data collected was in agreement with some previous publications reporting the interpretation of vibrational spectra of 1-isopropyl-4-methyl-1,4-cyclohexadiene [52,53]. Comparing the IR spectra for the pp–GT thin films with that of the monomer, it is evident that the number of absorption frequencies in the spectra has reduced significantly upon polymerization, particularly in the fingerprint region of the spectrum (1500 cm^{-1} and below). Peaks also broadened for the pp–GT thin films, indicating very high degrees of polymerization. This is further supported by the disappearance of the =C–H vibration at 3088 cm^{-1}.

Electron-generated dissociation of GT monomer (rather than thermally excited or by direct chemical reaction) forces the input RF power to strongly affect the nature of the chemically-reactive species that engage in polymerization and film formation. Considering the bond strengths for 1-isopropyl-4-methyl-1,4-cyclohexadiene, the C–C single bonds are likely to dissociate first to form reactive fragments. Dissociation of higher energy bonds will occur when RF power is increased, and hence, the resultant fragmentation of the precursor molecule and subsequent crosslinking will increase. The double bonds in 1-isopropyl-4-methyl-1,4-cyclohexadiene are likely to undergo saturation through a reaction with these reactive fragments. Furthermore, the temperature of the substrate will also increase as a result of the exposure of the substrate to a large amount of energy. This will result in a reduction in the retention of the original precursor moieties [54].

Figure 2. FTIR spectra (% transmittance *vs.* wavenumber, cm^{-1}) for γ-Terpinene monomer and pp–GT thin films.

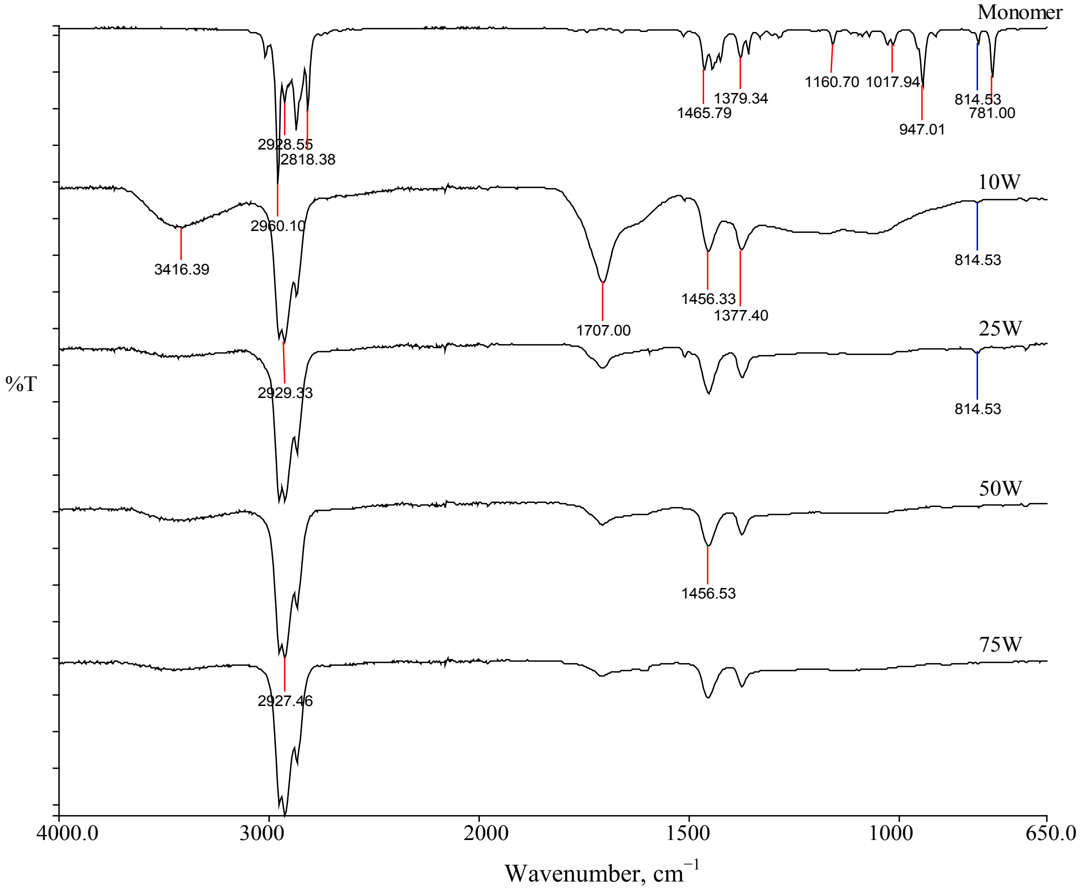

Table 1. FTIR assignments for γ-Terpinene monomer and plasma-polymerized γ-Terpinene (pp–GT) films, adapted from [55].

Assignment	**Group Frequency, cm^{-1}**	
	Monomer	**pp–GT Films**
ν (OH) of water	absent	3416 (medium to weak)
ν (=C–H)	3088 (weak)	absent
ν (C–H)	2818–2960 (medium to strong)	2872–2960 (strong)
ν (C=O)	absent	1707 (medium to weak, broad)
δ (C–H)	1300–1466 (medium to weak)	1377, 1456 (medium, broad)
ν (C–C)	947–1161 (strong to weak)	unresolved or absent
ω (C–H)	781 (strong), 815 (medium)	815 (medium to absent)

Vibrational modes: ν = stretching, δ = bending, ω = out of plane bending.

A broad absorbance band emerged at 3416 cm^{-1} (Figure 2) in the pp–GT spectrum that is considered to be the O–H stretching vibration of residual water. This is further supported by the absence of a C–O vibration. The infrared band associated with C–H stretching vibrations observed for the monomer also remained for the polymeric films; their intensity broadened, thus suggesting high degrees of cross-linking. Absorptions corresponding to C–H bending vibrations (between 1300 and 1466 cm^{-1}) decreased in magnitude and broadened with higher input RF power. Likewise, skeletal C–C vibrations between 947 and 1161 cm^{-1} vanished completely. A peak emerged at 1707 cm^{-1}, indicating the presence of carbonyl groups (C=O stretch), which were presumably formed from the reactions of radical intermediates with residual molecular oxygen and subsequent decompositions. The peak, however, decreased and eventually almost disappeared with higher RF power, possibly due to increased fragmentations and combinations of the carbon skeleton under these extreme conditions. The presence of C=O bonds in the polymer films obtained at lower powers aligns with the differences in the properties of these materials. In general, polymer materials containing C=O (and –OH) groups are characterized by a high-dielectric constant, because of their high polarizability [56] and lower hydrophobicity. In addition, these polymers are likely to be more unstable (chemically and mechanically) compared to hydrocarbon polymers, as C=O (and –OH) bonds allow increased interactions with polar solvents. The CA investigations in this study revealed that pp–GT films deposited at lower RF power were indeed less stable when in contact with common processing solvents, such as acetone or alcohol. The reduction or complete disappearance of the C=O moiety renders pp–GT more stable.

The FTIR findings are consistent with the results of elemental analysis (X-ray photoelectron spectroscopy (XPS)) of pp–GT thin films deposited at various RF power levels. The oxygen content significantly decreased from 11.8% to 2.1%, while the carbon fraction increased from 88.2% to 97.8% with RF deposition power increasing from 10 to 50 W (Table 2). This result showed a substantial reduction in magnitude of the H-bonded O–H stretch-related band for pp–GT fabricated under higher RF power conditions.

Table 2. Elemental composition of pp–GT thin films deposited at various RF power.

Peaks	**Atomic Fraction, %**		
	10 W	**25 W**	**50 W**
O 1s	11.8	5.3	2.1
C 1s	88.2	94.7	97.8

3.2. Contact Angle and Wettability

A CAH approach provides several parameters listed in Table 3, useful in quantitative evaluations of water/solid surface interactions. An increase in deposition power resulted in a greater values for the advancing CA and W_A and smaller values for the receding CA, CAH, γ_{SV} and W_S. The relatively low receding CA reflects higher liquid sorption and/or solid swelling observed in the films fabricated at lower RF power [39]. The relatively low CAH for films fabricated at high RF power may be the result of the lower content of unsaturated double bonds in the pp–GT films and the film being more chemically homogenous [57]. At high RF power, intense fragmentation takes place and a very little amount of the original monomer/oligomeric units get integrated into the film structure. At this condition, the plasma-polymerized film is also highly cross-linked, which prevents the rotational motion of the surface moieties away from the surface towards the bulk of the film. The low CAH for 75-W film is also consistent with the low surface roughness, which, in earlier investigations, was found to decrease with deposition power [26]. CAH increases, as the RF power is decreased, which might be attributed to the higher content of unsaturated double bonds in the pp–GT films and loose cross-linking [57]. Incorporation of many monomer and oligomer units also takes place during this process at low RF power. These may lead to a decrease in the homogenous surface chemical composition and an increase in surface roughness with the decrease in RF power.

Table 3. Wettability parameters of pp–GT thin films deposited at various RF power derived from contact angle hysteresis (CAH).

RF Power, W	θ_A, °	θ_R, °	*CAH*, °	γ_{SV} (mJ·m^{-2})	W_A (mJ·m^{-2})	W_S (mJ·m^{-2})
10	63.14	8.28	54.86	44.60	105.69	−39.91
25	69.25	17.43	51.82	40.27	98.59	−47.01
50	72.98	29.15	43.83	38.39	94.11	−51.49
75	73.53	36	37.53	38.91	93.44	−52.16

Dynamic CAs determined using other probing liquids, e.g., DIM and EG, showed similar trends.

The surface hydrophobicity/hydrophilicity of the pp–GT films of different RF power levels for different solvents based on the static CA measurements are summarized in Table 4. Independent of thickness, the application of the pp–GT coating affected the static CA values for all three probing liquid ($p < 0.05$): water, EG and DIM. According to Olivares-Navarrete *et al.* [58] a similar phenomenon is observed for Niobium coatings. Significant differences in static CAs were observed in the case of water for pp–GT films fabricated at different RF power. In all other cases, CA values were found in the same range.

Table 4. Static CAs for pp–GT thin film surfaces. DIM, diiodomethane.

Sample, W	CA ± SD, °		
	Water	Ethylene Glycol	DIM
10	61.03 ± 1.79	36.29 ± 2.56	36.56 ± 1.29
25	68.93 ± 0.88	37.44 ± 2.03	36.47 ± 2.24
50	72.72 ±1.47	41.97 ± 3.60	36.58 ± 2.01
75	80.72 ± 1.94	49.33 ± 1.25	38.70 ± 3.45

The static CA data presents important information regarding interactions between the surface and the liquid system. A relatively high rate of change in the water CA signifies the reorientation of functionalities at the solid-solvent interface [59]. From the raw data for EG (Figure 3), an initial rapid drop in CA was attributed to the absorption of the solvent into the pp–GT thin film. Subsequently, the CA remained relatively stable for the duration of recording. While this rate of change was considered insignificant, the positive ramp suggested the occurrence of the reorientation of functionalities at the interface. For the DIM data, all of the films were stable with time, and the highest CA was found for films fabricated at 75 W. These results indicate that pp–GT is more stable as the RF power is increased, due to an increase in the degree of cross-link density associated with these deposition conditions [7].

The initial water CAs, θ_0 suggested that pp–GT thin films deposited at higher RF power were more hydrophobic compared to the films fabricated at lower RF power, with CAs of 61.0° (10 W) and 80.7° (75 W). This was attributed to the reduction of hydrophilic moieties at the top surface of the polymer and the decrease in the oxygen content associated with the higher deposition power.

Figure 3. Representative static CA curves for pp–GT thin films for (**a**) water; (**b**) EG and (**c**) DIM.

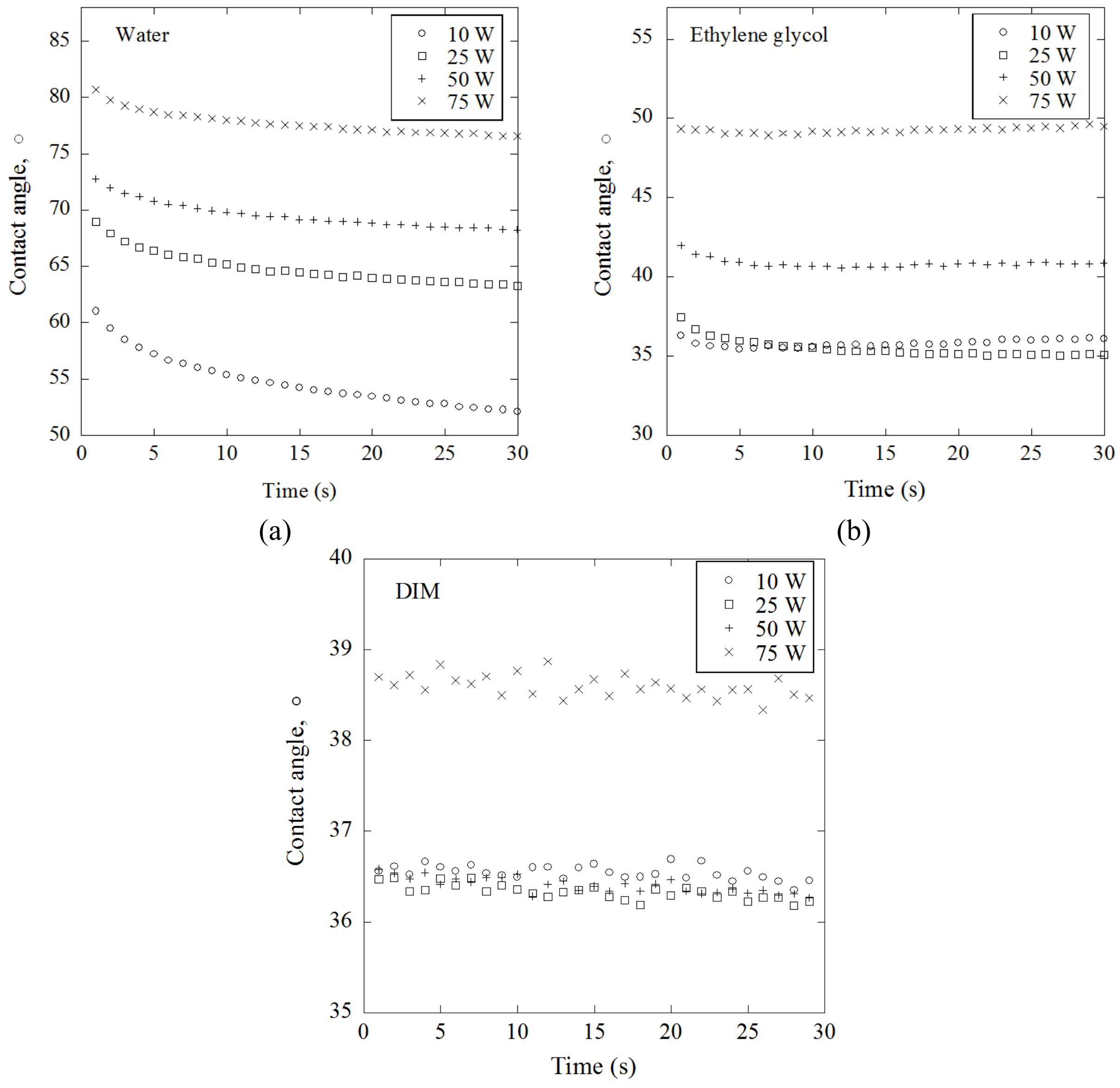

(a)

(b)

(c)

Investigating the evolution of the droplet profile may also be appropriate and meaningful to determine the wetting behaviour of thin films, especially if supported by considerations accounting for the phenomena involved at the solid/liquid interface [12]. The relationship between CA and the relevant surface phenomena can be simplified by the following general expression:

$$\theta(t) = \sum_{i=1}^{n} f_i(t) \tag{14}$$

where each $f_i(t)$ is related to one of the n independent phenomena involved (e.g., absorption, spreading, swelling and evaporation of the water drop). The derivative of $\theta(t)$ can be used to compute the θ evolution rate and predict the time required to reach the steady-state condition, $(\Delta\theta/\Delta t) \approx 0$.

$$\frac{\Delta\theta}{\Delta t} = \sum_{i=1}^{n} \frac{\Delta f_i(t)}{\Delta t} \tag{15}$$

The phenomena involved at the water droplet-polymer interface can also be profitably investigated by using a suitable image analysis procedure [12]. A reliable description of droplet evolution that depends on two major effects, namely, absorption and spreading, can be determined from a combined trigonometric (detection of θ) and geometric (changes in the droplet shape) approach. The absorption effect can be described as the sinking of the water droplet beneath the contact surface, with decreases in its volume (V) and contact area, but the volume is not affected in case of spreading effect, although it widens the contact area [12]. In this work, the detection of θ and the shape parameters (droplet height h, basal radius r, contact area and droplet volume V) determined by image analysis were used to describe absorption and spreading quantitatively, as well as their correlation with the surface topography of the films.

The evaporation of a sessile droplet can go through four consecutive stages: (i) spreading until the value of static advancing CA is reached; (ii) evaporation proceeds with a constant contact area and decreasing CA, until it reaches the receding value; (iii) evaporation with a constant receding CA and decreasing radius of the contact line; and (iv) evaporation with a decrease of both the radius of the contact line and CA until the droplet disappears. During Stage (i), the evaporation can be neglected [60]. In the present work, the contribution of evaporation to the total water droplet kinetics was examined directly by measuring the CA on pp–GT thin films. For films fabricated at 50 and 75 W, spreading phenomena was found to be in effect until static CA of 69.9° and 78.0° was reached. No significant difference between the water droplet volume values (Table 4) was found throughout the analysis. The effect of evaporation is therefore considered to be negligible for pp–GT thin films fabricated at 50- and 75-W RF power. The same trend was observed in case of poly(ethylene terephthalate) (PET) [12].

Given the negligible evaporation effects, the CA evolution was considered to be related to changes in the droplet volume and the solid/liquid surface contact area for all pp–GT thin films tested in this work. This would indicate that, at least at the early stages, two different physicochemical phenomena are occurring at the solid/liquid interface: absorption and spreading. At first glance, rather large differences in θ were observed within the first 30 s for the 10- and 25-W polymer thin films, which were confirmed by the data reported in Table 5 and by Figure 4.

The water droplet profile began to change once the droplet was in contact with the 10-W polymer thin film. Figure 4 shows that over the period of 0–10 s, the perceptible increase in the solid/liquid contact area on the pp–GT film fabricated at 10 W was accompanied by a decrease in volume, possibly because of the spontaneous diffusion of water inside the thin film via absorption. The drop surface area data suggests that, after this early phase, spreading began to take place and contributed to the overall kinetics of the evolution of the droplet profile. Both the absorption and spreading phenomena then continued to contribute, until the end of the 30-s period of analysis. The 25-W pp–GT thin film showed the same phenomena over the 0–10-s period. There was an early interaction of the surface and water that is evident from the increased drop surface area (Figure 4). After this early phase, the solid/liquid contact area remained stable for the remainder of the period of analysis. However, a decrease in volume suggests the evaporation phenomenon for that period of analysis.

Table 5. Main parameters derived from static water CA measurement of pp–GT thin films.

RF Power, W	**$\Delta\theta_{t30\text{-}t0}$, ° [a]**	**$\Delta V_{t30\text{-}t0}$, μL [b]**	**$\Delta A_{t30\text{-}t0}$, mm^2 [c]**	**Phenomenon**
10	−8.91 ± 0.72	−0.08 ± 0.07	0.51 ± 0.79	Absorption + spreading
25	−5.67 ± 1.09	−0.08 ± 0.05	0.15 ± 0.27	Absorption + evaporation
50	−4.47 ± 0.44	−0.07 ± 0.05	0.05 ± 0.11	Evaporation
75	−4.16 ± 0.03	−0.06 ± 0.01	−0.04 ± 0.02	Evaporation

[a] The CA variation during the time of analysis (30 s); [b] water droplet volume variation; [c] drop surface area variation.

Figure 4. Solid/liquid contact area (mm^2) evolution over time (30 s) for pp–GT thin films.

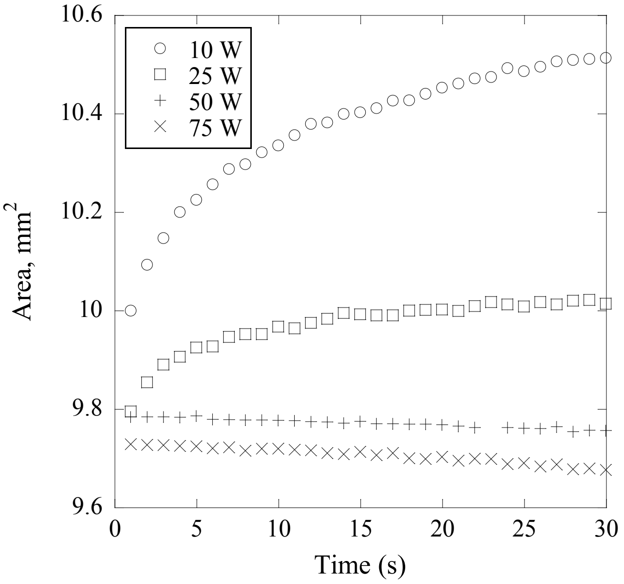

Figure 5 illustrates that curves for the pp–GT thin films fabricated at 10 W and 25 W could not attain a zero-order-rate state at the end of the 30-s analysis. Both absorption and spreading were therefore still occurring at the end of the analysis period at the solid/liquid interface.

Figure 5. The first derivative of the curves of static water CA evolution during the 30-s period of analysis.

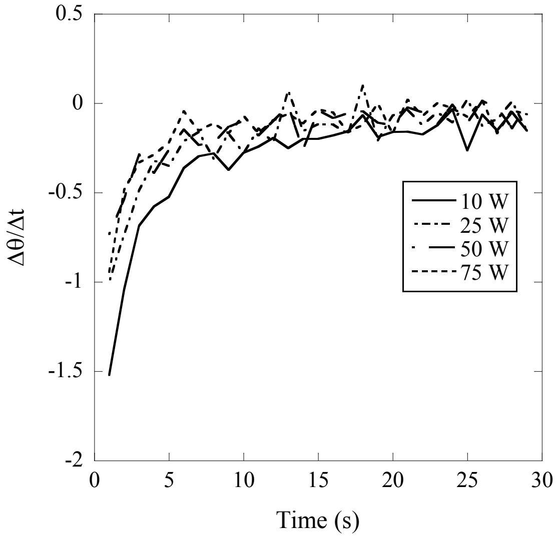

The water droplet profile of 50- and 75-W polymer thin films did not change substantially during the 30-s analysis, although the difference between θ_0 and θ_{30} was statistically significant ($p < 0.05$) (Table 4). According to the literature, these observations may be due to two factors: (i) the inclination of the water droplet to minimize its surface area when interacting with the polymer surface, which is capable of changing its free energy through the reorientation of certain polymer chains exposed at the solid/air interface [61]; and (ii) molecular conformation changes. The preferred orientation of functional groups could justify the θ values, as well as the decrease in the drop surface area (Figures 4 and 6).

Figure 6. Experimental heights of the droplet on pp–GT thin films.

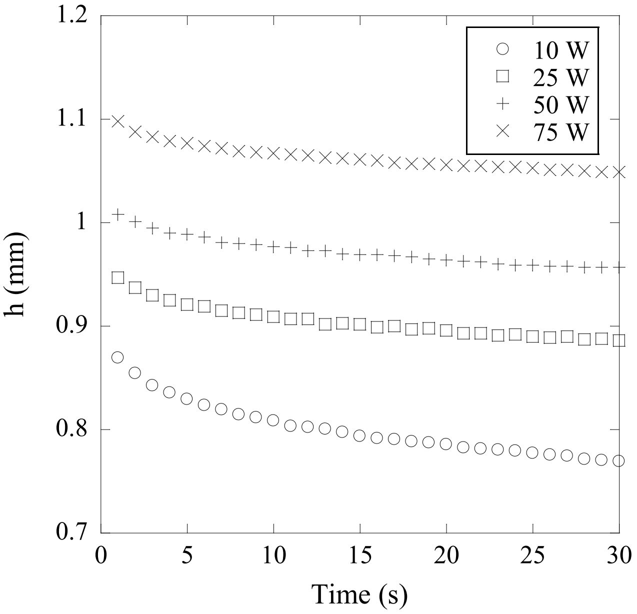

3.3. Contact Angle/Image Analysis Combined Approach

To gain information on the main driving forces governing drop evolution on pp–GT thin film surfaces, such as absorption, spreading, swelling and evaporation, and to determine their individual contributions to the overall wetting phenomenon, a combined CA/image analysis approach was adopted that enabled the spherical condition of the dome formed by the droplet at the solid/liquid interface to be assessed.

The shape of the water droplets changed with time, and pp–GT thin film fabricated at 10 W showed the most profound change observed from the CCD camera images. Physicochemical features of 10 W films and the inherent structural flexibility can explain this phenomenon. These two factors are recognized as crucial factors in aggregation on the molecular level [62]. The 10-W pp–GT thin films also showed the largest variations for both spreading and absorption. However, smaller effects were observed for 75-W films, where the evaporation phenomenon was detected, but was almost negligible ($\Delta A = -0.01$ mm^2). An indication of this is also provided in Figure 6, where the experimental heights of the water droplet are displayed.

As noticeable from Figure 6, the height of the water droplet on pp–GT thin film fabricated at 10 W dropped further and at a faster rate compared to the respective heights of droplets on films fabricated at other RF powers. This may be due to the wider and deeper undulations present in the 10 W film (Figure 7) compared to the films fabricated at 25, 50 and 75 W.

Figure 7. AFM image (1 × 1 μm^2) of the pp–GT film fabricated at 10 W.

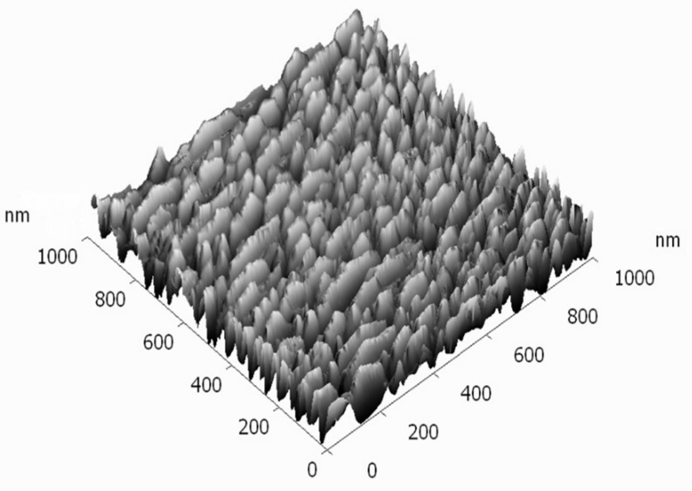

3.4. Effect of Surface Roughness on Wettability

Wetting of a surface by a liquid is influenced by the roughness of that surface [15]. Thin films of pp–GT were deposited at 75-W RF power on topographically-distinct surfaces of glass, Si, SiO_2 and ITO substrates to attain chemically similar, but morphologically different, pp–GT surfaces and, thus, to investigate the influence of roughness on the wetting properties of the material. Surface roughness was characterized by AFM, with the corresponding roughness values shown in Table 6. After the surface roughness characterization, wetting studies by CA measurements were carried out using the sessile drop technique, as described in the Experimental Section. A CA correlation with surface roughness, as determined by AFM, is evident from these results.

Table 6. RMS roughness and CA values of pp–GT thin films deposited on different substrates.

Substrate	RMS Roughness ± SD, nm	CA ± SD, °
Glass	0.30 ± 1.51	80.72 ± 1.94
SiO_2	5.06 ± 1.03	81.95 ± 0.98
Si	7.14 ± 1.58	82.08 ± 1.54
ITO	13.94 ± 1.27	83.80 ± 1.47

The measurement of the water CAs on the pp–GT films deposited on glass and SiO_2 substrates show a virtually constant or a very small increase in the static CA values (Table 6), while films deposited on Si and ITO present an increase by 2°–4°. This tendency, even if very small, confirms that the water CAs increase with the surface roughness. As expected from this limited variation in roughness, the variation range in the water CAs reported for pp–GT thin films was very small. The results from this work also show that surface roughness influences the wetting of the pp–GT, even at extremely low R_q values. Busscher *et al.* [63] and Hitchcock *et al.* [64] reported similar effects of roughness on the wettability of several polymers. The effect of surface roughness on the wettability of pp–GT is therefore needed to be considered for potential applications.

3.5. Surface Tension (SFT) Parameters

SFT parameters for pp–GT thin films fabricated at different RF power levels were derived using the Van Oss-Chaudhury-Good (VCG), Fowkes and Neumann approach and are summarized in Table 7. The CA data obtained for the solvents, together with the widely-used SFT parameters for water, DIM and EG [65] were employed in this study.

Table 7. The surface tension (SFT) components obtained via VCG, Fowkes and Neumann's approach for pp–GT thin films.

Approach	SFT Components, mJ/m^2	Solvent	10 W	25 W	50 W	75 W
VCG	γ^{LW}	–	41.3	41.3	41.3	40.3
	γ^{AB}	–	3.4	3.7	2.7	1.6
	$\gamma+$	–	0.2	0.3	0.2	0.1
	$\gamma-$	–	19.1	10.9	8.7	4.5
	γ_s	–	44.7	45	44	41.8
Fowkes	γ_s		52.6	48.8	47.1	43.4
Neumann	γ_s	water	40.1	33.6	30.6	24.5
		DIM	39.1	38.6	36.5	32.7
		EG	41.3	41.3	41.3	40.3

Most monopolar materials are water soluble [65] and their values of γ^- are relatively large. For all pp–GT thin films, γ^- was significantly higher than γ^+, indicating a monopolar nature. It is possible to use these values of γ^- to determine an upper limit above which solubility will occur. Van Oss *et al.* [66] demonstrated that for a given Solute 1 (monopolar surface 1)-solvent 2 (bipolar) combination, the following equation can provide that limit:

$$\gamma_{12}^{\mathrm{TOT}} = \left(\sqrt{\gamma_1^{\mathrm{LW}}} - \sqrt{\gamma_2^{\mathrm{LW}}}\right)^2 + 2\left(\sqrt{\gamma_1^{+}\gamma_2^{-}} - \sqrt{\gamma_1^{-}\gamma_2^{+}}\right) \tag{16}$$

Employing $\gamma_2^{\mathrm{LW}} \approx 40\ \mathrm{mJ/m^2}$, it was found that Equation (5) becomes negative. Interfacial tension therefore becomes negative for $\gamma_1^- > 28.31\ \mathrm{mJ/m^2}$. A negative interfacial tension between the material and water indicates the possibility of the penetration of water into the material, leading to repulsion between the molecules or particles and promoting solubilisation [66]. The pp–GT thin films have $\gamma^- < 28.31\ \mathrm{mJ/m^2}$ (Table 6). The films are therefore not water soluble. The 75-W film gave the lowest γ^- value, indicating that the hydrophobicity of the polymer increased with RF power.

The results obtained using Fowkes approach roughly compare with those obtained via VCG and Neumann's approaches. However, the VCG and Fowkes approaches are expected to be more accurate, as they require more than one CA measurements to determine SFT values. There was some variance in the values obtained using Neumann's approach between different solvents for each polymer film (Table 6). These values are smaller than those found with VCG approach, with the exception of the values for DIM. The total SFT (γ_s) was found between 41 and 45 $\mathrm{mJ \cdot m^{-2}}$ for all samples investigated using the VCG approach. Values between 43 and 52 $\mathrm{mJ \cdot m^{-2}}$ were found using the Fowkes approach. This is similar to the value of ≈44 $\mathrm{mJ \cdot m^{-2}}$ for PET obtained by Wu *et al.* [67], as well as 42 $\mathrm{mJ \cdot m^{-2}}$ for PMMA. The values are also consistent with those reported for plasma thin films deposited from other secondary plant metabolites, where total SFTs of 45–48, 36–40 and 31–37 $\mathrm{mJ \cdot m^{-2}}$ were found for thin films derived from linalyl acetate [68], *Lavandula angustifolia* essential oil [7] and terpinen-4-ol [69], respectively.

3.6. Wetting Behavior

The wettability of each solution on the pp–GT surface can be quantified by computing the spreading parameter $\Delta W = \gamma_L(\cos\theta - 1)$ [70]. It shows the extent to which the liquid will adhere to the surface relative to itself and, hence, indicates the ability of a liquid drop to stick to the solid surface during solution processing [71].

The pp–GT thin films fabricated at low RF power were characterized by increased wettability (Table 8). It is also observed that EG and DIM wets the pp–GT surface better than water. At $\theta = 0°$ and $\Delta W = 0$, the liquid can adhere well to the surface of the solid, and hence, complete wetting is observed. It is to be noted that the value of the work of spreading, W_S determined from the advancing and receding CAs are almost similar to the values of ΔW (calculated in this section), which gives the validation of the investigation.

Table 8. Spreading parameter (ΔW, mN/m) of pp–GT thin films.

Solvent	10 W	25 W	50 W	75 W
Water	−37.54	−46.63	−51.18	−61.10
EG	−9.31	−9.89	−12.31	−16.72
DIM	−9.99	−9.95	−10.00	−11.15

Another important illustration of the wetting behaviour of liquids on the pp–GT thin film surface can be performed from their wetting envelopes. These are the lines of constant equilibrium CA on a plot of the polar fraction (γ_L^{AB}) *versus* the dispersive fraction (γ_L^{LW}) of the liquid determined from the following equation [68]:

$$(1 + \cos\theta_a)\gamma_L = 2\left(\sqrt{\gamma_s^{LW}\gamma_L^{LW}} + \sqrt{\gamma_s^{AB}\gamma_L^{AB}}\right) \tag{17}$$

Figure 8 demonstrates the degree to which various liquids wet the pp–GT film surfaces fabricated at different RF power if γ_L^{AB} and γ_L^{LW} are known. It also illustrates the surface properties of ideal liquids for solution processing on the pp–GT thin films. By placing a boundary on the curve at a CA of 0°, complete wetting behavior can be determined. Liquids with surface energy components that lie above the line of $\theta = 40°$ will not wet the surfaces of pp–GT films sufficiently to enable suitable film formation from solution processing [71]. The points for water are lying on or between the 60° and 80° contour of the pp–GT wetting envelope, which means that it will not wet a pp–GT film surface, but rather, show a CA between 60° and 80°. This behaviour may be desirable if these films are considered as mechanically-flexible encapsulating coatings for organic electronics. The behaviour of chloroform and chlorobenzene was also examined, as these solvents are commonly used in the deposition of organic semiconducting layers from solution [72]. Both of them are found to lie within the 0° contour, indicating that each solvent will wet the pp–GT surface completely. If complete wetting of the surface by solution processing is needed for a specific application, both of these solvents would be appropriate in conjunction with the pp–GT thin film surface.

Figure 8. Wetting envelopes at 0°, 20°, 40°, 60° and 80° using surface tension components for pp–GT samples fabricated at (**a**) 10 W; (**b**) 25 W; (**c**) 50 W and (**d**) 75 W.

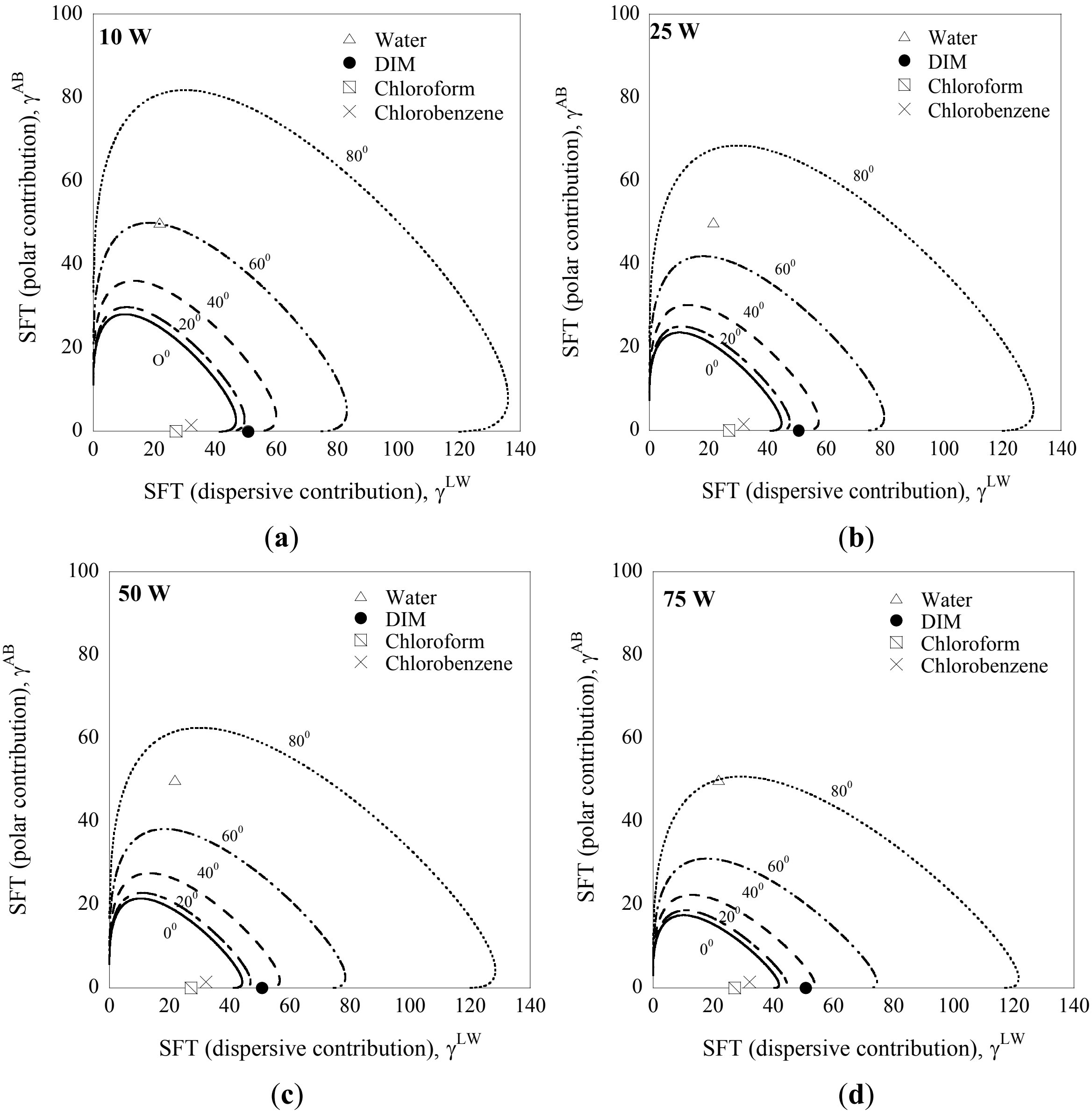

(**a**) (**b**)

(**c**) (**d**)

3.7. The Interfacial Tension and Solubility

The SFT parameters obtained using the VCG, Fowkes and Neumann's approach were used to calculate the interfacial tension between the solid and liquid given by Equations (7) and (8). The solubility of the solid (ΔG_{121}) in that liquid was then determined by incorporating interfacial tension values into Equation 6. Results using Equations (6)–(8) are presented in Table 9.

For $\Delta G_{121} >> 0$, the polymer is solvophilic for the solvent; for $\Delta G_{121} << 0$, the polymer is solvophobic for the solvent; for $\Delta G_{121} \approx 0$, the polymer is partially dissolved in the solvent. The values obtained (Table 9) indicate that the pp–GT polymer is solvophobic, and the strongest solvophobic response was found to be assigned to water, which is expected, as the CA values for water are found to be the most stable. The absence of negative γ_{SL} and γ_{12} values for the solvents investigated (Table 9), indicates that pp–GT is insoluble in the three liquids. ΔG_{121} values increased in magnitude with increasing RF power for all of the probe liquids, except DIM. This shows a less soluble behaviour for water and EG. However, measurements using DIM indicate swelling or partial dissolution of pp–GT thin films.

Table 9. ΔG_{121} values obtained using Equations (5)–(7) from the derived surface tension data.

Solvent	RF Power (W)	γ_s Data	SFT Parameters, mJ/m^2		Solubility, mJ/m^2	
			γ_{SL} (Equation (8))	γ_{12} (Equation (7))	$\Delta G_{121} = -2\gamma_{SL}$	$\Delta G_{121} = -2\gamma_{12}$
Water	10 W	VCG	9.43	9.41	−18.86	−18.82
		Fowkes	17.34		−34.68	
		Neumann	4.84		−9.68	
	25 W	VCG	18.85	18.82	−37.7	−37.64
		Fowkes	22.6		−45.2	
		Neumann	7.47		−14.94	
	50 W	VCG	22.37	22.39	−44.74	−44.78
		Fowkes	25.47		−50.94	
		Neumann	9		−18	
	75 W	VCG	30.11	30.11	−60.22	−60.22
		Fowkes	31.67		−63.34	
		Neumann	12.80		−25.6	
EG	10 W	VCG	6.01	6.03	−12.02	−12.06
		Fowkes	13.92		−27.84	
		Neumann	0.45		−0.9	
	25 W	VCG	6.92	6.99	−13.84	−13.98
		Fowkes	10.67		−21.34	
		Neumann	0.51		−1.02	
	50 W	VCG	8.31	8.32	−16.62	−16.64
		Fowkes	11.41		−22.82	
		Neumann	0.79		−1.58	
	75 W	VCG	10.57	10.67	−21.14	−21.34
		Fowkes	12.13		24.26	
		Neumann	1.45		−2.90	
DIM	10 W	VCG	3.89	3.87	−7.78	−7.74
		Fowkes	11.8		−23.6	
		Neumann	0.5		−1	
	25 W	VCG	4.17	4.17	−8.34	−8.34
		Fowkes	7.92		−15.84	
		Neumann	0.49		−0.98	
	50 W	VCG	3.2	3.19	−6.40	−6.38
		Fowkes	6.30		−12.60	
		Neumann	0.5		−1	
	75 W	VCG	2.20	2.21	−4.40	−4.42
		Fowkes	3.76		7.52	
		Neumann	0.61		−1.22	

According to the wetting envelopes for pp–GT thin films, the CAs for several important organic solvents typically used in organic electronics, e.g., chloroform and chlorobenzene, will be too low to be determined experimentally. Therefore, the parameter θ_S is assumed to be 0° for the purpose of calculating the solubility values for these solvents. These values were found to be strongly negative, indicating that the pp–GT films are insoluble for solvents employed in the processing of organic electronics.

4. Conclusions

The pp–GT films were successfully prepared and characterized. An FTIR analysis confirmed that exposure to an RF plasma field can effectively initiate the polymerization of the monomer. Some functional groups observed in the monomer were retained during the polymerization process, but the C=O stretching vibration (observed in pp–GT spectra) was not present in the monomer spectrum. An increase in RF power resulted in a reduction of the magnitude of the remaining groups, which was attributed to increased fragmentation and, consequently, polymerization of the monomer. RF power can therefore be an effective tool for the fabrication of polymer thin films with tuned properties.

The pp–GT films exhibited different wetting properties, as indicated by the investigation of CA analysis and wetting envelopes. The trends observed were directed by two main phenomena at the solid/liquid interface, namely absorption and spreading, which affect the overall wetting behaviour. This interpretation of the data was based on the assessment of the geometry of the water droplet placed on the film surfaces. The greatest absorption was detected for 10-W pp–GT films while using water as the solvent. Improved stability was observed for films fabricated at higher RF power with the increased hydrophobicity of the polymer surface, from 61.0° (10 W) to 80.7° (75 W). The polymer demonstrated a strong electron donor component and a negligible electron acceptor component and was therefore monopolar in nature. Wetting curves showed that the samples became more hydrophobic as the deposition energy was increased. Chloroform and chlorobenzene were both found to fall within the 0° boundary, indicating that they would completely wet the surface. Solubility results confirmed that the polymer would resist solubilisation from the solvents investigated.

The wettability and compatibility of pp–GT thin films with solvents utilized in the manufacturing of organic electronic devices has been investigated in this paper. From the wettability studies, it is concluded that pp–GT layers are suitable for encapsulation purpose and also for use in a variety of organic electronic devices requiring solution-processed layers.

Acknowledgments

Jakaria Ahmad greatly appreciates the financial support from the James Cook University Postgraduate Research Scholarship (JCUPRS). Kateryna Bazaka acknowledges funding from James Cook university (JCU) and Australian Research Council (ARC) (No. DE130101550).

Author Contributions

Jakaria Ahmad fabricated the thin films, performed tests, measured and assessed thin film characteristics and prepared the manuscript. Kateryna Bazaka contributed towards development of the characterization methods, data analysis and preparation of the manuscript. Michael Oelgemoeller assisted in the interpretation and analysis of the IR spectra and the preparation of this manuscript. Mohan V. Jacob coordinated and managed the project and the overall preparation of the manuscript.

Conflicts of Interest

The authors declare no conflict of interest.

References

1. Ahmafd, J.; Bazaka, K.; Anderson, L.J.; White, R.D.; Jacob, M.V. Materials and methods for encapsulation of OPV: A review. *Renew. Sustain. Energy Rev.* **2013**, *27*, 104–117.
2. Koti, R.S.; Sanjaykumar, S.R.; Hong, S.-J.; Song, C.E.; Kang, I.-N.; Lee, S.K.; Shin, W.S.; Moon, S.-J.; Lee, J.-C. 3,8-Dialkoxynaphthodithiophene based copolymers for efficient polymer solar cells. *Sol. Energy Mater. Sol. Cells* **2013**, *108*, 213–222.
3. Prakash, S.; Chakrabarty, T.; Singh, A.K.; Shahi, V.K. Polymer thin films embedded with metal nanoparticles for electrochemical biosensors applications. *Biosens. Bioelectron.* **2013**, *41*, 43–53.
4. Hierso, J.; Boy, P.; Vallé, K.; Vulliet, J.; Blein, F.; Laberty-Robert, C.; Sanchez, C. Nanostructured ceria based thin films (≤ 1 μm) as cathode/electrolyte interfaces. *J. Solid State Chem.* **2013**, *197*, 113–119.
5. Sownthari, K.; Suthanthiraraj, S.A. Synthesis and characterization of an electrolyte system based on a biodegradable polymer. *eXPRESS Polym. Lett.* **2013**, *7*, 495–504.
6. Hazrati, H.D.; Whittle, J.D.; Vasilev, K. A mechanistic study of the plasma polymerization of ethanol. *Plasma Process. Polym.* **2014**, *11*, 149–157.
7. Easton, C.D.; Jacob, M.V. Solubility and adhesion characteristics of plasma polymerized thin films derived from Lavandula angustifolia essential oil. *J. Appl. Polym. Sci.* **2010**, *115*, 404–415.
8. Bazaka, K.; Jacob, M.; Truong, V.K.; Crawford, R.J.; Ivanova, E.P. The effect of polyterpenol thin film surfaces on bacterial viability and adhesion. *Polymers* **2011**, *3*, 388–404.
9. Graham, M.; Cady, N. Nano and microscale topographies for the prevention of bacterial surface fouling. *Coatings* **2014**, *4*, 37–59.
10. Geoghegan, M.; Krausch, G. Wetting at polymer surfaces and interfaces. *Prog. Polym. Sci.* **2003**, *28*, 261–302.
11. Bollström, R.; Tuominen, M.; Määttänen, A.; Peltonen, J.; Toivakka, M. Top layer coatability on barrier coatings. *Prog. Organ. Coat.* **2012**, *73*, 26–32.
12. Farris, S.; Introzzi, L.; Biagioni, P.; Holz, T.; Schiraldi, A.; Piergiovanni, L. Wetting of biopolymer coatings: Contact angle kinetics and image analysis investigation. *Langmuir* **2011**, *27*, 7563–7574.
13. Kylián, O.; Polonskyi, O.; Kratochvíl, J.; Artemenko, A.; Choukourov, A.; Drábik, M.; Solař, P.; Slavínská, D.; Biederman, H. Control of wettability of plasma polymers by application of Ti Nano-Clusters. *Plasma Process. Polym.* **2012**, *9*, 180–187.
14. Xie, W.; Wang, J.; Berndt, C.C. Spreading Behavior and morphology of ethylene methacrylic acid (EMAA) deposits via the flame spray process. *Coatings* **2012**, *2*, 76–93.
15. Wenzel, R.N. Resistance of solid surfaces to wetting by water. *Ind. Eng. Chem.* **1936**, *28*, 988–994.
16. Cassie, A.B.D.; Baxter, S. Wettability of porous surfaces. *Trans. Faraday Soc.* **1944**, *40*, 546–551.
17. Gallezot, P. Conversion of biomass to selected chemical products. *Chem. Soc. Rev.* **2012**, *41*, 1538–1558.
18. Ostrikov, K.; Neyts, E.C.; Meyyappan, M. Plasma nanoscience: From nano-solids in plasmas to nano-plasmas in solids. *Adv. Phys.* **2013**, *62*, 113–224.

19. Michelmore, A.; Gross-Kosche, P.; Al-Bataineh, S.A.; Whittle, J.D.; Short, R.D. On the effect of monomer chemistry on growth mechanisms of nonfouling PEG-like plasma polymers. *Langmuir* **2013**, *29*, 2595–2601.
20. Irimia-Vladu, M. “Green” electronics: Biodegradable and biocompatible materials and devices for sustainable future. *Chem. Soc. Rev.* **2014**, *43*, 588–610.
21. Bazmi, A.A.; Zahedi, G. Sustainable energy systems: Role of optimization modeling techniques in power generation and supply—A review. *Renew. Sustain. Energy Rev.* **2011**, *15*, 3480–3500.
22. Pongprayoon, U.; Soontornsaratune, P.; Jarikasem, S.; Sematong, T.; Wasuwat, S.; Claeson, P. Topical antiinflammatory activity of the major lipophilic constituents of the rhizome of Zingiber cassumunar. Part I: The essential oil. *Phytomedicine* **1997**, *3*, 319–322.
23. Jacob, M.V.; Bazaka, K.; Weis, M.; Taguchi, D.; Manaka, T.; Iwamoto, M. Fabrication and characterization of polyterpenol as an insulating layer and incorporated organic field effect transistor. *Thin Solid Films* **2010**, *518*, 6123–6129.
24. Taguchi, D.; Manaka, T.; Iwamoto, M.; Bazaka, K.; Jacob, M.V. Analyzing hysteresis behavior of capacitance–voltage characteristics of IZO/C60/pentacene/Au diodes with a hole-transport electron-blocking polyterpenol layer by electric-field-induced optical second-harmonic generation measurement. *Chem. Phys. Lett.* **2013**, *572*, 150–153.
25. Anderson, L.J.; Jacob, M.V. Effect of RF power on the optical and morphological properties of RF plasma polymerised linalyl acetate thin films. *Appl. Surf. Sci.* **2010**, *256*, 3293–3298.
26. Ahmad, J.; Bazaka, K.; Jacob, M. Optical and surface characterization of radio frequency plasma polymerized 1-isopropyl-4-methyl-1,4-cyclohexadiene thin films. *Electronics* **2014**, *3*, 266–281.
27. Bazaka, K.; Jacob, M.V.; Taguchi, D.; Manaka, T.; Iwamoto, M. Investigation of interfacial charging and discharging in double-layer pentacene-based metal-insulator-metal device with polyterpenol blocking layer using electric field induced second harmonic generation. *Chem. Phys. Lett.* **2011**, *503*, 105–111.
28. Bazaka, K.; Jacob, M.V.; Truong, V.K.; Wang, F.; Pushpamali, W.A.; Wang, J.; Ellis, A.; Berndt, C.C.; Crawford, R.J.; Ivanova, E.P. Effect of plasma-enhanced chemical vapour deposition on the retention of antibacterial activity of terpinen-4-ol. *Biomacromolecules* **2010**, *11*, 2016–2021.
29. Al-Burtamani, S.K.S.; Fatope, M.O.; Marwah, R.G.; Onifade, A.K.; Al-Saidi, S.H. Chemical composition, antibacterial and antifungal activities of the essential oil of Haplophyllum tuberculatum from Oman. *J. Ethnopharmacol.* **2005**, *96*, 107–112.
30. Cheng, S.-S.; Liu, J.-Y.; Hsui, Y.-R.; Chang, S.-T. Chemical polymorphism and antifungal activity of essential oils from leaves of different provenances of indigenous cinnamon (Cinnamomum osmophloeum). *Bioresour. Technol.* **2006**, *97*, 306–312.
31. Breitmaier, E. Selected syntheses of terpenes. In *Terpenes*; Wiley-VCH Verlag GmbH & Co. KGaA: Weinheim, Germany, 2006; pp. 119–159.
32. Gengenbach, T.R.; Griesser, H.J. Deposition conditions influence the postdeposition oxidation of methyl methacrylate plasma polymer films. *J. Polym. Sci. A* **1998**, *36*, 985–1000.
33. J. A. Wllllam Co., Inc. Homepage. Available online: http://www.jawoollam.com (accessed on 3 July 2011).
34. Easton, C.D.; Jacob, M.V. Optical characterisation of radio frequency plasma polymerised Lavandula angustifolia essential oil thin films. *Thin Solid Films* **2009**, *517*, 4402–4407.

35. Marzec, K.M.; Reva, I.; Fausto, R.; Proniewicz, L.M. Comparative matrix isolation infrared spectroscopy study of 1,3- and 1,4-Diene monoterpenes (α-Phellandrene and γ-Terpinene). *J. Phys. Chem. A* **2011**, *115*, 4342–4353.
36. O'Toole, L.; Beck, A.J.; Ameen, A.P.; Jones, F.R.; Short, R.D. Radiofrequency-induced plasma polymerisation of propenoic acid and propanoic acid. *J. Chem. Soc. Faraday Trans.* **1995**, *91*, 3907–3912.
37. Watts, J.F. High resolution XPS of organic polymers: The Scienta ESCA 300 database. G. Beamson and D. Briggs. 280pp., £65. John Wiley & Sons, Chichester, ISBN 0471 935921, (1992). *Surf. Interface Anal.* **1993**, *20*, 267–267.
38. Strobel, M.; Lyons, C.S. An essay on contact angle measurements. *Plasma Process. Polym.* **2011**, *8*, 8–13.
39. Yuan, Y.; Lee, T.R. Contact angle and wetting properties. In *Surface Science Techniques*; Bracco, G., Holst, B., Eds.; Springer: Berlin, Germany, 2013; Volume 51, pp. 3–34.
40. Pogorzelski, S.J.; Rochowski, P.; Szurkowski, J. Pinus sylvestris L. needle surface wettability parameters as indicators of atmospheric environment pollution impacts: Novel contact angle hysteresis methodology. *Appl. Surf. Sci.* **2014**, *292*, 857–866.
41. Chibowski, E. Surface free energy of a solid from contact angle hysteresis. *Adv. Colloid Interface Sci.* **2003**, *103*, 149–172.
42. Good, R.J. Estimation of surface energies from contact angles. *Nature* **1966**, *212*, 276–277.
43. Van Oss, C.J. Long-range and short-range mechanisms of hydrophobic attraction and hydrophilic repulsion in specific and aspecific interactions. *J. Mol. Recognit.* **2003**, *16*, 177–190.
44. Kwok, D.Y.; Neumann, A.W. Contact angle measurement and contact angle interpretation. *Adv. Colloid Interface Sci.* **1999**, *81*, 167–249.
45. Shalel-Levanon, S.; Marmur, A. Validity and accuracy in evaluating surface tension of solids by additive approaches. *J. Colloid Interface Sci.* **2003**, *262*, 489–499.
46. Deshmukh, R.R.; Shetty, A.R. Comparison of surface energies using various approaches and their suitability. *J. Appl. Polym. Sci.* **2008**, *107*, 3707–3717.
47. Fowkes, F.M. Additivity of intermolecular forces at interfaces. I. Determination of the contribution to surface and interfacial tensions of dispersion forces in various liquids. *J. Phys. Chem.* **1963**, *67*, 2538–2541.
48. Tavana, H.; Neumann, A.W. Recent progress in the determination of solid surface tensions from contact angles. *Adv. Colloid Interface Sci.* **2007**, *132*, 1–32.
49. Zenkiewicz, M. Methods for the calculation of surface free energy of solids. *J. Achiev. Mater. Manuf. Eng.* **2007**, *24*, 137–145.
50. Fowkes, F.M. Donor-Acceptor interactions at interfaces. *J. Adhes.* **1972**, *4*, 155–159.
51. Fowkes, F.M. Attractive forces at interfaces. *Ind. Eng. Chem.* **1964**, *56*, 40–52.
52. Daferera, D.J.; Tarantilis, P.A.; Polissiou, M.G. Characterization of essential oils from lamiaceae species by fourier transform raman spectroscopy. *J. Agric. Food Chem.* **2002**, *50*, 5503–5507.
53. Schulz, H.; Özkan, G.; Baranska, M.; Krüger, H.; Özcan, M. Characterisation of essential oil plants from Turkey by IR and Raman spectroscopy. *Vib. Spectrosc.* **2005**, *39*, 249–256.
54. Lopez, G.P.; Ratner, B.D. Substrate temperature effects on film chemistry in plasma deposition of organics. I. Nonpolymerizable precursors. *Langmuir* **1991**, *7*, 766–773.

55. Coates, J. Interpretation of infrared spectra, a practical approach. In *Encyclopedia of Analytical Chemistry*; John Wiley & Sons, Ltd.: Hoboken, NJ, USA, 2006.
56. Bazaka, K.; Jacob, M.V. Post-deposition ageing reactions of plasma derived polyterpenol thin films. *Polym. Degrad. Stab.* **2010**, *95*, 1123–1128.
57. Shi, L. The investigation of polymer surface dynamics modified by plasma using dynamic contact angle method. *Eur. Polym. J.* **2000**, *36*, 987–992.
58. Olivares-Navarrete, R.; Olaya, J.J.; Ramírez, C.; Rodil, S.E. Biocompatibility of niobium coatings. *Coatings* **2011**, *1*, 72–87.
59. Alexander, M.R.; Duc, T.M. A study of the interaction of acrylic acid/1,7-octadiene plasma deposits with water and other solvents. *Polymer* **1999**, *40*, 5479–5488.
60. Semenov, S.; Starov, V.M.; Rubio, R.G.; Agogo, H.; Velarde, M.G. Evaporation of sessile water droplets: Universal behaviour in presence of contact angle hysteresis. *Colloids Surf. A Physicochem. Eng. Asp.* **2011**, *391*, 135–144.
61. Holly, F.J.; Refojo, M.F. Wettability of hydrogels. I. Poly (2-hydroxyethyl methacrylate). *J. Biomed. Mater. Res.* **1975**, *9*, 315–326.
62. Podestà, A.; Indrieri, M.; Brogioli, D.; Manning, G.; Milani, P.; Guerra, R.; Finzi, L.; Dunlap, D. Positively charged surfaces increase the flexibility of DNA. *Biophys. J.* **2005**, *89*, 2558–2563.
63. Busscher, H.J.; van Pelt, A.W.J.; de Boer, P.; de Jong, H.P.; Arends, J. The effect of surface roughening of polymers on measured contact angles of liquids. *Colloids Surf.* **1984**, *9*, 319–331.
64. Hitchcock, S.J.; Carroll, N.T.; Nicholas, M.G. Some effects of substrate roughness on wettability. *J. Mater. Sci.* **1981**, *16*, 714–732.
65. Wu, S.; Shanks, R.A. Solubility study of polyacrylamide in polar solvents. *J. Appl. Polym. Sci.* **2004**, *93*, 1493–1499.
66. Van Oss, C.J.; Chaudhury, M.K.; Good, R.J. Monopolar surfaces. *Adv. Colloid Interface Sci.* **1987**, *28*, 35–64.
67. Wu, W.; Giese, R.F., Jr.; van Oss, C.J. Evaluation of the lifshitz-van der waals/acid-base approach to determine surface tension components. *Langmuir* **1995**, *11*, 379–382.
68. Anderson, L.; Easton, C.; Jacob, M. Compatibility of plasma-deposited linalyl acetate thin films with organic electronic device fabrication techniques. *J. Mater. Sci.* **2013**, *48*, 4851–4859.
69. Bazaka, K.; Jacob, M.V. Solubility and surface interactions of RF plasma polymerized polyterpenol thin films. *Mater. Express* **2012**, *2*, 285–293.
70. De Gennes, P.G. Wetting: Statics and dynamics. *Rev. Mod. Phys.* **1985**, *57*, 827–863.
71. Wobkenberg, P.H.; Ball, J.; Kooistra, F.B.; Hummelen, J.C.; de Leeuw, D.M.; Bradley, D.D.C.; Anthopoulos, T.D. Low-voltage organic transistors based on solution processed semiconductors and self-assembled monolayer gate dielectrics. *Appl. Phys. Lett.* **2008**, *93*, doi:10.1063/1.2954015.
72. Cheng, X.; Caironi, M.; Noh, Y.-Y.; Newman, C.; Wang, J.; Lee, M.J.; Banger, K.; Pietro, R.D.; Facchetti, A.; Sirringhaus, H. Downscaling of *n*-channel organic field-effect transistors with inkjet-printed electrodes. *Org. Electron.* **2012**, *13*, 320–328.